UNIVERSITY OF CALIFORNIA SAN DIEGO

# Intense Proton Beam Heating and Transport in Dense Plasmas

A dissertation submitted in partial satisfaction of the
requirements for the degree
Doctor of Philosophy

in

Engineering Sciences (Engineering Physics)

by

Krish Ashvin Bhutwala

Committee in charge:

Farhat N. Beg, Chair
Alexey Arefiev
Christopher Holland
Antonio Sanchez
Mark Sherlock
Clifford Surko

2023

The dissertation of Krish Ashvin Bhutwala is approved, and it is acceptable in quality and form for publication on microfilm and electronically.

University of California San Diego

2023

# EPIGRAPH

*The highest forms of understanding we can achieve*

*are laughter and human compassion.*

— Richard P. Feynman

TABLE OF CONTENTS

LIST OF FIGURES

LIST OF TABLES

ACKNOWLEDGEMENTS

First I must thank my advisor, Farhat Beg, for agreeing to meet a young man aimlessly looking for his next step in life. The day he brought me on as a graduate student catapulted my scientific career, and I consider myself incredibly fortunate for all the opportunities he has given me since then. To my mentors Chris McGuffey, Joohwan Kim, and Mathieu Bailly-Grandvaux, I wholeheartedly appreciate your patience and guidance. I would be remiss if I did not also thank my peers along the way — Joe Strehlow, Nick Aybar, and Brandon Edghill. It's a tragedy that the pandemic hit and we couldn't follow each other's journeys in person, but I'll cherish our late nights finishing homework in the office, and conversations that were simultaneously meaningless and profound. I'm proud that I can still call you my close friends and former groomsmen.

To my wife, my best friend, who always had faith in me to persevere, even when I started to lose faith in myself. Marrying you was the singular best decision I have ever made. Despite our different fields, you inspire me to work harder and smarter than I thought I could. Still, I can always depend on winding down to our evenings cooking together, even when my "just wing it" attitude collides with your "follow the recipe" perspective. Exploring the food scenes with you in Los Angeles, San Diego, and Denver has made up core memories in my adult life, and I'm so grateful that we can explore the world together in the years to come. Thank you for supporting my dreams and making me a better person.

It takes a village, and my village is the reason I was able to complete this journey. I could not have thought of a better group of friends to lean on and laugh with than my day-ones from UCLA. As our lives settle in, I know that our reunions big or small will always be a source of joy and excitement in my life. To my parents, even though they would not understand a word of this dissertation, thank you for allowing me to pursue my passion for physics. I know this wasn't an easy career path for you to follow along with, but I hope I've made you proud regardless. Thanks also to my brother Neil, "for (not) bugging me all the time."

Lastly, I owe my entire love of math and science to my Raju uncle. Thank you for showing

me and Neil that thinking outside the box is not only fun, but also makes for success in life. I hope you know that those nightly walks of talking, laughing, and pondering your riddles will never be forgotten.

Chapter 5 contains a partial reprint as it appears in "Development of a platform at the matter in extreme conditions end station for characterization of matter heated by intense laser-accelerated protons" by **K. Bhutwala**, M. Bailly-Grandvaux, J. Kim, M. Dozières, E. Galtier, C. B. Curry, M. Gauthier, E. Cunningham, H. J. Lee, P. Forestier-Colleoni, A. Higginson, N. Aybar, R. Hua, B. Edghill, J. Strehlow, G. M. Dyer, S. H. Glenzer, J. B. Kim, N. Alexander, E. Del Rio, M. S. Wei, Y. Ping, A. McKelvey, G. W. Collins, F. N. Beg and C. McGuffey in *IEEE Transactions on Plasma Science* 48(8), 2751-2758 (2020). The dissertation author was the primary investigator and author of this publication. This work was supported in part by the U.S. DOE FES under Grants DE-SC0018253, FWP-100182 and SF-00515, in part by the University of California Office of the President Lab Fee under Grant LFR-17-449059, and in part by the U.S. DOE, Office of Science, Office of Basic Energy Sciences, under Grant DE-AC02-76SF00515. The work of Krish Bhutwala was supported by the U.S. DOE NNSA under Grant DE-NA0003876.

Chapter 6 contains a partial reprint as it appears in "Transport of an intense proton beam from a cone-structured target through plastic foam with unique proton source modeling" by **K. Bhutwala**, C. McGuffey, W. Theobald, O. Deppert, J. Kim, P. M. Nilson, M. S. Wei, Y. Ping, M. E. Foord, H. S. McLean, P. K. Patel, A. Higginson, M. Roth and F. N. Beg in *Physical Review E* 105(5), 055206 (2022). The dissertation author was the primary investigator and author of this publication. This material is based upon work supported by the U.S. DOE NNSA under the National Laser User Facility program with Award No. DE-NA0002034, the Laboratory Basic Science program, and the High Energy Density Laboratory Plasmas program with Award No. DE-NA0003876.

Chapter 7 contains a partial reprint as it appears in "Investigation of Resistive Magnetic Field Generation by Intense Proton Beams in Dense Plasmas" by **K. Bhutwala**, J. Kim, C.

McGuffey, M. Sherlock, M. Bailly-Grandvaux, and F. N. Beg in *Physics of Plasmas* 29(11), 113103 (2022). The dissertation author was the primary investigator and author of this publication.

This work was partially supported under the auspices of the U.S. DOE NNSA High Energy Density Laboratory Plasmas program by the University of California under Contract No. DE-NA0003876.

## VITA

| | |
|---|---|
| 2014 | B. Sc. in Physics & Applied Mathematics, University of California Los Angeles |
| 2016-2023 | Graduate Student Researcher, University of California San Diego |
| 2019 | M. S. in Engineering Sciences (Engineering Physics), University of California San Diego |
| 2023 | PhD in Engineering Sciences (Engineering Physics), University of California San Diego |

## PUBLICATIONS

**K. Bhutwala**, J. Kim, C. McGuffey, M. Sherlock, M. Bailly-Grandvaux, and F. N. Beg. "Investigation of Resistive Magnetic Field Generation by Intense Proton Beams in Dense Plasmas." *Physics of Plasmas* 29(11), 113103 (2022).

C. McGuffey, **K. Bhutwala**, R. F. Heeter, E. Marley, M. Bailly-Grandvaux, J. Emig, A. Higginson, J. Kim, R. C. Mancini, D. Mariscal, S. Fess, P. M. Nilson, W. Theobald, J. Vaughan, D. Zimmer and F. N. Beg. "Creation of warm, dense Si by rapid heating with intense, laser-driven protons and characterization by K-shell absorption spectroscopy." *Physical Review Letters* (Under Review).

**K. Bhutwala**, C. McGuffey, W. Theobald, O. Deppert, J. Kim, P. M. Nilson, M. S. Wei, Y. Ping, M. E. Foord, H. S. McLean, P. K. Patel, A. Higginson, M. Roth and F. N. Beg. "Transport of an intense proton beam from a cone-structured target through plastic foam with unique proton source modeling." *Physical Review E* 105(5), 055206 (2022).

S. Malko, W. Cayzac, V. Ospina-Bohorquez, **K. Bhutwala**, M. Bailly-Grandvaux, C. McGuffey, R. Fedosejevs, X. Vaisseau, An. Tauschwitz, J. I. Apiñaniz, D. De Luis Blanco, G. Gatti, M. Huault, J. A. Perez-Hernandez, S. X. Hu, A. J. White, L. A. Collins, K. Nichols, P. Neumayer, G. Faussurier, J. Vorberger, G. Prestopino, C. Verona, J. J. Santos, D. Batani, F. N. Beg, L. Roso and L. Volpe. "Proton stopping measurements at low velocity in warm dense carbon." *Nature Communications* 13(1), 1-12 (2022).

J. I. Apiñaniz, S. Malko, R. Fedosejevs, W. Cayzac, X. Vaisseau, D. De Luis, G. Gatti, C. McGuffey, M. Bailly-Grandvaux, **K. Bhutwala**, V. Ospina-Bohorquez, J. Balboa, J. J. Santos, D. Batani, F. N. Beg, L. Roso, J. A. Perez-Hernandez and L. Volpe. "A quasi-monoenergetic short time duration compact proton source for probing high energy density states of matter." *Scientific Reports* 11(1), 1-11 (2021).

A. Higginson, S. Zhang, M. Bailly-Grandvaux, C. McGuffey, **K. Bhutwala**, B. J. Winjum, J. Strehlow, B. Edghill, M. Dozières, F. S. Tsung, R. Lee, S. Andrews, S. J. Spencer, N. Lemos, F. Albert, P. King, M. S. Wei, W. B. Mori, M. J.-E Manuel and F. N. Beg. "Electron acceleration at oblique angles via stimulated Raman scattering at laser irradiance $> 10^{16}$ $W$ $cm^{-2}$ $\mu m^2$." *Physical Review E* 103(3), 033203 (2021).

D. Kawahito, M. Bailly-Grandvaux, M. Dozières, C. McGuffey, P. Forestier-Colleoni, J. Peebles, J. J. Honrubia, B. Khiar, S. Hansen, P. Tzeferacos, M. S. Wei, C. M. Krauland, P. Gourdain, J. R. Davies, K. Matsuo, S. Fujioka, E. M. Campbell, J. J. Santos, D. Batani, **K. Bhutwala**, S. Zhang and F. N. Beg. "Fast electron transport dynamics and energy deposition in magnetized, imploded cylindrical plasma." *Philosophical Transactions of the Royal Society A* 379(2189), 20200052 (2021).

**K. Bhutwala**, M. Bailly-Grandvaux, J. Kim, M. Dozières, E. Galtier, C. B. Curry, M. Gauthier, E. Cunningham, H. J. Lee, P. Forestier-Colleoni, A. Higginson, N. Aybar, R. Hua, B. Edghill, J. Strehlow, G. M. Dyer, S. H. Glenzer, J. B. Kim, N. Alexander, E. Del Rio, M. S. Wei, Y. Ping, A. McKelvey, G. W. Collins, F. N. Beg and C. McGuffey. "Development of a platform at the matter in extreme conditions end station for characterization of matter heated by intense laser-accelerated protons." *IEEE Transactions on Plasma Science* 48(8), 2751-2758 (2020).

M. Dozières, S. Hansen, P. Forestier-Colleoni, C. McGuffey, D. Kawahito, M. Bailly-Grandvaux, **K. Bhutwala**, C. M. Krauland, M. S. Wei, P. Gourdain, J. R. Davies, K. Matsuo, S. Fujioka, E. M. Campbell, J. L. Peebles, J. J. Santos, D. Batani, S. Zhang and F. N. Beg. "Characterization of an imploding cylindrical plasma for electron transport studies using x-ray emission spectroscopy." *Physics of Plasmas* 27(2), 023302 (2020).

ABSTRACT OF THE DISSERTATION

**Intense Proton Beam Heating and Transport in Dense Plasmas**

by

Krish Ashvin Bhutwala

Doctor of Philosophy in Engineering Sciences (Engineering Physics)

University of California San Diego, 2023

Farhat N. Beg, Chair

Intense proton beams driven by high-intensity lasers have several applications in high energy density science, including radiographing laboratory plasmas, producing secondary neutron sources, and generating extreme states of matter. Proton fast ignition (FI) for thermonuclear fusion is also an important potential application that requires proton beam intensities at or above $10^{12}\ A/cm^2$, higher than current capabilities. With greater beam intensities, however, come beam collective effects, requiring further investigations in beam transport and energy deposition. This dissertation describes experimental, computational, and theoretical studies of proton transport and energy deposition in warm and hot dense plasmas.

Towards generating extreme states of matter, an experiment conducted at the Matter

in Extreme Conditions (MEC) end-station at SLAC National Accelerator Laboratory showed that thin Al samples were heated by protons to approximately 1 $eV$, establishing a platform on which to further study intense proton heating as well as properties of warm and hot dense matter. Simulations further showed that the proton heating in the experiment was isochoric and that even higher temperatures may be reached with higher laser energy and focused proton beams.

Toward investigating the transport of intense protons beams through a coronal plasma, a second experiment on the OMEGA-EP laser at the Laboratory for Laser Energetics (LLE) imaged the proton beam cross section at various ($\sim mm$) depths within a plastic foam of comparable density. Simulations and post-processing were conducted to distinguish between the proton and electron beam cross-sections, revealing that protons retain their beam qualities while electrons scatter and contribute to an overall background emission. This study corroborates a major underlying assumption in FI that protons are less likely than electrons to scatter in their transport through coronal plasma. As previously mentioned, beam collective effects may alter this transport at higher intensities, even if scattering does not. For the first time, a theoretical model for resistive magnetic field generation for intense proton beams has been developed. Due to gradients in (coupled) sample temperature and beam current density, magnetic fields above 100 $T$ may be generated by proton beams with total energy 10 $J$. When considering the time-of-flight of laser-driven Maxwellian beams (not unlike proton FI), the model predicts an interesting self-similar evolution of the magnetic field with respect to the distance between proton source and sample foil.

This work has significant implications for the proton fast ignition scheme of inertial confinement fusion. For the necessary proton beam requirements to heat a dense fusion fuel to ignite, this work implies that beam transport and energy deposition will not be as trivial as previous studies have assumed. Indeed, these results motivate further studies on the transport of ultrahigh current density beams resulting from self-generated electromagnetic fields.

# Chapter 1

# Introduction

Energy is a peculiar thing. Theoretically, it is connected to the passage of time on unfathomably deep and profound scales. But at the same time, it is observable in our everyday lives, so much so that the layman gives it no second thought. In the modern age, it is a non-negotiable and readily assembled resource that powers daily life. To our knowledge, it is neither created nor destroyed; it only ever manifests different forms, and therein lies the key. Humankind's pursuit to make life easier and to understand nature have been accelerated by machinery that converts energy in some form (wind, hydro, solar, heat, chemical etc.) into work. The sources of our energy, therefore, play a grand role in guiding our society.

Figs. 1.1 shows the global energy consumption by source from the year 1800 (estimated consumption) until now. Since the industrial revolution, not only has the global energy consumption increased, but the rate of energy consumption across all sources is also increasing (1). This exponential growth of 3% on average per year implies that whatever sources we use today and in the future, they must be sustainable and scalable. For over a century, almost all of our energy has come from fossil fuels – coal, natural gas, crude oil and petroleum products. Apart from the geopolitical issues tangled with fossil fuels, they are now known to be an unsustainable energy source due to its limited quantities and severely negative climate impacts (30).

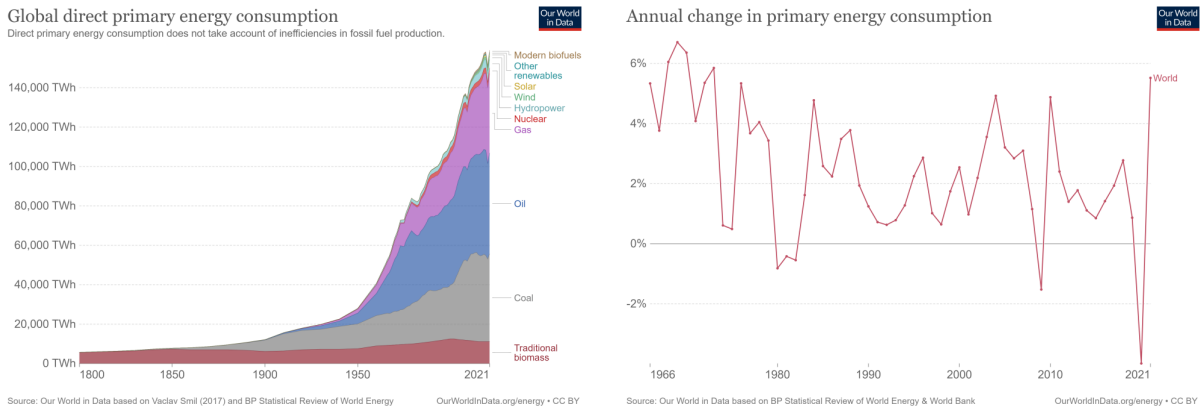


**Figure 1.1**: (a) Global annual energy consumption categorized by energy source, and (b) year-on-year percentage increase in global energy consumption. Data taken from Ref. (1).

Currently, the most sustainable alternative to fossil fuels is arguably nuclear energy for several reasons. Unlike nuclear fission fuel, most notably Uranium-235 which may be produced year-round, solar and wind energy largely depend on ambient weather conditions in the area. Per kilogram, U-235 contains 2-3 million times the usable energy in oil or coal, making it a much more fruitful energy source. This is fundamentally because the chemical energy extracted from fossil fuels originates in chemical bonds with energy scale $\sim eV$ per reaction, as opposed to the nuclear energy scaling of $\sim MeV$ per reaction. Even better, it is a near carbon emission-free source, and therefore has little climate impact. Nevertheless, nuclear fission has its drawbacks. For one, uranium is non-renewable and available in only finite quantities in the earth's crust. The largest issues, though, are the cost of nuclear power plant construction (which indirectly points toward public convincing of their safety and efficacy) and the proper disposal of radioactive nuclear waste. Suffice it to say that the process is complex and poses environmental and health risks in the long term.

On a subatomic scale, nuclear *fission* is the process by which unstable heavy elements split into two or more elements and release energy. The energy released is determined by the nuclear binding energy of the reactants and products. For an element with atomic number $Z$ and

mass number $A$, the nuclear binding energy $E_B$ is given by:

$$E_B = Zm_p c^2 + (A-Z)m_n c^2 - Mc^2 \tag{1.1}$$

where $m_p$, $m_n$, and $M$ are the proton mass, neutron mass, and nuclear mass, respectively. The higher the binding energy, the more stable the nucleus. The binding energy per nucleon $E_B/A$ is a good measure of nuclear stability and is shown in Fig. 1.2 over increasing mass number. Essentially, an increase in binding energy from reactants to products leads to a release of energy. Current nuclear power plants, thus, take advantage of heavy elements naturally decaying.

Nuclear *fusion*, on the other hand, may be an even more sustainable energy resource by bypassing all the obstacles of nuclear fission plants listed above. As shown in Fig. 1.2, fusion works opposite to fission in that energy is released when two light nuclei fuse together to create a more stable nucleus. The four most effective fusion reactions (for reasons that will be made clear later) are:

$$\begin{aligned}
\mathrm{D} + \mathrm{T} &\longrightarrow \alpha\,(3.52\,MeV) + n\,(14.06\,MeV) \\
\mathrm{D} + \mathrm{D} &\longrightarrow \mathrm{T}\,(1.01\,MeV) + p\,(3.02\,MeV) \quad (50\%) \\
&\longrightarrow {}^3\mathrm{He}\ (0.82\ \mathrm{MeV}) + n\,(2.45\,MeV) \quad (50\%) \\
\mathrm{D} + {}^3\mathrm{He} &\longrightarrow \alpha\,(3.6\,MeV) + p\,(14.7\,MeV)
\end{aligned}$$

where **D**euterium is $^2$H, **T**ritium is $^3$H, and an $\alpha$ particle is $^4$He. Immediately, we observe that the most common products in fusion reactions are less hazardous than the radioactive isotopes of heavier fission products. As well, deuterium is simply obtained via industrial extraction from seawater, and tritium may be produced by the fission of $^6$Li by neutrons.

But for all the clean energy that fusion promises, it is a monumental challenge to obtain controlled net energy surplus, let alone that on a commercial scale. Fusion may occur on colossal scales throughout our universe — indeed, this is how heavier elements were first formed in the early stages of the universe, and our own sun is powered by fusion — but these processes rely

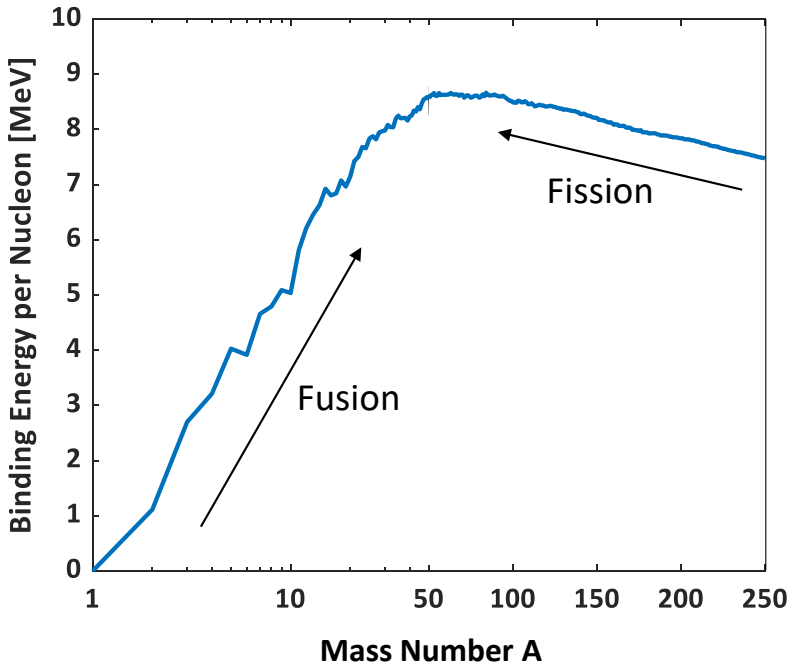


**Figure 1.2**: Nuclear binding energy per nucleon as a function of nuclear weight. Data taken from Ref. (2) and plotted in the style of Ref. (3).

on enormous length, time and mass scales untenable on Earth. The easiest way to accomplish significantly large gains on Earth is with (*uncontrollable*) hydrogen bombs. Our challenge, then, is to essentially create and harness the extreme conditions of the sun or a nuclear bomb on a smaller scale, in controlled laboratory setting. The next section discusses the fundamentals with which we may go about this analysis, and the experimental schemes that currently look most promising.

## 1.1 Fundamentals of Nuclear Fusion

A fundamental characteristic of fusion reactions is the cross section $\sigma$ of target particles of, say, type 1. For now, this represents the cross sectional area of that particle, but can be related to the probability of fusion reaction with beam particles (of type 2) in the following way. If target particles with density $n_1$ and area $A$ occupy a volume $dV = Adx$ in the way of beam particles,

then the probability of beam particles colliding with the volume is $dP = (n_1 dV)\sigma/A = n_1 \sigma dx$. The number of beam particles with density $n_2$ and velocity $v_2$ going through the volume is $dN_2 = n_2 A dx = n_2 A(v_2 dt)$ in a time $dt$. Then, we expect that the reaction rate (number of collisions per time) per unit volume is:

$$R_{12} = \frac{dN_2 dP}{dV dt} = n_1 n_2 \sigma v_2$$

Assuming both species have distribution functions $f_1(\mathbf{r}, \mathbf{v}_1, t)$ and $f_2(\mathbf{r}, \mathbf{v}_2, t)$ (see Sec. 2.1), and that the cross section depends on relative velocity $\sigma = \sigma(|\mathbf{v}_2 - \mathbf{v}_1|)$, we may generalize this to:

$$R_{12} = n_1 n_2 \langle \sigma v \rangle_{12} \tag{1.2}$$

where

$$\langle \sigma v \rangle_{12} = \frac{1}{n_1 n_2} \int d^3\mathbf{v}_1 \, d^3\mathbf{v}_2 \, f_1(\mathbf{r}, \mathbf{v}_1, t) f_2(\mathbf{r}, \mathbf{v}_2, t) \sigma(|\mathbf{v}_2 - \mathbf{v}_1|) |\mathbf{v}_2 - \mathbf{v}_1|$$

is the density-normalized *reactivity* of the reactants.

So, given the densities of two fusion reactants, most commonly deuterium (D) and/or tritium (T), to maximize the rate of fusion reactions, one must maximize the reactivity of the fuel. Apart from that, it is easy to check that the fractional mix of reactant species densities that yields the maximum reaction rate is a 50-50 mix. The evaluation of reactivity is vastly simplified if we assume both species have uniform density $n_i$ and have thermally equilibrated to a Maxwell-Boltzmann distribution function:

$$f_i(v) = n_i \left( \frac{m_i}{2\pi k_B T} \right)^{3/2} \exp\left( -\frac{m_i v^2}{2 k_B T} \right) \tag{1.3}$$

at temperature $T$. An analytic approximation for the reactivity for several common pairs of fusion reactants as functions of ion temperature is shown in Fig. 1.3. Clearly, DT reactions reach the highest reactivity, and begin to do so at temperatures of a few $keV$, the lowest compared to the

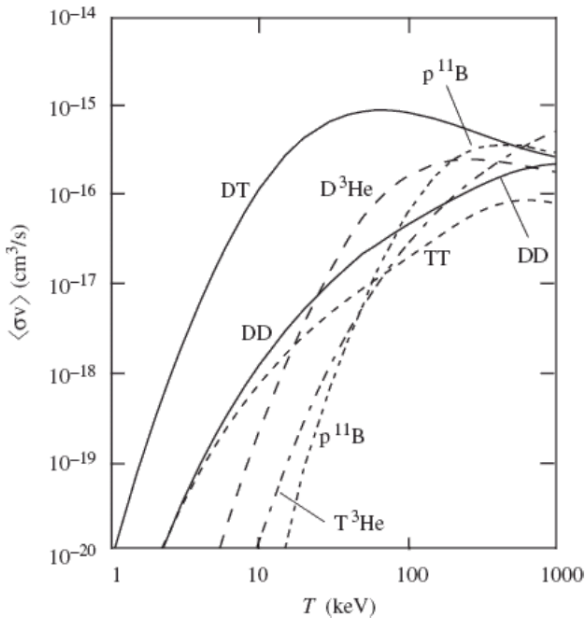


**Figure 1.3**: Reactivity of common pairs of fusion reactants as a function of temperature. Data taken from Ref. (3).

other fusion pairings. For this reason, most efforts towards achieving fusion have focused on igniting DT fuels.

But the nuclear fuel must also be self-sustaining in order to be a viable energy source. In other words, a fusion burn must generate enough energy to power external loads and maintain its fuel-burning temperatures as established above, while also overcoming energy losses. Using Eq. 1.2 We can estimate the power generated per unit volume from DT reactions as:

$$P_{fus} = R_{DT} Q_{DT} = \frac{n^2}{4} \langle \sigma v \rangle_{DT} \; Q_{DT} \tag{1.4}$$

where $n$ is the total fuel density $(n_D = n_T = n/2)$ and $Q_{DT}$ is the usable energy per reaction. For DT reactions, the neutron energy 14.1 $MeV$ is considered the usable energy since neutrons may freely escape, and the alpha particle energy 3.5 $MeV$ is used to self-heat the fuel. Radiative cooling due to *bremsstrahlung emission* from electrons is the primary mechanism for energy loss

in a fully ionized plasma, having a power loss per unit volume:

$$P_{brem} \propto n_e^2 T^{1/2} \tag{1.5}$$

We see that the reactivity must be large enough for the energy generation due to fusion to exceed the energy losses. This is embodied in the *Lawson Criterion*, originally calculated for magnetic confinement devices in Ref. (31) but generally applicable to thermonuclear fusion with a hot plasma. In essence, the fusion fuel must yield enough energy in a time dictated by the confinement configuration. In its original form, the fuel density $n$ and confinement time $\tau_c$ are related such that $n\tau_c$ must exceed a minimum value.

The critical issue, then, is to identify a confinement scheme for such a hot plasma in the necessary time. One overarching scheme is dubbed magnetic confinement fusion (MCF), in which particles are heated to the required temperatures and trapped by coiling magnetic field lines. This is most commonly done with a toroidal (donut) configuration in a tokamak device, where "toroidal" magnetic field lines combine with "poloidal" field lines so that a fusion plasma flows in a helical trajectory whose axis is normal to the cross sectional disks of the toroid. In general, MCF confines low-density plasmas with density $n \sim 10^{14}\ cm^{-3}$ in confinement times $\tau_c \sim$ seconds to minutes to satisfy the Lawson Criterion. In attempting to reach viable fusion energy, tokamaks run into issues of plasma instabilities relating to the inner walls.

On December 5, 2022, more energy was generated from a fusion burn than was used to ignite it, surpassing scientific breakeven in a controlled nuclear fusion test for the first time in history. A monumental achievement for fusion energy research in its own right, this was accomplished not from MCF, but from 192 high-intensity lasers housed in the National Ignition Facility (NIF) at Lawrence Livermore National Laboratory (LLNL). In an alternative confinement scheme, these lasers indirectly drove the the radial compression of a spherical capsule containing fusion fuel, igniting a fusion plasma within. By spherically irradiating the capsule, confinement

is achieved via the capsule's own inertia, hence the name inertial confinement fusion (ICF). This scheme as well as important variations will be explained in the following section.

## 1.2 Inertial Confinement Fusion

In ICF, a spherical capsule approximately 2 *mm* in diameter has three distinct layers for three essential purposes. The outermost thin shell is made of carbon, beryllium, or plastic to contain the fusion fuel inside and absorb the incident energy and ablate, hence the ablation layer. In *direct-drive* ICF, high-intensity lasers ($\sim 10^{14}\ W/cm^2$) uniformly irradiate this outer shell, causing a thin layer to ablate radially outward. This outward ablation has a rocket-like effect on the remaining shell, spherically compressing it and everything within. In *indirect-drive* ICF, the lasers instead irradiate the inner walls of a cylindrical *hohlraum*, made of a high-Z material (most often gold), which encompasses the capsule. As the hohlraum absorbs the laser energy, an x-ray bath is generated which more uniformly drives the rocket-like reaction to spherically implode the capsule as described above.

Regardless of the driver of the compression, directly underneath the capsule's ablation shell is a layer of frozen DT fuel making up the majority of the fuel mass to be burned. Within this DT ice layer, low-density ($\lesssim 1\ mg/cm^{-3}$) DT gas occupies the remainder of the capsule. As the DT ice is compressed by the ablation layer, the gas cannot escape and is thus also compressed. As $PdV$ work is done on the gas, its internal energy i.e. temperature increases until the pressure matches that of the compressed DT ice in an isobaric phase called stagnation. At this point, the temperature of the DT gas is at several *keV*, enough to spark the fusion reactions and form a *hot spot*. This implosion and stagnation evolution is depicted in Fig. 1.4, taken from a 1-D spherical simulation (3).

Following Rosen *et al.* (32) the confinement time for ICF may be estimated by assuming a capsule to be in the stagnation phase described above. Then, the amount of time before the hot

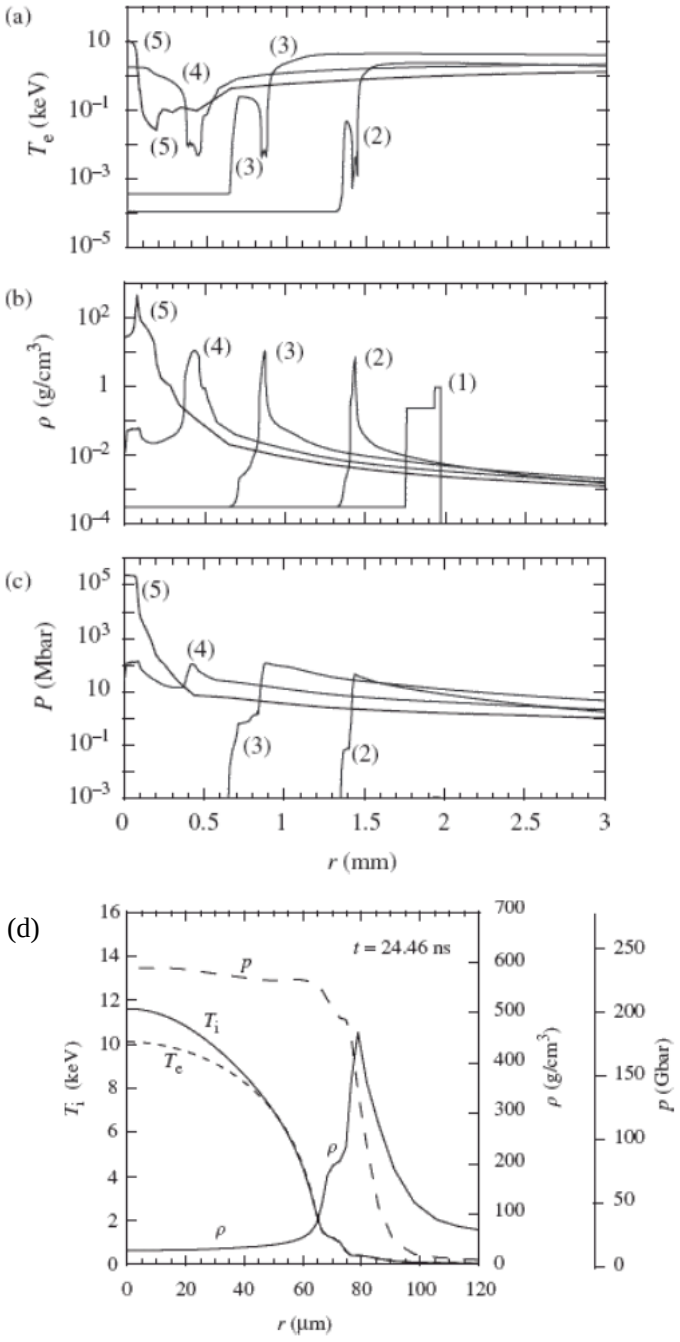


**Figure 1.4**: Evolution of radial profiles of electron temperature (a), density (b), and pressure (c) at (1) $t = 0$; (2) $t = 20$ *ns*, (3) $t = 22.4$ *ns*; (4) $t = 23.6$ *ns*; and (5) stagnation time $t = 24.46$ *ns* within capsule. (d) Capsule hot spot profiles at stagnation time $t = 24.46$ *ns*. Data taken from Ref. (3).

spot "realizes" there is a vacuum to expand into is dictated by the speed at which a rarefaction wave from the capsule surface can "communicate" this information. For a capsule with radius $R$, temperature $T$ and average DT mass $m_{DT} = 2.5\ amu$, the wave has sound speed $c_s \propto \sqrt{T/m_{DT}}$, so the confinement time is of order $\tau_c \propto R/c_s$. Assuming a uniform and constant density, a quick integration shows that:

$$\tau_c = R/4c_s \tag{1.6}$$

to account for the greater mass at larger radii.

In this confinement time between stagnation and fuel disassembly, as many fusion reactions as possible must take place. Following from the definition of reactivity in Eq. 1.2, we can calculate the burn rate of the DT fuel:

$$\frac{dn}{dt} = -\frac{n^2}{2}\langle\sigma v\rangle \tag{1.7}$$

Here we again assume that the total density is $n = 2n_T = 2n_D$ for a 50-50 mixture of deuterium and tritium, and that temperature is mostly constant until fuel disassembly. We solve this by integrating with time to obtain:

$$\frac{n(t)}{n_0} = \left(1 + \frac{n_0\langle\sigma v\rangle t}{2}\right)^{-1}$$

for initial fuel density $n_0$. The burn fraction of the fuel is defined by $f_b = 1 - n/n_0$, which, within a confinement time $\tau_c$, becomes:

$$f_b = 1 - \frac{n(\tau_c)}{n_0} = \frac{\frac{1}{2}\langle\sigma v\rangle n_0\tau_c}{1 + \frac{1}{2}\langle\sigma v\rangle n_0\tau_c}.$$

Noting that the fuel mass density is $\rho = nm_{DT}$ and plugging in Eq. 1.6, we obtain:

$$f_b = \frac{\rho R}{\rho R + \beta(T)} \tag{1.8}$$

where $\beta(T) = 8m_{DT}c_s/\langle\sigma v\rangle$ is primarily temperature-dependent (recall that $\langle\sigma v\rangle$ is *density-normalized*), approximately 6.0 $g/cm^2$ for 30 $keV$ fuel temperatures. For high gain, an appropriate burn fraction is $f_b \geq 1/3$, making our $\rho R \geq 3\ g/cm^2$. In essence, this is the ICF version of the Lawson Criterion insofar as a minimum burn fraction requires a minimum value of $\rho R \propto n\tau_c$ as mentioned in Sec. 1.1.

However, this applies to heating the entire fuel mass to 10 $keV$. In the conventional ICF scheme known as *central hot-spot* (CHS) ignition, the hot spot density is $\sim 50\ g/cm^3$, around 10% that of the adjacent DT ice layer at stagnation, and contains fewer than 5% of the fuel mass. As the hot spot reaches temperatures of several $keV$ at stagnation, fusion reactions are initiated. While the resulting neutrons may readily escape the hot spot and layers above, $(\rho R)_{HS} \approx 0.3\ g/cm^2$, which is approximately the stopping range of the resulting 3.5 $MeV$ $\alpha$-particles, which then deposit their energy toward heating the hot spot further. As they make their way to the outer reaches of the hot spot and impinge on the DT ice, a thin layer is heated to several $keV$, producing more fusion reactions, which produce more $\alpha$-particles, which heat the next thin layer, and so on. In this way, the $\alpha$-particles provide a self-heating burn wave propagating radially outward.

CHS ignition, however, does not come without obstacles. The analysis above is predicated on a precisely spherical compression, which in practice is not easily accomplished. The primary culprit is the hydrodynamic Rayleigh-Taylor (RT) instability, wherein perturbation amplitudes along the interface of two fluids of differing densities exponentially increase if the lower-density fluid pushes on the higher-density fluid. Everyday examples of this dynamic instability include water (denser) suspended above oil (less dense) and suddenly allowed to mix, or air (less dense) pushing into smoke (more dense) from a volcanic eruption or nuclear explosion, forming a

mushroom cloud. In ICF implosions, the less dense ablative shell pushes on the DT ice at the start of the implosion, and any mixing of the materials decreases the efficacy of the compression. Miniscule nonuniformities in the smoothness of the ablative shell (i.e. bumps) during fabrication may be exponentially amplified and cause such mixing, and therefore must be engineered extremely precisely – bumps on the 2 *mm* capsule are limited to 10 *nm*! Near stagnation, when the less dense DT gas pushes back on the DT ice, any mixing heats up the DT ice, decreasing the energy efficiency of ignition. Asymmetries in the spherical compression must be mitigated lest they beget unwarranted mixing.

In the next section, we introduce a different "flavor" of ICF in which the requirements on compression symmetry are drastically reduced, yet may promise even higher gains than CHS ignition.

### 1.2.1 Fast Ignition

In CHS ignition, the compression of the capsule and the heating of the hot spot are not independent of each other but instead are coupled – the parameters of the compression are tuned so that appropriate heating goes into the hot spot near stagnation. This unfortunately engenders vulnerabilities to instabilities as explained above. The fast ignition (FI) approach to ICF essentially separates the compression and heating phases of the capsule, relaxing the constraints put in place to mitigate RT instabilities (33). While there will usually be some semblance of hot spot formation at the center, the difference in density between the DT gas ($\lesssim 100\ g/cm^3$) and DT ice ($\gtrsim 500\ g/cm^3$) in CHS will be much larger than that in FI.

Whereas in CHS ignition the densities and temperatures are approximately inverted (see Fig. 1.4(d)) such that the compression is *isobaric* at stagnation, in FI the density is relatively uniform at $\sim 300\ g/cm^3$ so that the compression is *isochoric*. Fig. 1.5(a) shows a simplified schematic of the compression and heating in CHS vs. FI. With the density of the majority of the fuel less than that in CHS, less $PdV$ work is required to heat the gas, which in turn implies

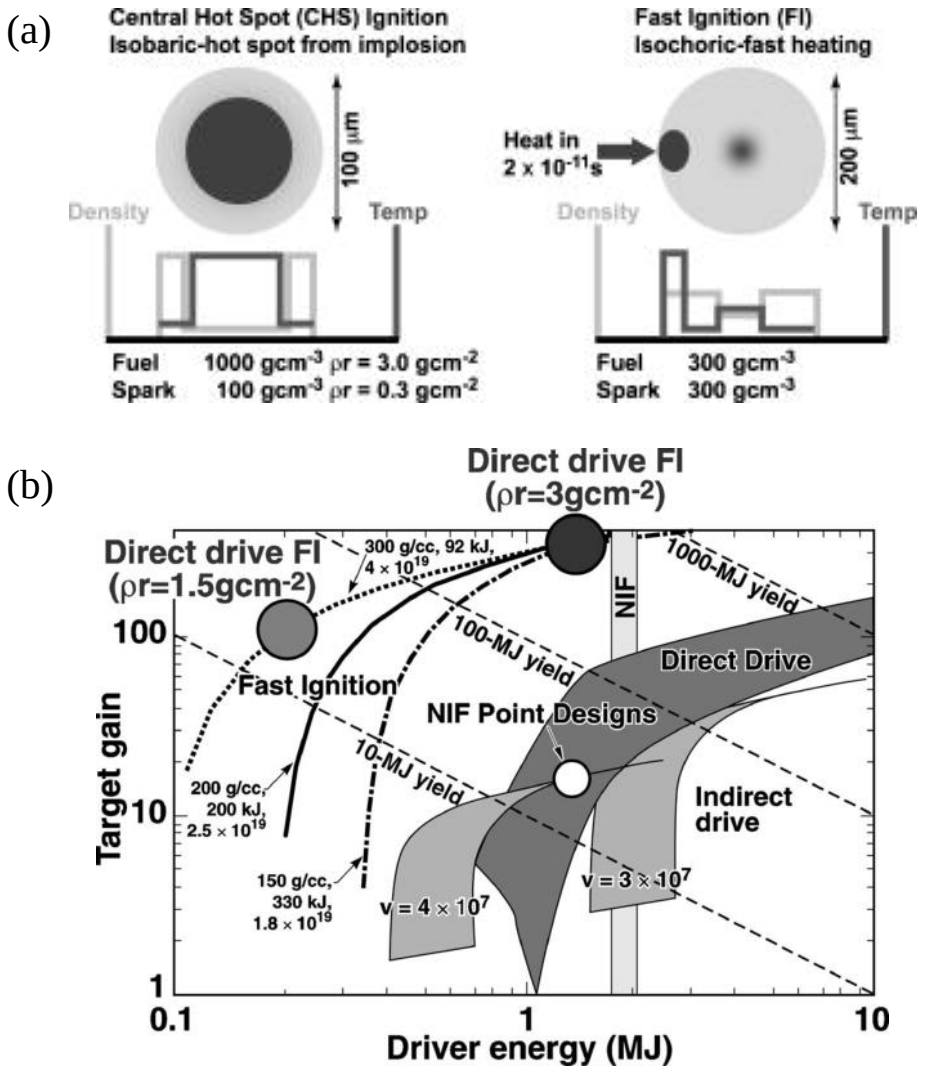


**Figure 1.5**: (a) Comparison of characteristic fuel assembly (a) and resulting target gain functions of driver energy (b) for the central hot spot ignition scheme and fast ignition scheme. Figures courtesy of Ref. (4).

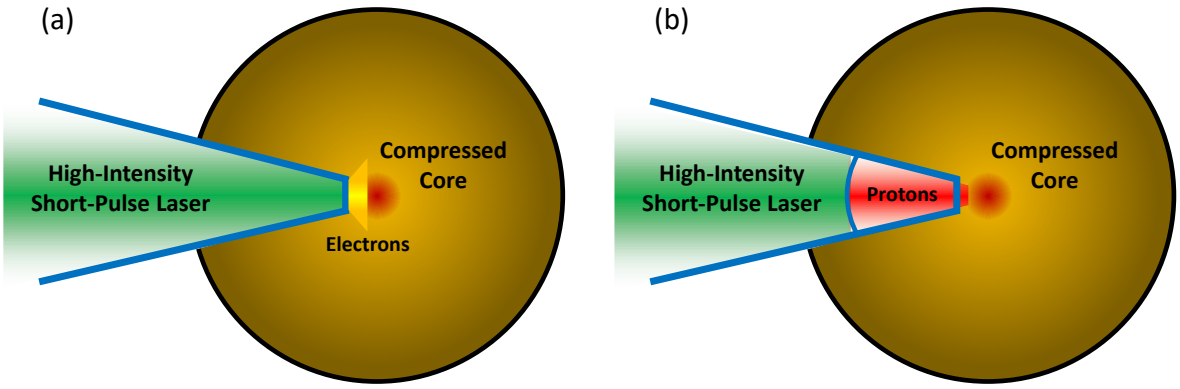


**Figure 1.6**: Target configurations for electron (a) and proton (b) fast ignition schemes.

less driver energy from the compression laser. Even more, because the fuel density is uniformly lower than that in CHS to achieve the same $\rho R$, more fuel mass may be used, leading to more fuel burned and theoretically larger gains! These fundamental differences in the energetics and gain are shown in Fig. 1.5(b). For reference, the point designs for the aforementioned Dec. 5 pioneering NIF shot are shown toward the left, with about an order of magnitude more driver energy required to achieve less gain!

In FI, since less work is done on the gas, an external heating source is necessary to ignite the fusion reactions and propagate an $\alpha$-particle burn wave similar to that in CHS. When Tabak *et al.* (33) first proposed FI, an intense laser pulse first irradiated the capsule to radially eject the ablated plasma via the ponderomotive force (see Sec. 2.7.5), clearing a channel up to the critical density (see Sec. 2.7.1). This is followed by a relativistically intense main ignitor pulse with intensity $I_L \gtrsim 10^{19}\ W/cm^2$ accelerating $\sim MeV$ electrons to heat the core to ignition temperatures and spark fusion reactions. This initial approach proved difficult, however, when it was shown that filamentary structure formation and laser defocusing from the critical surface thwarted the formation of clean channels (34).

In lieu of a preliminary laser pulse to form the channel, efforts turned toward incorporating a re-entrant cone into the side of the spherical capsule, as shown schematically in Fig. 1.6(a). In

principle, the cone acts as a barrier to the coronal plasma so that a clear channel is maintained for the main ignitor beam. The cone has a flattened tip that impinges on the central hot spot so that the generated hot electrons are as close as possible to the hot spot without being damaged from the compression.

Proof-of-concept experiments and simulations have been conducted on a smaller scale to assess the viability of electron FI. Kodama *et al.* (35) reports on one such experiment at the GEKKO laser facility in Osaka, Japan, wherein 1.2 $kJ$ of laser energy with pulse length 1 $ns$ was used to spherically compress a deuterated polystyrene (plastic doped with deuterium, or CD) shell with diameter 500 $\mu m$ and thickness 7 $\mu m$ with an embedded gold cone. At maximum compression, a second ignitor beam delivered 60 $J$ of laser energy in 0.5 $ps$ at the cone tip (50 $\mu m$ from shell center) to generate hot electrons to couple with and heat the compressed core. Core heating was quantified by the thermonuclear neutron yield using time-of-flight neutron detectors. To replicate the neutron yield with only a spherical CD shell implosion (without an embedded cone or ignitor beam), 2.6 $kJ$ of laser energy was needed, demonstrating the energy efficiency of the FI approach compared to CHS ignition.

Theobald *et al.* (36) reports on another experiment at the OMEGA laser facility in Rochester, NY USA wherein 20 $kJ$ of UV laser energy imploded an 870 $\mu m$ diameter CD shell with inserted gold cone, followed by a 1 $kJ$ ignitor beam (OMEGA-EP) with pulse length 10 $ps$ aimed at the cone tip (50 $\mu m$ away from shell center) around the time of peak compression. Again, the heating efficiency of the core by the short-pulse laser was inferred via the neutron yield. A 4x increase in neutrons was observed with the ignitor beam incident within a 100 $ps$ window around peak compression, which, according to simulations, corresponds to a heating efficiency of $3.5 \pm 1.0\%$.

The distance between the cone tip and hot spot is crucial to the configuration because laser-driven hot electrons have been shown experimentally (37) to have wide divergence angles ($50^\circ$ on average) and broad angular distributions – the more distance to travel, the more likely

that hot electrons miss the $\sim 50\ \mu m$ wide hot spot. In Kodama *et al.* outlined above, the estimated electron coupling efficiency (electron energy $\rightarrow$ core heating) was $24 \pm 3\%$, primarily due to the divergence and scattering of hot electrons in transit to the hot spot. With the right characteristics, proton beams are perhaps an attractive alternative energy carrier to the scatter-prone electrons, as detailed in the next section.

**Proton Fast Ignition**

Soon after the discovery of high intensity laser-driven proton beams (further details in Sec. 3.1), Roth *et al.* (38) immediately recognized them as an alternative to electrons for FI. Fundamentally, protons have far more inertia than electrons by three orders of magnitude, making protons that much less prone to scattering in transit to the compressed core. Also, protons and ions deposit almost all of their energy in a well-defined region near their stopping range (see Sec. 3.2.1), so that longitudinally "aiming" for the compressed core amounts to tuning the particle energies. A potential configuration for proton FI is shown in Fig. 1.6(b), similar to electron FI insofar as a re-entrant cone allows a high-intensity short pulse to accelerate protons from a curved foil and focus them through the cone tip. Crucially, protons accelerated in such a way have transit time scales of several tens of *ps*, less than the confinement time in ICF compressed cores. The focusability of laser-driven cone-guided proton beams has also been demonstrated through experiment and simulations (see Sec. 3.1.3).

Based on a parametric simulation study by Atzeni *et al.* (39) for fast particles on ignition, Roth *et al.* (38) conducted a preliminary analysis on the proton beam characteristics required for ignition. For a precompressed DT fuel, the optimal values for total proton beam energy $E_{ign}$,

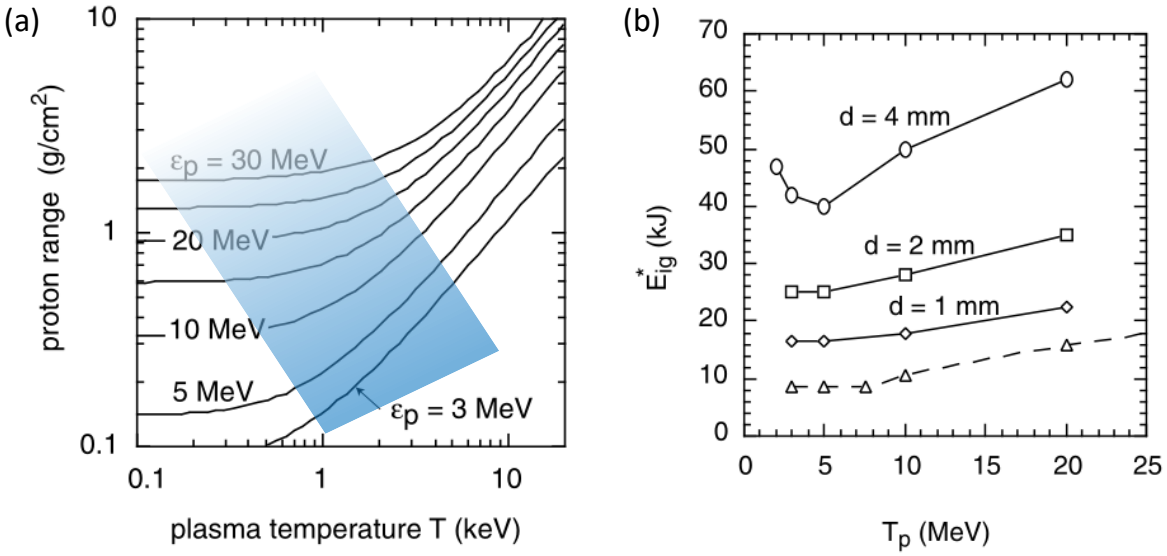


**Figure 1.7**: (a) Proton range in DT fuel vs. ion temperature. The gradient shading roughly links arriving proton energies with DT temperatures. (b) Minimum proton beam energy to ignite a *homogeneous* DT fuel assembly for varying beam temperatures and gap distances. Figures taken from Ref. (5).

proton beam pulse duration $\tau_p$, and focal spot radius $r_p$ scale as:

$$\begin{aligned} E_{ign} &= (140\ kJ)\ \hat{\rho}^{-1.85} \\ \tau_p &= (54\ ps)\ \hat{\rho}^{-0.85} \\ r_p &= (60\ \mu m)\ \hat{\rho}^{-0.97} \end{aligned} \tag{1.9}$$

where $\hat{\rho} = \rho/(100\ g/cm^3)$ is the normalized fuel density. This assumes a simple proton beam with flat radial and temporal profiles for proton energy bandwidth $15-23\ MeV$, yielding a range $\rho R = 0.3-1.5\ g/cm^2$ appropriate for a hot spot.

In a more detailed study, Atzeni *et al.* (5) conducted 2D simulations with the code DUED (40) to determine the minimum proton beam energy $E_{ign}$ required to ignite a precompressed homogeneous DT capsule ($\rho = 400\ g/cm^3$). DUED accounts for proton-fuel interaction and plasma hydrodynamics, including equation-of-state, collisional transport, and nuclear reactions.

For simplicity, the analysis assumed a cylindrical proton beam with an exponential energy spectrum $dN/d\varepsilon_p \propto \exp(-\varepsilon_p/T_p)$ for average proton energy $T_p$, originating a distance $d$ from the fuel. This transit and energy spectrum entail a velocity dispersion, where the high energy protons reach the fuel first, followed gradually by lower energy protons. Fig. 1.7(a) shows the proton range as a function of plasma temperature for various initial proton energies $\varepsilon_p$. In theory, as the high energy protons arrive and begin to heat the fuel to ignition temperatures, the subsequent lower energy protons experience an increased range due to the temperature increase, allowing them to deposit their energy in roughly the same region. The approximately overlaid blue shading indicates the time evolution of the relevant regime from top left to bottom right.

The results of the simulations varying the gap distance $d$ and average proton energy $T_p$ are shown in Fig. 1.7(b). The distance between proton source and compressed fuel plays a large role in the heating evolution, since larger gap distance results in larger transit times and greater velocity dispersion. In other words, given a constant window of time, a shorter gap distance means less dispersion and more energy deposited in that window. For this reason, we observe that with increasing gap distance comes increasing $E_{ign}$. Furthermore, for all practical gap distances simulated, the average proton energy that minimizes $E_{ign}$ lies between $5-10\ MeV$. For a 1 *mm* gap, we observe that broadband proton beams with average energy $T_p = 5\ MeV$ require a minimum total beam energy of 15 $kJ$, larger than that predicted from Eqs. 1.9 by 50%. With an estimated laser-to-proton conversion efficiency of $\sim 10\%$, the required laser energy comes out to $\sim 150\ kJ$.

Temporal *et al.* (6) conducted a similar analysis using 2D simulations, but took it a step further by including the dynamics of fuel capsule implosion as the proton beam creates a hot spot. The implosion is simulated with a 1D radiation-hydrodynamics code SARA (41) up to a time close to maximum compression, and the resulting fuel assembly is then mapped onto DUED to simulate ignition via injected proton beams. It should be noted that the implosion simulation predicted peak fuel densities of 625 $g/cm^3$, corresponding to an ideal beam radius of $r_b \approx 10\ \mu m$

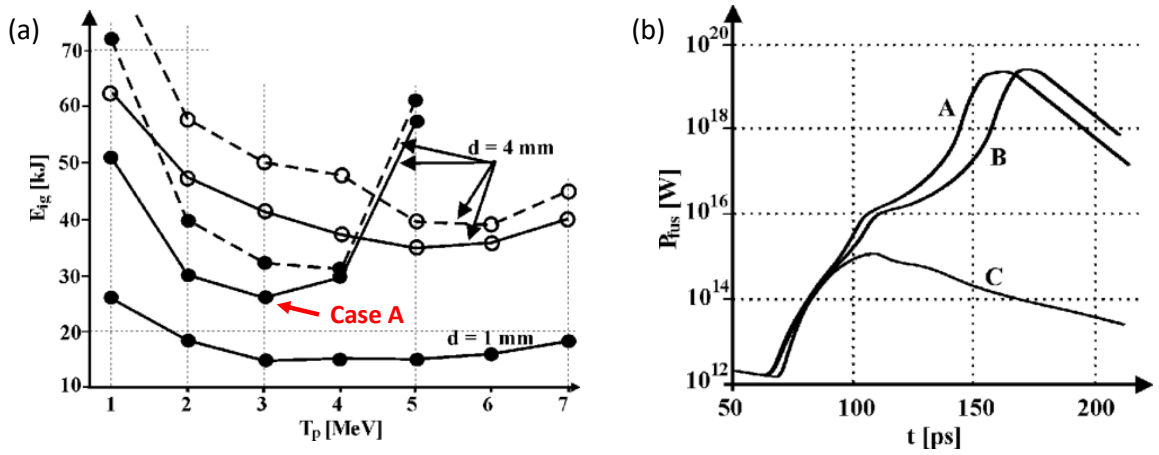


**Figure 1.8**: (a) Minimum proton beam energy required to ignite a *simulated* DT fuel assembly for varying beam temperatures and source-fuel gap distances. (b) Evolution of fusion power output of proton beam cases A, B, and C impinging on simulated fuel assembly. Figures taken from Ref. (6).

according to Eqs. 1.9. Two proton energy distributions, the exponential distribution as above and a potentially more accurate Maxwellian distribution $dN/d\varepsilon_p \propto \varepsilon_p^{1/2} \exp(-\varepsilon_p/T_p)$, where now the average proton energy is $1.5T_p$), were compared to assess its effect on $E_{ign}$. The results of the simulations are shown in Fig. 1.8(a). For gap distance $d = 4\ mm$, we observe that the Maxwellian proton spectrum (solid lines) requires lower $E_{ign}$ compared to the exponential distribution (dashed lines). This is because the effective pulse length of the exponential distribution is slightly longer, and beam power is lower for $\varepsilon_p \geq 2T_p$. We also observe that $E_{ign}$ is lower for the simulated DT sphere, primarily because of the increased fuel density.

With a closer evaluation of Case A with $E_{ign} = 26\ kJ$ as indicated in Fig. 1.8(a), it was observed that much of the fusion power was produced in a time interval corresponding to the fuel region mass $0.9 \leq \rho R \leq 1.4\ g/cm^2$, or proton energy range $7 \leq \varepsilon_p \leq 19\ MeV$. This spurred further investigation by simulating a Case B where only protons in this energy range, making up 40% of the beam energy or 10.5 $kJ$, were injected into the fuel; and a Case C where the total proton spectrum was used, but with slightly less total beam energy (24 $kJ$ vs. 26 $kJ$). Fig. 1.8(b) shows the resulting fusion power outputs from each case. Naturally, we expect Case C to fail

to ignite (considering that $E_{ign}$ is the *minimum* energy required for ignition), which we observe around $t \approx 105\ ps$ when the fusion burn is quenched in Case C. But remarkably, Case B ignites and follows a similar fusion power evolution as in Case A! Even though Case C contained more than double the beam energy as in Case B, Case C failed to ignite. This demonstrated (albeit via simulation) that only a fraction of the beam energy corresponding to a particular proton bandwidth is necessary for ignition!

Both electron FI and proton FI employ a re-entrant cone-in-shell configuration to protect an incoming ignitor laser from the coronal plasma. Both schemes attempt to efficiently convert the ignitor laser energy into DT fuel heat, and both schemes have their pros and cons. While the conversion of laser energy to hot electrons may be high $(30-40\%)$ (42), the coupling of those hot electrons to heat the fuel is quite low due to scattering and divergence. While the conversion of laser energy to protons is low (up to 15%), the coupling of protons to heat the fuel is in principle much higher since protons are less prone to scattering and exhibit Bragg peak energy deposition. Still, proton beam transport in the extreme conditions of a compressed capsule have yet to be studied. The speed of $MeV$ protons is comparable to that of thermal $(keV)$ electrons in the capsule, placing this interaction in a regime of energy deposition that has only recently been investigated experimentally (43). Indeed, further theoretical and experimental investigations into intense beam transport and stopping power are necessary to gain a fuller understanding of proton FI.

## 1.3 Intense Proton Beams in High Energy Density Science

In the preceding section, theory and simulations dictated the necessary proton beam characteristics to achieve ignition: total energy $E_{ign} \approx$ 10-30 $kJ$, average proton kinetic energy $T_p \approx$ 5-10 $MeV$, and beam radius $r_p \approx$ 15-50 $\mu m$. Assuming the proton beam pulse length is $\tau_p \sim 50\ ps$, these characteristics are equivalent to a time-averaged proton beam current density

$\langle J_p \rangle \gtrsim 10^{12}\ A/cm^2$. While laser-driven proton beams can at present achieve the necessary beam radii and kinetic energies, their current densities are limited to $\sim 10^9\ A/cm^2$ due to total beam energy of several joules. Nevertheless, with continued research into higher laser pulse energies and laser-to-proton conversion efficiency, we may expect this current density to reach the above conditions.

As it stands, ICF is not the only application for these laser-driven proton sources. Because of their relatively short pulse duration (several 10s to 100s *ps*) and broadband energy spectrum (up to several 10s of *MeV*), these proton beams have found other applications in high energy density science. Proton deflectometry and radiography techniques have been used to diagnose electromagnetic fields and density perturbations in transient laser-generated plasmas (44). When aimed at secondary thin foil samples, proton beams have demonstrated fast heating capabilities to the warm dense matter regime (14), the significance of which will be discussed later in this dissertation. If aimed at Beryllium samples, laser-driven *deuteron* sources have been shown to generate intense, collimated beams of neutrons (45; 46) which have further industrial and academic applications in biology and medicine. To an extent, a major increase in beam current densities may benefit the above applications.

Yet, with higher current densities come potentially new obstacles in the form of beam transport and energy deposition. Although proton transport and heating is fairly well understood for low current densities ($\lesssim 10^9\ A/cm^2$), investigations of the role of plasma collective effects with high proton current densities have only recently begun. Already, studies have shown that with current densities not much greater than what is presently achievable, beam transport is affected by self-generated resistive magnetic fields (25; 47). Also, recent experiments have shown that discrepancies in proton energy deposition arise with increased current density (48). Indeed, as continuing research and technology allow ever increasing proton beam intensities, further investigations of beam transport will be necessary to unlock new regimes of high energy density science. This dissertation builds on previous research to gain a fuller understanding of intense

proton beam transport and energy deposition in warm and hot dense plasmas.

## 1.4 Outline of the Dissertation

**CHAPTER 2** provides an introduction to the physics of plasmas, including basic concepts that provide intuition. Fundamental length scales, time scales, and dimensionless parameters which characterize the plasma regimes are also introduced to provide a conceptual foundation. The treatment of particle collisions in various plasma regimes are explicated so that they may be applied to later topics in this dissertation. High-intensity laser-plasma interactions are discussed along with four primary laser absorption mechanisms through plasma electrons.

**CHAPTER 3** introduces the target normal sheath acceleration (TNSA) mechanism, which is the primary and most thoroughly understood mechanism for the acceleration of proton and heavy ion beams from high-intensity lasers incident on thin foils. Theoretical models for TNSA are discussed and compared with experimental investigations. Parametric studies on the laser-to-proton energy conversion efficiency and beam focusing methods are summarized. Since these proton beams may be incident on secondary samples, proton stopping power i.e. energy deposition models are discussed for a range of proton and ambient material properties.

**CHAPTER 4** outlines the fundamentals of a powerful tool used in this dissertation – simulations. Various types of simulations used in the study of plasma physics are introduced, and particle-in-cell (PIC) simulations in particular are explained in greater detail, including common algorithms and computational techniques. The primary code used in this dissertation is the hybrid fluid-PIC code LSP, whose algorithms combine the treatment of kinetic and fluid particles. This is advantageous for intense proton beam transport simulations by relaxing some code stability conditions that fully kinetic codes must satisfy. The treatment of particle collisions and effective resistivities in LSP is summarized. Previous work on the implementation and benchmarking of the proton stopping power model presented in Ch. 3 is described.

**CHAPTER 5** gives the setup details and results from an experiment comparing sample heating due to laser-driven protons from flat and curved foils. This experiment was conducted at the Matter in Extreme Conditions (MEC) end-station at SLAC National Accelerator Laboratory, and was the first experiment to provide a platform upon which proton heating and transport experiments may be done at this facility. Simulations of proton heating using the LSP stopping power module discussed in Ch. 4 are given and compared with experimental results.

**CHAPTER 6** describes a second experiment investigating the transport of intense cone-guided proton beams through low-density foam samples. Conducted on the OMEGA-EP laser at the Laboratory for Laser Energetics (LLE), this experiment utilized the spherical crystal imager (SCI) diagnostic to essentially provide cross sectional images of the proton beam through foam transit. This is accomplished when energetic protons and electrons "knock out" Cu K-shell electrons, generating Cu-$K_\alpha$ emission. To distinguish between electron- and proton-induced emission, a multi-step simulation and post-processing method was used whose results were compared with experiment. Applications to proton FI and impacts on previous experimental results for proton transport are discussed.

**CHAPTER 7** develops a theoretical model for intense proton beam heating and magnetic field generation in dense plasmas. The transport of intense proton beams induces a neutralizing background current which generates resistive magnetic fields. Depending on gradients in resistivity or current density, these fields may act to focus or defocus the proton beam. The semi-analytic model introduced here predicts the evolution of these resistive fields, and is benchmarked with LSP simulations with good agreement. Limits of the model and applications to proton FI are discussed.

**CHAPTER 8** summarizes the results from experiments, simulations, and theory presented in this dissertation, and provides conclusions. Future work on a self-consistent fluid beam transport model is proposed and discussed.

## 1.5 Role of the Author

The experiment detailed in Ch. 5 was designed by C. McGuffey and M. Bailly-Grandvaux, with appreciated on-site coordination with and assistance by C. Curry and MEC staff. The author assisted with experimental setup and target characterization, as well as aiding in pointing and carrying out laser shots. J. Kim provided guidance and training for the use of LSP for proton heating simulations. Using the experimental results of proton energy spectra (analyzed by M. Gauthier), the author carried out all LSP simulations for proton heating of aluminum and polypropylene targets.

The experiment detailed in Ch. 6 was designed by C. McGuffey, W. Theobald, and O. Deppert with excellent support from the OMEGA-EP laser operation team and target fabrication by General Atomics. The author devised the multi-step simulation approach and carried out simulations and post-processing for Cu-$K_\alpha$ emission, with guidance from J. Kim. To most accurately reflect the proton beam source as experimentally measured, the author developed a multi-injection algorithm which injects a proton beam according to both a measured energy spectrum $dN/d\varepsilon_p$ as well as an energy-dependent half-angle divergence function $\theta(\varepsilon_p)$ (which may be measured with radiochromic film).

Concerning the work in Ch. 7, the author was motivated by the previous proton transport simulation work in Ref. (47) and developed the model further by incorporating temperature-dependent resistivity and heat capacity variation. With advisory support on theory from M. Sherlock, the author then developed a script to numerically solve the coupled set of first-order ordinary differential equations governing B-field generation and material heating, detailed further in Ch. 7. The author also ran the LSP simulations to benchmark the results of the semi-analytic model.

# Chapter 2

# Plasma Theory & Laser-Plasma Interactions

One of the first things everyone learns in their grade-school science class is that there are three phases of matter – solid, fluid, and gas. The solid state of matter, the subject of condensed matter physics, is characterized by the organized crystalline structure adopted by atoms making up a material at low temperatures. Add enough heat, and the atoms gain enough energy to partially overcome the inter-atomic bonds to become fluid. Heat it further, and the atoms gain yet more energy to break free of all bonds and become airborne as a gas (which incidentally is often modeled as a fluid). Heat it even further, and we reach the well-established fourth state of matter – the plasma. Here, electrons overcome the *intra*-atomic forces and break free from the nuclei, resulting in a hot gas of individually charged particles. The plasma state, indeed the most prominent matter state in our universe, has been the subject of a century of research (49) and is rich in both fundamental science and application. A basic overview of the physics of plasmas relevant to this dissertation is presented in the following sections.

## 2.1 Plasma Kinetic and Fluid Models

We begin with the heart of kinetic plasma theory – the distribution function. For each particle species within a plasma (electrons, ions), the distribution function $f(\mathbf{r},\mathbf{v},t)$ for that species represents the number of particles within a phase-space volume $d^3r\,d^3v$, i.e. with position between $\mathbf{r}$ and $\mathbf{r}+d\mathbf{r}$ and velocity between $\mathbf{v}$ and $\mathbf{v}+d\mathbf{v}$. Note that in three-dimensional space, $f(\mathbf{r},\mathbf{v},t)$ is a 7-D equation. In the presence of an external force $\mathbf{F_{ext}}$ and particle collisions, the evolution of the distribution function is governed by the Boltzmann Equation:

$$\frac{\partial f}{\partial t}+\mathbf{v}\cdot\boldsymbol{\nabla} f+\frac{\mathbf{F_{ext}}}{m}\cdot\frac{\partial f}{\partial \mathbf{v}}=\left(\frac{df}{dt}\right)_{coll} \tag{2.1}$$

where $m$ is the species' particle mass, $\partial/\partial\mathbf{v}$ is the velocity-space gradient, and $(df/dt)_{coll}$ is the collision term. The Boltzmann equation essentially states that particle numbers are conserved as they flow through phase space.

The zeroth moment of Eq. 2.1 is obtained by integrating each term in velocity space and simplifying:

$$\frac{\partial n}{\partial t}+\boldsymbol{\nabla}\cdot(n\boldsymbol{u})=0 \tag{2.2}$$

where $n(\mathbf{r},t)=\int f(\mathbf{r},\mathbf{v},t)\,d^3v$ is the particle number density in space and $\boldsymbol{u}(\mathbf{r},t)=\int \mathbf{v}\,f(\mathbf{r},\mathbf{v},t)\,d^3v$ is the average particle velocity. The force term vanishes because it is assumed independent of velocity (in the case of the magnetic force, $\partial/\partial\mathbf{v}\perp\mathbf{v}$) and the collision term vanishes due to conservation of momentum. This is regarded as the fluid continuity equation, essentially stating that on a macroscopic scale, a change in fluid particle quantity in one region of space (first term on LHS) must be accompanied by the flux of fluid particles along the boundary of that region (second term on LHS). If there were any particle sources (+) or sinks (-) in the system, the appropriate terms would appear on the RHS.

Subsequently, the first moment of Eq. 2.1 is obtained by multiplying by $m\boldsymbol{v}$ and again

integrating in velocity space:

$$mn\left(\frac{\partial \boldsymbol{u}}{\partial t}+(\boldsymbol{u}\cdot\boldsymbol{\nabla})\boldsymbol{u}\right)+\boldsymbol{\nabla}\cdot\mathbf{P}=n\mathbf{F}_{\mathbf{ext}} \tag{2.3}$$

where $\mathbf{P}$ is the pressure tensor related closely to the momentum flux density. The diagonal terms of the pressure tensor constitute the scalar pressure $P$, often related to temperature equilibria through the ideal gas law $P=nk_BT$, and off-diagonal terms relate to shear or viscous stresses. Eq. 2.3 is regarded as the fluid momentum conservation equation. Similar to the continuity equation, this states that a change in the momentum of a fluid particle must be accompanied by a momentum flux density (the pressure tensor), and momentum sources and sinks i.e. external forces are accounted for on the RHS.

The most prominent external force in the plasma fluid description is the Lorentz force,

$$\mathbf{F}_{\mathbf{ext}}=q\left(\mathbf{E}+\frac{\boldsymbol{u}}{c}\times\mathbf{B}\right) \tag{2.4}$$

where $q$ is the particle charge, $c$ is the speed of light, and $\mathbf{E}$ and $\mathbf{B}$ are the electric and magnetic fields, respectively. Because plasmas may largely comprise charged particles, Maxwell's equations governing electromagnetic field generation must be included to close the system of fluid equations described above:

$$\boldsymbol{\nabla}\cdot\mathbf{E}=4\pi\rho \tag{2.5}$$

$$\boldsymbol{\nabla}\cdot\mathbf{B}=0 \tag{2.6}$$

$$\boldsymbol{\nabla}\times\mathbf{E}=-\frac{1}{c}\frac{\partial\mathbf{B}}{\partial t} \tag{2.7}$$

$$\boldsymbol{\nabla}\times\mathbf{B}=\frac{4\pi}{c}\mathbf{J}+\frac{1}{c}\frac{\partial\mathbf{E}}{\partial t} \tag{2.8}$$

where

$$\begin{aligned} \rho(\mathbf{r},t) &= \sum_s q_s n_s(\mathbf{r},t) \\ \mathbf{J}(\mathbf{r},t) &= \sum_s q_s n_s(\mathbf{r},t)\boldsymbol{u}_s(\mathbf{r},t) \end{aligned} \tag{2.9}$$

are the charge and current density summed over all species $s$.

## 2.2 Debye Shielding & Plasma Length Scales

A defining characteristic of an ideal plasma involves the scale length over which external charges may be shielded out. Assume we have a fully ionized plasma with electron density $n_e$ and ion density $n_i$. To preserve quasi-neutrality,

$$Zn_i \approx n_e \tag{2.10}$$

where $Z$ is the atomic number of the ion. To a good approximation, the ions may be treated as immobile relative to the electrons since ions' inertia is far greater than electrons'.

If an artificial charge is suddenly placed within the plasma, an electric potential is introduced and the electrons will react much faster than the ions to re-establish equilibrium. Assuming thermal equilibrium at temperature $T$ in the presence of an electric potential $\Phi(r)$, we may express the electron density according to Maxwell-Boltzmann statistics:

$$\begin{aligned} n_e &= n_0 \ \exp\left(\frac{e\Phi}{k_B T}\right) \\ n_i &= \frac{n_0}{Z} \ \exp\left(\frac{-Ze\Phi}{k_B T}\right) \end{aligned} \tag{2.11}$$

where $e$ is the elementary charge, $n_0$ is the electron density when $r \to \infty$ and $\Phi \to 0$ when $r \to \infty$. This essentially means that the mobile electrons act to form a sheath around the new charge,

and that any spontaneous electric potential gradients are balanced by the electron pressures. Combining Eqs. 2.11 with Poisson's equation $\boldsymbol{\nabla}^2\Phi = 4\pi e(n_e - Zn_i)$ and assuming $Ze\Phi \ll k_B T$, we may approximate the electric potential to first order:

$$\boldsymbol{\nabla}^2\Phi = \frac{4\pi e^2 n_0(1+Z)}{k_B T}\Phi \tag{2.12}$$

The *Debye length* $\lambda_D$ pops out as the characteristic scale length over which fields are shielded out by the electrons (the ion contribution is frequently omitted).

$$\lambda_D \equiv \sqrt{\frac{k_B T}{4\pi e^2 n_0}} \approx \sqrt{\frac{T\ [eV]}{n_0\ [10^{21}\ cm^{-3}]}}\ (0.23\ nm) \tag{2.13}$$

As the plasma electron density increases, the Debye length decreases because electrons within a smaller Debye sphere are sufficient to shield the encompassed charge. By contrast, if electrons have a higher temperature, they are more agitated and augment the Debye sphere. For an ionized gas with scale length $L$, any sporadic pockets of charge are shielded locally over a scale length $\lambda_D$, maintaining the overall equilibrium of the plasma. In this sense, the Debye length characterizes the neutrality of a plasma insofar as it is considered "quasi-neutral" when $\lambda_D \ll L$.

The statistical treatment of the above discussion is valid only if there are enough electrons within a Debye sphere to shield out a charge. Hence, another characteristic of a plasma is precisely this number of electrons, which must satisfy the criterion:

$$N_D \equiv n_0 \lambda_D^3 \approx \frac{0.013 \times \left(T\ [eV]\right)^{3/2}}{\left(n_0\ [10^{21}\ cm^{-3}]\right)^{1/2}} \gg 1 \tag{2.14}$$

Hereafter, the Boltzmann constant $k_B$ which commonly accompanies temperatures will be dropped, and temperatures $T$ will assume units of energy (usually $eV$).

**Other Plasma Length Scales**

While the Debye length is a fundamental plasma scale length for any plasma, other length scales determine the regimes in which various relevant physics effects must be taken into account. The mean distance between free electrons in a plasma is the *Wigner-Seitz radius*, and may be easily derived by assuming only one electron encompasses a Wigner-Seitz sphere:

$$r_{WS} = \left(\frac{4\pi n_e}{3}\right)^{-1/3} \approx \frac{0.62\ nm}{\left(n_e\ [10^{21}\ cm^{-3}]\right)^{1/3}} \tag{2.15}$$

Accounting for electrostatic fields, the Landau length $r_0$ among free electrons is defined as the distance at which the Coulomb energy between any two electrons equals the mean kinetic energy (determined by the electron temperature) of each:

$$r_0 = \frac{e^2}{T_e} \approx \frac{1.44\ nm}{T_e\ [eV]} \tag{2.16}$$

For any two particle species $\alpha$ and $\beta$ with masses $m_\alpha$ and $m_\beta$ and charges $Z_\alpha e$ and $Z_\beta e$, a generalized Landau length may be determined in the center-of-mass frame of a system of two example particles. Given the relative velocity of the particles $\Delta v_{\alpha\beta} \equiv |\langle v_\alpha \rangle - \langle v_\beta \rangle|$ and reduced mass $\mu_{\alpha\beta} \equiv m_\alpha m_\beta/(m_\alpha + m_\beta)$, the Landau length is:

$$r_{\alpha\beta} = \frac{Z_\alpha Z_\beta e^2}{\mu_{\alpha\beta}\Delta v_{\alpha\beta}^2} \tag{2.17}$$

Quantum mechanical effects must also be accounted for when scale lengths approach the de Broglie wavelength $\lambda_{dB} = h/p$, where $h$ is Planck's constant and $p$ is the particle momentum. For a typical plasma electron with thermal velocity $v_{th,e} = \sqrt{T_e/m_e}$, the de Broglie wavelength becomes:

$$\lambda_{dB} = \frac{h}{m_e v_{th,e}} \approx \frac{1.73\ nm}{\sqrt{T_e\ [eV]}} \tag{2.18}$$

Similar to the generalized Landau length, quantum effects between any two particle species may be accounted for at the generalized de Broglie wavelength:

$$\lambda_{dB,\alpha\beta} = \frac{h}{\mu_{\alpha\beta}\Delta v_{\alpha\beta}} \tag{2.19}$$

## 2.3 Plasma Oscillation

As with all physical systems, characteristic spatial scales are only part of the big picture. While the Debye length characterizes the fundamental spatial scale of a plasma, the fundamental time scales must also be determined. We may start by assuming, as before, a fully ionized plasma at equilibrium, where the (effectively immobile) ions form a neutralizing background fluid. If all the electrons are artificially displaced a short distance $\delta x \ll \lambda_D$ in the $x$ direction, this space charge separation would beget an electrostatic field acting to re-establish equilibrium. The electrostatic field would essentially mimic that of a parallel-plate capacitor, $\mathbf{E} = 4\pi e n_0 \delta x\, \hat{\mathbf{x}}$. Assuming no other forces at play, the individual electron equation of motion is:

$$\frac{d^2\delta x}{dt^2} = -\frac{4\pi e^2 n_0}{m_e}\delta x \tag{2.20}$$

with electron mass $m_e$. Clearly, high frequency harmonic oscillation ensues with *electron plasma frequency*

$$\omega_{p,e} = \sqrt{\frac{4\pi e^2 n_0}{m_e}} \approx \sqrt{n_0\ [10^{21}\ cm^{-3}]}\ (1.8\ rad/fs) \tag{2.21}$$

Plasma oscillations occur on time scales $\tau_{p,e} \sim \omega_{p,e}^{-1}$, which may be interpreted as that at which quasi-neutrality is re-established after small perturbations. Note that the scenario above assumed there were no electron collisions, and that the plasma frequency is dependent only on the free electron density. With collisions, electron temperatures may be established, and plasma oscillations are allowed to propagate. In this case, we note that the electron thermal velocity

unites plasma oscillation with the Debye length:

$$v_{th,e} = \lambda_D \omega_{p,e} \approx \sqrt{T_e\ [eV]}\ (0.42\ \mu m/ps) \tag{2.22}$$

## 2.4 Coulomb Coupling

Given the plethora of length and time scales introduced above, we may be able to classify plasmas based on the relative energies acting on the particles. Recalling the reasoning behind the Landau length, the *plasma coupling parameter* $\Gamma$ is defined as the ratio of the Coulomb coupling energy to the kinetic energy of electrons:

$$\Gamma = \frac{e^2}{r_{WS} T_e} \approx \frac{2.3 \times \left(n_e\ [10^{21}\ cm^{-3}]\right)^{1/3}}{T_e\ [eV]} \tag{2.23}$$

where the Wigner-Seitz radius was chosen to yield an average potential energy between electrons. In the case $\Gamma \ll 1$, the electrons' kinetic energy outweighs the Coulomb potential, in which case electric fields sparsely bump electron trajectories and are therefore practically collisionless. The dynamics of this *weakly coupled* plasma are governed by collective effects. In the opposite case of $\Gamma \gg 1$, the kinetic energy of the electrons is insufficient to overcome the Coulomb potential. This *strongly coupled* plasma is characterized by fluid or solid structure, where electron dynamics are governed primarily by fields.

Reducing Eq. 2.13, 2.14, 2.15 and 2.23 to their scalings with density $n_0$ and temperature $T_e$, we observe that they are related by

$$N_D \propto \Gamma^{-3/2} \tag{2.24}$$

In essence, when the Debye sphere is largely populated ($N_D \gg 1$), the potential is shielded out quickly and electron-electron interactions are sparse in both time and space, suitable for ideal

plasmas and conducive to dominant collective effects. The scalings suggest that weakly coupled plasmas generally run hot with low density, similar to gases, whereas strongly coupled plasmas run cold with high density, much like fluids or solids.

## 2.5 Warm Dense Matter and Electron Degeneracy

So far, we have introduced two overarching plasma regimes – ideal and non-ideal. *Warm dense matter* (WDM) is considered the intermediate state and is the subject of a highly active field of research. It is "warm" because its temperatures $T_e \sim$ 1-100 $eV$ are high enough to partially but not fully ionize atoms i.e. not as hot as ideal plasmas, and "dense" with densities $n_e \sim 10^{21}$-$10^{23}$ $cm^{-3}$ close to solid state. Electrons, as *indistinguishable* fermions, must abide by the Pauli exclusion principle, wherein at most one electron may occupy a quantum state in a system. In a many-electron system, electrons are energetically assembled from the ground state up, ultimately leading to a Fermi-Dirac energy distribution function

$$f_{FD}(E) = \frac{1}{1+\exp\left(\frac{E-E_F}{T_e}\right)} \tag{2.25}$$

where $E_F$ is the Fermi energy characteristic of the WDM regime and takes the form:

$$E_F = \frac{\hbar^2}{2m_e}(3\pi^2 n_e)^{2/3} \approx \left(n_e\,[10^{21}\ cm^{-3}]\right)^{2/3}\ (0.36\ eV) \tag{2.26}$$

with free electron number density $n_e$. Typical Fermi energies are 7 $eV$ for copper, 11.7 $eV$ for aluminum, and 5.5 $eV$ for gold, all at room temperature.

The plasma degeneracy parameter $\Theta$ is defined as the ratio of the electron kinetic energy

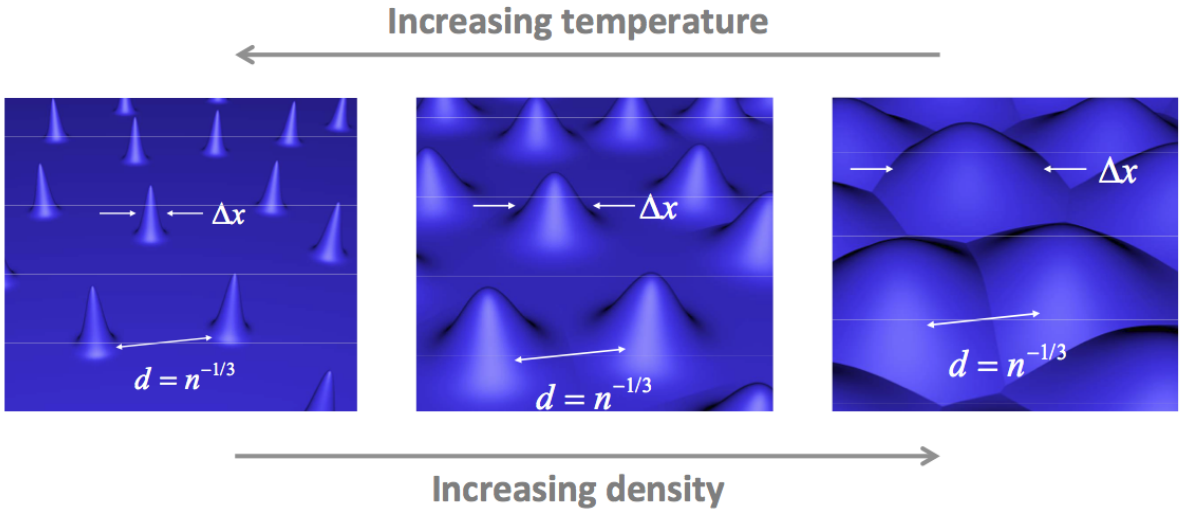


**Figure 2.1**: Concept illustration of electron degeneracy when temperature and density are varied. Wigner-Seitz radius is here represented by $d$ while deBroglie wavelength is represented by $\Delta x$. Figures taken from Ref. (7).

$T_e$ to the characteristic energy at which quantum mechanical effects must be accounted for:

$$\Theta = \frac{T_e}{E_F} \approx \frac{2.74 \times \left(T_e\ [eV]\right)}{\left(n_e\ [10^{21}\ cm^{-3}]\right)^{2/3}} \tag{2.27}$$

In particular, it describes the point at which the Pauli exclusion principle precludes electrons (fermions) from bunching into the same quantum states. This may be seen if we compare the typical inter-electron distance with quantum electron scale lengths:

$$\Theta \propto \left(\frac{r_{WS}}{\lambda_{dB}}\right)^2 \tag{2.28}$$

Low electron temperatures ($\Theta \lesssim 1$) implies that the average inter-electron distance is less than quantum scale lengths. In this case, the *degenerate* plasma obeys Fermi-Dirac statistics along with Eq. 2.25 to accurately model the quantum behavior of electrons. Fig. 2.1 illustrates the degeneracy parameter with respect to Eq. 2.28 as temperature and density vary.

In the ideal plasma limit with high electron temperatures and/or low densities ($\Theta \gg 1$),

quantum effects are negligible and the *nondegenerate* electrons act as classical particles in thermal equilibrium. It can be shown in this case that Eq. 2.25 reduces to the classical Maxwell-Boltzmann (or *Maxwellian*) energy distribution:

$$f_{MB}(E) \propto \exp\left(-\frac{E-E_F}{T_e}\right) \tag{2.29}$$

## 2.6 Collisions in Dense Plasmas

Collisions play a fundamental role in plasma dynamics. For one, using a fluid or kinetic model to describe a plasma system is largely determined by the frequency and manner of particle collisions. Fundamentally, collisions manifest the exchange of energy and momentum among particles and fields, whatever the state of matter. The length and time scales associated with these exchanges vary significantly in astrophysical or laboratory experiments, but they allow estimations of the negligible processes. In particular, the collisions of electrons with various objects, including other electrons, largely determines the essential dynamics at play in many scenarios (50).

The following sections describe the electron collision frequencies $\nu_e$ and the relaxation times $\tau_e = 1/\nu_e$ relevant to this dissertation. One may interpret the collision frequency as not only the number of collisions, but also the probability of encountering a collision event, per unit time. The complementary length scale is the electron mean free path $\lambda_{mfp}$, and these two parameters are generally linked by the average or characteristic electron velocity $v_{th}$ in the medium:

$$\lambda_{mfp} = \frac{v_{th}}{\nu_e} \tag{2.30}$$

### 2.6.1 Electrons in Lattice

In solids close to room temperature, atoms have a quasi-static lattice arrangement with vibrations determined by the ion temperature $T_i$. These lattice vibrations are represented by phonons which may propagate and collide with electrons. As previously explained, electrons in this state are strongly coupled and degenerate, so that they travel at approximately the Fermi velocity $v_F = \sqrt{2E_F/m_e}$. In the limit of cold solids where the bulk ion temperature $T_i \ll E_F$, the electron collision frequency is calculated with the expression (51; 52):

$$\nu_{e-ph} \approx k_s \frac{2e^2}{\hbar^2 v_F} T_i \approx k_s \frac{T_i\,[eV]}{\left(n_e\,[10^{21}\ cm^{-3}]\right)^{1/3}} \left(1.87 \times 10^{16}\ Hz\right) \tag{2.31}$$

where $k_s$ is a unitless constant used to match with room temperature measurements. The first approximation is made in the cold solid limits of $v_F \ll c$ and $\hbar\omega_{pi} \ll T_i$ where $\omega_{pi}^2 = 4\pi Z^2 e^2 n_i/m_i$ is the ion plasma frequency.

As cold solids are heated and approach the Fermi temperature $T_e \lesssim E_F$, more electrons gain kinetic energy and become free above melting temperature, entering into the fluid regime. Electron-electron interactions begin to dominate the electron collision frequency, determined by (53; 54):

$$\nu_{e-e} = A_\nu \frac{T_e^2}{\hbar E_F} \approx A_\nu \frac{\left(T_e\,[eV]\right)^2}{\left(n_e\,[10^{21}\ cm^{-3}]\right)^{2/3}} \left(4.2 \times 10^{15}\ Hz\right) \tag{2.32}$$

where $A_\nu$ is a unitless constant varying with materials. Since electron-electron and electron-phonon interactions are independent processes, we approximate the total electron collision frequency in the cold regime $T_e < E_F$ by adding the two primary contributions:

$$\nu_e^{cold} = \nu_{e-e} + \nu_{e-ph} \tag{2.33}$$

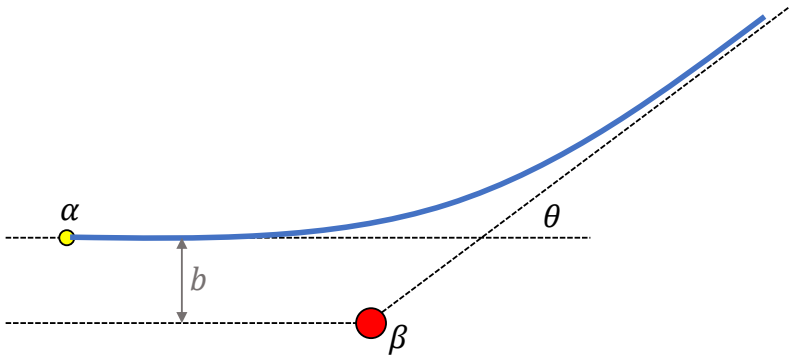


**Figure 2.2**: Classical configuration of particle α scattering off particle β in their center-of-mass reference frame, with scattering angle θ dependent on the impact parameter $b$.

### 2.6.2 Electrons in Ideal Plasma

In the ideal plasma regime where $\Theta \gg 1$ and $\Gamma \ll 1$, atoms are assumed approximately fully ionized. Electrons are therefore nondegenerate and interact primarily with each other in binary Coulomb collisions. Consider an isolated classical system in which one particle of species α approaches with impact parameter $b$ and scatters off another particle of species β via the Coulomb potential, as in Fig. 2.2. It has been established that in the center of mass reference frame particle α exhibits a hyperbolic trajectory with scattering angle θ such that:

$$\tan\frac{\theta}{2} = \frac{b_\perp}{b} \tag{2.34}$$

where

$$b_\perp \equiv \frac{q_\alpha q_\beta}{\mu_{\alpha\beta} v_{\alpha\beta}^2} \tag{2.35}$$

is the impact parameter for the particular case of $\theta = 90^\circ$ scattering. Here, the particles have charges $q_\alpha$ and $q_\beta$, reduced mass $\mu_{\alpha\beta} = m_\alpha m_\beta/(m_\alpha + m_\beta)$, and relative velocity $\mathbf{v}_{\alpha\beta} = \mathbf{v}_\alpha - \mathbf{v}_\beta$.

As the impact parameter increases indefinitely, the scattering angle $\theta \to 0$, and we may infer that small-angle deflections far outnumber large-angle deflections. Assuming small-angle elastic collisions for a particle α moving with initial velocity $v_\parallel$, Eq. 2.34 allows us to approximate

the transverse velocity gain per collision $\Delta v_\perp = v_\parallel \tan\theta \approx 2v_\parallel b_\perp / b$. Due to the equal probability of scattering in one transverse direction or the other, we expect $\Delta v_\perp$ to vanish over many collisions, but that its square $(\Delta v_\perp)^2$ should not. The number of particles $\beta$ that particle $\alpha$ will encounter in a time $\Delta t$ between impact parameters $b$ and $b+db$ is $n_\beta(v_\parallel \Delta t)(2\pi b\, db)$. The cumulative spread of $(\Delta v_\perp)^2$ over $\Delta t$ is then obtained by integrating their product over the impact parameter:

$$\sum \left(\Delta v_\perp\right)^2 = \int \left(2v_\parallel \frac{b_\perp}{b}\right)^2 n_\beta (v_\parallel \Delta t)(2\pi b\, db) = 8\pi v_\parallel^3 b_\perp^2 n_\beta \Delta t \ln\Lambda \tag{2.36}$$

where $\Lambda = b_{max}/b_{min}$ will be discussed shortly.

Typically in an ideal plasma, repeated small-angle deflections add to a large-angle deflection. In this sense, we may define a relaxation time $\tau$ as the time over which the initial momentum of particle $\alpha$ converts to transverse momentum:

$$v_\parallel^2 \simeq \sum \left(\Delta v_\perp\right)^2 = 8\pi v_\parallel^3 b_\perp^2 n_\beta \tau \ln\Lambda \tag{2.37}$$

The corresponding collision frequency is naturally the inverse of the relaxation time. For mobile *e*lectrons colliding with (practically) immobile fully ionized *i*ons, $b_\perp \approx Ze^2/m_e v_e^2$ and the electron collision frequency is

$$\nu_e^{sp} = \frac{1}{\tau} = \frac{8\pi n_i Z^2 e^4}{m_e^2 v_e^3} \ln\Lambda \approx \frac{n_i\ [10^{21}\ cm^{-3}]\ Z^2\ \ln\Lambda}{\left(T_e\ [eV]\right)^{3/2}}\ \left(7.7\times 10^{15}\ Hz\right) \tag{2.38}$$

assuming the electrons have self-thermalized to temperatures $T_e$. The above collision frequency for an ideal plasma is conceptually derived from the *Sp*itzer model (55), at which a more rigorous derivation with accurate numerical multipliers (e.g. for electrons with Maxwellian distributions, etc.) may be obtained.

Eq. 2.38 highlights the main scalings with density, temperature, and the "Coulomb logarithm" $\ln\Lambda$. This log of the ratio of $b_{max}$ to $b_{min}$ quantifies the relative importance of small-

vs. large-angle deflections. Recalling that plasma electrons exhibit Debye shielding, we may infer that impact parameters are significant up to approximately the Debye length, i.e. $b_{max} \sim \lambda_D$. Of course, in the derivation of Debye shielding, it is assumed that many particles within the Debye sphere are contributing to the screening, so naturally a lower limit for $b_{max}$ should be the inter-electron distance, so

$$b_{max} = \max(\lambda_D, r_{WS}) \tag{2.39}$$

On the other end, small impact parameters yield large-angle deflections, the threshold for which may be approximated by $b_\perp$. At impact parameters sufficiently close where quantum effects must be accounted for, we may use for $b_{min}$ the deBroglie wavelength:

$$b_{min} = \min(b_\perp, \lambda_{dB}) \tag{2.40}$$

As an example, we may take for electrons scattering off ions

$$\Lambda = \frac{\lambda_D}{b_\perp} \propto \frac{T_e^{3/2}}{n_e^{1/2}} \tag{2.41}$$

Even though $\Lambda$ depends on temperature and density, their containment within the logarithm suppresses these very dependencies. Recalling Eq. 2.14 and noting that $\Lambda \propto N_D$, we observe that the plasma condition implies $\Lambda \gg 1$. In general, $\ln\Lambda$ ranges between 5 and 20 over a wide range of plasmas including intense laser-generated plasmas and thermonuclear fusion cores.

### 2.6.3 Electrons in Dense Plasmas

We have so far observed that the electron collision frequency increases with electron temperature in the condensed matter regime ($T_e \lesssim E_F$), but decreases with temperature in the Spitzer regime ($T_e \gg E_F$). Assuming constant electron density, we may infer that in the intermediate temperature range $T_e \gtrsim E_F$, the electron collision frequency must reach a local maximum within

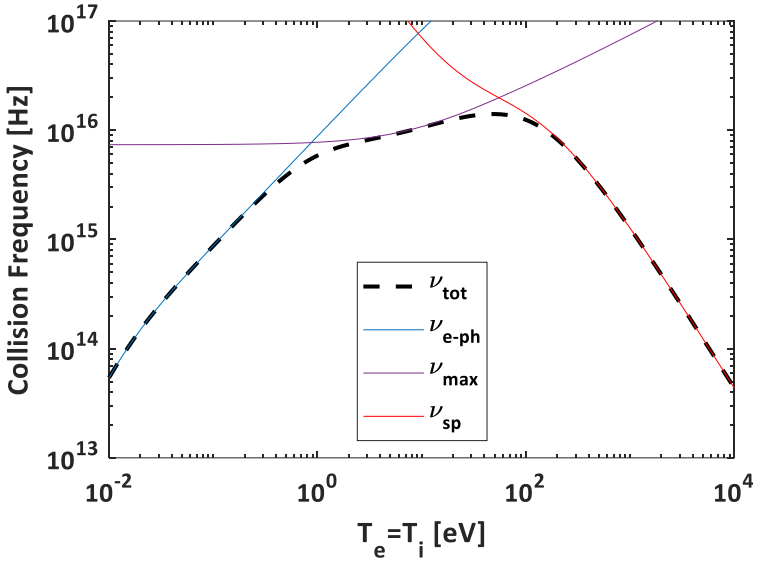


**Figure 2.3**: Harmonic mean of electron collision frequencies in cold (blue), warm (purple), and hot (red) regimes for solid density aluminum.

the WDM regime.

Eq. 2.30 shows that an upper limit of the electron collision frequency corresponds to a lower limit of the electron mean free path between collisions. It is reasonable to constrain $\lambda_{mfp}$ by noting that on average, any one electron travels at least the inter-atomic spacing before encountering another collision, i.e. $\lambda_{mfp} \geq r_i$. Therefore, using Eq. 2.30, the maximum electron collision frequency is:

$$\nu_e^{max} = \frac{v_{ch}}{r_i} \tag{2.42}$$

where in this regime, $v_{ch} = \sqrt{(T_e + E_F)/m_e}$ is the characteristic electron velocity and $r_i = n_i^{-1/3}$ is the inter-atomic spacing. The Drude model, which will be explained in Sec. 4.3, shows that plasma resistivity is proportional to the total electron collision frequency. In this context, the maximum collision frequency shown above for the WDM regime provides the fundamental mechanism for *collisional* or *resistive saturation*, which has been demonstrated experimentally (56; 22) and computationally (57; 58) in metals such as copper and aluminum.

Having introduced the electron collision frequency in the condensed matter (Eq. 2.33), warm dense matter (Eq. 2.42) and Spitzer (Eq. 2.38) regimes, we are interested in combining them into one smooth analytic expression applicable to all regimes. Taking cue from Ref. (52), the total electron collision frequency $\nu_e^{tot}$ is calculated via a harmonic mean of each regime's relaxation time:

$$\left(\nu_e^{tot}\right)^{-2} = \left(\nu_{e-e} + \nu_{e-ph}\right)^{-2} + \left(\nu_e^{sp}\right)^{-2} + \left(\nu_e^{max}\right)^{-2} \tag{2.43}$$

In combining the individual collision frequencies this way, to first order the lowest calculated collision frequency has the greatest impact $\nu_e^{tot}$. At the intersection of two regimes, $\nu_e^{tot}$ is not far from either of their corresponding collision frequencies while still allowing a smooth i.e. differentiable transition. This bodes well for the unclear intersection of the warm dense matter regime ($T_e \gtrsim E_F$) to Spitzer regime ($T_e \gg E_F$); we note that the cutoff is roughly five to ten times the Fermi energy (56; 59; 60). Fig. 2.3 depicts the total collision frequency of solid aluminum as a function of temperature, along with its comprising asymptotes for each regime described above. The Eidmann-Chimier model above has been used in laser-plasma interaction modeling as in Refs. (52; 59; 60).

## 2.7 Laser-Plasma Interactions

Having outlined the important quantities and characteristics of plasmas, we are now in a position to discuss the interactions of electromagnetic waves in plasmas. In this section, we will first derive the basic dispersion relations for a light wave in plasma and deduce the limits of its propagation. With high intensity lasers, various mechanisms for laser energy absorption into the plasma come to light (pun intended). We outline four dominant mechanisms, which vary with plasma gradients and laser intensities up to relativistic levels.

### 2.7.1 Laser Dispersion in Plasma

The dispersion relation relates the wave vector $|\mathbf{k}_L| = 2\pi/\lambda_L$ to the frequency $\omega_L$ for wavelength $\lambda_L$ of an electromagnetic wave, and governs its propagation through a medium. To start simply, let us assume propagation in a vacuum i.e. source terms $(\rho, \mathbf{J}) = 0$ in Maxwell's Equations 2.5-2.8. Taking the curl of Faraday's Law (Eq. 2.7) and using the curl identity $\boldsymbol{\nabla} \times (\boldsymbol{\nabla} \times \mathbf{A}) = \boldsymbol{\nabla}(\boldsymbol{\nabla} \cdot \mathbf{A}) - \nabla^2 \mathbf{A}$ we obtain:

$$\nabla^2 \mathbf{E} = \frac{1}{c} \frac{\partial}{\partial t} (\boldsymbol{\nabla} \times \mathbf{B})$$

noting that $\nabla \cdot \mathbf{E} = 0$. Inserting Ampere's Law (Eq. 2.8) with $\mathbf{J} = 0$, we obtain the wave equation for the electric field:

$$\nabla^2 \mathbf{E} = \frac{1}{c^2} \frac{\partial^2 \mathbf{E}}{\partial t^2} \tag{2.44}$$

Similarly, if we instead took the curl of Ampere's Law and inserted Faraday's Law, we would obtain the wave equation for the magnetic field:

$$\nabla^2 \mathbf{B} = \frac{1}{c^2} \frac{\partial^2 \mathbf{B}}{\partial t^2} \tag{2.45}$$

Assuming both fields oscillate in space and time as:

$$\begin{aligned} \mathbf{E} &\propto \exp[\, i(\mathbf{k}_L \cdot \mathbf{r} - \omega_L t)\, ] \\ \mathbf{B} &\propto \exp[\, i(\mathbf{k}_L \cdot \mathbf{r} - \omega_L t)\, ] \end{aligned} \tag{2.46}$$

we may make the substitutions $\boldsymbol{\nabla} \to i\mathbf{k}$ and $\partial/\partial t \to -i\omega$ into Eqs. 2.44-2.45 to obtain the familiar dispersion relation for electromagnetic waves in vacuum:

$$k_L^2 c^2 = \omega_L^2 \tag{2.47}$$

Of course, taking either Ampere's or Faraday's Law individually and using the above dispersion, we note that the electric and magnetic fields are orthogonal to one another and to the direction of propagation $\hat{\mathbf{k}} \times \mathbf{E} = \mathbf{B}$, painting the common picture of a light wave.

When this vacuum-propagating light wave is incident onto plasma, the oscillating fields drive plasma motion, and the source terms may no longer be nonzero. This is manifested by adding the current term from Ampere's Law into Eq. 2.44:

$$\nabla^2 \mathbf{E} = \frac{1}{c^2}\frac{\partial^2 \mathbf{E}}{\partial t^2} + \frac{4\pi}{c^2}\frac{\partial \mathbf{J}}{\partial t} \tag{2.48}$$

Assuming again that ions are relatively immobile compared to electrons, the laser will primarily couple to the electrons, whose equation of motion is then:

$$m_e \frac{\partial \mathbf{v}_e}{\partial t} = -e\left(\mathbf{E} + \frac{\mathbf{v}_e}{c} \times \mathbf{B}\right) \tag{2.49}$$

Assuming for a moment that the electric field is not intense enough to accelerate electrons relativistically, we may ignore the magnetic component. Then,

$$\frac{\partial \mathbf{J}}{\partial t} \approx -e n_e \frac{\partial \mathbf{v}_e}{\partial t} = \frac{n_e e^2}{m_e}\mathbf{E} \tag{2.50}$$

Physically, this means that an oscillating wave induces oscillatory motion in the plasma. Plugging this back into Eq. 2.48 and replacing $\nabla$ and $\partial/\partial t$ as before, we obtain the dispersion relation:

$$\frac{k_L^2 c^2}{\omega_L^2} \equiv \varepsilon = 1 - \frac{\omega_{p,e}^2}{\omega_L^2} \tag{2.51}$$

where $\varepsilon$ is the dielectric function. Note that in vacuum, $\omega_{p,e} = 0$ and we recover Eq. 2.47.

This brings to bear a crucial property of laser propagation in plasma. As the plasma frequency approaches the laser frequency, the wave vector approaches zero, which means there

exists a critical plasma density $n_{cr}$ above which the laser cannot propagate. This may be found by equating the laser and plasma frequencies:

$$n_{cr} = \frac{m_e \omega_L^2}{4\pi e^2} = \frac{1.1 \times 10^{21}\ cm^{-3}}{\left(\lambda_L\ [\mu m]\right)^2} \tag{2.52}$$

where we have used $\omega_L = 2\pi c/\lambda_L$. In an *overdense* plasma ($n_e > n_{cr}$ or $\omega_{p,e} > \omega_L$), $\varepsilon < 0$ and $k_L$ becomes imaginary so that and the fields exponentially decay (recall Eqs. 2.46). The scale length over which the field attenuates is given by the skin depth:

$$\delta = \frac{1}{k_L} = \frac{c}{i\omega_L\sqrt{\varepsilon}}, \tag{2.53}$$

which is real since in this case $\varepsilon < 0$. Beyond the critical surface i.e. where $n_e = n_{cr}$, the laser becomes evanescent; on a macroscale, the laser simply reflects off the critical surface.

### 2.7.2 Inverse Bremsstrahlung

The preceding analysis assumes that electrons, having been excited by the laser, are thereafter undisturbed, as described in Eq. 2.50 by not accounting for ions. Coupled with Eq. 2.46, this shows that any energy imparted to electrons in a half-cycle of the laser would be reversed in the the next half-cycle (in mathematical terms, $\mathbf{v}_e \propto i\mathbf{E}/\omega_L$ follows behind $\mathbf{E}$ by a phase angle). Evidently, when a laser propagates into and subsequently leaves a plasma, the electrons have no net energy gain and are ultimately left with the same energy as before the laser arrived!

While ions may still be approximated as immobile due to their large inertia, their effect on laser absorption does not end there. As analyzed in Sec. 2.6.2, electrons indeed undergo collisions with ions, and precisely this process is behind *collisional* absorption. In essence, electrons may be dephased, or "knocked out" of the electric field oscillation upon collisions with ions, and may therefore steal the laser energy it had absorbed before the dephasing. This mechanism is

also called inverse bremsstrahlung because it is the bremsstrahlung process (photon produced by electron deflections from ions) in reverse (photon absorbed). Following the analysis in (61), this mechanism is investigated by adding a collisional damping term to Eq. 2.49 (again assuming non-relativistic motion):

$$\frac{\partial \mathbf{v}_e}{\partial t} = -\frac{e\mathbf{E}}{m_e} - \nu_{ei}\mathbf{v}_e \tag{2.54}$$

where $\nu_{ei}$ is evaluated from Eq. 2.38. Following the shorthands ($\nabla$ and $\partial/\partial t$) from the preceding derivation, the electron velocity is now:

$$\mathbf{v}_e = \frac{-ie}{m_e(\omega_L + i\nu_{ei})}\mathbf{E} \tag{2.55}$$

and the new current density is:

$$\mathbf{J} = -en_e\mathbf{v}_e = \frac{i\omega_{p,e}^2}{4\pi(\omega_L + i\nu_{ei})}\mathbf{E} = \sigma\mathbf{E} \tag{2.56}$$

where $\sigma$ is the electrical conductivity of the plasma.

Plugging our modified current density into Eq. 2.48, we obtain the dispersion relation for collisionally damped fields in plasma:

$$\frac{k_L^2c^2}{\omega_L^2} \equiv \varepsilon = 1 - \frac{\omega_{p,e}^2}{\omega_L^2}\,\frac{1 - i\frac{\nu_{ei}}{\omega_L}}{1 + \frac{\nu_{ei}^2}{\omega_L^2}} \tag{2.57}$$

As before, wave damping occurs when the wave number becomes imaginary. If we assume that $\nu_{ei} \ll \omega_L$, we may approximate the wave number above to first order in $\nu_{ei}/\omega_L$:

$$k_L \approx \frac{\omega_L}{c}\sqrt{1 - \frac{\omega_{p,e}^2}{\omega_L^2}}\left(1 + i\,\frac{\omega_{p,e}^2}{\omega_L^2}\frac{\nu_{ei}}{2\omega_L}\frac{1}{1 - \frac{\omega_{p,e}^2}{\omega_L^2}}\right) \tag{2.58}$$

Noting that $n_e/n_{cr} = \omega_{p,e}^2/\omega_L^2$, we may obtain the inverse bremsstrahlung damping rate $\kappa_{IB}$ by

doubling the imaginary part of $k_L$:

$$\kappa_{IB} = 2\,\mathbb{I}\{k_L\} \approx \frac{\nu_{ei}}{c}\,\frac{n_e/n_{cr}}{\sqrt{1-n_e/n_{cr}}} \tag{2.59}$$

We observe that the laser damping rate is greatest as it approaches the critical surface. It is also most dominant for high-Z, low temperature plasmas through its dependence on electron-ion collision frequency. Collisional absorption is the dominant laser absorption mechanism for laser intensities under $\sim 10^{15}\ W/cm^2$ (62), and preferentially heat low-energy non-relativistic electrons (63).

### 2.7.3 Resonance Absorption

When a high intensity laser irradiates a target, it is often the case that this generates a blow-off, or coronal plasma. This in turn creates an electron density gradient stretching from the target surface into the vacuum, over a gradient scale length $L_n \equiv n_e/\boldsymbol{\nabla} n_e$. For a laser whose propagation direction is parallel to this gradient i.e. $\mathbf{E}\cdot\boldsymbol{\nabla} n_e = 0$, the laser permeates the plasma up to the critical density according to Eq. 2.51. If, however, the laser propagates at an angle relative to the plasma gradient with a co-planar polarization i.e. $p$-polarized or $\mathbf{E}\cdot\boldsymbol{\nabla} n_e \neq 0$, the electric field of the laser will have a component in the direction of the plasma gradient. This scenario is depicted in Fig. 2.4, wherein a laser is incident from vacuum onto a plasma at an angle $\theta_0$ relative to the density gradient (or target normal). Using Snell's Law of refraction along with the fact that the refractive index of a plasma is $n_{ref} = \sqrt{\varepsilon}$ with Eq. 2.51, we find that the laser gradually refracts up the plasma gradient and reflects when $n_e = n_{cr}\cos^2\theta_0$, notably before reaching critical density!

At this turning point, the electric field is fully parallel to the density gradient and drives longitudinal density oscillations, which generate electrostatic fields and excite electron plasma waves (EPW) down the density gradient. If part of the electric field tunnels through and reaches

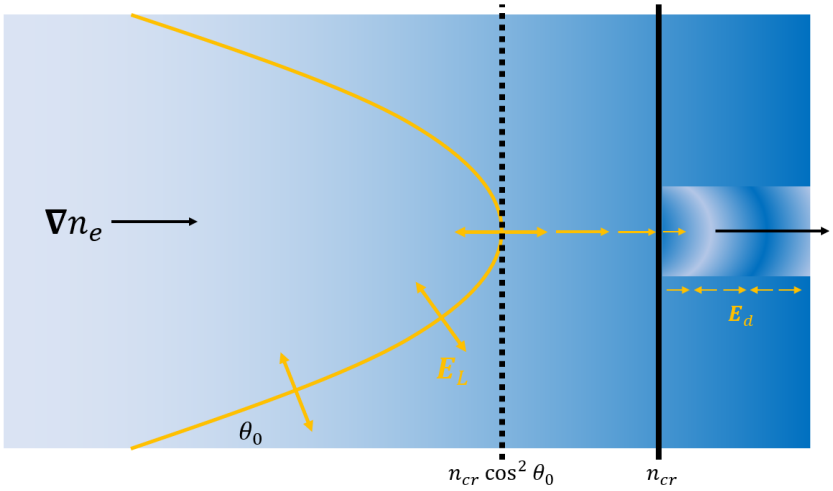


**Figure 2.4**: Resonance absorption configuration – laser incident at angle $\theta_0$ with the plasma gradient direction reflects when plasma density is a fraction of the critical density, but may still drive electron plasma waves beyond critical density if the laser field reaches the critical surface.

the critical density where $\omega_{p,e} = \omega_L$, the EPW is resonant with the laser frequency. This laser absorption mechanism, called *resonance absorption*, is inherently a *collisionless* process, unlike inverse bremsstrahlung from the previous section. The electrostatic *d*riving field is given by (64):

$$\mathbf{E}_d = \frac{\varepsilon(n_e)\phi(\tau)}{\sqrt{2\pi\omega_L L_n/c}}\,\mathbf{E} \tag{2.60}$$

where $\tau = (\omega_L L_n/c)^{1/3}\sin\theta_0$ relates the density scale length to the incidence angle, and

$$\phi(\tau) \approx 2.3\tau\, e^{-2\tau^3/3} \tag{2.61}$$

describes the exponential decay of the field between the laser reflection point and critical density. An underlying assumption here is that the density varies linearly ($n_e/n_{cr} = z/L_n$) and gently across one laser wavelength, $L_n \gg \lambda_L$.

Energy transfer then occurs when the electron plasma wave is damped, generally through Landau damping. Assuming a small damping frequency $\nu \ll \omega_L$, the fraction of laser energy

absorbed by the plasma may be approximated by (64):

$$f_{RA} \approx \phi^2(\tau)/2 \tag{2.62}$$

If the laser incidence angle is close to normal, the longitudinal electric field is brief and narrow; if the incidence angle is close to 90°, the field significantly decays and plasma waves are inefficiently excited. The optimum incidence angle for maximum laser energy absorption is such that $\tau = (1/2)^{1/3} \approx 0.8$. Resonance absorption is the dominant mechanism for laser intensities between $\sim 10^{15} - 10^{17}\ W/cm^2$, when the laser is able to heat the plasma to high enough temperatures that electrons become collisionless $\left(\text{recall that } \nu_{ei} \propto T_e^{-3/2}\right)$. Particle-in-cell simulations (65; 66) have shown that hot (relativistic) electrons are accelerated from overdense to underdense plasma regions, forming a high-energy Maxwellian tail whose temperature scales as

$$T_{hot} \sim \left(T_e\ [keV]\ I_L \lambda_L^2\ \left[10^{16}\ W cm^{-2} \mu m^2\right]\right)^{1/3} (14\ keV) \tag{2.63}$$

over the background Maxwellian distribution characterized by cold temperature $T_e$ at critical density.

### 2.7.4 Vacuum Heating

With resonance absorption, we observe that as the density scale length $L_n$ decreases, $\phi(\tau)$ also decreases, and with it the laser absorption fraction. Assuming the laser is still obliquely incident and therefore reaches a turning point where the electric field is along target normal, if the density gradient becomes too steep relative to the laser wavelength $L_n \ll \lambda_L$, the electric field may be intense enough to pull electrons free from the plasma into vacuum within half a laser cycle. In the next half-cycle, these electrons are accelerated back into the plasma, and with enough energy to clear the critical surface, they may break free from the laser oscillation as well!

This may be demonstrated by first noting the equation of motion for an electron within an electromagnetic field:

$$m_e\ddot{x} = -eE_L\cos(\omega_L t) \tag{2.64}$$

We are omitting the magnetic field term from the Lorentz force for now because we assume nonrelativistic motion, to be justified later. Integrating Eq. 2.64 once, we may define the electron *quiver* speed $v_{osc} \equiv eE_L/m_e\omega_L$ due to the oscillating E-field. Noting that the laser intensity in vacuum is related to its electric field via the Poynting vector $I_L = \langle S \rangle = cE_L^2/8\pi$, we may define the laser parameter $a_0$ as the normalized vector potential:

$$a_0 = \frac{v_{osc}}{c} = \frac{p_{osc}}{m_e c} = \frac{eE_L}{m\omega_L c} \approx 0.85\sqrt{I_L\lambda_L^2\,[10^{18}\ W cm^{-2}\mu m^2]} \tag{2.65}$$

From this estimation, laser intensities exceeding $\sim 10^{18}\ W/cm^2$ (usually $\lambda_L \sim \mu m$) are dubbed relativistic, since at these intensities the electron quiver velocities approach light speed. Integrating a second time gives the electron oscillation amplitude $x_{osc} \equiv eE_L/m_e\omega_L^2$, which may be compared with the plasma density scale length as:

$$\frac{x_{osc}}{L_n} = \frac{eE_L}{m\omega_L^2 L_n} = \frac{eE_L}{m\omega_L c}\,\frac{c}{\omega_L L_n} \sim a_0\,\frac{\lambda_L}{L_n} \gg 1 \tag{2.66}$$

for intensities $\gtrsim 10^{16}\ W/cm^2$. It is clear that electric fields are strong enough to pull electrons into vacuum, then launch them back beyond the critical surface and into the plasma. This mechanism, called *vacuum heating* or Brunel heating, was first investigated by Brunel (67) in 1987.

Assuming the laser pulls out sheets of electrons at a time, we may approximate these sheets as the cathode of a dynamic capacitor model driven by a standing electrostatic wave with amplitude $E_d = 2E_L\sin\theta_0$, where the factor of 2 arises from the reflected wave – the laser trajectory in Fig. 2.4 is modified such that incident and reflected waves are mostly linear, since refraction only occurs close to the critical surface. The areal charge density $\sigma \equiv dq/dA$ is then

found by equating the driving electric field with the classic capacitor field:

$$\sigma = \frac{2E_L \sin\theta_0}{4\pi} \tag{2.67}$$

Assuming electron sheets are pulled every laser cycle, the power gained by electrons per unit area is then:

$$I_{VH} \sim \left(\frac{1}{2} m_e v_d^2\right) \frac{\sigma}{e}\, \omega_L = \frac{v_d E_d^2}{8\pi} \tag{2.68}$$

where $v_d \equiv eE_d/m_e\omega_L$, and the absorption fraction from vacuum laser intensity is:

$$f_{VH} = \frac{I_{VH}}{I_L} \sim 8a_0 \sin^3\theta_0 \tag{2.69}$$

A more empirical formulation for the laser absorption fraction $f_{VH}$ has been given by Brunel (67):

$$f_{VH} \approx \frac{\eta}{2\pi}\, \frac{\sin^3\theta_0}{\cos\theta_0}\, 8a_0 \tag{2.70}$$

where $\eta$ is an efficiency factor measuring how much electron oscillations go towards heating the plasma. Kato et al. (68) later determined that the efficiency depends on the plasma density like $\eta \approx \left(1 - \omega_L^2/\omega_{p,e}^2\right)^{-1}$. For laser intensities $\sim 10^{16}\ W/cm^2$ and density gradient $L_n/\lambda_L \sim 0.1$, absorption fractions may be as large as 70% (62). As the intensity increases to relativistic levels, however, the absorption fraction levels off around 10-15% as another absorption mechanism begins to dominate, as described in the next section.

### 2.7.5 Ponderomotive Force & J×B Heating

Theoretically, it is often assumed that lasers (electromagnetic waves) are plane wave and spatially homogeneous. A resting charged particle in the vicinity of the laser would then experience an equal and opposite displacement in one half cycle of the field oscillation as in the next, essentially oscillating about an equilibrium position. In reality, lasers are often spatially

inhomogeneous, more intense along the laser axis and decaying outward. This inhomogeneity has the fundamental effect of pushing particles towards regions of less intensity, for the following reason. A particle initially at rest on the laser axis would be displaced by the field, in one half-cycle, to a region with a less intense field. In the next half-cycle, the decreased field intensity manifests as a smaller displacement, not quite reaching the initial position. On average over the course of many field oscillations, the particle exhibits a drift toward regions of less intense fields due to the so-called *ponderomotive force*, essentially because the less intense fields cannot fully restore the particle to the regions of more intense fields.

To demonstrate this analytically, we may start with the equation of motion of a charged particle (charge $q$, mass $m$) in the vicinity of a linearly polarized laser field with $\mathbf{E} = E(x)\cos(\omega_L t)\hat{\mathbf{x}}$. In this scenario, we may assume the laser propagates in the $+z$ direction, but since the motion of the particle is along the $x$-axis, we may take $z = 0$ (for now, we assume the particle motion is nonrelativistic). The equation of motion of the particle is then:

$$m\ddot{x} = qE(x)\cos(\omega_L t) \tag{2.71}$$

We may break up the motion into the guiding center motion $x_0(t)$ associated with the (slow) spatial variation of the electric field, and an oscillatory component $x_1(t)$ associated with the (fast) oscillation ($\sim \omega_L$) of the electric field, so that $x = x_0 + x_1$. Plugging this into Eq. 2.71 and Taylor expanding around the guiding center $x_0$, we obtain:

$$m(\ddot{x_0} + \ddot{x_1}) = q\left(E(x_0) + x_1 \left.\frac{\partial E}{\partial x}\right|_{x_0}\right)\cos(\omega_L t) \tag{2.72}$$

Straightaway, the Taylor expansion implicitly assumes that $x_1 \ll E/\left.\frac{\partial E}{\partial x}\right|_{x_0}$ i.e. the scale length of the electric field gradient is much larger than the oscillation amplitude due to the electric field. By breaking up the motion into fast oscillation and slow drifts, we also recognize that $\ddot{x_1} \gg \ddot{x_0}$ i.e. the acceleration of the guiding center will generally be much smaller than that of

the oscillation. Then, to zeroth order in space, we have $m\ddot{x_1} = qE(x_0)\cos(\omega_L t)$ whose solution is easily found to be:

$$x_1(t) = -\frac{q}{m\omega_L^2}E(x_0)\cos(\omega_L t) \tag{2.73}$$

To first order in space, we have for the ponderomotive force on the guiding center:

$$F_p = m\ddot{x_0} = qx_1\left.\frac{\partial E}{\partial x}\right|_{x_0}\cos(\omega_L t) = -\frac{q^2}{m\omega_L^2}E(x_0)\left.\frac{\partial E}{\partial x}\right|_{x_0}\cos^2(\omega_L t) \tag{2.74}$$

After cycle-averaging the oscillation $\langle\cos^2(\omega_L t)\rangle$ and generalizing the spatial gradient, we obtain the cycle-averaged ponderomotive force:

$$\langle F_p\rangle = -\frac{q^2}{4m\omega_L^2}\boldsymbol{\nabla}E^2 \tag{2.75}$$

Uniquely, the $-q^2$ implies (1) that both ions and electrons respond in the same direction, and (2) this direction is toward lesser field intensities. Since electrons are far more mobile than ions, the ponderomotive force drives steep charge separation, and the corresponding electrostatic field may accelerate ions over longer time scales.

The preceding analysis assumed that the laser intensity was not relativistic i.e. $a_0 \ll 1$. At relativistic intensities, the magnetic field component in the Lorentz force cannot be ignored and the electron motion is consequently very different. For relativistic intensities, we may start with the simplified case of a normally incident uniform plane wave $\mathbf{E} = E_0\hat{\mathbf{x}}\, e^{i(k_L z - \omega_L t)}$ where $\hat{\mathbf{a}}$ propagating in the $\hat{\mathbf{z}}$ direction and polarized in the $\hat{\mathbf{x}}$ direction. Conceptually, we predict that the electric field will accelerate the electrons from rest along $\hat{\mathbf{x}}$. Since the magnetic field is orthogonal to both $\hat{\mathbf{x}}$ and $\hat{\mathbf{z}}$, it will then accelerate the moving electrons longitudinally so that the electron motion remains in the $x$-$z$ plane.

The equation of motion for an electron fluid is:

$$\frac{\partial \mathbf{p}}{\partial t} + (\mathbf{v}\cdot\boldsymbol{\nabla})\mathbf{p} = -e\left(\mathbf{E} + \frac{\mathbf{v}}{c}\times\mathbf{B}\right) \tag{2.76}$$

Using the relativistic momentum $\mathbf{p} = \gamma m_e \mathbf{v}$, where $\gamma = \sqrt{1+a_0^2}$ for circularly polarized light and $\gamma = \sqrt{1+a_0^2/2}$ for linearly polarized light, and the electromagnetic vector and scalar potentials to replace $\mathbf{E} = -\frac{1}{c}\frac{\partial \mathbf{A}}{\partial t}$ and $\mathbf{B} = \boldsymbol{\nabla}\times\mathbf{A}$, Eq. 2.76 becomes:

$$\frac{\partial \mathbf{p}}{\partial t} + \frac{(\mathbf{p}\cdot\boldsymbol{\nabla})\mathbf{p}}{\gamma m_e} = \frac{e}{c}\frac{\partial \mathbf{A}}{\partial t} + \frac{e}{\gamma m_e c}\left(\mathbf{p}\times\boldsymbol{\nabla}\times\mathbf{A}\right) \tag{2.77}$$

An electric potential term $\boldsymbol{\nabla}\Phi$ may be added to modify the electric field, but it would generally drop into the final results (Eq. 2.79) untouched.

We may decompose the momentum and Eq. 2.77 into its longitudinal $(\hat{\mathbf{z}}, \|)$ and transverse $(\hat{\mathbf{x}}, \perp)$ components, noting that $\mathbf{p}\times\boldsymbol{\nabla}\times\mathbf{A} = \boldsymbol{\nabla}(\mathbf{A}\cdot\mathbf{p}) - (\mathbf{p}\cdot\boldsymbol{\nabla})\mathbf{A}$ where $\mathbf{A} = A(z,t)\hat{\mathbf{x}}$ and $\boldsymbol{\nabla}\to\partial/\partial z$. The transverse component is:

$$\left(\frac{\partial}{\partial t} + v_\parallel\frac{\partial}{\partial z}\right)\left(p_\perp - \frac{eA}{c}\right) = \frac{d}{dt}\left(p_\perp - \frac{eA}{c}\right) = 0 \tag{2.78}$$

The differential operator on the left hand side of Eq. 2.78 represents the time rate of change in the frame of reference of the electron, or $d/dt$. This can be seen by making the change of variable $\xi = k_L z - \omega_L t$ and noting that its total time derivative is $d\xi/dt = k_L v_\parallel - \omega_L$. From this result, we may define the canonical momentum $\mathbf{P} = \mathbf{p} - e\mathbf{A}/c$ noting that $P_\perp = 0$ and $P_\parallel = p_\parallel$. Plugging this back into Eq. 2.77 and solving for the longitudinal component yields:

$$\frac{dp_\parallel}{dt} = -m_e c^2 \boldsymbol{\nabla}(\gamma - 1) \tag{2.79}$$

This is the relativistic ponderomotive force, often associated with a ponderomotive

potential bearing a striking resemblance to the kinetic energy:

$$U_p = m_e c^2(\gamma - 1) \tag{2.80}$$

Taking the nonrelativistic limit ($a_0 \ll 1$) of Eq. 2.79 for linearly polarized light, we easily recover Eq. 2.75. The primary difference between the two is that with relativistic laser intensities, electrons propagate along with the laser far more than transversely, mainly due to the $\mathbf{J} \times \mathbf{B}$ term. This acceleration and subsequent plasma heating mechanism is consequently dubbed $J \times B$ *heating*, dominant for laser intensities $\gtrsim 10^{18}\ W/cm^2$ (69). The J×B force may be represented as:

$$F_p = -\frac{m_e c^2\ \boldsymbol{\nabla}\left(a_0^2\right)}{4}\left(1 - \cos(2\omega_L t)\right) \tag{2.81}$$

where the second term is the oscillating component. Similar to vacuum heating, electrons are pulled out into vacuum and accelerated into the plasma, but here at twice the laser frequency. At relativistic velocities, electrons may clear the critical surface and dephase from the laser. The hot electrons resulting from this mechanism assume an effective temperature scaling with the ponderomotive potential:

$$T_{hot} \approx \left(\sqrt{1 + \frac{I_L \lambda_L^2}{1.37 \times 10^{18}\ W cm^{-2} \mu m^2}} - 1\right)\ 511\ keV \tag{2.82}$$

This has been demonstrated both computationally (70) and experimentally (71; 72). The experiments explained in this dissertation have used relativistic laser intensities, making J×B heating the primary heating mechanism to drive hot electrons.

# Chapter 3

# Proton Acceleration & Transport

When a high-intensity laser interacts with a cold (read: room temperature) solid target, the various laser absorption mechanisms described in the preceding section effect a wide energy spectrum of electrons. Laser intensities ranging between $10^9$ - $10^{21}$ $W/cm^2$ may interact with steep or gentle density gradients at various times in the target evolution. For this reason, and because they are far more mobile than ions, electrons are the primary absorbers of laser energy, gaining kinetic energies from $keV$ up to several tens of $MeV$. After the laser couples primarily with the electrons, the electrons are free to transfer their energy to other radiation particles, including neutrons, gamma and x-ray photons, positrons, and significant to this dissertation, ions.

## 3.1 Target Normal Sheath Acceleration

The hot electrons $\left(\gtrsim MeV\right)$ traveling close to the speed of light are essentially collisionless $\left(\nu_{ei} \propto T_e^{-3/2}\right)$ and disperse quickly throughout the $\sim \mu m$-size target within tens of femtoseconds. Electrons at the high-energy tail of the spectrum are able to fully escape the target (73), but a significant number of electrons assemble a spatial charge separation over the target surface area and consequently an electrostatic sheath field. Electrons reaching the rear surface thereafter may not have enough kinetic energy to overcome the potential, so they reflux back

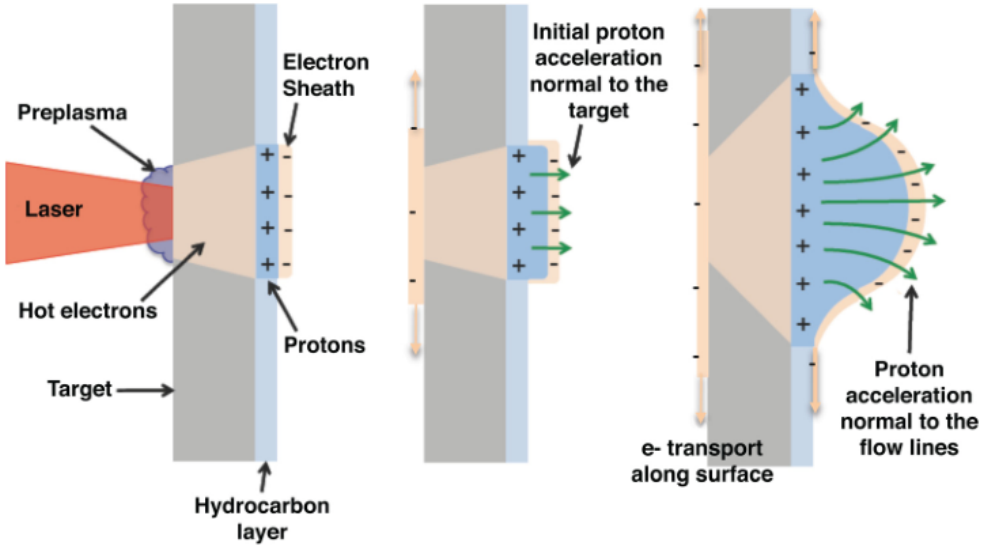


**Figure 3.1**: TNSA mechanism: hot electrons generated from relativistic laser-matter interaction form a strong sheath field at target rear surface, which ionizes and accelerates hydrogen atoms away from the surface. Figure taken from Ref. (8).

into the target and spread out transversely. As these hot electrons thermally equilibrate toward a Boltzmann distribution $n_{hot} \sim \exp(e\Phi/T_{hot})$, we would expect that the sheath field scales with the characteristic energy of the hot electrons over the hot electron Debye length:

$$E \approx \frac{T_{hot}}{e\lambda_D} \approx \sqrt{\frac{T_{hot}\ [MeV]}{n_{hot}\ [10^{21}\ cm^{-3}]}}\ (4.25\ MV/\mu m) \tag{3.1}$$

where $T_{hot}$ is given by Eq. 2.82 and $\lambda_D$ is for the hot electron population.

This sheath field is actually strong enough to instantly ionize atoms on the rear surface, where there is usually a thin hydrocarbon contaminant layer (oils, water vapor etc.) (74). Once ionized, ions as heavy as oxygen are accelerated in the direction of the sheath field normal to the surface. Having the highest charge-to-mass ratio, protons are preferentially accelerated toward the electrons forming a quasi-neutral expanding plasma and mitigating further field acceleration for surface ions thereafter. This ion acceleration mechanism is illustrated in Fig. 3.1 and aptly named *target normal sheath acceleration* (TNSA) because the generated electric sheath always directs ions normal to the surface. It was first explained by Wilks *et al.* (75) and is the most thoroughly

understood laser-ion acceleration mechanism since its discovery. Classic TNSA assumes that the laser does not penetrate deep into the target, especially to the rear surface affecting the charge separation and sheath field (76; 77). The following sections introduce a simple fluid model for TNSA, and outline significant experimental and computational studies to optimize proton beam characteristics over the past couple of decades.

### 3.1.1 Analytic 1D Expansion Models

The plasma expansion may be analytically investigated in 1-D where ions at rest with density $n_i$ occupy the half-infinite space $z < 0$ with a sharp front, and electrons with temperature $T_e$ excited by an intense laser pulse are continuous over all space according to the Boltzmann distribution:

$$n_e = n_0 \, \exp\left(\frac{e\Phi}{T_e}\right) \tag{3.2}$$

where $n_0$ is the initial electron density in the undisturbed plasma ($z \to -\infty$). Combining this with Poisson's equation

$$\frac{d^2\Phi}{dz^2} = 4\pi(n_e - Zn_i) \tag{3.3}$$

and noting that $n_i(z > 0) = 0$, one can show (78) that at $t = 0$ the electrons form a cloud extending beyond the ion front given by:

$$\begin{aligned} \left.\frac{e\Phi}{T_e}\right|_{z>0} &= -1 - 2\ln(1+\hat{z}) \\ \left.\frac{\mathsf{e}n_e}{n_0}\right|_{z>0} &= (1+\hat{z})^{-2} \end{aligned} \tag{3.4}$$

where $\mathsf{e} = 2.718..$ is Euler's number and $\hat{z} = z/\lambda_D\sqrt{2\mathsf{e}}$ is the normalized sheath distance. The corresponding solutions for $z < 0$ may be solved numerically, and the full solutions are depicted in Fig. 3.2(a). From this, we observe that the electric field at the ion front is indeed $E \sim T_e/e\lambda_D$.

As the electron sheath begins to pull the ions out into vacuum and expand the plasma for

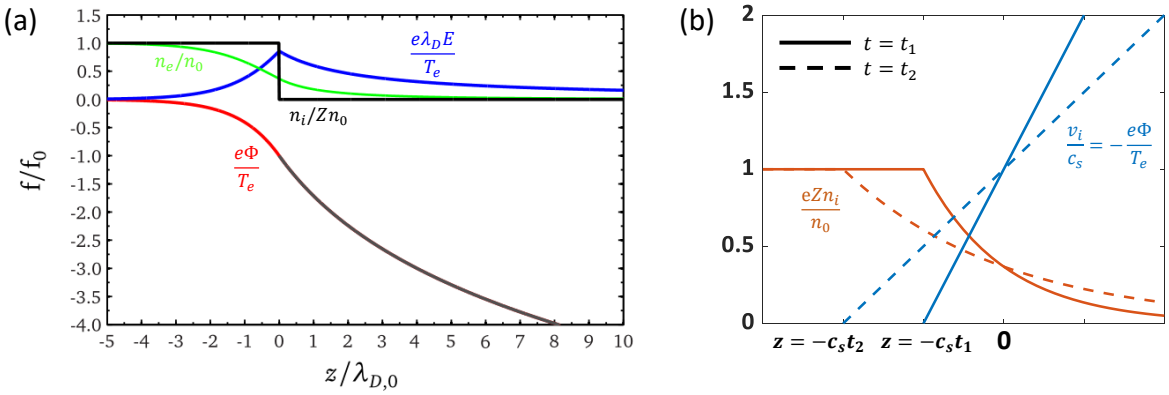


**Figure 3.2**: (a) Ion and electron density profiles along with electric potential and field profiles (9) for a neutral plasma occupying the half-infinite space $z < 0$. (b) Self-similar plasma expansion solution for ion density, velocity, and electric potential at $t_2 > t_1 > 0$ (10).

$t > 0$, the ions may be modeled via the fluid continuity equation:

$$\frac{\partial n_i}{\partial t} = -\frac{\partial}{\partial z}(n_i v_i) \tag{3.5}$$

and the fluid momentum equation with the electrostatic force:

$$\frac{\partial v_i}{\partial t} + v_i \frac{\partial v_i}{\partial z} = -\frac{Ze}{m_i}\frac{\partial \Phi}{\partial z} = -\frac{c_s^2}{n_i}\frac{\partial n_i}{\partial z} \tag{3.6}$$

where $c_s \equiv \sqrt{ZT_e/m_i}$ is the ion sound speed. Here, we assume ions are collisionless so that we may neglect the pressure term. The last equality assumes that quasi-neutrality $(n_e \approx Zn_i)$ and an *isothermal* electron Boltzmann distribution (Eq. 3.2) are maintained throughout expansion. A solution to Eqs. 3.5-3.6 exists when the self-similar velocity variable $\xi = z/c_s t$ is used (79; 10):

$$\begin{aligned} \frac{v_i}{c_s} &= 1 + \frac{z}{c_s t} \\ \frac{eZn_i}{n_0} &= \exp\left(-\frac{z}{c_s t} - 1\right) \\ \frac{e\Phi}{T_e} &= -\frac{z}{c_s t} - 1 \end{aligned} \tag{3.7}$$

from which we may derive that the self-similar electric field $E_{ss} = -d\Phi/dz = T_e/ec_st$ decreases with the ion density scale length $L_i \equiv c_st$. Depicted by Fig. 3.2(b), this solution describes an ion rarefaction wave initialized at $z = 0$ moving backward with speed $-c_st$ and ion front propagating forward with velocity $c_st$. By combining particle energies $\varepsilon_i = m_i v_i^2/2$ with the density equation, we may obtain the self-similar ion energy spectrum (ions per unit energy per unit surface area):

$$\frac{dN_i}{Ad\varepsilon_i} = \frac{n_0 c_s t}{Z^2 T_e}\sqrt{\frac{ZT_e}{2\varepsilon_i}}\,\exp\left(-\sqrt{\frac{2\varepsilon_i}{ZT_e}}\right) \tag{3.8}$$

The self-similar solution, however, is only valid while $\lambda_D < L_i$, or $\omega_{p,i}t < 1$ where $\omega_{p,i} = \sqrt{4\pi n_0 Ze^2/m_i} = c_s/\lambda_D$ is the ion plasma frequency. As the plasma expands, the hot electrons disperse and their density decreases, which increases their Debye length. Mora numerically solves Eqs. 3.2, 3.3, 3.5, and 3.6 without assuming quasi-neutrality to obtain an ion beam with a finite-velocity beam front (11). This gives rise to a varying electric field in space with a sharp peak at the beam front whose characteristics are:

$$E_{fr} \approx \frac{4T_e}{ec_st} \tag{3.9}$$

$$v_{fr} \approx 2c_s \ln(2\tau) \tag{3.10}$$

$$z_{fr} \approx 2c_st(\ln 2\tau - 2) \tag{3.11}$$

where $\tau = \omega_{p,i}t/\sqrt{2e} \gg 1$ is assumed. The charge separation, electric field and ion energy distribution are compared with the self-similar solutions in Fig. 3.3 at varying times. Importantly, the ion front also gives rise to a cut-off energy given by:

$$\varepsilon_{max} = 2ZT_e\ \ln^2 2\tau \tag{3.12}$$

Mora later describes an adiabatic model of plasma expansion where electrons gradually impart their energy to the fields and ions and therefore exhibit decreasing temperature with time

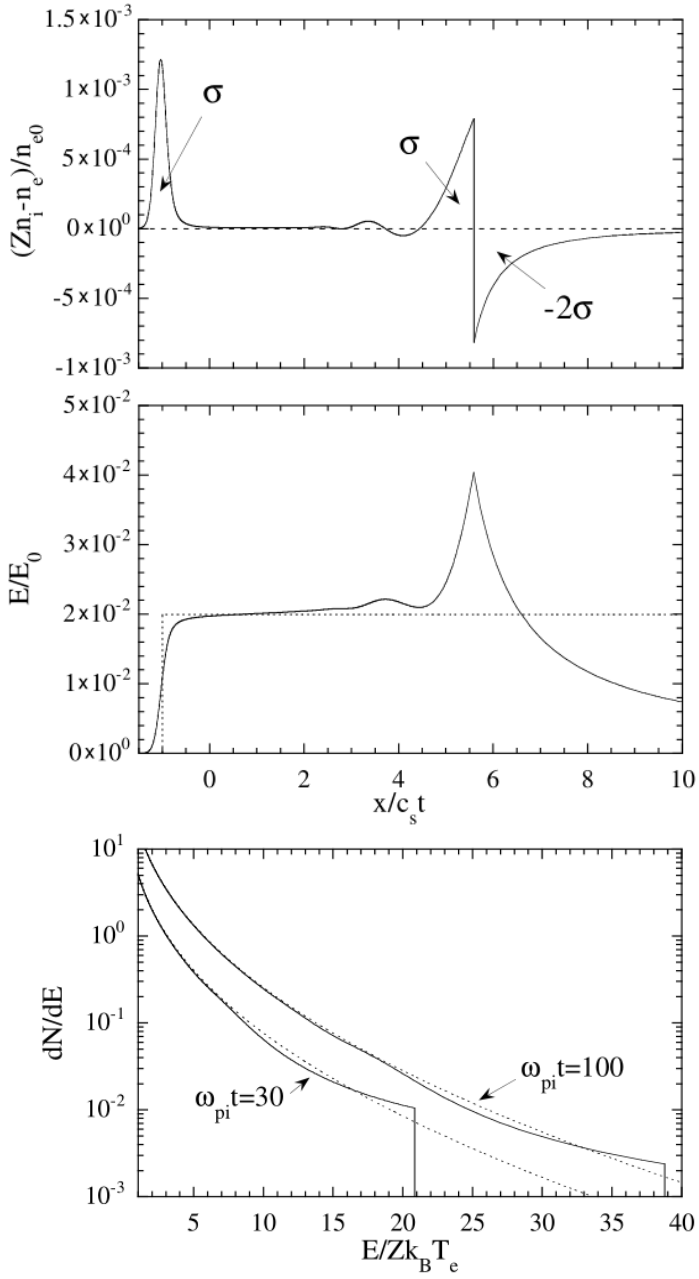


**Figure 3.3**: Numerical solutions to ion fluid expansion without the quasi-neutrality assumption, compared with self-similar solutions (Eqs. 3.7) shown in dotted curves. Figures taken from Ref. (11).

(80; 81). These 1D expansion models also predict a time-dependent ion energy distribution given by:

$$\frac{dN_i}{Ad\varepsilon_i} = \frac{n_0 R_0}{Z\sqrt{\varepsilon_i T_{eff}}} \exp\left(-\frac{\varepsilon_i}{T_{eff}}\right) \tag{3.13}$$

where $R_0$ is the initial characteristic scale length of the plasma, and $T_{eff}$ is the time-dependent effective electron temperature which converges to the (measured) hot electron temperature $T_e$ as $t \to \infty$.

### 3.1.2 Previous Studies on Maximum Proton Energy and Conversion Efficiency

Soon after the TNSA mechanism was discovered (82), it was immediately recognized that these laser-accelerated protons could be a viable alternative to electrons in the fast ignition scheme introduced in Sec. 1.2.1 (38). To that end, prolific research was conducted to optimize three primary proton beam properties – laser-to-proton energy conversion efficiency (CE), maximum proton energy $\varepsilon_{max}$ and/or Maxwellian beam temperature $T_p$, and proton focusing techniques. As previously discussed, these are the primary beams characteristics driving the proton fast ignition scheme.

Mackinnon *et al.* (83) experimentally demonstrated that TNSA protons exhibited several times higher $\varepsilon_{max}$ and $T_p$ on thinner targets ($\sim 3\ \mu m$) compared to thicker targets ($\sim 100\ \mu m$). Using 2D particle-in-cell simulations, Sentoku *et al.* (84) showed that when the target thickness $L$ is less than half the laser pulse length $L_p$, electron recirculation in the target enhances the hot electron density at the rear surface, which enhances the sheath field and therefore proton acceleration. The maximum proton energy was found to scale inversely with target thickness, $\varepsilon_{max} \propto 1/L$. Recognizing that the hot electron density plays a significant role in proton energy, Hey *et al.* (85) investigated the role of target thickness on CE and found that it too exhibits a $1/L$ scaling for thick targets ($L \gg c_s T_e/(d\varepsilon_e/dt)$). This is because the electron energy loss rate

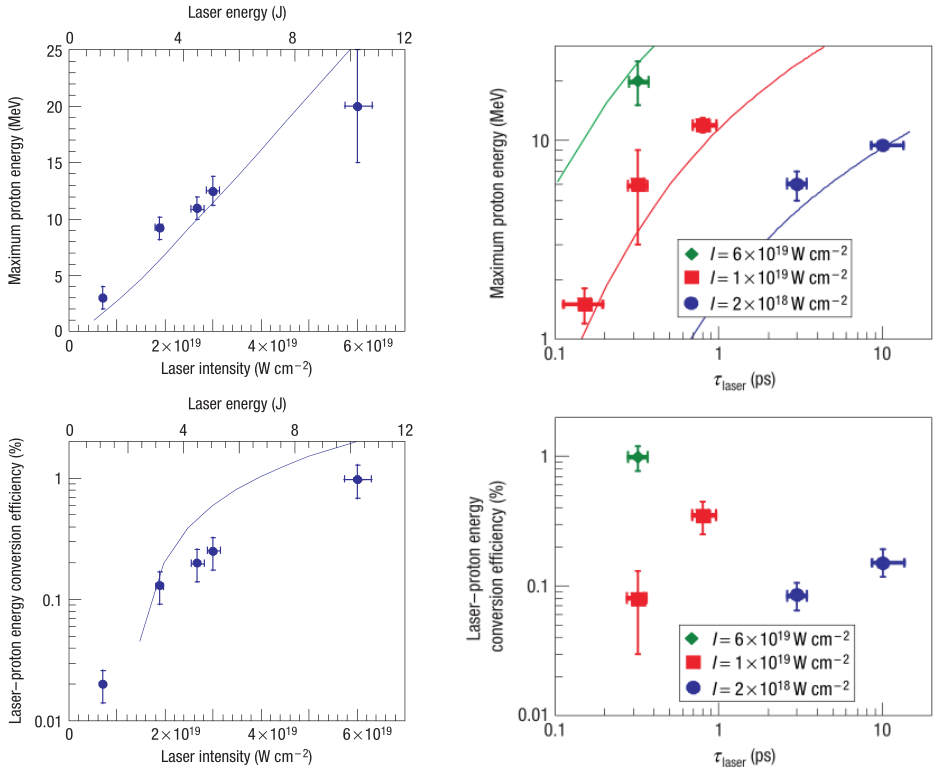


**Figure 3.4**: Variation of maximum proton energy $\varepsilon_{max}$ and laser conversion efficiency to TNSA protons with laser's intensity and pulse duration. Curves represent theoretical model by Mora (11). Figures taken from Ref. (12).

$d\varepsilon_e/dt$ due to bulk plasma collisions far exceeds that due to adiabatic expansion.

Fuchs *et al.* (12) later investigated the dependence of CE and $\varepsilon_{max}$ on laser intensity $I_L \sim 10^{18}$ - $10^{19}$ $W/cm^2$ and pulse duration $\tau_L \sim 0.1$ - $10$ $ps$ using thin aluminum foils. This was accomplished by varying either the laser energy $E_L$ or $\tau_L$ while keeping the other – and laser spot size – constant. The experimental results were also compared with the fluid model predictions for $\varepsilon_{max}$ (Eq. 3.12) and $dN/d\varepsilon$ (Eq. 3.8). As shown in Fig. 3.4, $\varepsilon_{max}$ and CE both increase with increasing $E_L$, and are in rough agreement with the isothermal model. The model's accuracy was more keenly assessed when keeping the pulse energy constant and varying $\tau_L$, with experimental results showing good agreement. It should be noted, however, that in utilizing Eq. 3.8, the acceleration time used was $t_{acc} = 1.3\tau_L$ to best fit to the experimental data.

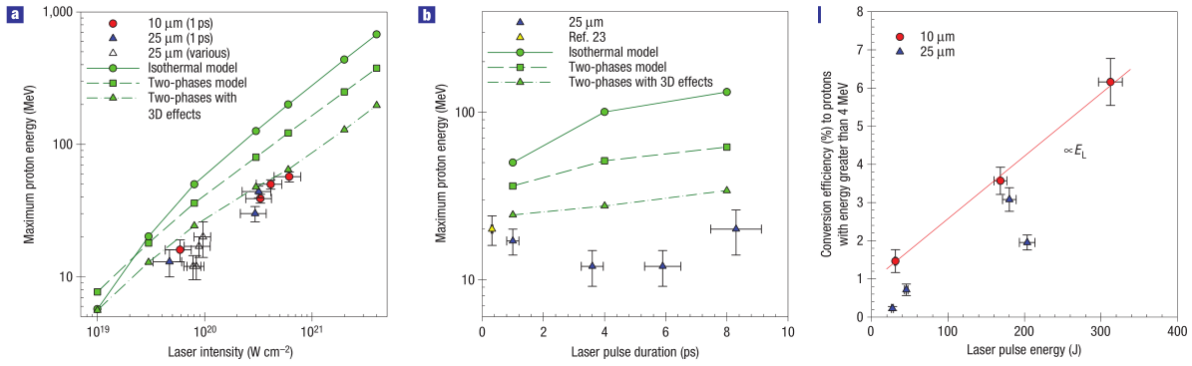


**Figure 3.5**: Experimental results measuring $\varepsilon_{max}$ and CE for higher laser energies and pulse durations. Figures taken from Ref. (13).

Robson *et al.* (13) expanded on Fuchs' work by increasing the laser energy and intensity range up to 400 $J$ and $6 \times 10^{20}$ $W/cm^2$, respectively, over 10 $ps$. They also compare their experimental results with not only the model above but also a revised two-phase model in which the hot electron temperature first rises linearly then decreases according to the adiabatic model. While the isothermal model predicts CE and $\varepsilon_{max}$ sufficiently accurately for laser intensities up to $6 \times 10^{19}$ $W/cm^2$, it is insufficient at higher intensities. As shown in Fig. 3.5(a-b), the revised 1D two-phase model gets closer to experimental results, and including 3D effects (radial expansion of hot electrons and ceasing the proton acceleration when a particular 3D expansion geometry is reached) brings the model sufficiently close to experimental results. The laser-to-proton energy CE also increases by an order of magnitude at higher intensities.

### 3.1.3 Previous Studies on Beam Focusing

With the TNSA mechanism, the incidence angle of the laser pulse on target plays a minor role in the resulting proton beam – in particular, the initial proton acceleration was more or less normal to the rear surface regardless of laser incidence angle. This led scientists to investigate whether beam focusing is possible through simple target geometry. Ruhl *et al.* (86) ran 3D particle-in-cell simulations to model the proton acceleration resulting from intense laser interaction with

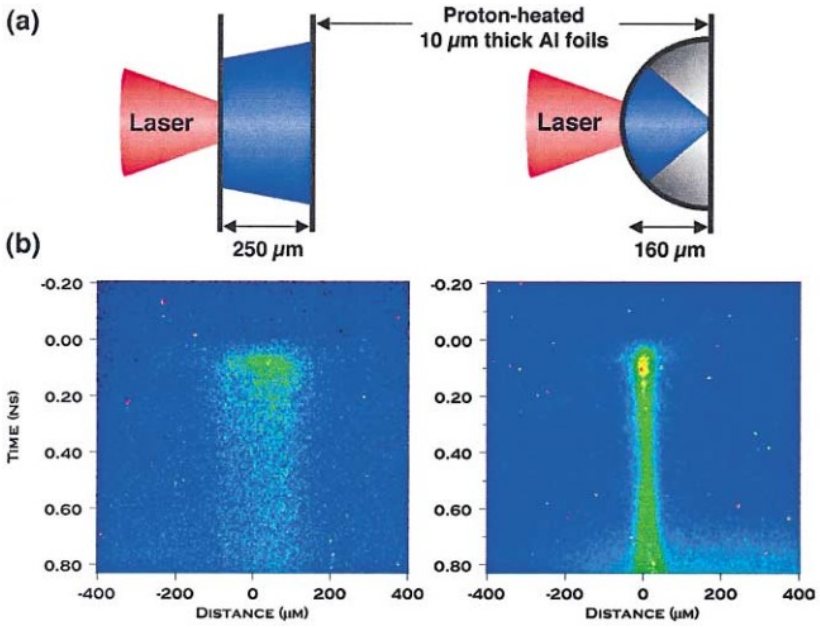


**Figure 3.6**: (a) Configurations of proton heating from flat and curved foil targets, with (b) their corresponding heating profile evolution from rear surface thermal emission. Figures taken from Ref. (14).

spherical thin foil targets. With spherical foils, all rear surface normal vectors point toward the sphere center, so the protons would in principle focus to that point. The simulations modeled the interaction of $10^{21}$ - $10^{22}$ $W/cm^2$ laser with a spherical shell with thickness 15 $\mu m$ and radius 22 $\mu m$, and results indicated that this method can indeed focus TNSA protons to a spot near the spherical center.

Focusing with spherical targets was first experimentally demonstrated by Patel *et al.* (14), in which protons were accelerated from 10 $\mu m$ thick flat foils and from 10 $\mu m$ thick hemispherical ("hemi") shells. To demonstrate both focusing and heating capabilities, the protons in both cases were directed toward secondary 10 $\mu m$ aluminum foils. The schematic and results may be seen in Fig. 3.6. Planckian thermal emission at wavelength 570 $nm$ from the secondary samples was recorded using streaked optical pyrometry, where the horizontal axis represents 1D space and the vertical axis represents time. The more narrow and brighter emission from the hemi shell

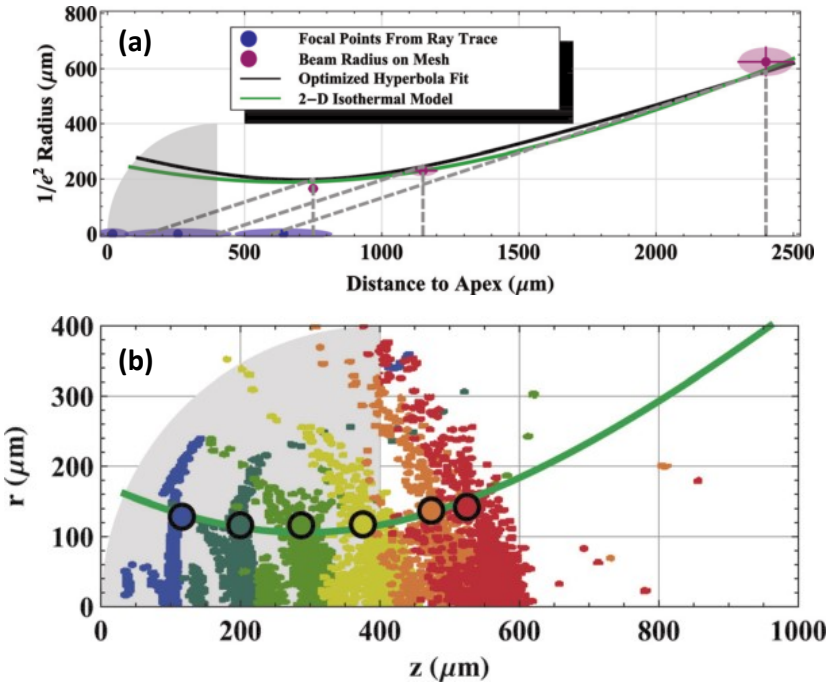


**Figure 3.7**: Comparison of beam radius measurements (a) and simulation results (b) with 2D isothermal expansion model (green curves). Six colors in (b) represent accelerated bunch of carbon ions at times $t = 8,\ 16,\ 24,\ 32,\ 40$, and 44 *ps* from left to right. Figures taken from Ref. (15).

demonstrates better focusing and, importantly, higher heating (up to $23 \pm 6\ eV$) compared with the flat foil target. Importantly, this confirmed that laser-driven focused proton beams are capable of heating thin samples to the warm dense matter regime, setting the foundations for a warm dense matter research platform.

With the studies on hemi focusing of proton beams, the question still remained of whether the quasi-neutral proton plasma jet focused ballistically to reach a 0D focal point. Offerman *et al.* (15) demonstrated that although the protons' trajectories are initially normal to the spherical surface, they follow a hyperbolic curve as shown in Fig. 3.7. In the interest of proton fast ignition, the hemispherical shell was reduced to a partial hemisphere attached to a conical structure ("hemi-cone"), which has the dual advantage of shielding the proton ignitor beam from the imploding target and channeling the proton beam through the cone tip. In principle, the hot electrons

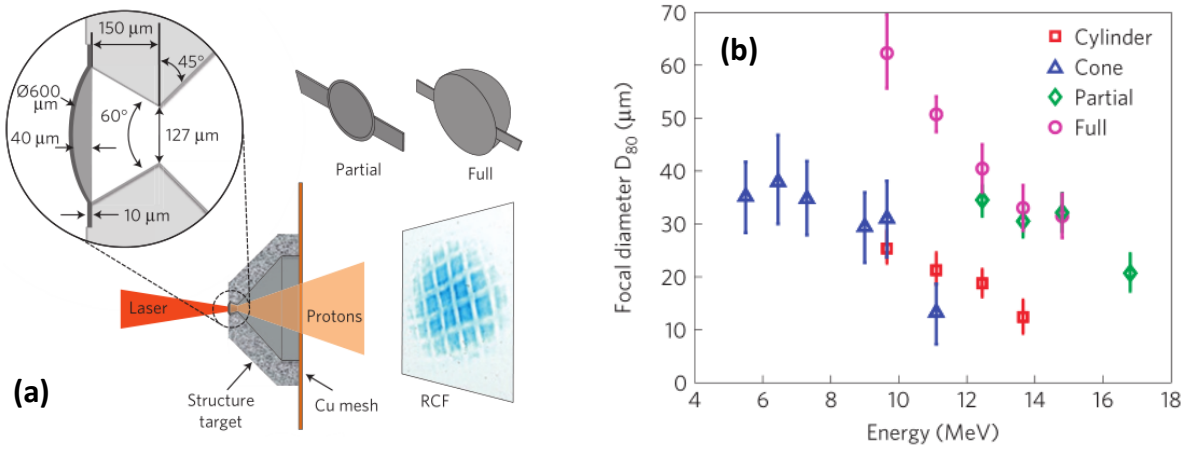


**Figure 3.8**: Experimental setup (a) of laser-driven cone-guided proton beam generation from various structured targets. Focal diameters of resulting beams as a function of proton energy shown in (b). Figures taken from Ref. (16).

generated from the laser interaction with the hemi-cap permeate the entire hemi and travel into the cone, generating an additional sheath structure along the interior cone surface that assist in focusing the protons.

Bartal *et al.* (16) was the first to experimentally compare proton beam characteristics among partial hemi, full hemi, and hemi-cone structured targets, as shown in Fig. 3.8(a). As shown in Fig. 3.8(b), the proton focal diameters from hemi targets are significantly larger than those from conic structures. In the context of fast proton heating, McGuffey *et al.* (17) demonstrated that kilojoule-class multi-*ps* lasers coupled with hemi-cone structured targets are quite effective at isochorically heating warm and hot dense plasmas. Measuring the sample temperature via Cu-$K_\alpha$ emission spectroscopy, they compared the heating capabilities of protons from hemi, hemi-wedge, and hemi-cone structures and found that the latter produced a more tightly focused area on a thin Cu sample heated to 100 *eV*, as shown in Fig. 3.9.

Simulations (8; 18) further showed that the electric fields in the plasma and along the cone surfaces are the primary drivers of beam focusing in hemi-only and hemi-cone targets. With hemi-only targets, the hot electrons propagating transversely along the curved surface generate focusing sheath fields further out longitudinally that assist in focusing the protons. In the hemi-cone targets,

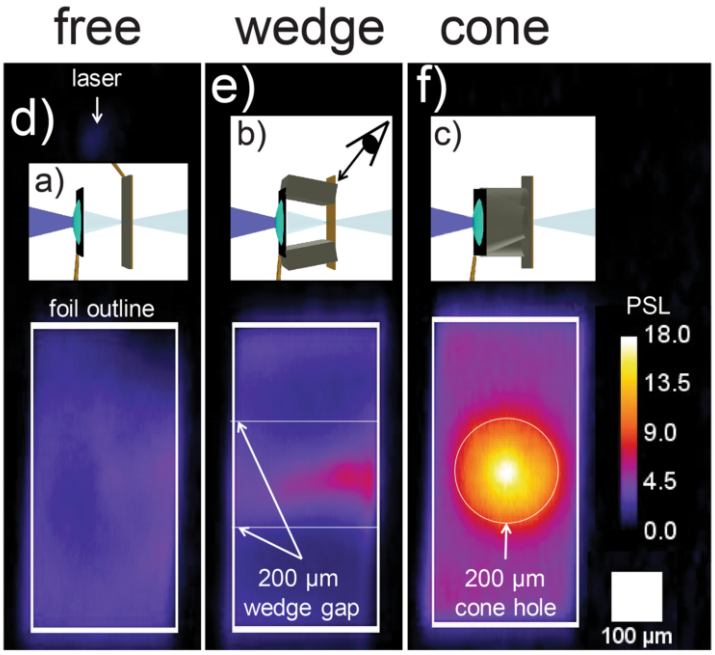


**Figure 3.9**: Comparison of measurement of Cu foil heating by laser-driven protons from (a,d) free-standing hemi, (b,e) hemi-wedge structure, and (c,f) hemi-cone structure. Figure taken from Ref. (17).

the hot electrons further propagating through the cone bulk maintain a focusing sheath field well into the vacuum interior, significantly extending and enhancing the proton focusing all the way to the cone tip. This may be seen in Fig. 3.10(a-f). However, a direct result of hot electron expansion into the cone is their absence behind the hemi surface. With fewer hot electrons, the longitudinal sheath field along the hemi surface decreases significantly at later times leading to a measurable decrease in proton acceleration, as shown in Fig. 3.10(g-r). Simulations show that this results in a factor of 3 decrease in CE, as shown in Fig. 3.11. Ultimately, the addition of a cone structure significantly increases the focusing of the proton beam to the necessary spot size, but unfortunately at the expense of the energy conversion efficiency.

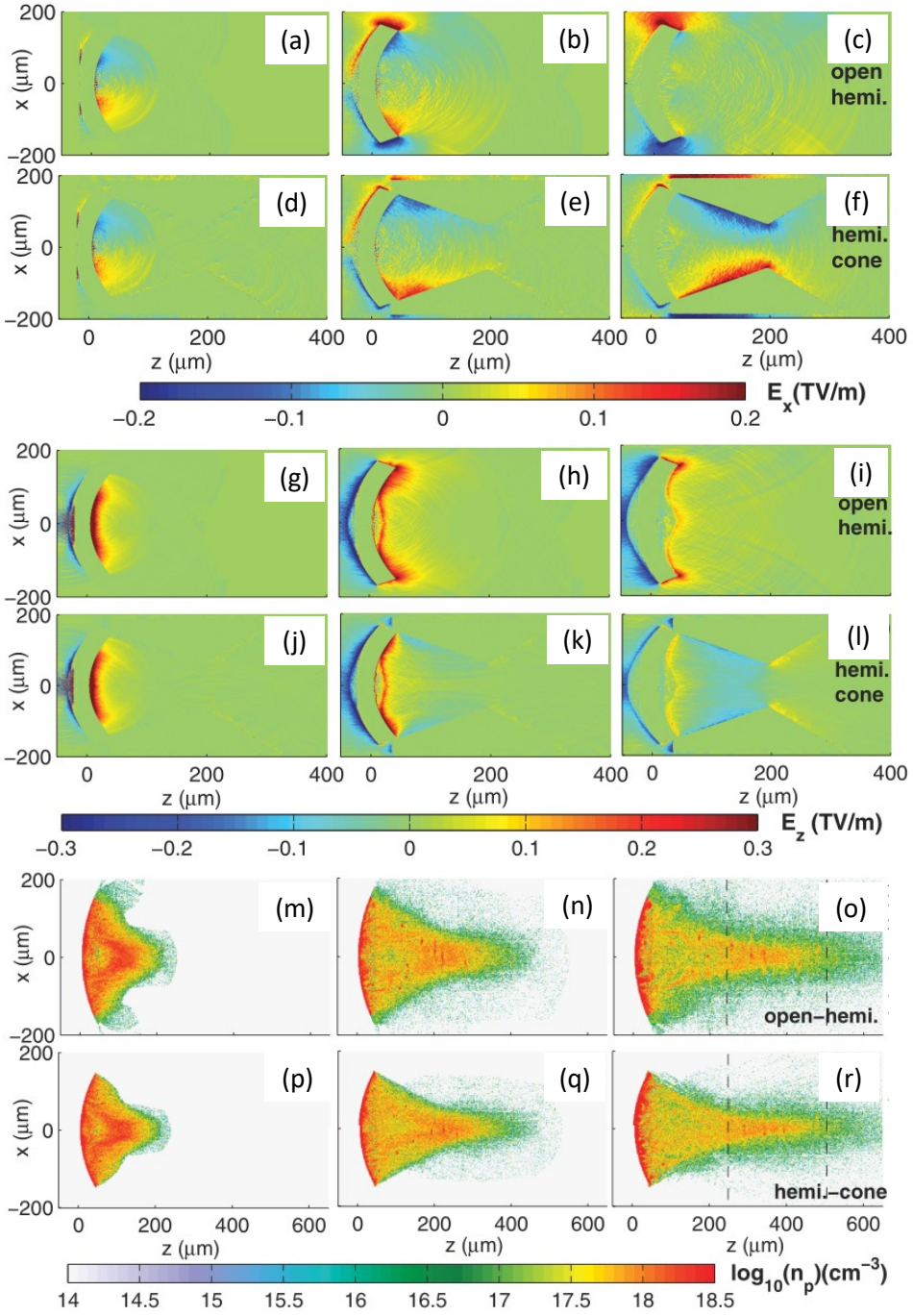


**Figure 3.10**: Simulation results of transverse (a-f) and longitudinal (g-l) fields resulting from laser interaction of freestanding hemi (respective top rows) vs hemi-cone (respective bottom rows) targets, resulting in proton acceleration as shown in density map (m-r). Figures taken from Ref. (18).

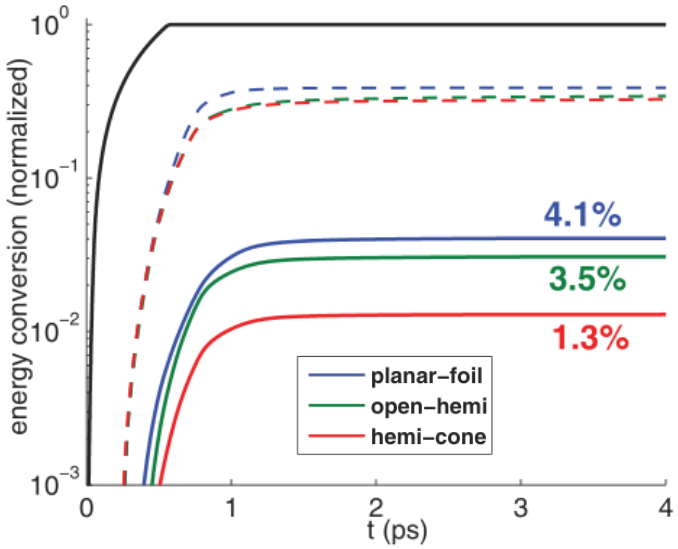


**Figure 3.11**: Simulation results of laser energy conversion efficiency to protons (solid colored curves) for flat foil, freestanding hemi, and hemi-cone targets. Black line shows the total laser energy and dashed lines show the intermediate laser conversion to hot electrons. Figure taken from Ref. (18).

## 3.2 Proton Stopping and Energy Deposition

The preceding section discussed the generation of quasi-neutral, energetic proton beams via intense laser irradiation of thin targets. This discovery led to an onslaught of proposed applications, including warm dense matter sample generation, proton radiography and imaging, inertial confinement fusion schemes, and possibly even medical therapy. All of these applications, however, necessitate an understanding of how these protons transport through various media such as solids and plasma. One fundamental aspect in particular has been the subject of over a century of investigation, from the time that charged particles revealed their existence, before even Bohr's atomic model. Here, we discuss the dynamics with which energetic protons are able to deposit their energy and gradually slow down as they penetrate a medium. The *stopping power* $\mathbf{S} \equiv -dE_K/d\boldsymbol{l}$ is defined as the incremental kinetic energy loss $dE_K$ of a projectile particle per unit path length $d\boldsymbol{l}$ in its transport through a medium. This is dependent on both targets parameters (density, temperature, ionization state) as well as projectile parameters (energy, charge

state).

### 3.2.1 Stopping Power from Bound Electrons

In the early days of stopping power investigation circa late 1800s, models were more or less inconclusive, since in the first place an accurate model of the atom did not exist. Soon after Niels Bohr put forth the classical prototypical atomic model establishing a central heavy nucleus with orbiting electrons, he published a pioneering analysis in 1913 on the slowing of projectile ions via electromagnetic interactions with target atoms (87). Using a configuration and analysis similar to that in Fig. 2.2 wherein an ion projectile (atomic number $Z_p$, mass $m_p$, and speed $v_p$) within a target (density $n_i$, atomic number $Z$) passes near a bound electron $(e,\ m_e)$ with impact parameter $b$, Bohr calculated that the stopping power of the projectile is:

$$S = \frac{4\pi Z_p^2 Z n_i e^4}{m_e v_p^2}\, L \tag{3.14}$$

where $L$ is the *stopping number*, Bohr's version of which is the Coulomb logarithm $L_{Bohr} = \ln(b_{max}/b_{min})$. With his new atomic model in which electrons harmonically oscillate with atomic resonance frequency $\omega$, Bohr noted that no energy would be transferred if the interaction was long compared with the orbital frequency, so $b_{max} \sim v_p/\omega$. Also, Rutherford's elastic scattering model should also dictate that the distance of closest approach is $b_{min} \sim Z_p e^2/m_e v_p^2$, yielding Bohr's classical nonrelativistic model for stopping power:

$$S_{Bohr} = \frac{4\pi Z_p^2 Z n_i e^4}{m_e v_p^2} \ln\left(\frac{C m_e v_p^3}{Z_p e^2 \omega}\right) \tag{3.15}$$

where $C = 2\mathrm{e}^{-\gamma_E}$ and $\gamma_E \approx -0.5772..$ is Euler's constant.

As quantum mechanics gradually developed, stopping power theory developed alongside it. Using the Born series approximation for the quantized momentum transfer of ions scattering

off bound electrons (quantum analogy to Bohr's approach), Bethe (1930) developed the first fully quantum theory of stopping power (88). While the pre-factor remained the same as in Eqs. 3.14-3.15, the stopping number proposed by Bethe read as:

$$L_{Bethe} = \ln\left(\frac{2m_e v_p^2}{\langle I\rangle}\right) \tag{3.16}$$

where $\langle I\rangle$ is the weighted mean excitation energy per bound electron and may be written as $\hbar\langle\omega\rangle$.

Soon after, Bloche (1933) analyzed the differences between the classical (Bohr) and quantum (Bethe) approaches and found that the quantum approach was still correct for large impact parameters or low momentum transfer. For large momentum transfers, he found that quantum wave packets would still scatter classically, validating the Bohr approach. He bridged the two formulas by adding a correction to the Bethe equation to obtain the Bethe-Bloche stopping number (89):

$$L_{B-B} = \ln\left(\frac{2m_e v_p^2}{\langle I\rangle}\right) + \Psi(1) - \mathbb{R}\left\{\Psi\left(1 + i\,\frac{Z_p e^2}{\hbar v_p}\right)\right\} \tag{3.17}$$

where $\Psi$ is the digamma function and $\Psi(1) = -\gamma_E$ is Euler's constant. It is interesting to note that by plugging in $\langle I\rangle = \hbar\langle\omega\rangle$ and asymptotically expanding $\mathbb{R}\Psi(1+iy) \approx \ln y + 1/12y^2$ in the limit $Z_p e^2 \gg \hbar v_p$, we recover the Bohr stopping number with a quantum correction:

$$L_{B-B} \approx \ln\left(\frac{2m_e v_p^3}{Z_p e^2 \omega}\right) - \frac{1}{12}\left(\frac{\hbar v_p}{Z_p e^2}\right)^2 \tag{3.18}$$

For completeness, we also include the relativistic Bethe-Bloche stopping number with various correction terms (90):

$$L_{B-B}^{rel} = \ln\left(\frac{2m_e c^2 \gamma_p^2 \beta_p^2}{\langle I\rangle}\right) - \beta_p^2 + \Psi(1) - \mathbb{R}\left\{\Psi\left(1 + i\,\frac{Z_p \alpha}{\beta_p}\right)\right\} - \frac{\sum_j C_j}{Z} - \frac{\delta}{2} \tag{3.19}$$

where $\alpha \equiv e^2/\hbar c \approx 1/137$ is the fine structure constant, $\beta_p = v_p/c$ and $\gamma_p$ is the projectile's

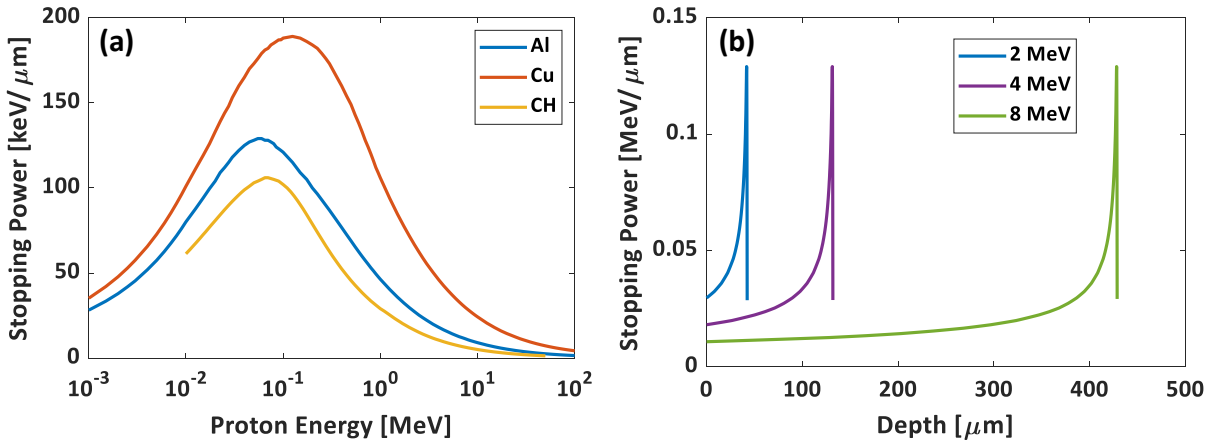


**Figure 3.12**: (a) Proton stopping power from bound electrons as a function of proton energy for various media. (b) Stopping power of protons with varying initial energies as a function of penetration depth in solid-density room temperature aluminum, clearly displaying the Bragg peak.

Lorentz factor. The first term is the relativistic analog to Eq. 3.16, and the second term is the relativistic spin contribution (91). The next two terms represent the Bloche correction (Eq. 3.17) to harmonize with the classical Bohr model. The $j^{th}$ *shell corrections* $C_j/Z$ come into play when the projectile velocity is not much faster than the bound electron velocity, i.e. orbital shells must be considered in energy transfer. Fortunately, this correction is maximized at about 6%. The *density effect* $\delta/2$ corrects for target polarization by the projectile, i.e. the interaction fields are reduced by the dielectric of the medium. Eq. 3.19 is the most widely used stopping number for ion projectiles interacting with bound electrons. A significant assumption is the projectile charge state $Z_p$ be constant, which could break down at low velocities as the projectile may capture electrons. This begets a lower energy limit of $\sim 1\ MeV/amu$.

The stopping power of protons for various target materials may be found in the **p**roton **st**opping power **a**nd **r**ange (PSTAR) (92) database, or may be simulated using the **s**topping and **r**ange of **i**ons in **m**atter (SRIM) software (93). These resources take into account the contributions listed in Eq. 3.19 as well as those from the relatively heavy atomic nuclei. Although infrequent, nuclear stopping power plays a significant role at relativistic proton energies, but is generally

negligible by a factor of $Zm_i/m_e$ relative to electronic stopping power. In Fig. 3.12(a), we observe that the increase of stopping power with decreasing kinetic energy is characterized by the $v_p^{-2}$ term in the pre-factor, and gives rise to the *Bragg peak*, shown explicitly in Fig. 3.12(b) near the well-defined stopping range. These energy deposition curves are unique to protons and dictates that the slower the proton, the more energy it deposits such that most of the proton energy is deposited close to its stopping depth. Physically, as the proton velocity eventually slows to close to the electron thermal velocity, their interactions become significantly stronger and quickly draw out the remaining proton energy. This peculiar feature makes protons well-suited for cancer therapy — instead of x-rays depositing damaging radiation to tissue above and below a tumor site, a proton may deposit minimal energy to surrounding tissue and maximum energy to the tumor site. The sharpness of the Bragg peak depends on the assumption of cold materials i.e. $(T_e \ll 1\ eV)$. At finite temperatures, the Bragg peak effect is diminished, as explained in Sec. 3.2.3.

### 3.2.2 Stopping Power from Free Electrons

The preceding section dealt with the stopping power of ions due to electrons bound to the atomic nucleus. This is highly relevant for room temperature materials and gases whose atoms have not been ionized (excepting valence electrons). In dense and ideal plasmas, however, atoms are at least partially ionized and free electrons abound. These free electrons indeed contribute to the slowing of ions in the plasma, but must be treated differently from bound electrons. Assuming for now that the plasma is fully ionized, the pre-factor in Eq. 3.14-3.15 remains the same insofar as the density of free electrons is $Zn_i$. Then, following Jackson (91) in the center-of-mass frame of binary collisions between energetic ions and free electrons (equilibrated to a thermal Maxwellian distribution), the stopping number is:

$$L_{free} = G\left(\frac{v_p}{v_{th}}\right)\ln\left(\frac{0.764}{b_{min}}\frac{v_p}{\omega_{p,e}}\right) \tag{3.20}$$

where $v_{th} \equiv \sqrt{2T_e/m_e}$ introduces a dependence on electron temperature to the stopping number and

$$G(\xi) = \mathrm{erf}(\xi) - \frac{2}{\sqrt{\pi}}\,\xi \exp\left(-\xi^2\right) \tag{3.21}$$

is a modified error function. The inclusion of $G(v_p/v_{th})$ is a result of a rigorous treatment of ion-electron collision frequencies (94) and ensures that $L_{free} \to 0$ as $v_p \to 0$. The Coulomb logarithm in Eq. 3.20 contains similar $b_{max} \sim v_p/\omega_{p,e}$ as in Bohr's model and thus accounts for local plasma excitations. The minimum impact parameter, however, now decides between the classical distance of closest approach or the quantum electron deBroglie wavelength,

$$b_{min} = \max\left(\frac{Ze^2}{m_*\langle \mathbf{u}\rangle^2}, \frac{\hbar}{2m_*\langle \mathbf{u}\rangle}\right) \tag{3.22}$$

where $\mathbf{u} = \mathbf{v}_p - \mathbf{v}_e$ is the projectile velocity relative to electrons, and $m_* \equiv m_e m_p/(m_e + m_p) \approx m_e$ is the binary reduced mass.

### 3.2.3 Comprehensive Stopping Power Models

In the preceding sections, the evaluation of electronic stopping powers are largely founded on binary collision and scattering theory. While the presented equations agree sufficiently well with experiments in their own regimes of applicability, each regime offers significantly different results. In the warm dense matter regime, present in astrophysical objects and ICF implosions, atoms are partially ionized, so that both bound and free electrons are present in varying proportions. Configurations such as these require comprehensive stopping power models to account for a number of variables, including relative projectile speeds, impact parameter ranges, and target temperatures and densities. The following models have been proposed to gain a clearer picture of stopping power and apply to a wide range of target and projectile parameters.

**Ad-Hoc Bound + Free Formulation**

Since the preceding sections primarily distinguish between bound and free electrons, it is only natural to have a *bound + free model* in which the two are combined such that each applies to its intended population (95; 96; 97). An important parameter is therefore the average ionization (charge) state $Z^*$ of the plasma as a function of density and temperature. This is often calculated via the Saha equation or using the equation of state (EOS) of the target material. In this scheme, It is not uncommon to replace $Z$ in the common pre-factor with $Z^*$ or $(Z-Z^*)$, insofar as those stopping calculations pertain to the bound or free electrons per atom:

$$S_{b+f} = \kappa_p \left[ (Z-Z^*) n_i \, L_b + Z^* n_i \, L_f \right] \tag{3.23}$$

for (new) pre-factor $\kappa_p = 4\pi Z_p^2 e^4 / m_e v_p^2$, bound electron density $(Z-Z^*)n_i$ coupled with stopping number $L_b$, and free electron density $Z^* n_i$ coupled with stopping number $L_f$.

In essence, Eq. 3.23 simply adds the stopping power due to bound electrons $S_b = \kappa_p (Z - Z^*) n_i L_b$ to that due to free electrons $S_f = \kappa_p Z^* n_i L_f$ in an *ad-hoc* way $S_{b+f} = S_b + S_f$. In our treatment, $L_b$ is given by Eq. 3.19 (omitting the shell correction and density effect terms), and $L_f$ is given by Eq. 3.20. Fig. 3.13 compares the bound and free stopping powers as a function of incident proton energy for various temperatures of solid-density aluminum. Note that the stopping powers change by only $\sim 10\%$ in going from room temperature to 10 $eV$, but changes significantly in shape and magnitude as the temperature increases further.

In treating the bound and free electrons separately, the distinguishing parameter is a locally *averaged* ionization state $Z^*$ based on material temperature and density. One drawback of this is an establishment of local thermodynamic equilibrium (LTE), which is not guaranteed for small time scales. The bound + free model also ambiguously defines the boundary between "slow" and "fast" projectile ions relative to electrons. Nevertheless, this model yields reasonably accurate results for the proton energies and dense ICF plasmas that are relevant to this dissertation

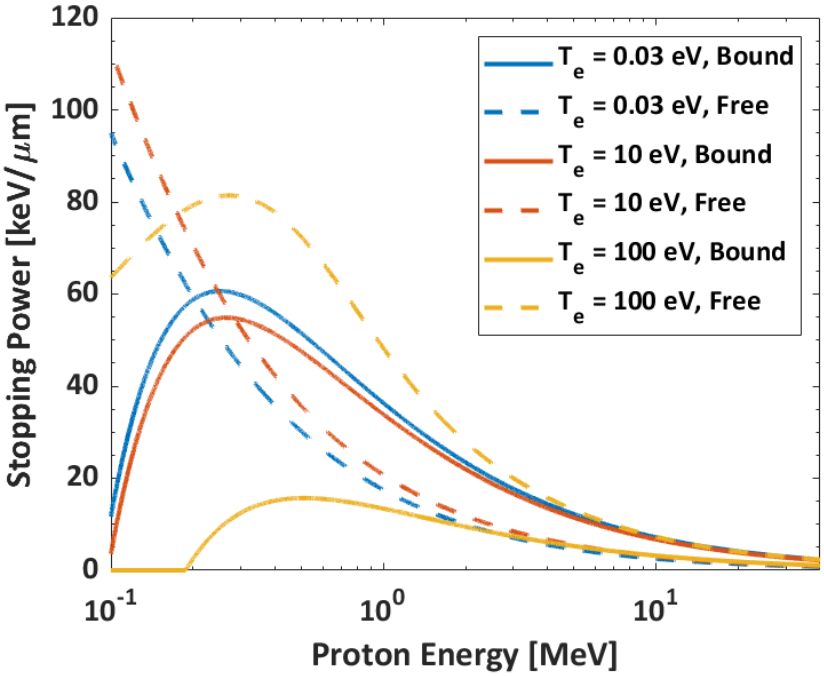


**Figure 3.13**: Electronic stopping power contributions in solid-density aluminum as functions of incident proton energy, for room and warm dense matter temperatures.

(96; 98) and is therefore used in both the hybrid-PIC simulations explained in Sec. 4.4 as well as in theoretical calculations explored in Chapter 7.

### Dielectric Formulation

An alternative, possibly more holistic approach to a comprehensive stopping power model is the self-consistent dielectric formulation by Lindhard and associates (99; 100; 101). They consider the ion projectile as a source of an electric field perturbation in a free electron gas medium. In other words, the ion projectile locally polarizes the medium, and the induced electric field acts to slow the projectile i.e. lose energy. This formulation of stopping power is distinct from the bound + free formulation, and draws the attention and analysis toward the medium's properties rather than toward a magnified view of the projectile and binary collisions. At zero temperature, the stopping power of an ion projectile through a uniform free electron gas is given

by:

$$S_{Lh} = \frac{4\pi Z_p^2 e^4}{m_e v_p^2}\, n_e L_{Lh}(n_e, v_p) \tag{3.24}$$

where $n_e$ is the electron number density and $L_{Lh}$ is again the stopping number. It is clear that the pre-factor still matches that in Eq. 3.14 (for $n_e = Zn_i$), and the physics of this new approach is contained in the stopping number:

$$L_{Lh}(n_e, v_p) = \frac{i}{\pi\omega_{p,e}^2} \int_0^\infty dk \int_{-kv_p}^{+kv_p} d\omega\, \frac{\omega}{k} \left( \frac{1}{\varepsilon(\omega, k)} - 1 \right) \tag{3.25}$$

where $\varepsilon(\omega, k)$ is the local dielectric function in the projectile's trajectory. Here, plasma excitations and electron screening is taken into account.

Eq. 3.24 may be extended to nonuniform electron gases with $n_e(\mathbf{r})$ by using a local density approximation (LDA) (102), wherein the density is assumed uniform in smaller volume elements and then summed to obtain the total stopping power:

$$S_{Lh}^{LDA} = \frac{4\pi Z_p^2 e^4}{m_e v_p^2} \int d^3r\, n_e(\mathbf{r}) L_{Lh}(n_e, v_p) \tag{3.26}$$

Wang *et al.* (103) showed that for protons with energy $\gtrsim MeV$, the effective interaction time $\tau_{eff} \sim |\nabla n_e| / n_e v_p$ on the length scales of atomic shell structure ($\sim$ Bohr radius) is still far less than the plasma oscillation period $\omega_{p,e}^{-1}$, meaning the LDA is appropriate in this formulation. They then extended the zero-temperature formulation of Lindhard to include a temperature dependence on the stopping number, yielding a self-consistent generalized stopping power formula:

$$S_{Lh}^{gen} = \frac{4\pi Z_p^2 e^4}{m_e v_p^2} \int d^3r\, n_e(\mathbf{r}) L_{Lh}(n_e, T_e, v_p) \tag{3.27}$$

The difficulty with this formulation comes down to choosing (1) an atomic-scale electron density distribution model for $n_e(\mathbf{r})$, and (2) a temperature-dependent dielectric function, both sufficiently accurate over a large range of ICF-relevant temperatures and densities. The former may

utilize the first-principles average-atom model in the self-consistent approach for astrophysical and laboratory plasmas (SCAALP) based on density-functional theory (DFT). The latter utilizes the random phase approximation (RPA) proposed by Maynard and Deutsch (104). Taken together, this stopping power calculation is quite sophisticated in that the nonlinear differential equations for DFT must be solved throughout the projectile's trajectory. While this level of sophistication yields a more accurate and self-consistent stopping power calculation, the spatial and temporal resolutions that make this calculation accurate are far more resolved than those relevant to this dissertation. Also, the dielectric formulation is not readily implemented in a plasma simulation code alongside other computationally expensive algorithms outlined in the following chapter. For these reasons, the dielectric formulation will not be used in this dissertation. In contrast, the bound + free model is a relatively simple equation which may be evaluated quickly. Its only requirement is a sufficiently accurate calculation of $Z^*$, which as we will see may be readily implemented into plasma simulation codes. In the next chapter, we introduce the computational tools necessary to self-consistently simulate the transport and stopping power of intense proton beams. In doing so, the simply evaluated bound+free stopping power model may be benchmarked against the state-of-the-art quantum theoretical SCAALP for the proton beam and target parameters relevant to this dissertation.

# Chapter 4

# Numerical Methods & Simulations

As with all science and technology, the study of plasma physics has been drastically improved through the use of computers. Acting as both an aide to and motivator for laboratory experiments, computer simulations have been integral to our understanding of many plasma phenomena, not the least of which include laser-plasma interactions, plasma turbulence, laboratory astrophysics, and others. In general, when studying a plasma phenomenon, an experiment may be performed, after which a simulation may be conducted to mimic the experiment as closely as possible. Comparing the simulation and experimental results, the simulation methods may then be appropriately modified to better reflect the underlying physics. Once they reflect the experiment sufficiently accurately, simulations may be used to further predict another or more advanced plasma phenomenon, at which point the process starts over. In this way, experiments and simulations iterate in tandem to advance the study of plasmas.

At their core, computer simulations attempt to solve the equations governing plasma dynamics. The methods with which they do so generally fall into three camps which reflect the underlying equations. Kinetic Vlasov-Fokker-Planck (VFP) codes evolve the distribution functions of particle species in time through electromagnetic field interactions, collisions, diffusion etc. While there may be fewer equations to solve i.e. Eq. 2.1 along with Maxwell's equations,

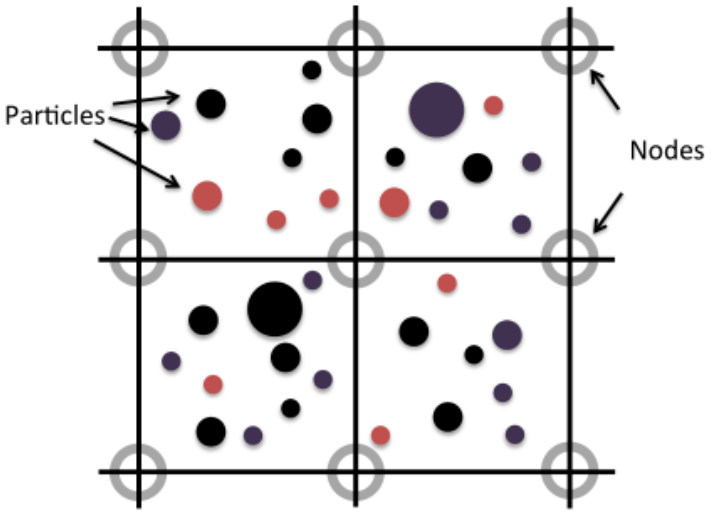


**Figure 4.1**: Basic particle-in-cell configuration of macroparticles among a grid of nodes. Figure taken from Ref. (19)

the multidimensional phase space requires the distribution function itself to be between 3- and 7-D, which makes phenomena like collisions impressively complex to compute. Zooming out to macroscopic plasma flows, the magnetohydrodynamic (MHD) or fluid approach solves the fluid continuity and momentum equations (Eqs. 2.2-2.3) along with energy conservation and Maxwell's equations to model plasma dynamics and shock physics on larger length and time scales. MHD codes are useful when quasi-neutrality is assumed and the plasma Debye length and plasma oscillation time need not be resolved.

The kinetic particle-in-cell (PIC) approach is a fundamentally different approach wherein a large number of particles, once assembled for $t = 0$, are simulated to move under the influence of various forces in 1- to 3-D space. Because of the immense processing power needed to simulate the dynamics of so many particles at small time scales, PIC simulations use macroparticles. Each macroparticle represents a large number of particles of a single species – electrons, protons, ions etc., thereby conserving the charge-to-mass ratio of real particles. As shown in Fig. 4.1, macroparticles exist over a grid of "cells", and may be summed, averaged, or otherwise operated on to yield continuous quatities such as density, temperature, current, pressure etc.

PIC's basic method is the following: at one time step, source quantities like charge and current densities are calculated from the instantaneous position and velocities of all macroparticles, according to Eq. 2.9. These quantities are then used to compute the electromagnetic fields according to Ampere's and Faraday's Laws:

$$\begin{aligned} \frac{\Delta \mathbf{E}}{\Delta t} &= c\boldsymbol{\nabla} \times \mathbf{B} - 4\pi \mathbf{J} \\ \frac{\Delta \mathbf{B}}{\Delta t} &= -c\boldsymbol{\nabla} \times \mathbf{E}, \end{aligned} \tag{4.1}$$

where $\Delta t$ is a time step. The electromagnetic fields are calculated on an overlaid discretized grid and interpolated to the macroparticles' positions. Since each macroparticle conserves charge-to-mass ratio, the Lorentz force on all macroparticles are calculated and act almost equivalently to individual particles.

In the time-*explicit* PIC algorithm, the particles' momenta advances are usually calculated in a leap-frog scheme, or staggered with positions advance in half-integer time steps:

$$\frac{\Delta \mathbf{p}}{\Delta t} = \frac{\mathbf{p}_{n+1/2} - \mathbf{p}_{n-1/2}}{\Delta t} = \frac{q}{m}\left(\mathbf{E}_n(\mathbf{x}_n) + \frac{\langle \mathbf{p} \rangle_n}{\gamma_n mc} \times \mathbf{B}_n(\mathbf{x}_n)\right) \tag{4.2}$$

$$\frac{\Delta \mathbf{x}}{\Delta t} = \frac{\mathbf{x}_{n+1} - \mathbf{x}_n}{\Delta t} = \frac{\langle \mathbf{p} \rangle_n}{\gamma_n m} \tag{4.3}$$

where $\Delta t$ is a time step and $\gamma_n$ and $\langle \mathbf{p} \rangle_n = (\mathbf{p}_{n+1/2} + \mathbf{p}_{n-1/2})/2$ are the Lorentz factor at and averaged momentum around the $n^{\text{th}}$ time step, respectively. We observe that the fields $\mathbf{E}_n$ and $\mathbf{B}_n$ are calculated alongside particles' positions in the integer time steps. As mentioned, the $q/m$ dependence allows the forces on the macroparticles to be equivalent to those on real particles. In the particle-push stage, the macroparticles evolve in space to their next positions and velocities in the subsequent time step.

To maintain numerical accuracy and stability, it is reasonable to have to limit the time step relative to the spatial step. In particular, for explicit time integration schemes for differential

equations, the *Courant-Friedrichs-Lewy* (CFL) condition (105) must be met:

$$\sum_{i}^{N} \frac{u_i \Delta t}{\Delta x_i} \leq C_{max} \tag{4.4}$$

where $\Delta x_i$ and $u_i$ are the spatial step and the velocity in the $i^{\text{th}}$ dimension, respectively, $N$ is the number of spatial dimensions used, and $C_{max} \sim N$ for explicit solvers. The CFL condition implies that the time step should be chosen such that the largest speed encountered in the simulation e.g. for a wave should not move more than $\Delta x_i$ in one time step. This ensures that the numerical solution remains stable in time. For plasma simulations, the condition on the time step is even stronger i.e. $\Delta t < \omega_{p,e}^{-1}$ to resolve plasma oscillation, and that on the spatial grid is $\Delta x_i < \lambda_D$ to resolve the Debye length. For solid density plasmas where $n_e \sim 10^{23}\ cm^{-3}$, the requisite time step is $\Delta t \ll 1\ fs$, which makes any meaningful simulation long and computationally expensive. The hybrid fluid-PIC simulation code LSP (106) utilizes a *direct-implicit* time integration scheme that greatly relaxes the time step conditions, as discussed in the following section.

## 4.1 Direct-Implicit Method

To relax the previously mentioned strong stability conditions such that we may have $\omega_{p,e}\Delta t \gg 1$ and $\Delta x_i/\lambda_D \gg 1$, LSP utilizes a direct implicit $(D_1)$ time integration algorithm (107; 108). This scheme is particularly beneficial for simulations involving near solid-density plasmas, where the Debye length and plasma frequency do not play important roles in the dynamics and therefore need not be resolved. With larger time steps, the direct-implicit scheme is able to evolve the plasma dynamics over time scales $\sim$ several 10s of $ps$, as opposed to $\lesssim ps$ of standard explicit PIC schemes. This is at the cost of resolving high-frequency modes, but, importantly, also at the cost of exact energy conservation, as will be discussed in the next section.

In this algorithm, the particles' momenta push follows Eq. 4.2 except that the electric field

is modified to include both past and future fields:

$$\mathbf{E}_n(\mathbf{x}_n) \rightarrow \frac{\mathbf{E}_{n-1}(\mathbf{x}_{n-1}) + \mathbf{E}_{n+1}(\mathbf{x}_{n+1})}{2} \tag{4.5}$$

However, this requires knowledge of the future field before it is calculated. Actually, particles are pushed twice: first assuming no future electric field $\mathbf{E}_{n+1}(\mathbf{x}_{n+1}) = 0$, and again with a linear correction term to predict the effect of the future field. This new scheme may be summarized by $\mathbf{p}_{n+1/2} = \langle \mathbf{T} \rangle \mathbf{A}_i$. The (dimensionless) magnetic field rotation tensor is:

$$\langle \mathbf{T} \rangle = \frac{1}{1+\Omega^2} \begin{bmatrix} 1+\Omega_1^2 & \Omega_1\Omega_2 + \Omega_3 & \Omega_1\Omega_3 - \Omega_2 \\ \Omega_1\Omega_2 - \Omega_3 & 1+\Omega_2^2 & \Omega_2\Omega_3 + \Omega_1 \\ \Omega_1\Omega_3 + \Omega_2 & \Omega_2\Omega_3 - \Omega_1 & 1+\Omega_3^2 \end{bmatrix} \tag{4.6}$$

where

$$\mathbf{\Omega} = \frac{q\mathbf{B}_n}{2\gamma mc}\,\Delta t \tag{4.7}$$

is the relativistic angular rotation vector normalized to the time step, and subscripts denote axes directions. The source vectors are used for the two pushes:

$$\mathbf{A}_1 = \frac{q\mathbf{E}_{n-1}}{m}\frac{\Delta t}{2} + \mathbf{p}_{n-1/2} + (\mathbf{p}_{n-1/2} \times \mathbf{\Omega}) \tag{4.8}$$

$$\mathbf{A}_2 = \frac{q\mathbf{E}_{n+1}}{m}\frac{\Delta t}{2} \tag{4.9}$$

Before the second particle push, the linear correction term to the future electric field is calculated via perturbation analysis of the current density. In lieu of the details, we present the resulting susceptibility tensor given by:

$$\langle \mathbf{S} \rangle = \frac{\rho}{\gamma_{n+1/2}}\frac{q}{m}\frac{\Delta t}{2}\left(\langle \mathbf{T} \rangle - \frac{\mathbf{v}_{n+1/2}\mathbf{v}_{n+1/2}}{c^2}\right) \tag{4.10}$$

which is incorporated into Ampere's law to determine the future electric field via a current perturbation $\delta\mathbf{J} = \langle\mathbf{S}\rangle\mathbf{E}$:

$$\frac{\partial \mathbf{E}}{\partial t} = \boldsymbol{\nabla}\times\mathbf{B} - (\mathbf{J} + \delta\mathbf{J}) \tag{4.11}$$

Essentially, the algorithm averages the past $(n-1)^{\text{th}}$ EM fields and particle momenta with the future $(n+1)^{\text{th}}$ quantities, and then linearly corrects the fields through the susceptibility term.

## 4.2 Hybrid Fluid Method

Fully kinetic simulations run into issues with numerical heating/cooling due to the finite size of macroparticles and grid discretization, leading to artificial particle interactions and energy transfer fluctuations. Likewise, intrinsic to the implicit time integration algorithm discussed in the previous section is non-exact conservation (dissipation) of energy, as detailed in Ref. (109). Combined with large time and spatial steps, numerical cooling is likely to occur as slow-moving particles may artificially encounter drag and decelerate.

Uniquely, LSP evades this issue by allowing certain macroparticles to represent non-relativistic Maxwellian-distributed particle ensembles, often dubbed "fluid" particles. This is, however, a partial misnomer since neither the Navier Stokes equations (Eqs. 2.2-2.3) nor MHD equations are invoked in the macroparticles' advancements. Actually, fluid macroparticles obey the same kinetic equations as their kinetic counterparts except for the elastic scattering terms, which are replaced by a pressure gradient force term for intra-species collisions and a frictional force term for inter-species collisions. But the primary difference in implementing fluid macroparticles is that they obey an additional energy equation:

$$\frac{3}{2}n_i\frac{dT_i}{dt} = -n_iT_i\,\boldsymbol{\nabla}\cdot\mathbf{v}_i + \boldsymbol{\nabla}\cdot(\kappa\boldsymbol{\nabla}T_i) + 2m_in_i\sum_j\frac{T_j-T_i}{m_j\tau_{ji}} + \sum_j\nu_{ji}\frac{m_im_j}{m_i+m_j}\left|\frac{\mathbf{p}_i}{m_i}-\frac{\mathbf{p}_j}{m_j}\right|^2 \tag{4.12}$$

where $n_i$, $T_i$, $\mathbf{v}_i$, $\mathbf{p}_i$ and $m_i$ are, respectively, the density, temperature, velocity, momentum and

particle mass of fluid species $i$, $\kappa$ is the thermal conductivity, and $\tau_{ji}$ and $\nu_{ji}$ are the thermalization time and collision frequency between species $j$ and $i$. From left to right, the terms on the RHS are $PdV$ work, thermal conduction, inter-species energy exchange, and Ohmic heating, all contributing to the time rate of change of energy density.

By also obeying an internal energy equation, the issue with energy conservation and numerical cooling is mostly resolved. While the fluid macroparticles still advance kinetically to new positions and momenta, their internal energies are advanced and saved such that any numerical cooling effects are mostly balanced by changes in internal energy. This is particularly advantageous for energy conservation in dense plasmas for long simulation times (110). In the simulations relevant to this dissertation, background electrons and background ions making up the dense plasma (Al, Si, polypropylene, etc.) are given the fluid macroparticle treatment, as long as neither species incurs temperatures above 10s of $keV$. The simulated beam protons and beam electrons incident on these dense plasmas are treated kinetically.

## 4.3 Collisions and Resistivity

Since solid-density plasmas are extremely relevant to this dissertation, treatment of particle collisions must be given special scrutiny. LSP utilizes primarily two approaches for particle collisions. High-energy relativistic particles (mostly electrons) are treated as test particles and given binary collision and scattering treatment with collective processes, as detailed in (111). For slow-moving particles, LSP assigns either a binary scattering method or a statistical scattering method. The binary scattering method evaluates binary Coulomb collisions for randomly selected pairs of particles in each grid cell. This yields accurate results when particles exhibit non-Maxwellian distributions (read: non-thermalized), but is more computationally expensive.

The statistical scheme treats particle collisions with the Jones algorithm (112), which utilizes a grid-based "collision field" to mediate the collisional forces among particles within

each cell. This scheme advantageously conserves energy and momentum exchange locally. The momentum and energy transfers among different species are given by:

$$\Delta \mathbf{p}_i = m_i \Delta t \sum_j \left( \frac{\mathbf{p}_j}{m_j} - \frac{\mathbf{p}_i}{m_i} \right) \nu_{ji} \tag{4.13}$$

$$\Delta T_i = \Delta t \sum_j \left[ \frac{4 m_i^2 n_i^2}{m_j \tau_{ji}} (T_j - T_i) + \frac{2}{3\gamma} \nu_{ji} \frac{m_i m_j}{m_i + m_j} \left| \frac{\mathbf{p}_j}{m_j} - \frac{\mathbf{p}_i}{m_i} \right|^2 \right] \tag{4.14}$$

where the energy equation is akin to the final two terms in Eq. 4.12 i.e. thermalization and Ohmic heating. We note that these equations assume that the particles in each cell follow a drifting Maxwellian distribution characterized by an average drift momentum as well as a temperature for the energy variation.

The preceding discussion on the treatment of particle collisions in LSP is important because it governs the collective dynamics of dense plasmas in a PIC setting. On a microscopic scale, test particles transporting through materials encounter resistance in their trajectory due to collisions with background electrons and ions. This resistance induces an electric field given by Ohm's law, $\mathbf{E} = \eta \mathbf{J}_c$ for resistivity $\eta$ and current density $\mathbf{J}_c$ in the conductor. In some fluid and hybrid-PIC simulation codes (113), resistivity is input as simply another property of a simulated dense solid. In LSP by contrast, an effective resistivity emerges as a direct consequence of Coulomb collisions among background particles. The collision frequencies used by LSP in Eqs. 4.12-4.13 for fluid particles are taken from the Lee-More model (114) with corrections by Desjarlais (28). The required inputs for this model are ion density, local electron temperature, and locally averaged ionization state $Z^*$, which in turn depends on electron temperature and density. We utilize the Prism Opacity and EOS code (PrOpacEOS) (24) to generate EOS tables for the average charge state as a function of density and temperature.

Using the Drude model for resistivity

$$\eta = \frac{m_e}{e^2 n_f} \nu_e \tag{4.15}$$

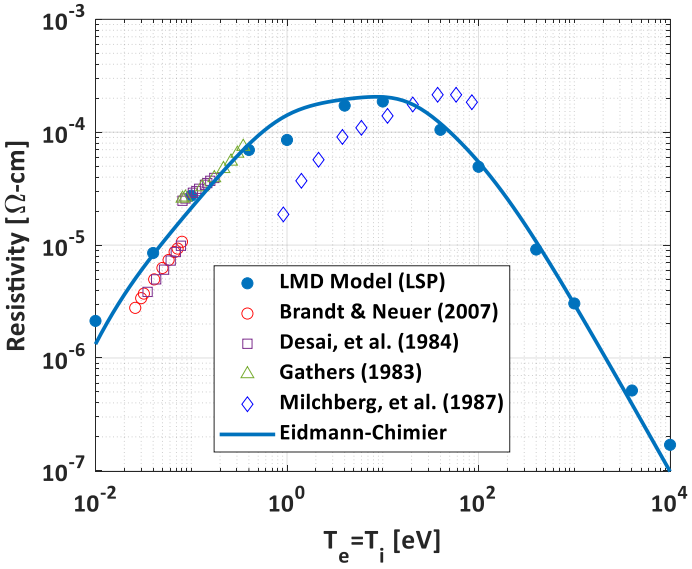


**Figure 4.2**: Comparison of experimental measurements (20; 21; 22; 23), LSP LMD model outputs, and Eidmann-Chimier analytical model output of solid-density aluminum resistivity as a function of temperature.

where $n_f$ is the free electron density and $\nu_e$ is the total electron collision frequency, we may compute the effective resistivity simulated by LSP and compare it with the Eidmann-Chimier model of total electron collision frequencies (54) introduced in Sec. 2.6, i.e. Eq. 2.43. Fig. 4.2 shows the experimental (20; 21; 22; 23), computational, and analytical resistivity of aluminum assuming solid density. The blue curve shows the continuous Drude resistivity using the analytic model of Eq. 2.43. We note that $n_f$ is actually dependent on the charge state $Z^*$ gathered from PrOpacEOS as a function of temperature. We observe that with the proper parameters, this analytic model agrees quite well with the effective resistivity calculated by the LMD model used in LSP (solid blue dots). Both are also in relative agreement with experimental measurements, except for Milchberg *et al.* The discrepancy is likely due to the assumption of electron-ion thermal equilibrium in the analytic model, which is broken in Milchberg's ultra-short pulse laser-matter interaction experiments to measure resistivity.

## 4.4 Benchmark of Proton Stopping Power

Of significant importance to an accurate simulation of proton transport and energy deposition is the numerical modeling of stopping power. In Sec. 3.2.3, we introduced two widely used comprehensive stopping power models – the analytic bound + free formulation (Eq. 3.23), which is relatively easy to implement and computationally inexpensive; and the dielectric formulation (Eq. 3.27), which is more accurate but requires a sophisticated atomic-scale electron density and dielectric function for the medium. Implementing the dielectric model into LSP would be cumbersome and greatly increase the computational expense. Instead, it is more efficient to verify that both models yield similar results for the proton energies and dense plasma conditions relevant to this dissertation.

Kim *et al.* (25) were the first to implement the bound + free stopping power model i.e. Eq. 3.23 into LSP and used it to investigate the self-consistent transport of intense proton beams in materials. To briefly reiterate, the bound electron stopping number is given by Eq. 3.19. Within this expression, the mean excitation energy $\langle I \rangle$ is a function of the local charge state as in (96):

$$\langle I \rangle (Z^*) = \frac{Z^2}{(Z-Z^*)^2} \langle I \rangle (Z-Z^*) \tag{4.16}$$

where the scaling $\langle I \rangle (Z-Z^*) = 16(Z-Z^*)^{0.9}$ is used from empirical data. Also in this expression, the shell correction term is based on experimental shell corrections matching stopping powers to the NIST database (90), and the density effect correction is excluded. The free electron stopping number is given by Eq. 3.20. As previously mentioned, PrOpacEOS is used to obtain the necessary charge state $Z^*$ of the material given the electron density and temperature. Fig. 4.3 shows the temperature dependence of the average charge state of aluminum, as calculated by PrOpacEOS.

To benchmark this newly LSP-implemented stopping power module, proton stopping simulations were conducted and compared with simulations using the self-consistent approach

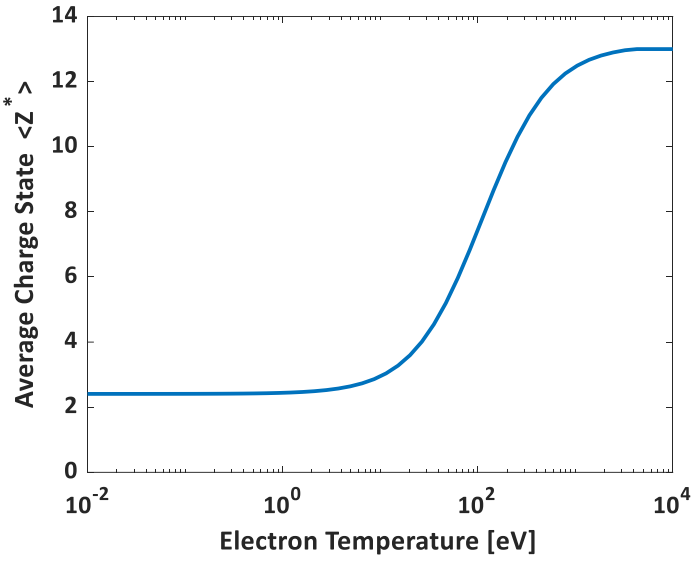


**Figure 4.3**: PrOpacEOS (24) output of average charge state of solid-density aluminum as a function of electron temperature.

for astrophysical and laboratory plasmas (SCAALP) along with the random phase approximation (RPA) under the dielectric formulation (26). Fig. 4.4 displays the results from this simulation comparison. In Fig. 4.4(a), several discrete LSP simulations evaluate the projected range of protons with varying initial energies as they slow through constant-temperature solid-density aluminum. These simulations agree quite well with SCAALP's theoretical stopping range calculations (black curves). The small discrepancy for 1 $MeV$ protons at high temperatures may be explained in Fig. 4.4(b), where we observe that the stopping power models significantly diverge for proton energies below 1 $MeV$ and at or above 100 $eV$ temperatures. Even so, the proton energies relevant to this dissertation fall between several $MeV$ up to several tens of $MeV$, for which range the bound + free stopping power model is sufficiently accurate.

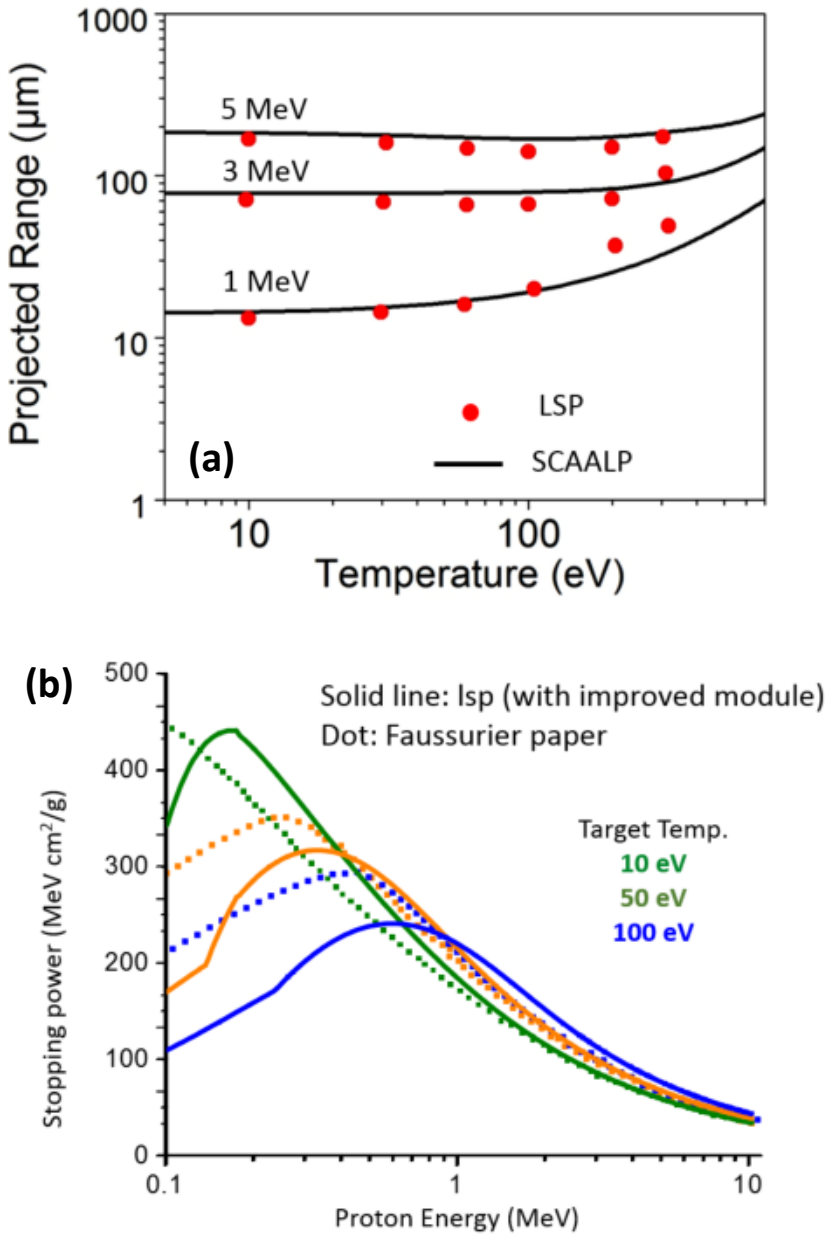


**Figure 4.4**: (a) Comparison of proton stopping range from novel LSP dynamic stopping module (25) with that from SCAALP (26). (b) Proton stopping power as a function of energy at varying temperatures in the warm dense matter regime using the new LSP module and SCAALP. Figure taken from Ref. (27).

# Chapter 5

# Development of a platform at the Matter in Extreme Conditions end station for characterization of matter heated by intense laser-accelerated protons

## 5.1 Introduction

Warm dense matter (WDM) is an extreme state of matter in which the thermal energy, Coulomb energy, and Fermi energy of a system are all within an order of magnitude of each other. This corresponds to temperatures $\sim 1-100\ eV$ and densities $1-100\times$ solid density, at the very intersection of condensed matter physics and ideal plasma physics. Understanding the dynamics of WDM is important in modelling systems compressed to states of extreme pressure and temperature, including planetary and sub-stellar objects (115; 116; 117) and capsules for thermonuclear inertial confinement fusion (ICF) (118).

The advent of chirped-pulse amplified lasers near the turn of the century made possible the

creation of warm dense states of matter on a time scale much shorter than that of hydrodynamic expansion, i.e. isochoric heating. In direct laser heating, a high-intensity laser deposits much of its energy into the first $\sim 100$ *nm* of a solid, confined to a skin depth beyond critical density (i.e. the density beyond which the laser can no longer propagate and evanescently decays). The hot electrons resulting from laser absorption scatter through and subsequently heat the rest of the material. Unlike direct laser irradiation, proton and heavy ion beams follow a Bragg curve when passing through materials; as the particle loses energy to the material, its energy loss rate increases. The particle beam may volumetrically and more uniformly heat the sample as long as its thickness is less than the depth at the Bragg peak for the relevant proton/ion energies in the beam.

Over the last two decades, the target normal sheath acceleration (TNSA) mechanism for such beams has been investigated at length (119). Protons accelerated via relativistic laser interactions with thin foil targets have demonstrated isochoric heating of materials to WDM conditions, and much higher sample temperature was reached when the target foil was spherically curved, focusing the protons (14). Further experiments with corroborating simulations have shown that uniform heating over the thickness of materials (several $\mu m$) is achievable with appropriate proton or ion sources ($\gtrsim 100$ *keV* per nucleon, $\gtrsim 10^9$ $A/cm^2$) (120; 121; 25). The isochoric and uniform heating possible with laser-accelerated ions has been combined with high-resolution imaging techniques that probe the heated materials to enable measurements to benchmark equation-of-state models (122; 123).

In this manuscript, we detail for the first time the characterization of proton-driven isochorically heated samples at the Matter in Extreme Conditions (MEC) end-station at SLAC National Accelerator Laboratory's LCLS, which employs both a high-intensity optical laser and a high brightness x-ray source driven by a free electron laser (FEL). The energetic protons produced by the optical beam heat material to WDM conditions, which may then be probed by the precision-timed LCLS beam. Previous proton-heated WDM studies involve experimentally

verifying equation-of-state values (124; 125) and improving proton stopping power calculations (126; 25; 127; 128) at various high-intensity laser facilities. The record peak brightness of the FEL combined with ultrashort pulse duration and $\sim 10\ \mu m$ focal spot allows for an unprecedented high-resolution x-ray scattering diagnostic. Warm dense matter generated from direct laser irradiation has been successfully characterized via XRTS on several MEC experiments (129; 130), yet that from proton heating has not yet been characterized by the same method on MEC. The goal of the experiment was to heat Al and polypropylene (PP) targets to WDM conditions using laser-accelerated protons and measure the spatial and temporal evolution of the temperature in the targets. Here we show that the MEC laser-driven proton source is suitable for heating and present our first attempts to simultaneously probe the sample with the FEL.

## 5.2 Experimental Setup

Fig. 5.1 depicts the top-down view of the experimental layout, with sample raw data from each diagnostic and a 3-D rendering of the target orientation with respect to the optical and LCLS beams.

The linearly polarized MEC optical laser ($\lambda_L = 800\ nm$, peak power 20 $TW$) delivered about 0.7 $J$ on target with pulse duration 45 $fs$. The laser spot size was about 7 $\mu m$ focused with an f/6 off-axis parabola (OAP), yielding peak intensities above the relativistic limit and close to $10^{19}\ W/cm^2$ onto the Cu source foil at 15° incidence. The Cu was either flat or a spherical cap (hereafter referred to as "hemi"). The LCLS beam operated in self-amplified spontaneous emission (SASE) mode with pulse energy 3 $mJ$, photon energy $h\nu \approx 7.49\ keV$ ($> 10^{12}$ photons), and spot size 10 $\mu m$. Several sample foil species were heated: 1.1 $\mu m$ (thick) Al, 650 $nm$ (thin) Al, and 3.8 $\mu m$ PP ($C_3H_6, 0.9\ g/cm^3$).

The targets were arranged on cartridges to simplify alignment. Each of 68 cartridges had an aluminum frame with silicon wafer comb-cut slot structures. Each slot comprised a

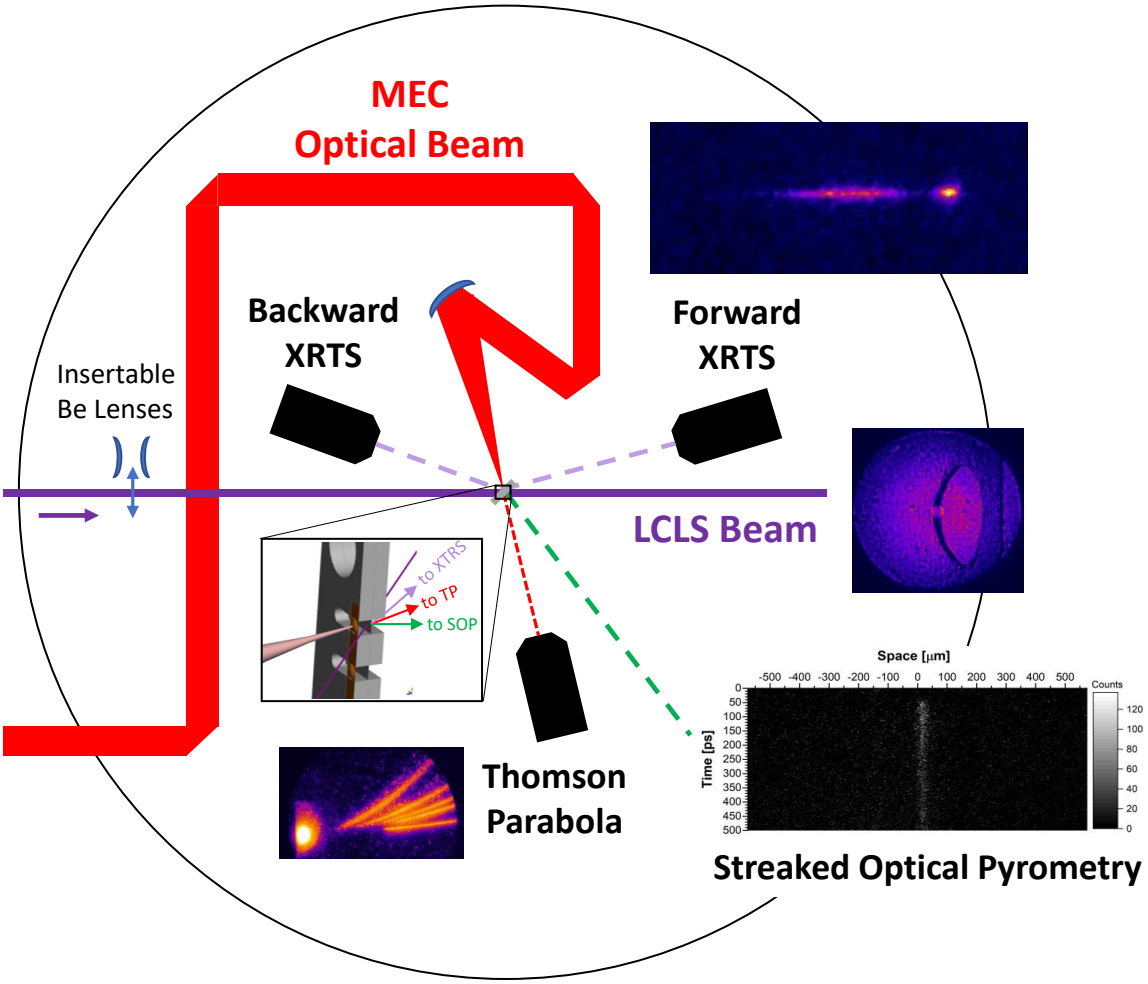


**Figure 5.1**: Experimental setup within the MEC chamber, with an enlarged view of the target orientation with respect to beamlines

hemispherically curved (for proton beam focusing) or flat Cu source foil (3.8 $\mu m$ thick) and a flat sample foil separated by a $300-400$ $\mu m$ vacuum gap. The latter was absent in shots measuring proton beam spectra.

Target alignment proved to be a major obstacle for experimental execution, given that the Rayleigh range of the optical beam focal point was $\sim 75$ $\mu m$. The OAP mirror alignment axes were chosen to be colinear with the incident laser wavefront (k-vector) so that the focus could be moved in space without introducing aberrations. Unfortunately, this meant translation of the OAP axis could not be colinear with the hemi axis, making it tedious to properly orient targets with both the LCLS and optical beams. In addition, the parallelism and wrinkling of the two foils, coupled with variations of the gap distance, strongly complicated the target alignment to the beams. For the future use of the platform, it is essential to use targets that are individually characterized or nearly identical.

Beryllium lenses were inserted in the target chamber to expand the LCLS beam spot to 900 $\mu m$ and backlight the target area. This technique proved useful, albeit time-consuming, for subsequently aligning the parabolic mirror and targets to the LCLS beam axis before each shot. A sample LCLS radiograph (pre-shot) is shown in Fig. 5.1 (center right). The curved limb-darkened features outline the Cu hemi, enabling alignment of the target and sample to the optical laser focal plane and LCLS axis, respectively. The bright spot at the apex of the hemi is the bright center of the defocused LCLS radiation profile. The dark vertical line to the right of the hemi is the edge of the Cu foil in the cartridge slot. The sample can be seen to the right. Cu hemi foils were replaced with flat foils to improve proton beam reproducibility at the cost of beam focusing. Proton beam intensities on-target decreased by an order of magnitude, and consequently heated the target foils to several eV, as opposed to the intended 10s of $eV$.

Proton beam spectra were measured by a Thomson Parabola (TP) spectrometer in line with target normal. Particles passing through the TP are collected on a micro-channel plate (MCP) with a phosphorescent screen and recorded by a CCD camera. Particle species appear as parabolic

traces with curvature dependent on charge-to-mass ratio, where more energetic particles collect closer to the vertex (represented by a bright spot). These are directly translated to energy spectra via a MATLAB interface developed based on the technical parameters of the TP. The benefits of this system include high spatial resolution $(80-100\,\mu m)$ and high repetition rate $(1-5\,Hz)$ (131). The distinguishable parabolic traces shown in Fig. 5.1 reflect the varying charge-to-mass ratio of different ion species. The central bright spot represents x-rays and neutral particles whose trajectories would be unaffected by the fields within the TP. The lowest parabolic trace represents protons (with the highest charge-to-mass ratio), while the higher traces with smaller curvature represent several charge states of carbon and oxygen.

Streaked optical pyrometry (SOP) (132) was fielded to enable measurement of the temperature evolution of the heated target rear surface with high temporal resolution. As the aluminum foil is heated, it generates a black-body (Planckian) emission spectrum dependent only on its temperature. The field of view of the streak camera focused on the intersection of the proton source normal with the Al foil sample, presumably the point of maximum temperature on the rear surface. Specifically, since light cannot penetrate beyond the critical density, the streak camera collected most of the thermal ($450\pm50$ *nm* FWHM) emission at its (rear) critical surface, where the density is $(5.6\pm1.2)\times10^{21}\ cm^{-3}$, for absolute temperature measurement in one dimension. The SOP was absolutely calibrated prior to the experiment using the doubled Ti:Saph Europa laser at the Lawrence Livermore National Laboratory (125) — using the wavelength sensitivity from the manufacturer of the streak camera (Hamamatsu S20) and *in-situ* measurements of the optical transmission through optics and filters with a 450 *nm* laser diode, we could convert the counts on the detector to an emitted temperature, assuming black-body emission.

X-ray Thomson Scattering (XRTS) (133) measurements of the LCLS beam have proven an invaluable asset to the precise characterization of WDM state properties (temperature, density) on MEC. Two x-ray spectrometers were placed to measure the scattering of the LCLS beam in the forward and backward direction with respect to proton beam direction. The scattering spectra can

enable density and temperature characterization of the heated samples. Both spectrometers were calibrated by irradiating standard metal foils and measuring the fluorescence of the characteristic K-shell emission lines.

A sample TP spectrum is shown in Fig. 5.2. The proton beam exhibited a maximum kinetic energy of 2.5 $MeV$ and temperature of 250 $keV$, as shown with the fitted dashed line. These beam properties are consistent with previous TNSA studies (134). The projected cold-stopping range of 750 $keV$ protons through Al and PP are 9.4 $\mu m$ and 14.3 $\mu m$, respectively. The sample foils were therefore sufficiently thin to be volumetrically heated by the protons. The low-energy fall-off of the proton spectrum below 790 $keV$ is due to the circular edge of the MCP which cuts off the proton trace, as can be seen in Fig. 5.1 (bottom center).

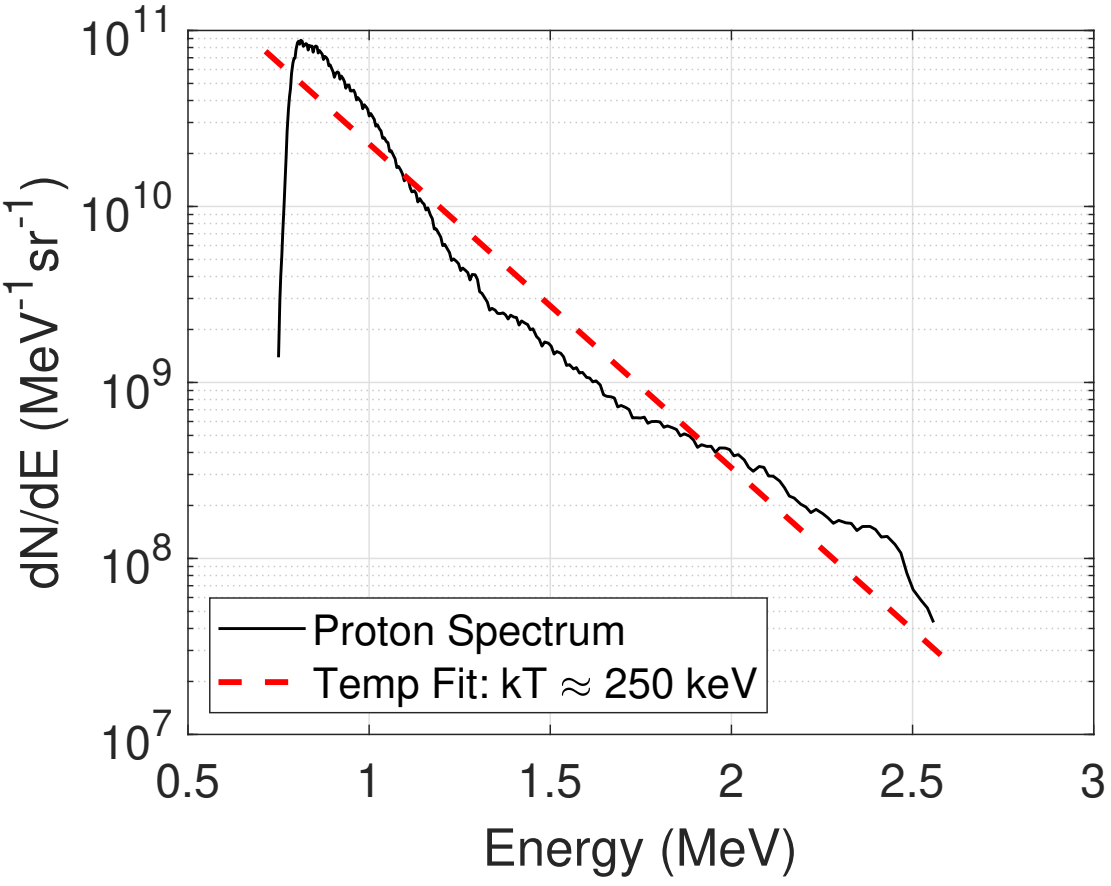


**Figure 5.2**: Sample proton energy spectrum from Thomson Parabola spectrometer

The XRTS spectrometers were calibrated by irradiating cold 30 $\mu m$ Ni targets and 650 $nm$ Al targets (with Fe contaminant typically under 7000 parts per million per manufacturer) with the FEL. Fig. 5.3 depicts the calibration spectrum of cold Al and Ni targets, showing a clear elastic scattering peak of the 7.49 $keV$ LCLS beam on both targets, unresolved 7.47 $keV$ Ni-$K_\alpha$ and the 7.06 $keV$ Fe-$K_\beta$ peak with the Al target. Irradiation of Cu by the optical laser, however, masked the LCLS x-ray signal with bremsstrahlung emission over the same energy bandwidth such that the background noise was comparable to the scattered x-ray signal.

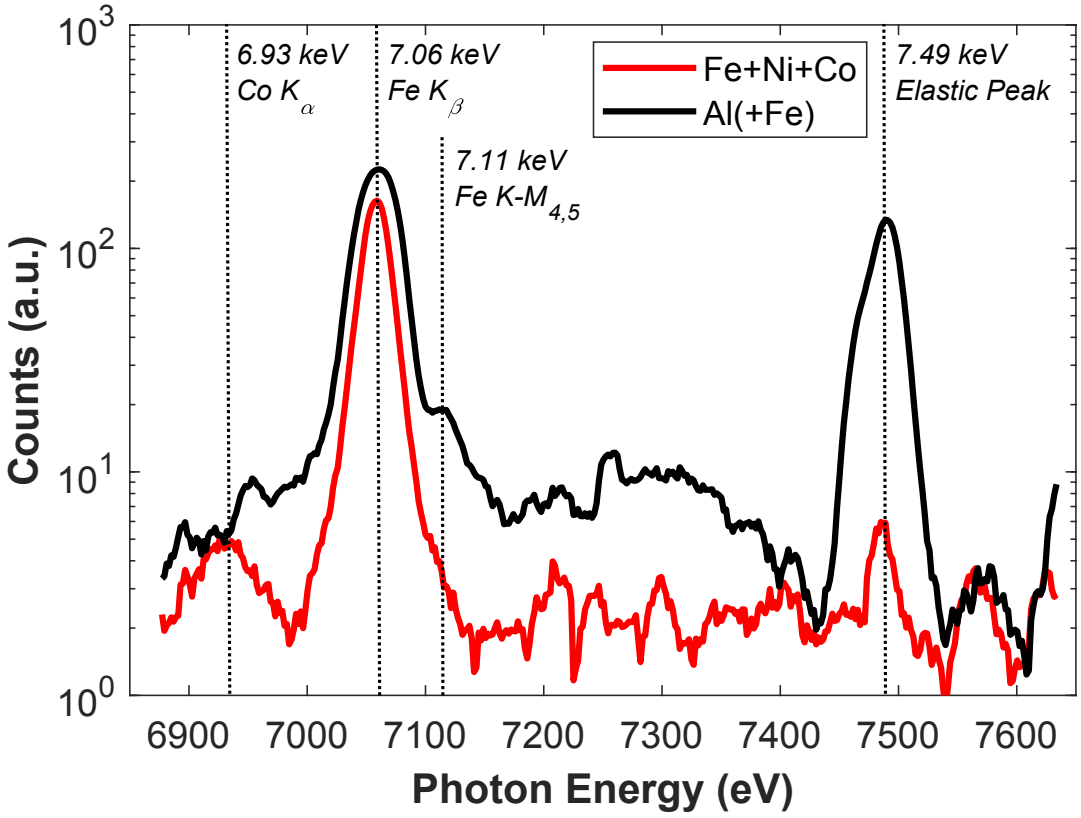


**Figure 5.3**: X-ray spectra of cold nickel-iron-cobalt alloy and iron-contaminated aluminum samples for calibration

## 5.3 Results & Analysis

Simulations of proton-heating were performed using LSP and HELIOS independently. 2D simulations of the proton heating were performed using the hybrid-PIC code LSP with an advanced dynamic proton stopping power module (47). Protons and co-propagating electrons were initialized as kinetic particles, whereas target ions and electrons were initialized as fluid particles with EOS table (from Prism's PrOpacEOS software (24)) dynamically updating target conditions. The total proton beam energy was 2.88 *mJ* (0.5% of laser energy) with energy spectrum approximately matching that taken from the experimental TP data (Fig. 5.2). It should be noted that proton time-of-flight was not taken into account in LSP simulations, albeit the total energy of the proton beam passing through the targets remained accurate. Whereas the higher energy protons phenomenologically reach the target before the lower energy protons, the entire proton spectrum continuously bombarded the target foil for 10 *ps* i.e. both low energy and (fewer) high energy protons reached the target at any one point in time. To simulate greater energy deposition at the center of the beam, the spatial distribution of proton density was Gaussian in the transverse direction and independent of proton energy.

In the 2D LSP simulations, the proton beam (along with co-propagating electrons) was injected into the Cartesian $(x\text{-}z)$ simulation space and heated the target foils (thin/thick Al, PP) from the left. Two beam sizes were injected, 300 $\mu m$ and 50 $\mu m$, corresponding to an unfocused beam from a flat source foil and a focused beam from curved foil, respectively. Fig. 5.4(a) depicts the resulting temperature map of the 1.1 $\mu m$ Al foil after all protons in a focused beam of diameter 50 $\mu m$ have passed through. Since the temperature is more or less constant longitudinally, the central dashed line perpendicular to beam propagation represents the target electron temperature at the rear facing surface, to be compared with the SOP diagnostic results. The temperature map follows a self-similar distribution for all other combinations of target material/thickness and proton beam diameter.

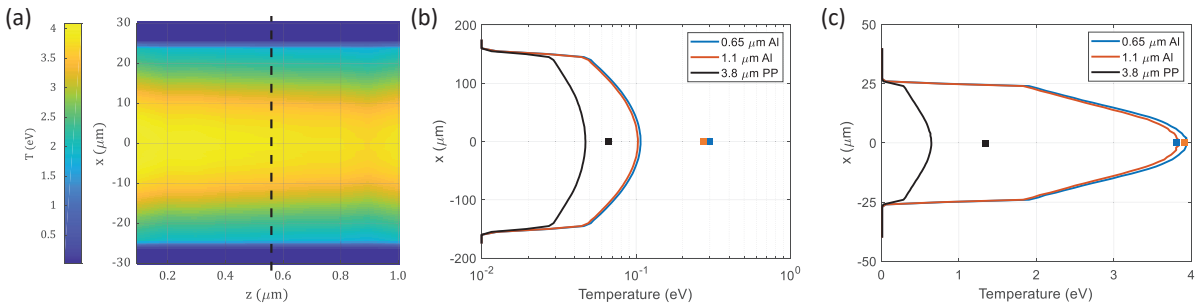


**Figure 5.4**: (a) Simulated temperature map of Al target. Temperature lineouts of different materials (dashed line) are shown in (b) for the 300 $\mu m$ unfocused proton beam and (c) for the 50 $\mu m$ focused beam. Peak temperatures from 1D HELIOS simulations are shown as filled squares with corresponding colors.

Figs. 5.4(b) and (c) show the transverse temperature variation mid-thickness for each target from a 300 $\mu m$ (unfocused) beam and a 50 $\mu m$ (focused) beam, respectively. In both cases, the PP is heated to a final temperature several times cooler than that of aluminum. In the case of the unfocused beam, the simulated final temperature of Al is 0.1 $eV$. Had the beam been focused by the Cu hemis (as opposed to flat Cu foils), simulations show that the Al could have reached temperatures up to $\sim 4$ $eV$, as shown in Fig. 5.4(c). Beam intensity increases by a factor of 36 with the focused beam, so proton energy deposition and resulting temperature increased by a similar factor.

We also used the code HELIOS (135), which is a 1D radiation-hydrodynamics code that can model target ionization and hydrodynamic evolution of a plasma. The code provides a particle beam module as a source of external radiation. The proton beam is input with a beam power and proton kinetic energy varying in time and thus allows for the proton time-of-flight to be accounted for. We again used Prism's PrOpacEOS tables for the material equation of states and opacity, and the Spitzer conductivity model for the plasma thermal conduction. The proton beam stopping power is calculated using the ion deposition model of Mehlhorn (Eqs. 3.19-3.23). The overlaid points in Fig. 5.4(b-c) corresponding to each target represent the peak temperatures from the 1D HELIOS simulations (135). Unlike LSP, the HELIOS simulations do not include proton

scattering within the target, confining the heat transfer to the single dimension and thus slightly overestimating the peak temperature when below 1 $eV$. This effect is suppressed for temperatures of several $eV$ or higher because heat conductivity tends to decrease with increasing temperature.

In Fig. 5.5(b), the experimental SOP data from a proton-heated 0.65 $\mu m$ Al foil are shown as a light red band (including uncertainty) using a lineout width of 40 $\mu m$ and smoothed with a moving average of 13 $ps$ corresponding to the streak temporal resolution of the 300 $\mu m$ slit used). Given the noise of the raw data (main contribution to measurement error), we estimate a peak temperature of $0.9 \pm 0.15$ $eV$. We compare the time history of the temperature measured by the SOP diagnostic via 1D-hydrodynamic simulations with the code HELIOS. The proton beam intensity is input in the particle beam module of the code, accounting for energy dispersion from proton time-of-flight. We assume a single-exponential energy distribution, for which an analytic formula of the proton beam intensity may be derived (6):

$$I(t) = \frac{8\left(\frac{W}{\tau}\right)\left(\frac{\tau}{t}\right)^5 \mathrm{e}^{-(\tau/t)^2}}{\pi\phi^2} \tag{5.1}$$

where $\tau = d/\sqrt{2T_p/m_p}$ is the characteristic transit time of a proton beam with temperature $T_p$ over a source-target gap distance $d$, $W$ the total proton beam energy and $\phi$ the proton beam diameter (FWHM) incident on target. Using $d = 300$ $\mu m$, $T_p = 250$ $keV$, $W = 2.8$ $mJ$ and $\phi = 140$ $\mu m$, we report in Fig. 5.5(a) the map of electron temperature in radius-time phase space. The dashed black line represents the rear-side surface on which the SOP imaging was focused.

In Fig. 5.5(b), we added the corresponding lineouts varying the proton beam diameters: 300 $\mu m$ (half-angle divergence of 26°) in purple, 150 $\mu m$ $(14^\circ)$ in blue, 140 $\mu m$ $(13^\circ)$ in teal and 130 $\mu m$ $(12^\circ)$ in light green. It appears that, for the measured proton spectrum parameters, the simulated temperature evolution matches fairly well the data for the case of a relatively low beam divergence of $13 \pm 1^\circ$ ($\phi = 140 \pm 10$ $\mu m$). This divergence seems rather low compared to what is usually measured for a TNSA proton beam from a flat foil ($\sim 20^\circ$ (136)), unless the total energy

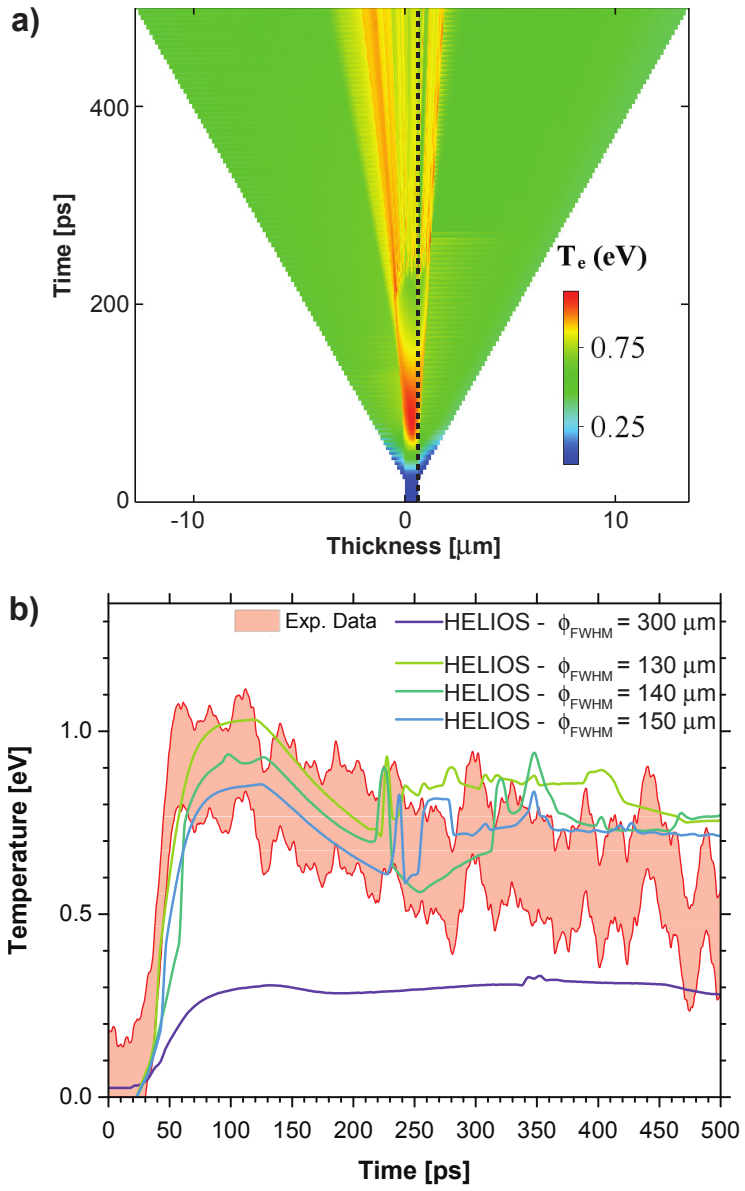


**Figure 5.5**: For 0.65 $\mu m$ Al foil heated by the proton beam: (a) Simulated (1D HELIOS) evolution of the Al electron temperature. (b) Temperature evolution at the target rear-side recorded by the SOP diagnostic (red). Lineouts from additional HELIOS simulations varying the proton beam size are shown.

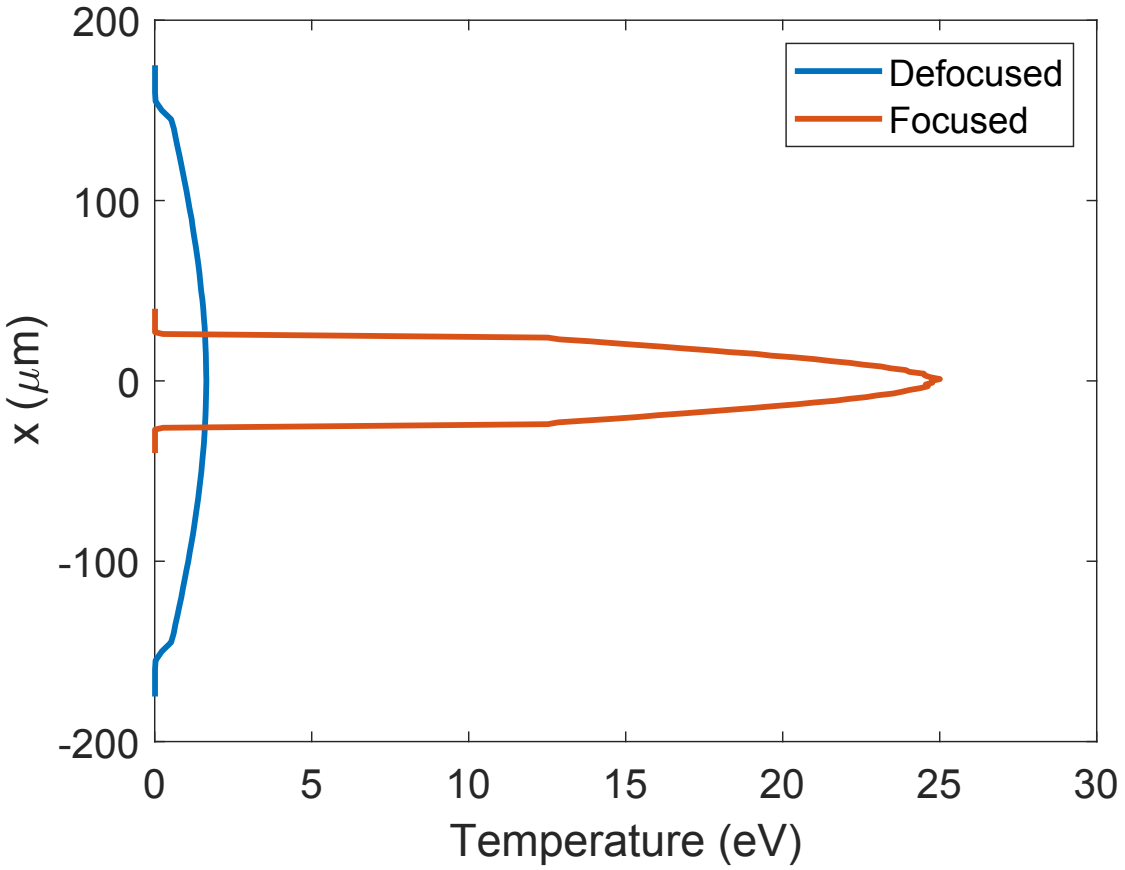


**Figure 5.6**: Simulated temperature distribution from LSP of 1.1 $\mu$m Al target heated by focused and unfocused proton beams. Proton beams are accelerated via TNSA by a laser pulse of energy 10 J and intensity $\sim 10^{20}$ W/cm$^2$

of the proton beam was higher on that particular shot $(7\ mJ$ is required for a divergence of $20^{\circ})$. Yet, the similar rise and leveling of the temperature evolution is notable and suggests that the input for the proton beam temperature was correct.

Additional LSP simulations were performed to predict the temperature of proton-heated aluminum, where the protons are accelerated via TNSA by a high-intensity short pulse laser of energy 10 $J$, as opposed to the 0.5 $J$ in MEC. A proton energy spectrum with temperature 2.57 $MeV$ and maximum proton energy 30 $MeV$ results from roughly the same laser parameters as MEC except the above total laser pulse energy (137). Fig. 5.6 shows the resulting temperature distribution from the high energy LSP simulations for a focused $(50\ \mu m)$ and unfocused $(300\ \mu m)$ proton beam. Ideally, protons would focus onto the target foil and would be expected to heat Al to $\sim 25\ eV$. Assuming we are able to properly focus the proton beams onto the target and heat the material to several 10s of $eV$, we would then be able to probe the material and contribute to improved modeling of the elusive state of matter.

## 5.4 Acknowledgements

Chapter 5 contains a partial reprint as it appears in "Development of a platform at the matter in extreme conditions end station for characterization of matter heated by intense laser-accelerated protons" by **K. Bhutwala**, M. Bailly-Grandvaux, J. Kim, M. Dozières, E. Galtier, C. B. Curry, M. Gauthier, E. Cunningham, H. J. Lee, P. Forestier-Colleoni, A. Higginson, N. Aybar, R. Hua, B. Edghill, J. Strehlow, G. M. Dyer, S. H. Glenzer, J. B. Kim, N. Alexander, E. Del Rio, M. S. Wei, Y. Ping, A. McKelvey, G. W. Collins, F. N. Beg and C. McGuffey in *IEEE Transactions on Plasma Science* 48(8), 2751-2758 (2020). The dissertation author was the primary investigator and author of this publication. This work was supported in part by the U.S. DOE FES under Grants DE-SC0018253, FWP-100182 and SF-00515, in part by the University of California Office of the President Lab Fee under Grant LFR-17-449059, and in part by the U.S. DOE, Office

of Science, Office of Basic Energy Sciences, under Grant DE-AC02-76SF00515. The work of Krish Bhutwala was supported by the U.S. DOE NNSA under Grant DE-NA0003876.

# Chapter 6

# Intense proton beam transport from a cone-structured target through plastic foam with unique proton source modelling

## 6.1 Introduction

It is well known that the irradiation of thin foil targets by high intensity ($> 10^{18}\ W/cm^2$), short-pulse ($0.01 - 10\ ps$) lasers generates laminar proton beams with $MeV$ energies and extreme current densities (82). Typical beam parameters at present include proton energies up to 100 $MeV$ and current densities up to $\sim 10^9\ A/cm^2$ from structured targets that improve proton focusing. The advantage of these laser-accelerated proton beams lies in their short bunch duration, typically on the order of the laser pulse duration ($\sim ps$) at their source, and 100 $ps$ or less as they disperse over $mm$ distances. Combined with their favorable deposition characteristics, this makes them particularly effectual in isochoric heating of thin foils to warm dense regimes (14; 138; 123; 125; 139; 17), proton radiography of rapidly evolving high energy density plasmas (140; 141; 142), and the proton Fast Ignition (FI) scheme of inertial confinement fusion (ICF)

(38; 77).

Although the various mechanisms of laser-driven proton acceleration have been and continue to be well-studied, the transport and heating capabilities of these intense proton beams through low-density plasma is not. Ultra-low density plastic foams which, when heated to high temperatures, can reasonably stand in for low-density plasma have become available, opening up this field of research to the lab setting. Proton heating has recently been used to create warm dense carbon from plastic foams (143), offering equation-of-state studies of these complex regimes. Proton heating could also facilitate the study of low-rate nuclear reactions in astrophysical objects with near-solid density and *keV* temperatures (144), as well as thermal conductivity measurements in the WDM regime (125). Following the simulation work on the dynamics of intense beam transport in solids (47), investigating how proton heating and transport change in low-density foams are of great interest in their own right.

When short-pulse laser-accelerated laminar proton beams were discovered and attributed to target normal sheath acceleration (TNSA (82; 75)), they were also immediately recognized as a viable charged particle beam for FI. Protons' large inertia (compared to electrons) makes them less susceptible to electromagnetic fields present in the coronal plasma outside the compressed core, thereby mitigating transport instabilities that plague electron FI (145; 146). Energetic protons also exhibit a Bragg peak in energy deposition, which means the majority of a proton's energy is deposited near their stopping range. Crucially, since laser-accelerated proton beams have a broadband energy spectrum, the high-energy protons arrive at and heat the DT capsule, which (depending on material characteristics) may extend the stopping range of lower-energy protons (147) arriving later.

Proton FI has been explored in-depth (38; 77), and the proton beam requirements to reach ignition have been evaluated numerically (6; 5). However, strong assumptions on transport through the coronal plasma near the cone tip to the compressed core are made in the rigid beam models applied. A study of beam transport in FI with an accurate accounting of beam

divergence, which is known to depend on proton energy, has not been presented. Characterizing the transport of proton beams with energy 10s of $kJ$ in these conditions will be necessary for proton FI. Resistive magnetic fields have already been shown to collimate hot electron beams with high current densities ($10^{11}\ A/cm^2$) within carbon samples (148). In ultra-low density gas jet targets with $n_e \sim 10^{19}\ cm$, collective effects significantly alter the scattering of ion beams (149). Simulations have shown that simultaneous heating and self-generated fields have a significant effect on the transport of proton beams with current density $\gg 10^9\ A/cm^2$ (47).

Here, we present an experimental study on transport of intense laser-driven protons in low-density plastic foams and show a modeling approach using 2D hybrid-PIC simulations. The experiment evaluated the transport of laser-accelerated cone-focused proton beams through low-density foam blocks by measuring the beam cross section at different depths. In Section 6.2, the experimental results are presented, including measurements of the proton spectra from different target types. X-ray emission images are also presented which provide evidence that the protons are still beam-like when they reach the back layer of the target. In Section 6.3, we provide simulations of transport in the foam and post-processing to validate the experimental x-ray images. We present a unique approach to modeling the proton beam source, taking into account the energy-dependent divergence of typical TNSA proton beams. By post-processing the simulated particle information, we produce synthetic x-ray emission profiles and compare them to the experimental measurements.

## 6.2 Experimental Setup and Results

The experiment was carried out on the OMEGA-EP laser, where a backlighter beam of energy 700 $J$, pulse length 10 $ps$ and intensity $10^{18}\ W/cm^2$ irradiated a hemispherical cap ("hemi") attached to a hollowed cone structure, accelerating and focusing protons through the cone tip and into a carbonized resorcinol-formaldehyde (CRF) foam block of density 0.38 $g/cm^3$.

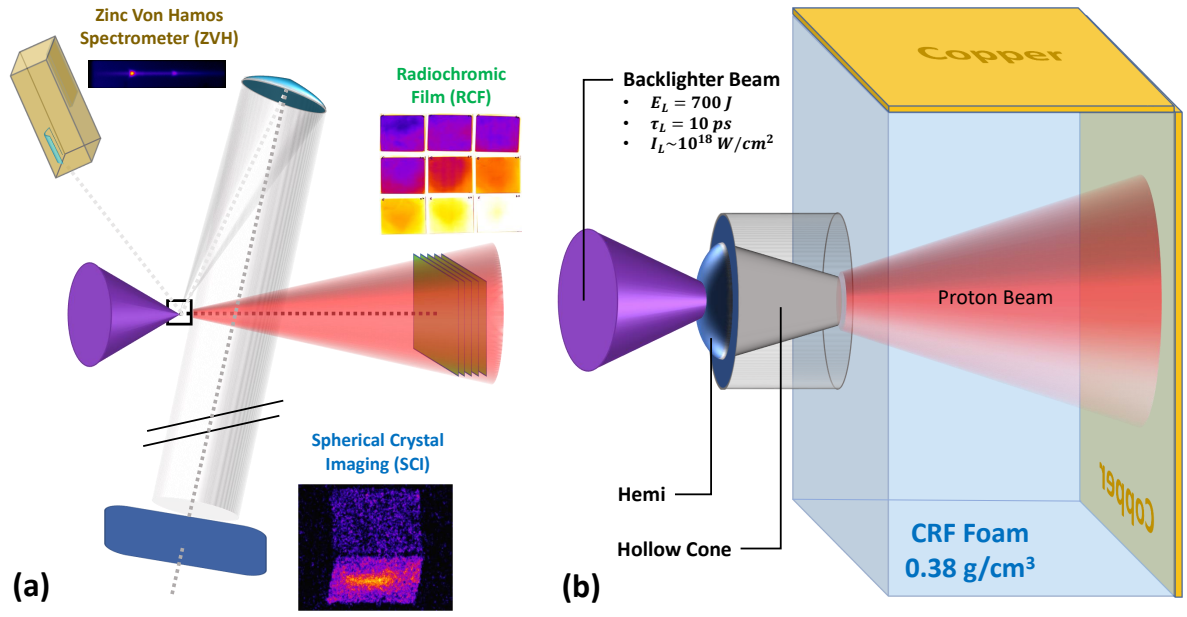


**Figure 6.1**: (a) Experimental setup, wherein proton beam (red) is characterized by the RCF pack, while the transport interaction is captured by the SCI and ZVH. (b) Magnified target structure, where copper-plated foam block had a depth of either 550 $\mu m$ or 1000 $\mu m$.

The diamond-like carbon hemi and cone opening were glued together and flush (diameter 300 $\mu m$, also the hemi's radius of curvature). The cone length was 300 $\mu m$ and had far-field tip diameter 200 $\mu m$. The far-field cone bulk surface was also glued to the foam. The foam block was 1.0 $mm \times 1.5$ $mm$ in the laser-facing dimensions, with depths of either 0.55 $mm$ or 1.0 $mm$ to reveal the proton beam profile. CRF foam was chosen for its low density and therefore low proton stopping and scattering to elucidate the transport of protons. Cu foils 10 $\mu m$ thick were glued onto the top and rear faces of the foam block to act as tracer layers that give Cu-$K_\alpha$ emission for the planar visualization of energetic electrons and protons. The experimental setup is shown in Fig. 6.1.

### 6.2.1 Radiochromic Film Diagnostic

Radiochromic film (RCF) packs were fielded on this experiment to diagnose the emerging proton beams' spatial profiles and spectra. RCF darkens as a result of energy deposition, and dose

measurements can be extracted from the darkening of the films (150). A pack of 6.35 *cm* square films was placed 16 *cm* behind the target opposite the hemi structures, i.e. directly facing the rear Cu foil, if present, on every shot. Because of the long standoff distance, only a portion of the beam was intercepted by the first several layers in each pack. Each successive layer of radiochromic film in the pack marks an increasing penetration energy required by protons to reach that film. A pack contained 13 aluminum filters interleaved with ten films of type HD-v2 and two of type MD-55; the films' penetration energies spanned $3.5 - 60\ MeV$. Monte Carlo calculations of proton energy deposition in the film pack were convolved with guesses of the energy distribution (an exponential spectrum capped below $0.5\ MeV$) for comparison to the measured doses using the approach described in Ref. (151). The particle count and temperature of the proton distribution were varied to determine the best-fit spectrum through a residual minimizing routine utilizing the dose on films 2 through film 10 (or through the last film with measurable dose). The beam energy incident on the film is found by integrating the best-fit spectrum.

The fit temperature and energy presented in Fig. 6.2(b) include only what intercepted the packs and fit to data beyond the first layer. The whole proton beam, therefore should have a representative temperature that is lower (we estimate only slightly lower) than the fit value, while the total beam energy is considerably higher than the presented values. To estimate the full energy of the beam, we employed a dataset taken in a different shot day with hemi targets and RCF with standoff only $\sim 8\ cm$. In that dataset, at each of the layer energies, a ratio was found of the total dose divided by the dose contained in the square cone corresponding to this experiment, and the present dataset was weighted accordingly. The proton transport simulations (see Sec. 6.3) were based on this full extrapolated energy and the fit temperature. The films were scanned before the recent refined scanning techniques presented in Ref. (152) and are no longer viable.

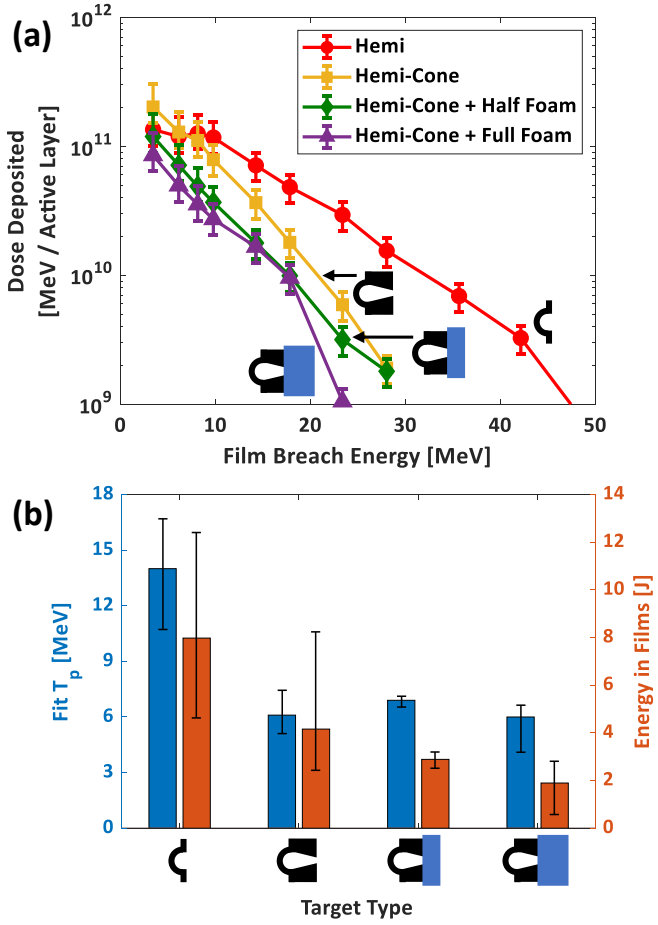


**Figure 6.2**: Proton beam information derived from the RCF data. (a) Dose received by films vs. film breach energy from various structured targets. (b) Comparison of beam characteristic temperature and total energy through the film solid angle from each target type.

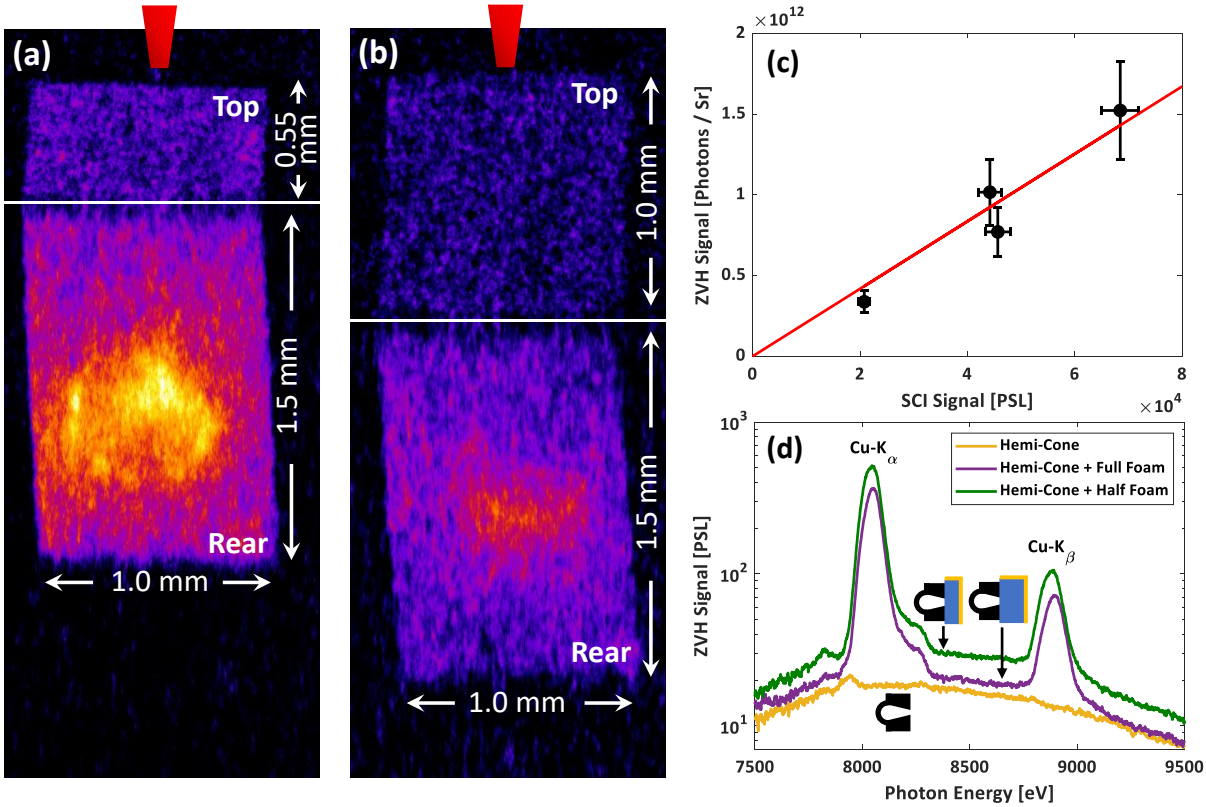


**Figure 6.3**: (a-b) SCI images of Cu-$K_\alpha$ emission from the top and rear side of foam blocks. (c) Linear correlation between integrated signals from ZVH and SCI, indicating that Cu-$K_\alpha$ photon energy did not shift significantly from the cold value. (d) ZVH spectra for various target structures.

### 6.2.2 X-ray Diagnostics

The spherical crystal imager (SCI) (153) was the primary diagnostic to visualize the Cu-$K_\alpha$ emission from energetic electron and proton collisions with Cu K-shell electrons. The imaging system comprises a spherically bent concave quartz crystal above the foam block 27° from the zenith and 276 *mm* away, and an image plate detector $\sim 2.4$ *m* from the foam block in the opposite direction. The crystal refocuses incoming $8048 \pm 6$ *eV* photons from the target onto the image plate.

The Zinc von Hamos (ZVH) spectrometer was also used in this experiment to capture the time-integrated X-ray emission spectrum from various targets. This spectrometer contains a

Highly-Ordered Pyrolytic Graphite (HOPG) crystal cylindrically bent along the non-dispersive axis, thereby focusing $7-10$ $keV$ x-ray emission in first order along one dimension. The spectrometer was calibrated for the Cu-$K_\alpha$ emission by comparing the measured signal on image plates with an absolutely calibrated single-photon counting camera (154). The ZVH viewed the target from above the laser axis.

### 6.2.3 Experimental Results

Fig. 6.2 shows the proton beam characteristics derived from the RCF data from targets with varying additional components, from a simple hemi to a hemi-cone target to a hemi-cone-foam package. The cone affects beam generation in two ways. On the one hand, hot electrons are able to escape from the hemi and into the cone structure, establishing a sheath field along the cone's inner surface, which has been shown to focus the protons (17). On the other hand, this migration leaves fewer electrons reverting back into the hemi and sustaining the electrostatic field to accelerate protons from the rear hemi surface. This results in better proton focusing at the cost of total proton beam energy. The latter affect can be seen in Fig. 6.2(b), where there is a factor of two decrease in both beam temperature and energy in going from a hemi-only to hemi-cone structure. Similarly, there is a decrease in the maximum proton energy from hemi-only (42 $MeV$ detected) to hemi-cone (28 $MeV$ detected) structure, shown in Fig. 6.2(a). When adding 0.55 $mm$- and 1 $mm$-thick foams, the total beam energy continues to decrease due to proton stopping, while the beam temperature does not change significantly from 6 $MeV$. The dynamics of ion acceleration with these structures are studied experimentally, theoretically, and computationally in Refs. (16; 18).

Fig. 6.3(a-b) depicts the experimental cross sectional view of the proton- and electron-induced Cu-$K_\alpha$ emission from two foam length cases, with a laser depiction (red) to clarify perspective. A raw SCI image is shown inset in Fig. 6.1(a), but here we have separated the top and rear portions and stretch them to account for the viewing angle 63° above the equatorial plane.

The top foils exhibit a relatively uniform emission, while the rear foils exhibit a brighter emission in a centralized spot, indicative of a forward-propagating particle beam, likely energetic protons. The size of the central bright spot corresponds to $< 20^{\circ}$ cone angle from the hemi apex, much narrower than would be expected from a beam of hot electrons (145), which typically exhibits substantial scattering and divergence within materials. This suggests that protons retain their beam-like qualities within the foam, and the spatial continuity of their intensities suggests little or no break-up of a proton beam. The experimental x-ray beam profiles were analyzed by radially binning and summing the signal to yield an experimental profile of $dY_{K\alpha}/dAd\Omega$. Simulations of protons and hot electrons are explored in Sec. 6.3, and their results will be compared with experimental results in Sec. 6.4.

Looking at the full set of data, the SCI signal integrated over the target region and the ZVH spectra integrated Cu-$K_\alpha$ peak were linearly correlated, as shown in Fig. 6.3(c). This suggests that the Cu did not get hot enough to alter the Cu-$K_\alpha$ emission energy outside of the response window of the crystal imager (155). Fig. 6.3(d) shows the spectra obtained when protons and hot electrons impinge on the Cu foils for the various targets. The base continuum shown for the hemi-cone target is brought on by hot electrons refluxing in the hemi and cone structures, which still occurs when foam is added. The added continuum from foam targets (green, purple) represents the particles propagating through the Cu end foils, shown in gold in the pictograms. Interestingly, the brightest continuum emission (by a factor of 1.5) occurred in the sample with less Cu (2 $mm^2$ in half-foam vs 2.5 $mm^2$ in full-foam), indicating that the number of particles finding their way to Cu was significantly higher in the half-foam target such that it overcame the reduced number of Cu atoms. Because the rear foil emission from the half-foam target has a steep decline at the left and right edges, some particles were likely able to escape through the sides of the foam. The line emission, above continuum, was also greater by a factor of 1.5 for the half-foam case than for the full-foam shot. The reduced emission in the full-foam case is roughly in line with the reduced proton beam energy leaving the target shown in Fig. 6.2(b).

## 6.3 Simulations

Simulations of proton transport were carried out to validate the experimental results and investigate the dynamics of intense proton beam transport within the foam. The hybrid fluid-PIC code LSP (106) was used to simulate both energetic protons and electrons moving through the foam, with resulting Cu-$K_\alpha$ emission calculated through manual post-processing. LSP uses an implicit algorithm wherein background plasma electrons and ions are simulated as fluid particles, relaxing the space and time resolution requirements to avoid artificial grid heating. This is particularly advantageous for simulating the dense plasmas present in the experiment without resolving plasma oscillations over the long time scale of 10s of *ps*. Grid-based collisional effects in the background species are estimated using the Jones algorithm (112). The simulation strategy is depicted in Fig. 6.4. In one set of simulations, kinetic protons and/or hot electrons were injected into a 1 *mm* foam block. Extraction planes at depths of 0.55 *mm* (half-foam, red) and 1.0 *mm* (foam rear, black) were set up to collect the position and momentum of all passing particles – see Fig. 6.4(a). In a second set of simulations, the extracted particles from either depth were re-injected into 10 $\mu m$ Cu, with extraction planes set up every 1 $\mu m$ in depth – see Fig. 6.4(b). Post-processing of these extraction planes yielded the Cu-$K_\alpha$ emission according to the particle energies and positions – see Fig. 6.4(c). We point out that with this strategy, we do not simulate the interface effects between different materials.

In all simulations, the background materials were initialized as ion and electron plasma fluid species with starting temperature $T_0 = 1\ eV$. Based on chemical analysis, the CRF foam had composition like $C_{12}H_4O$; it was simulated as a single fluid ion species with density $1.4 \times 10^{21}\ cm^{-3}$, with complementing electron fluid species. Calculations of the electron collision frequencies within the foam target with this initialization were dubious, so electromagnetic field advancement was switched off. We note that previous simulations with similar current densities showed insignificant differences in proton transport when fields were switched on or off, which

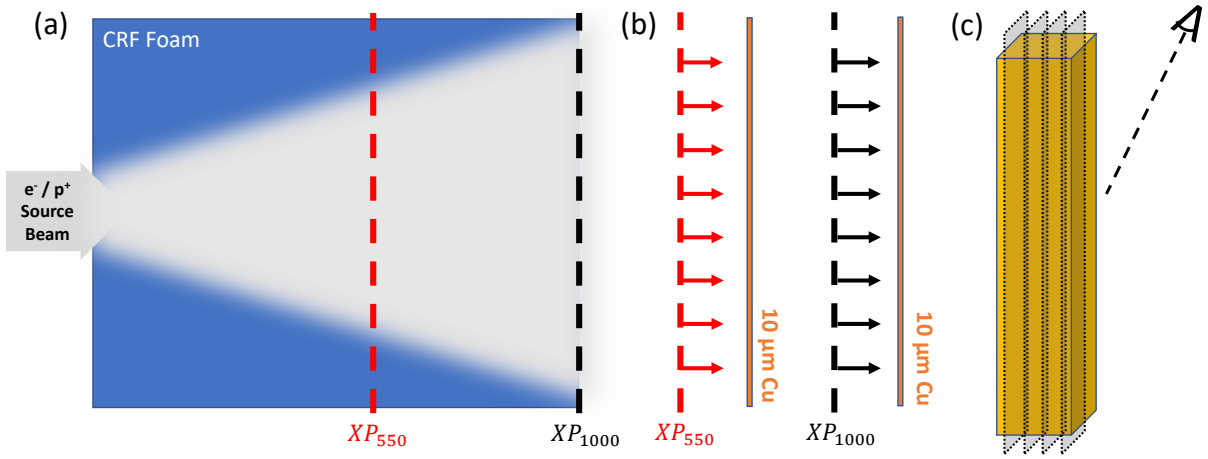


**Figure 6.4**: (a) Protons and electrons are injected into CRF foam with extraction planes at 550 $\mu m$ and 1000 $\mu m$ depths. (b) Extracted particles are re-injected into 10 $\mu m$ of Cu, with extraction planes set every $\mu m$ in depth. (c) Post-processing the Cu-extracted particles reveals the x-ray emission profile reaching the diagnostic.

may justify this omission of fields. Cu ions were also initialized as a fluid plasma with density $8.5 \times 10^{22}\ cm^{-3}$. The charge state of Cu ions was determined by Prism's PrOpacEOS (24) based on the local density and temperature. The energy deposition and scattering of kinetic proton and hot electron species into the foam are governed by a Monte-Carlo approach within the "dEdx" module using present values of the local target thermodynamic state as in (25). Energy deposition into Cu is governed by an advanced dynamic proton stopping power module (47), wherein the bound and free electron contribution to stopping power are added together based on the charge state.

### 6.3.1 Protons' Source Treatment

In order to reconstruct the proton beam incident on the foam, we use the proton energy spectrum measured from RCF data corresponding to the hemi-cone structure. This is modelled as a Maxwellian $dN/d\varepsilon_p \propto \exp(-\varepsilon_p/T_p)$ with characteristic beam temperature (average proton energy) $T_p = 6.1\ MeV$. The beam energy incident on the RCF was 4.16 $J$, but given the small solid angle subtended by RCF 16 $cm$ behind the target, this is less than the actual total beam

energy. When compared with previous experiments using similar target structures and short-pulse laser parameters (17), the total beam energy is scaled up to 14 $J$. We also assume an approximately Gaussian current density profile $J(x) = J_0 \exp\left(-x^2/\sigma^2\right)$ (156) with on-foam beam radius $\sigma = 45\ \mu m$. The current density is cut off to zero for $x > 100\ \mu m$ corresponding to the cone's opening radius through which protons enter the foam. Combining the Maxwellian spectrum, total beam energy, Gaussian profile, and beam pulse 10 $ps$ to mimic the OMEGA-EP laser pulse duration, the peak current density is calculated as $J_0 = 3.6 \times 10^9\ A/cm^2$. Using these fundamental inputs for the beam, we can implement beam divergence in two ways, described in the following paragraphs, using transverse thermal distributions.

From previous simulations used in Ref. (17), we gather a single transverse thermal distribution with $T_\perp = 105\ keV$, corresponding to the divergence of the outgoing beam from the cone structure. Note that this *transverse* temperature is independent of the aforementioned *longitudinal* temperature $T_p$ used in the Maxwellian energy spectrum $dN/d\varepsilon_p$. We will call the above proton beam implementation the single-injection (SI) source, since all the parameters described above are encompassed in a single proton source injection.

It has been shown, however, that TNSA protons exhibit a non-trivial energy-dependent maximum divergence (82; 157). The half-opening angle of the lowest energy protons is typically around $25^\circ - 30^\circ$, and that of the highest energy protons is $6^\circ$ or lower. In between, a parabolic fit can be used to match experimental data (157; 158), represented here as $\theta_{max}(\varepsilon_p)$. We implement this energy dependence by splitting the beam into multiple injections, each covering a different bin of proton energies. A transverse temperature $T_i^\perp$ can then be individually assigned to each $i^{th}$ injection that determines the approximate opening angle for that injection. This implementation can be used for any $\theta_{max}(\varepsilon_p)$ empirically found from experiments. We will call this beam implementation the multi-injection (MI) source. Note that the fundamental beam parameters described in the first paragraph of this section are still utilized in the MI source. The details of the MI source algorithm are explained as follows.

Assigning a transverse temperature amounts to implementing a Gaussian transverse velocity distribution

$$dN/dv_\perp \propto \exp\left(-v_\perp^2/{v_{th}^\perp}^2\right) \tag{6.1}$$

where ${v_{th}^\perp}^2 = 2T_\perp/m_p$. With this setup, a transverse temperature $T_i^\perp$ corresponding to the maximum opening angle for the $i^{th}$ injection (representing the longitudinal energy bin $E_i \leq \varepsilon_p < E_{i+1}$) can be determined in the following way. The maximum half-opening angle of an injection is determined by the maximum transverse velocity and the minimum longitudinal velocity in that injection. Since the transverse velocity distribution (Eq. 6.1) is Gaussian, $v_\perp$ substantially (by 98%) decays by $v_\perp = 2v_{th,i}^\perp$ – this can be used as an approximate maximum transverse velocity. The minimum longitudinal velocity is determined by the lower limit of the energy bin $v_i = \sqrt{2E_i/m_p}$. The maximum half-opening angle is then $\theta_{max} \approx \tan^{-1}(2v_{th,i}^\perp/v_i) = \tan^{-1}\left(2\sqrt{T_i^\perp/E_i}\right)$. Here we assume nonrelativistic protons. The transverse temperature is then determined by matching this with the parabolic fit $\theta_{max}(E_i)$:

$$T_i^\perp = \frac{E_i}{4}\tan^2\left(\theta_{max}(E_i)\right) \tag{6.2}$$

It must also be ensured that an injection's *minimum* half-opening angle does not stray far from $\theta_{max}(\varepsilon_p)$. The minimum half-opening angle is governed by an injection's upper energy limit $E_{i+1}$ (also the lower limit of the subsequent energy bin). Given the lower energy limit $E_i$ and transverse temperature $T_i^\perp$ of an injection, the upper energy limit $E_{i+1}$ can be determined by comparing the half-opening angle of the $i^{th}$ injection's *highest* energy protons $\theta = \tan^{-1}(2v_{th,i}^\perp/v_{i+1}) = \tan^{-1}\left(2\sqrt{T_i^\perp/E_{i+1}}\right)$ with the maximum half-opening angle predicted by $\theta_{max}(E_{i+1})$:

$$\delta\theta = \theta_{max}(E_{i+1}) - \tan^{-1}\left(2\sqrt{\frac{T_i^\perp}{E_{i+1}}}\right) \tag{6.3}$$

In this way, the energy bins can be deduced recursively, starting from the minimum proton

beam energy $E_1 = \varepsilon_{p,min}$ and ending when the maximum proton energy is reached. For these simulations, 5° is used as a threshold of $\delta\theta$ i.e. the maximum half-opening angle is approximately within 5° of $\theta_{max}(\varepsilon_p)$, empirically taken from Ref. (158).

A comparison of the SI and MI source implementations is shown in Fig. 6.5. Figs. 6.5(a) and (c) depict the dispersion of the SI and MI sources, respectively, by distinguishing the particle energy map 10 *ps* after injection. The lines approximate the opening angle trajectory of the lowest (purple) and highest (red) energy protons. For the SI source, albeit there is a difference in opening angle, it is seen more blatantly with lower energy protons. The red lines are almost parallel, indicating that the opening angle is negligible for high energy protons, which is not necessarily seen experimentally. The highest energy protons' opening angle in the MI source, however, is non-negligible, conforming with past experiments. Figs. 6.5(b) and (d) are the corresponding scatter plots of the opening angle vs. particle energy for the SI and MI sources. Even though the plot is saturated at low energies and low angles, the upper bound of half-opening angle as a function of particle energy defines the correspondence to $\theta_{max}(\varepsilon_p)$. Whereas the SI source has a concave, almost hyperbolic $\theta_{max}(\varepsilon_p)$, the MI source more accurately follows the empirically found parabolic profile of $\theta_{max}(\varepsilon_p)$. Thus, we can more accurately simulate the proton beam energy spread (and therefore the energy deposition) with the MI source.

Note that $\theta_{max}(\varepsilon_p)$ from a hemi-cone structure likely differs with that from a flat foil; Simulations have shown that even when the cone structure successfully reduces the proton beam radius, the laser intensity and cone tip material have a significant effect on the beam divergence after the tip, altering $\theta_{max}(\varepsilon_p)$ substantially (156; 159). In extreme cases, proton beam hollowing can occur due to the strong magnetic fields generated at the cone tip.

### 6.3.2 Electrons' Source Treatment

Hot electrons resulting from the laser interaction with the hemi were also implemented to evaluate their contribution to Cu-$K_\alpha$ generation. The hot electron source was taken from

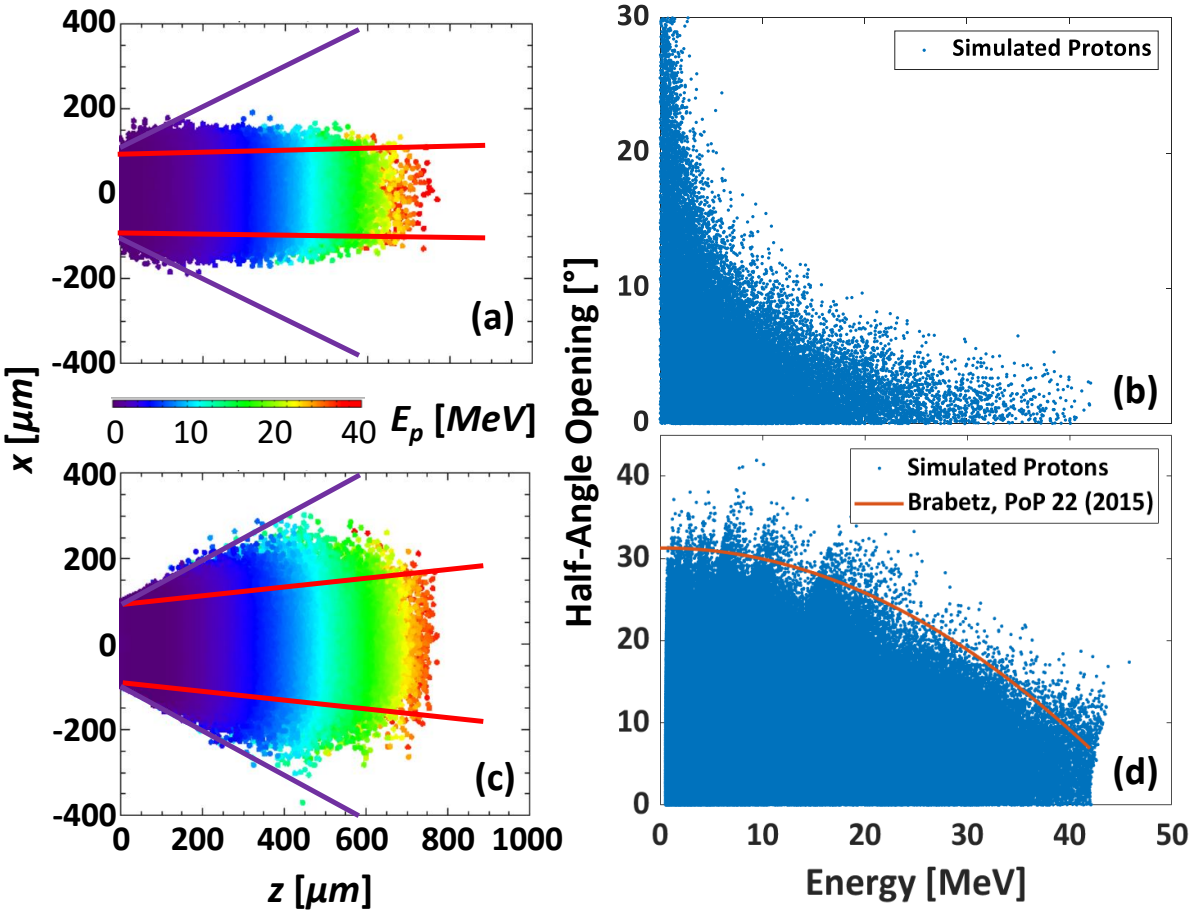


**Figure 6.5**: To compare SI (top) and MI (bottom) source injections into vacuum: (a) and (c) show the proton energy maps 10 *ps* after injections. (b) and (d) depict the particle energy dependence of maximum half-opening angle. In (d), the empirically measured half-angle opening curve is overlaid for comparison.

simulations similar to those in Ref. (17) (hemi-cone), with the primary exception being laser energy (target structure and other laser parameters were identical). Kinetic electrons were extracted at the end of the cone and, in a separate simulation, re-injected into the foam. These simulated hot electrons had source radius 100 $\mu m$, total particle count $1.3 \times 10^{15}$, and duration 40 $ps$. They exhibited a Maxwellian distribution with temperature $T_h \approx 2\ MeV$ and a large initial divergence (half-opening angle $\sim 50^\circ$) that will be important for the resulting Cu-$K_\alpha$ profiles.

### 6.3.3 Simulation Results - Transport & Heating

The results of the proton and electron transport simulations are shown in Fig. 6.6, at various times of transport. The simulations were run for 75 $ps$ to allow ample time for most protons (with enough energy to significantly induce Cu-$K_\alpha$ emission) to reach the extraction planes at 0.55 $mm$ and 1.0 $mm$. Fig. 6.6(a) shows the proton beam density and induced electron temperature within the foam. The protons' trajectories are mostly ballistic, suggesting that the incident angles at which protons are injected are mostly conserved in their transport through the foam. Indeed, compared to solid density, the low density of the foam reduces the collision frequency significantly, in turn reducing the scattering of the protons.

Interestingly, Fig. 6.6(b) shows the foam electron population reaching temperatures up to several $keV$, corresponding to the energetic protons' energy deposition. At higher divergence angles and/or greater depths in the foam, the temperature peaks at several hundreds of $eV$. This is likely due to the energy-dependent beam divergence implementation, as explained in Sec. 6.3.1. Because the transverse velocity distribution is Gaussian for all particles, the majority of particles will still be propagating longitudinally, so most of the deposited energy will still be longitudinal, with a smooth fall-off in the transverse direction. Protons with energy below 5 $MeV$ will deposit all of their energy within 1 $mm$ and stop within the foam. Because the overall temperature of the proton beam is 6 $MeV$, there will be a substantial amount of protons depositing their energy at half-angles of $20 - 30^\circ$.

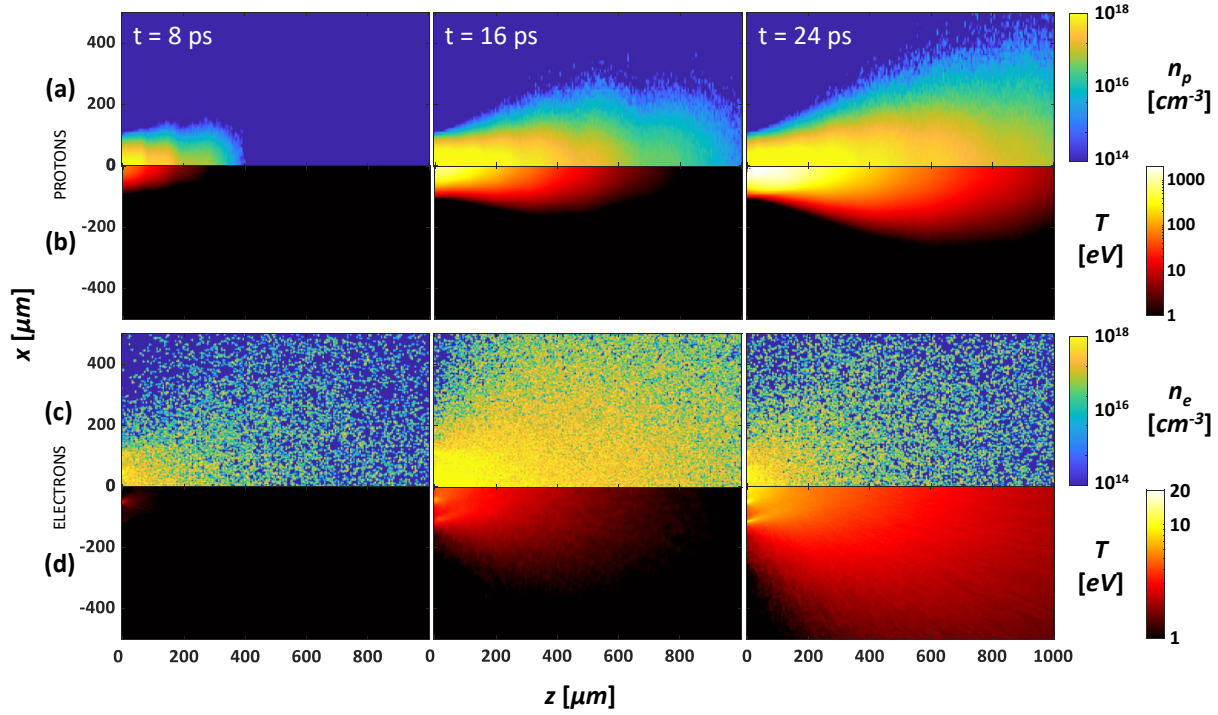


**Figure 6.6**: Simulation results of proton (a) and electron (b) transport through plastic foam target at $t = 8,\ 16,$ and 24 *ps* relative to laser irradiation of the hemi. Particle densities are shown in sub-top maps and resulting foam electron temperatures are shown in sub-bottom maps.

The results of the hot electron transport simulation are shown in Fig. 6.6(c-d), also at three different times of transport. Recall that these hot electrons originate from the laser-hemi interaction in a previous simulation, and the effects of that simulation are imprinted in the foam simulations here. For example, the line of electron heating visible in Fig. 6.6(d) at $z = 0,\ |x| \approx 110\ \mu m$ is due to a significant population of hot electrons that traveled through the cone bulk along its surfaces before entering the foam. These hot electrons mostly retain their high energies and are able to induce Cu-$K_\alpha$ emission at both depths of Cu. The increased electron density for $|x| < 100\ \mu m$ represents both hot electrons directed forward into the cone vacuum early as well as electrons co-propagating with the protons.

### 6.3.4 Post-Processing for Cu-K$_\alpha$ Profiles

The extraction planes set in $\delta z$ spacing within the Cu recorded the position and momentum (and therefore energy) of all proton/electron particles traversing Cu foils. To calculate the Cu-K$_\alpha$ emission profile due to these particle collisions, we compute the total ionization cross section by summing the individual cross section per particle according to their energies (160; 161) and binning them in $x$ to obtain the transverse profile $\Delta\sigma(x)$. Assuming the particle energy remains approximately constant over the spacing between extraction planes $\delta z$, the total Cu-K$_\alpha$ yield is $n\Delta\sigma(x)\delta z$. In addition, the total yield must be reduced according to (1) the solid angle collected by the SCI, and (2) the opacity of Cu. Since the spherical crystal is sufficiently far from the foam block covering a small solid angle, the angle of emission ($27^\circ$) can be treated as constant. The amount of Cu through which photons pass, however, depends on which extraction plane they originate, i.e. the extraction planes closer to the Cu rear travel through less Cu. Taken together, the total emission density can be expressed as:

$$\frac{dY_{K\alpha}}{dx} = \sum_{i=0}^{9} \left[\frac{d\sigma}{dx}\right]_i n\delta z e^{-\kappa_\nu \rho L(i)} \tag{6.4}$$

where $\kappa_\nu$ is the mass attenuation coefficient of Cu at photon energy $h\nu = 8.048\ keV$, and $n$ and $\rho$ are the number- and mass-density of Cu, respectively. $L(i) = (10\ \mu m - i\delta z)/\sin(27^\circ)$ is the length of Cu that photons from the $i^{th}$ extraction plane pass through, and $\delta z = 1\ \mu m$ spacing.

Energy conservation among the particles and fluids is held during the simulations, with the primary transfer of energy being proton energy deposition given to the background electrons and ions. However, as the Cu-K$_\alpha$ calculations were performed in post-processing, the radiated energy loss was not represented during the simulation. From the particle data collected in the simulations of transport in copper and calculated emission based on cross-sections, we find that the total energy conversion efficiency from "beam" protons to Cu-K$_\alpha$ x-rays is 0.5%, and that from "beam" electrons is 1.0%. This means that the Cu-K$_\alpha$ radiation was not a significant loss,

and energy was therefore approximately conserved.

## 6.4 Discussion

Since the target cone structure is in direct contact with the cone bulk, hot electrons have yet another means of escape. These electrons not only have a wide divergence beyond the cone due to enhanced magnetic fields at the cone tip (156), but also scatter relatively quickly throughout the low-density foam. Both of these attributes contribute to the approximate uniformity of the electron population at the top Cu foil. This is confirmed in our 2D simulations of hot electron transport through foam in Fig. 6.6(b). While the electron population is nonuniform near the foam front, they diverge and scatter quickly enough to uniformly populate the top (and bottom) of the foam. It should be noted that the foam height was larger in the experiment than what was simulated, which would only make the electrons reaching the top foil more uniform.

Crucially, hot electron simulations through foam also show that the population is relatively uniform at foam depth 1 *mm*. The central bright spots on the foam rear, therefore, must at least partially be due to the proton beam. This is confirmed in our 2D simulations of proton beam transport through the foam in Fig. 6.6(a). There are orders of magnitude fewer (if any) protons reaching the top of the foam compared to the rear, leaving the uniform population of electrons noted above. On the foam rear, there is a densely populated central region of protons that decays radially, matching the experimental x-ray emission profile.

The post-processed Cu-$K_\alpha$ radial emission profiles at both foam depths are displayed in Fig. 6.7, calculated as described in Sec. 6.3.4. At both 0.55 *mm* and 1 *mm* depths, hot electron-driven emission is significant at large radii and exhibits a gradual incline towards the center. Proton-driven emission, on the other hand, is primarily on-axis and drives up the centralized total emission profile (solid curve). This sheds light on the qualitative features within the SCI images in Fig. 6.3. The half-foam target (Fig. 6.3(a)) exhibits a more pronounced central peak –

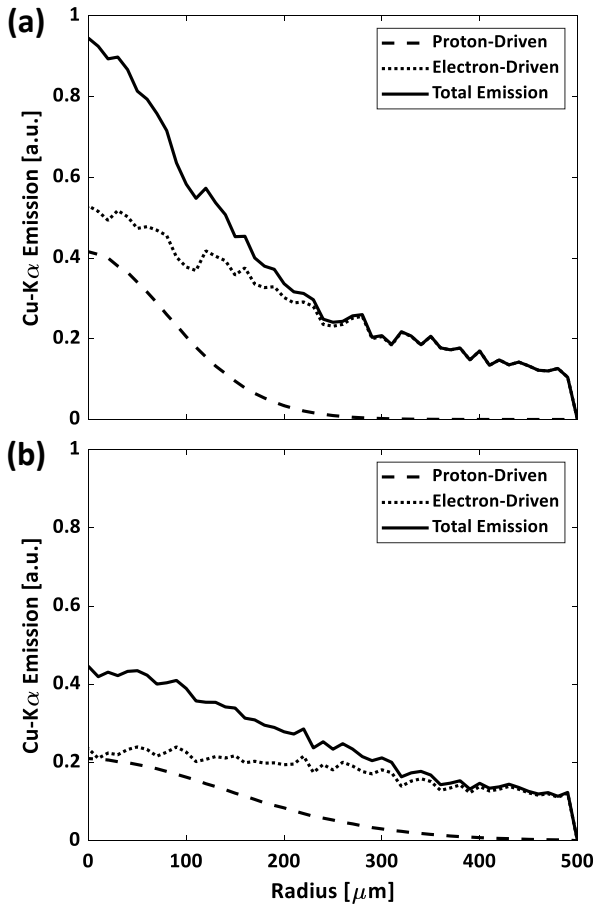


**Figure 6.7**: Cu-$K_\alpha$ radial emission profiles from simulation post-processing of 0.55 *mm* (a) and 1.0 *mm* (b) foam depths, where arbitrary units refer to the same scale. The total emission profile (solid curve) is subdivided into its component electron-driven (dotted curve) and proton-driven (dashed curve) emissions.

visually by a sharp change in gradient around $r = 250\ \mu m$ – compared to the full-foam target in Fig. 6.3(b). Simulations show that this may be attributed to protons whose emission is confined to $r = 250\ \mu m$, whereas electron emission is gradual up to $r = 500\ \mu m$. This indicates that the protons retained their beam-like qualities experimentally.

The qualitative agreement between simulations and experiment suggests that the proton beam propagates without filamenting through the low-density foam. An additional simulation was run with electromagnetic field calculations switched on, and only small magnetic fields ($\sim 10\ T$) were observed with no noticeable effects on proton beam transport. This is because space-charge

effects do not play an important role since the beam is neutralized by the relatively high density of background electrons compared to protons. The resulting low resistive magnetic field is reasonable if we consider the current density gradient. With peak current density $J_0 \sim 10^9\ A/cm^2$ and beam transverse scale length $\gtrsim 100\ \mu m$, the current density gradient is not significant enough to generate a focusing magnetic field (47). Simulations have shown, however, that decreasing the cone tip diameter can further focus proton beams (17), presumably up to a limit. Proton beam requirements for FI include total beam energy 10s of $kJ$ (with Maxwellian temperature several $MeV$) fit into a spot size of $\sim 20 \pm 10\ \mu m$ on the compressed core. To achieve this, the peak proton current density must be orders of magnitude larger than was attained in this experiment, which begets much steeper current density gradients. At these levels, self-generated magnetic fields will almost certainly affect the transport of the beam through a coronal plasma. Whether the fields act to self-consistently focus or defocus the beam depends on a number of properties of the transport medium as well as beam stopping power. Efforts to mitigate unstable transport effects or use them to our advantage (i.e. focus the beam) must be investigated experimentally, analytically, and computationally in order to best determine the prospects of proton FI.

Honrubia and Murakami (162) explored the effects of proton beam divergence (beyond the cone) on proton FI requirements, yet the beam model assumes that a proton's deflection angle after the cone was chosen at random, while within a fixed beam divergence. The randomized deflection angle does not take into account the energy-dependence of beam divergence, i.e. higher energy protons are more likely to have a lower deflection angle. Nevertheless, they determined that proton beams with diameter $20 - 30\ \mu m$ and divergence half-angle below $10^\circ$ have minimum ignition energy below $20\ kJ$ (assuming the beam is injected $\sim 90\ \mu m$ away from the compressed core). Temporal *et al.* (6) determined that the proton bandwidth $7 - 19\ MeV$ was crucial to ignition from a proton beam with temperature $T_p = 3\ MeV$ and diameter $20\ \mu m$ at the compressed core. Our analysis shows that the divergence of a particular bandwidth of protons may actually be less than the total divergence of the beam. Given a fixed overall beam divergence, confining

the crucial bandwidth of the proton beam to the necessary divergence may further relax the proton beam intensity requirements. In our analysis, the $7-19\ MeV$ proton bandwidth still has a divergence half-angle between $25^\circ$ and $30^\circ$, but further experimental and/or computational work is necessary to explore the energy-dependence of proton beam divergence beyond cone structures.

More recent work (19) has shown interesting effects of self-generated fields in hemi-cone targets. In hemi-cone structures with open cone tips, high-energy protons ($> 30\ MeV$) exhibit an annular profile, while lower energy protons appear focused in the region that would otherwise be within the annulus. This was not observed with a hemi-cone structure with closed tip. A possible explanation was that transverse electric fields generated near the open cone tip over-focused the highest energy protons which arrived early in time. At later times, some combination of a decaying electric field and lower energy protons arriving did not produce an annular effect. In the case of this work, because the foam block was in direct contact with the cone, one may argue that it was analogous to an enlarged cone tip, in which case an annular effect would not have been observed. Nevertheless, proton FI studies (6) have shown that, given the necessary beam energy, the proton spectral window primarily responsible for ignition is between 7 and 19 $MeV$ for a compressed core with density 625 $g/cm^3$. Since the highest energy protons are outside of this range, the annular effect may not be detrimental to ignition success. That being said, it would be interesting to find the foam (plasma) density below which this annular profile effect starts to appear, and which parameters increase or decrease the proton energy threshold at which the annular effect occurs.

The foam temperature evolution observed in simulations due to proton energy deposition is also unexpectedly high. Analogous simulations were performed with the exact same proton source model, but using solid aluminum ($\rho = 2.7\ g/cm^3$) and vitreous carbon foam (with identical $\rho_{foam} = 0.38\ g/cm^3$) instead of the foam. In these alternate material cases, the temperature map had the same characteristic contours as in Fig. 6.6(a), which was expected given the energy deposition and beam divergence. In the case of vitreous carbon foam, the fluid electron temperature

still reached several $keV$, while that in Al reached a maximum of 150 $eV$, which is consistent with previously run simulations with roughly similar beam parameters.

One possible explanation for the exorbitant temperatures in the low-density foam is as follows. At least in metals at high temperatures $T_e \gtrsim E_F \sim eV$, the electron heat capacity is modeled as an ideal gas of free electrons, i.e. $du/dT \propto n_f$. Because the density of the foam is about ten times lower than that of Al, the heat capacity of the foam could also be proportionately lower. This means it takes far less energy to change the temperature of the foam by an arbitrary degree than it does to change the temperature of Al by the same degree. Even when SRIM calculations (90) show that peak stopping power i.e. energy deposited in Al is quadruple that in CRF foam, the order of magnitude difference in density (and heat capacity) outweighs the stopping power calculations. We should note that these simulations can be made more accurate with better equation-of-state modeling of plastics. Since the material spends very little time in the cold solid regime, we can neglect those heat capacity models.

## 6.5 Acknowledgements

Chapter 6 contains a partial reprint as it appears in "Transport of an intense proton beam from a cone-structured target through plastic foam with unique proton source modeling" by **K. Bhutwala**, C. McGuffey, W. Theobald, O. Deppert, J. Kim, P. M. Nilson, M. S. Wei, Y. Ping, M. E. Foord, H. S. McLean, P. K. Patel, A. Higginson, M. Roth and F. N. Beg in *Physical Review E* 105(5), 055206 (2022). The dissertation author was the primary investigator and author of this publication. This material is based upon work supported by the U.S. DOE NNSA under the National Laser User Facility program with Award No. DE-NA0002034, the Laboratory Basic Science program, and the High Energy Density Laboratory Plasmas program with Award No. DE-NA0003876.

# Chapter 7

# Theoretical Model for Resistive Field Generation

## 7.1 Introduction

Understanding the dynamics of intense particle beam propagation through plasma has numerous scientific applications, including for accelerators and colliders (163; 164), neutron source generation (165), and inertial confinement fusion (38; 77). In conventional linear accelerators, strong quadrupole magnets are used to steer and focus particle beams along their trajectory. Space-charge and current neutralization degree play key roles in ion beam transport through low-density plasma, which has been well investigated through experiments, theory and simulations (166; 167). In warm and hot dense plasma, however, the background electron density generally outnumbers the beam density, and beam transport largely depends on macroscopic characteristics such as self-generated fields, stopping power and conductivity. In this regard, the transport of intense ion beams through warm and hot dense plasma is wide open for scientific exploration.

The continuous advancement of short pulse lasers has opened this area of research, as

laser-driven energetic proton beams with high current densities ($> 10^9\ A/cm^2$) and short bunch duration ($\sim\ ps$) are now routinely generated in experiments (17; 168). Already, these laser-driven proton beams are used to produce warm dense matter samples for pump-probe experiments (125; 169). As the laser to proton energy conversion efficiency, and subsequently proton beam current density, continue to increase, it will be necessary to account for collective effects as they propagate through dense plasma. For sufficiently intense proton beams incident on solids, self-generated resistive magnetic fields within materials may be capable of focusing or defocusing the proton beam itself. Simulations have shown that current densities $\sim 10^{10}\ A/cm^2$ can induce magnetic fields $\gtrsim 100\ T$, enough to affect the trajectory of the protons within the material (47; 170).

Here, we investigate and introduce a simple analytic model to estimate the magnetic field generation produced by intense proton beams. In Sec. 7.2, we review the analytic model used to find the induced resistive magnetic fields, noting the mechanism differences between energetic protons and hot electrons. In Sec. 7.3, the model is solved numerically and compared with hybrid particle-in-cell (PIC) simulations for both monoenergetic and Maxwellian beam sources. Various beam parameters are modified to observe their effects on magnetic field generation. In Sec. 7.4, these effects are discussed and explained in relation to the analytic model. This will ultimately aid in our understanding and estimation of field generation without the need to run computationally expensive simulations for several different cases.

## 7.2 Theory & Semi-analytic Model

In order to study the propagation and collective effects of intense proton beams, it helps to consider that of hot electrons. When high-intensity lasers irradiate matter, the atoms are ionized and the freed electrons are accelerated (becoming "hot" electrons) through the material. If unimpeded, the energy stored within the magnetic field induced by their current is unreasonably

large and unsustainable (171); therefore the electron beam must inductively draw a return current composed of background electrons (172; 173). This allows propagation of the hot electrons by neutralizing the total current within the material $\mathbf{J}_c + \mathbf{J}_b = 0$, where $\mathbf{J}_c$ and $\mathbf{J}_b$ are background electron current density and beam current density, respectively. Since the density of background electrons is far greater than that of the beam electrons, the background electrons' speed need not be very high to neutralize the beam current density.

However, the resistance encountered by the background electrons in the return current generates an electric field, which can be simply calculated by Ohm's Law $\mathbf{E} = \eta \mathbf{J}_c$ with material resistivity $\eta$. Furthermore, a spatial gradient in this resistive electric field drives a resistive magnetic field according to Faraday's Law:

$$\begin{aligned} \mathbf{E} &= -\eta \mathbf{J}_b \\ \frac{\partial \mathbf{B}}{\partial t} &= \nabla \times \eta \mathbf{J}_b \end{aligned} \tag{7.1}$$

This resistive magnetic field is generated by two processes: (i) the neutralization of the beam current, and (ii) any spatial gradients in either the current density or the material resistivity. This phenomenon has been investigated both computationally (174; 175) and experimentally (176; 177). Importantly, this includes resistivity gradients due to temperature gradients, since resistivity $\eta(T_e)$ depends strongly on material temperature. In many practical cases where current density is strongly centralized and decays radially, e.g. Gaussian radial distribution, azimuthal resistive magnetic fields are generated.

Previously, assuming Ohmic heating via intense hot electron beam propagation, Davies found analytic solutions for temperature evolution, and subsequently resistivity and field evolution from Eq. 7.1 (178). These solutions assumed a simplified temperature dependence of resistivity and a constant heat capacity, yet proved remarkably useful in understanding the effects of different heating regimes. Two regimes were independently considered — cold ($\eta \propto T_e$ for $T_e \ll T_F$) and Spitzer ($\eta \propto T_e^{-3/2}$ for $T_e \gg T_F$). The Fermi temperature $T_F$ is typically within 10s of $eV$ for

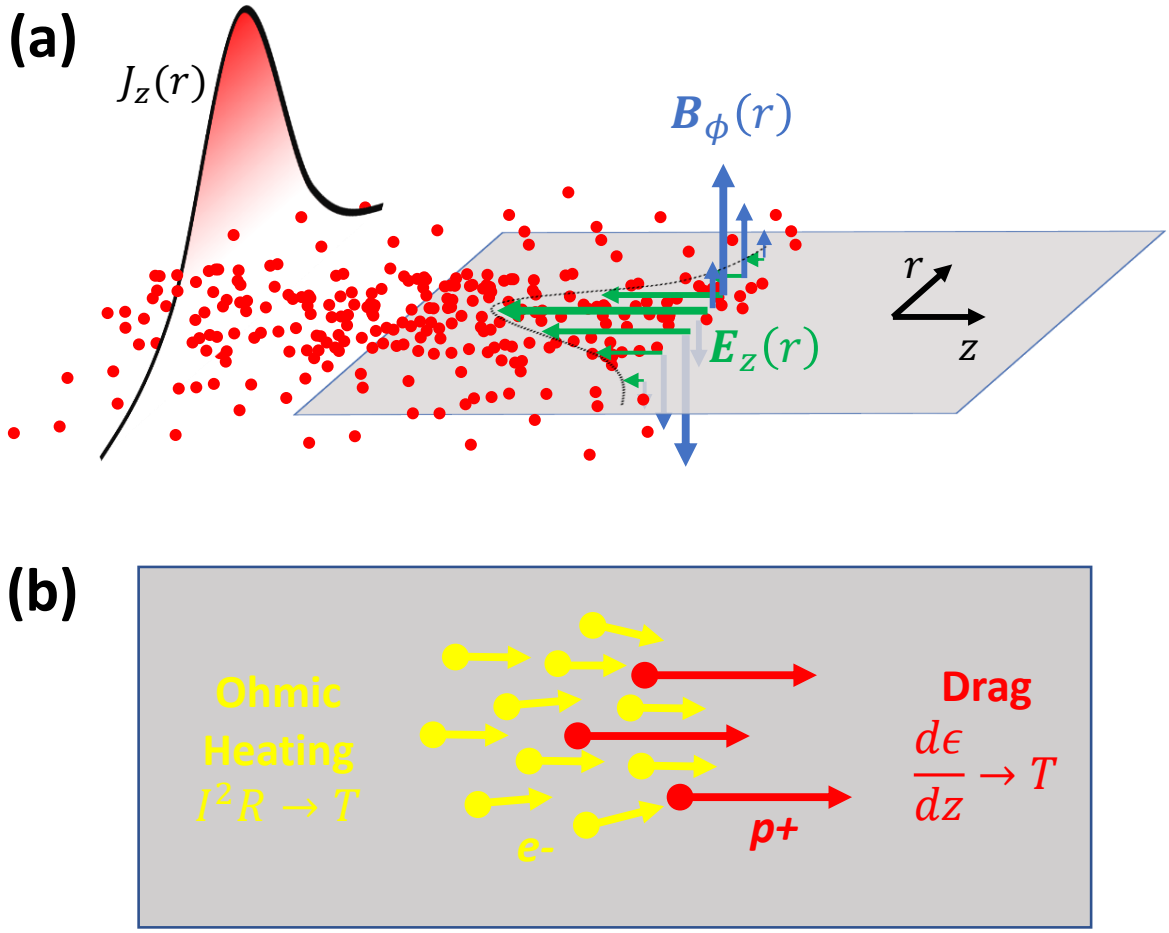


**Figure 7.1**: (a) Illustrative model of resistive fields (green, blue) generated from intense proton beam (red) transport. (b) Primary heating mechanisms are Ohmic (yellow) and drag heating (red), which beget temperature and resistivity gradients.

metals ($T_F = 12\ eV$ for aluminum and $7\ eV$ for copper) and is a marker for the warm dense regime, since electrons are partially degenerate at these temperatures. Nardi *et al.* (60) used a more sophisticated model for resistivity and heat capacity to compare theoretical target heating with experimental results in femtosecond laser-matter interactions. This model takes into account collisional saturation in the warm dense regime, or $\eta \sim \eta_{max}$ for $T_e \sim T_F$. Variations of this resistivity model were used also by Passoni *et al.* (59).

In this work, we apply a variation of the above model to intense proton beams, which are capable of heating cold foils to temperatures over $1eV$, generating warm and hot dense plasmas on

a time scale shorter than thermal expansion. Fig. 7.1(a) is an apt illustration of the field generation from proton beams, wherein the beam current density induces a neutralizing current and resistive electric fields (green). Gradients in this field subsequently induce azimuthal magnetic fields (blue). Fig. 7.1(b) illustrates the two primary heating mechanisms: Ohmic heating (yellow) brought on by the resistance encountered by the background electron return current; and drag heating (red) as protons gradually deposit their energies during transport.

We neglect thermal conduction in this model since particle beam heating occurs on much shorter time scales. Ohmic heating is given by

$$P_{Ohm} = C_v \frac{dT_e}{dt}\bigg|_{Ohm} = \eta J^2 \tag{7.2}$$

where $C_v$ is the temperature-dependent volumetric heat capacity. This is analogous to the macroscale power dissipation by resistors $P = I^2R$. In this formulation, it is important to note that $J$ is technically the current density of the *background electrons*, which was shown earlier to be equal and opposite to the *beam* current density. As the beam particles themselves propagate through the material, they impart their energy to the bulk electrons via collisions. This collisional (drag) heating is expressed as (173)

$$P_{drag} = C_v \frac{dT_e}{dt}\bigg|_{drag} = \frac{J}{e}\frac{d\varepsilon}{dz} \tag{7.3}$$

where $e$ is the elementary charge and $d\varepsilon/dz$ is the temperature-dependent particle stopping power. Combining both heat sources, we obtain a first-order ordinary differential equation for temperature,

$$C_v \frac{dT_e}{dt} = \eta J^2 + \frac{J}{e}\frac{d\varepsilon}{dz} \tag{7.4}$$

which may be solved numerically. $T_e(t)$ may then be used to calculate the resistivity and in turn the resistive fields from Eq. 7.1.

Before following this path, it is important to take a closer look at Eq. 7.4. In particular, let the ratio of the two source terms be given by

$$S_0 = \frac{P_{drag}}{P_{Ohm}} = \frac{d\varepsilon/dz}{e\eta J} \tag{7.5}$$

which can be interpreted as the ratio of averaged collisional (drag) force to the resistive electric force, both experienced by the beam particles. Since current densities and stopping power of hot electrons typically differ from those of protons, $S_0$ will also differ. Considering resistivity of the form $\eta = \eta_0(T/T_0)^{\alpha}$, $\alpha = 1$ approximates the cold regime and $\alpha = -1.5$ approximates the hot (Spitzer) regime. Between these extremes lies warm dense matter, which will be discussed later.

### 7.2.1 Heating by Hot Electrons vs. Protons

Short-pulse laser-driven electron beams typically exhibit current densities $J_e \sim 10^{13}\ A/cm^2$ and stopping power $d\varepsilon_e/dz \sim 5\ MeV/cm$ (for 5 MeV electrons at room temperature Al), yielding $S_0 \sim 0.06$ (resistivity is material-dependent). This indicates that Ohmic heating is dominant, accordant with Davies' neglect of drag heating (178). This is clearly seen in Fig. 7.2, which plots the numerical solutions to Eq. 7.4 for the cold ($\alpha = 1$) and hot ($\alpha = -1.5$) regimes independently, assuming constant resistivity and heat capacity. In both regimes, $S_0 = 0$ (blue) discounts drag heating completely. These curves match previous results (178). For hot electron beams which typically have $S_0 \ll 1$ (red), it is clear that drag heating does not significantly increase the temperature and resistivity. Because resistive fields arise from spatial gradients in resistivity, insignificant differences in resistivity beget insignificant differences in resistive fields.

Laser-driven proton beams, on the other hand, typically exhibit $J_p \sim 10^9\ A/cm^2$ and $d\varepsilon_p/dz \sim 400\ MeV/cm$ (17; 168), yielding $S_0 > 1000$. Contrary to hot electron beams, drag heating is now the dominant heating mechanism, shown clearly in Fig. 7.3. In the same vein as Fig. 7.2, $S_0 = 0$ disregards drag heating, yielding the same blue curves. For $S_0 \gg 1$ (typical for

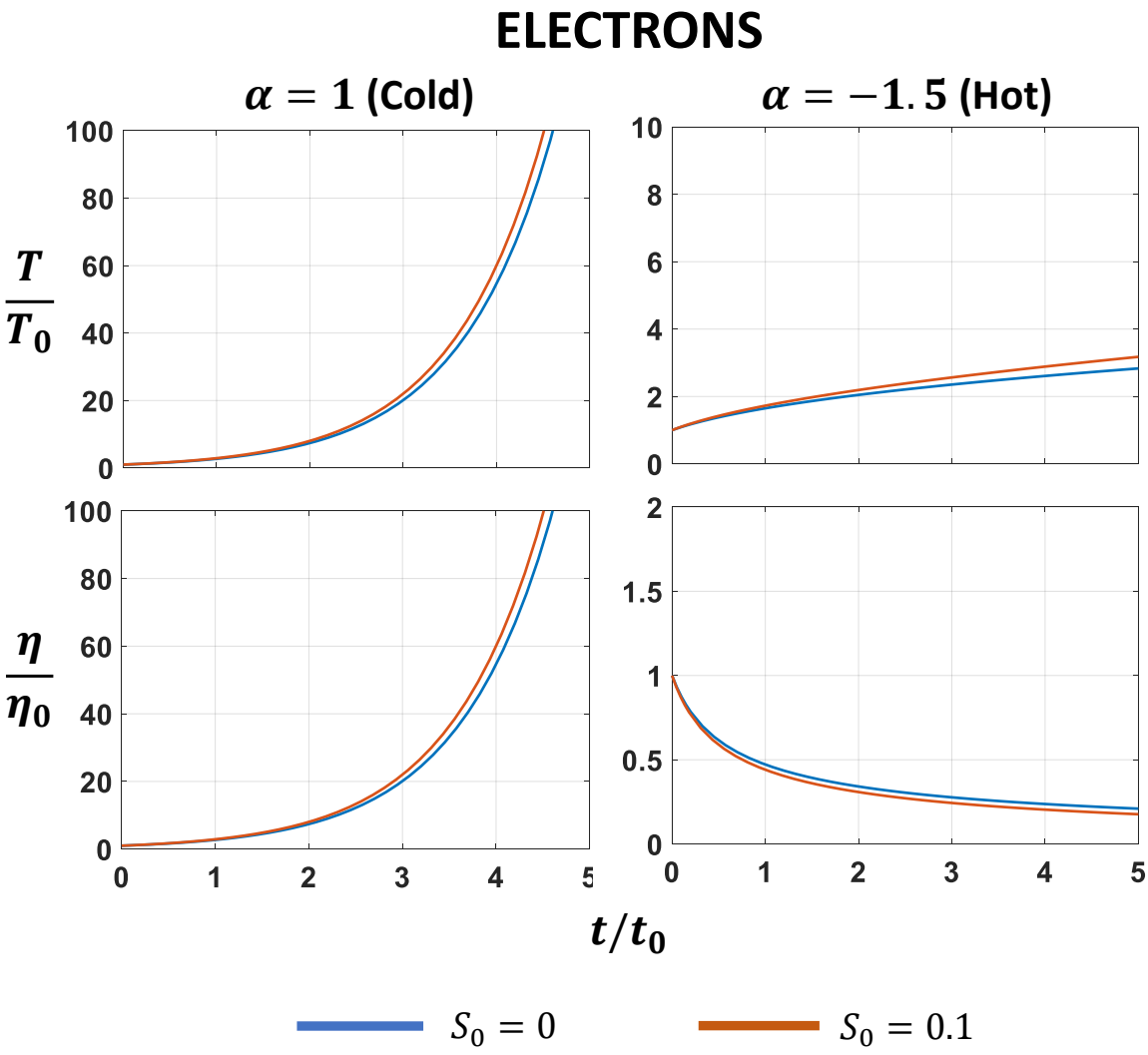


**Figure 7.2**: Resistivity and temperature evolution of hot electron beam-heated targets in the cold ($\alpha = 1$) and hot ($\alpha = -3/2$) plasma regimes. Hot electron beams exhibit $S_0 \ll 1$ (red), showing that drag heating is negligible when compared with Ohmic heating only ($S_0 = 0$, blue).

intense proton beams), the numerical solutions to Eq. 7.4 are shown in red and yellow for both cold and hot regimes. When $S_0 > 1000$, we clearly see orders of magnitude difference in heating. For $\alpha = 1$, this can even be seen analytically by solving Eqs. 7.1 and 7.4 assuming constant stopping power (valid for particle energies $\sim MeV$ and/or thin foils):

$$\frac{T}{T_0} = \frac{\eta}{\eta_0} = (1+S_0)e^{t/t_0} - S_0$$

where $t_0 = C_v T_0/\eta_0 J^2$ is the characteristic Ohmic heating time scale. For $S_0 = 0$, this reverts back to the single exponential solution shown in blue in Figs. 7.2-7.3 and in (178). For $S_0 \gg 1$, the temperature and resistivity increase by approximately a factor of $S_0$, which underlies the several orders of magnitude increase in temperature and resistivity for protons. Even though $S_0$ has a spatial dependence through $J$, this factor of $S_0$ will propagate through to augment the magnetic field as well.

### 7.2.2 Resistivity & Heat Capacity Model

So far, we have analyzed the cold and hot regimes independently, whereas in reality, resistivity follows a continous function of temperature. In light of this, resistivity will be calculated from the Drude model:

$$\eta = \frac{m_e \nu_e}{e^2 n_f} \tag{7.6}$$

where $e$ and $m_e$ are respectively the electron charge and mass, $n_f$ is the free electron density, and $\nu_e$ the total electron collision frequency. Note that the free electron density implicitly depends on temperature via the mean ionization state of the material. Thus, calculating resistivity boils down to calculating the electron collision frequency. The Eidmann-Chimier model (54) smoothly interpolates the electron collision frequency among the cold, hot, and warm dense regimes. In the cold condensed matter regime $T_e \ll T_F$ (Fermi temperature), electron-phonon collision frequency $\nu_{e\text{-}ph}$ and electron-electron collision frequency $\nu_{e\text{-}e}$ are dominant (51; 53). These

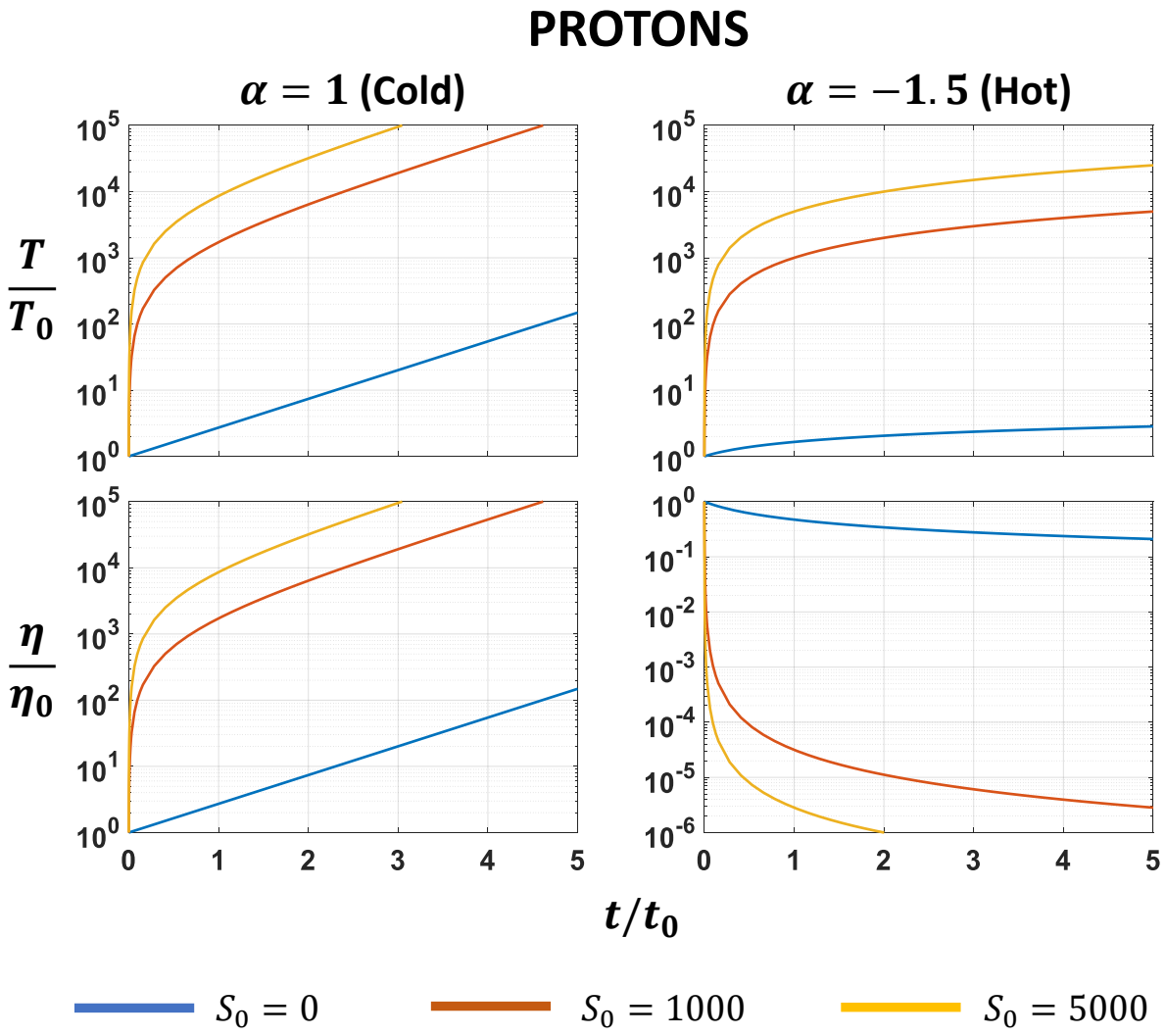


**Figure 7.3**: Resistivity and temperature evolution of proton beam-heated targets in the cold ($\alpha = 1$) and hot ($\alpha = -3/2$) plasma regimes. Intense proton beams exhibit $S_0 \gg 1$ (red, yellow), making drag heating dominant in temperature and resistivity evolution by several orders of magnitude.

collision frequencies describe the classical interaction of background electrons with lattice ions ($\nu_{e\text{-}ph}$) and with themselves ($\nu_{e\text{-}e}$). For the hot plasma regime $T_e \gg T_F$, wherein atoms are approximately fully ionized, we use the classic **Sp**itzer collision frequency $\nu_{sp}$ describing the Coulomb interaction among free electrons (55). For the intermediate regime $T_e \sim T_F$, electron degeneracy and ion correlation effects come into play, invalidating the Spitzer formulation. An upper limit on the electron collision frequency is obtained by noting that the electron mean free path must exceed the inter-atomic distance $r_0$, or $\nu_e < \nu_{max} = v_e/r_0$ with electron thermal speed $v_e$. This is equivalent to collisional or resistive saturation, and has been shown both experimentally (56; 22) and computationally (57; 58).

Thus, a harmonic average of the corresponding relaxation times is used to calculate the total electron collision frequency, and therefore resistivity, across a broad temperature range:

$$\nu_e^{-2} = (\nu_{e\text{-}ph} + \nu_{e\text{-}e})^{-2} + \nu_{max}^{-2} + \nu_{sp}^{-2} \tag{7.7}$$

Further details on this model can be seen in Sec. 2.6. Fig. 7.4(a) displays the resultant $\eta(T)$ of solid-density aluminum from room temperature to 10 $keV$, along with experimental measurements (22; 23; 21; 20). It should be noted that at low temperatures, the electron-phonon collision frequency naturally depends on the ion temperature. While electron-ion thermal equilibrium is assumed in the model above, this is invalid for ultra-short pulse laser-matter interactions, which formed the basis of resistivity measurements by Milchberg *et al.* and possibly the reason for their discrepancy. Nonetheless, resistive saturation is still apparent with a similar $\eta_{max}$ as in the Eidmann-Chimier model.

The resistivity calculated from the model by Lee and More (114) with Desjarlais ionization pressure correction (28) (LMD model) is also plotted in Fig. 7.4(a) for comparison with the Eidmann-Chimier model. The hybrid-PIC code LSP (106) was used here to calculate the electron collision frequency (LSP LMD module) for solid-density aluminum at the marked electron and

ion temperatures. This was then plugged into Eq. 7.6 to calculate the corresponding resistivities, which show good agreement with the Eidmann-Chimier model for resistivity. Further details on this model and its benchmarking can be seen in Sec. 4.3.

As in Eq. 7.2-7.4, we must also consider the dependence of material heat capacity on bulk temperature. In the hot plasma regime, free electrons behave approximately as an ideal gas, yielding volumetric heat capacity $C_v = \frac{3}{2} n_f$. For temperatures below this regime, the heat capacity calculation is deferred to tabulations made by Lin Zhigilei and Celli (29) for various metals, since the complexity of the calculation is outside the scope of this work. The two regimes are then smoothly interpolated to yield a piecewise formulation of $C_v(T_e)$. Fig. 7.4(b) displays the total heat capacity of Al at solid density from room temperature to 10 $keV$. Beyond 5 $eV$, the heat capacity is still temperature-dependent because the free electron density depends on the mean ionization state, which in turn is temperature dependent.

### 7.2.3 Proton Stopping Power Model

The final component to model before solving Eq. 7.4 is the particle stopping power. In this work, the proton stopping power is calculated by summing free- and bound-electron contributions independently to cover partially and fully ionized plasmas (25):

$$\frac{d\varepsilon_p}{dz} = \kappa_0 \left[ (Z - Z^*) n_i L_b + Z^* n_i L_f \right] \tag{7.8}$$

with common stopping factor $\kappa_0 = 4\pi e^4 / m_e v_p^2$, bulk temperature-dependent mean ionization state $Z^*$, and bound and free electron density $(Z - Z^*)n_i$ and $Z^* n_i$, respectively. Estimation of the ionization degree $Z^*$ of aluminum was interpolated from tabulated equation of state (EOS) properties generated by the software Prism PrOpacEOS (24). The bound electron stopping number $L_b$ is calculated from the high-energy limit of the Bethe-Bloche expression (179; 89; 90) taking into account the excitation and ionization of target electrons. The free electron stopping

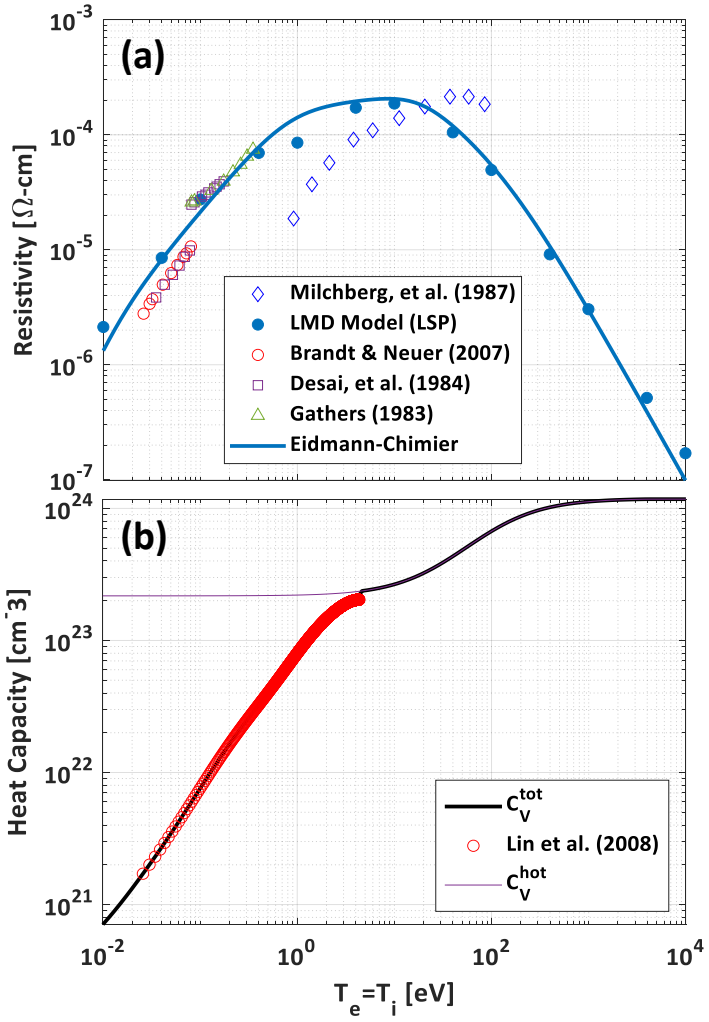


**Figure 7.4**: (a) Comparison of experimental Al resistivity measurements with Eidmann-Chimier model (22; 23; 21; 20) and LMD model (28). (b) Semi-analytic model for volumetric heat capacity of Al, using tabulated values (29) up to 5 $eV$ and free electron gas model thereafter.

number $L_f$ is calculated accounting for simple binary collisions and plasma oscillation excitations (96). Ultimately, the total stopping power depends on the proton energy, the target material and its temperature, assuming constant density for time scales $\sim$10s of picoseconds.

## 7.3 Magnetic Field Generation

Having modeled the temperature dependence of resistivity, heat capacity, and proton stopping power, and assuming a radially varying beam current density, we are finally in a position to solve Eq. 7.4 and Eq. 7.1 numerically. After testing, the sufficient time resolution for the calculation was determined to be 1 $fs$ to start converging to the real solution. Aluminum resistivity and heat capacity has been well investigated and modeled as in Fig. 7.4 so will be used as the surrogate bulk material in this work with initial temperature $T_0$. In all cases, we consider a rigid beam model where the beam current density is unidirectional and axisymmetric with a Gaussian radial profile $\mathbf{J} \propto \exp\left(-r^2/r_0^2\right)\hat{\mathbf{z}}$ with characteristic radius $r_0$. Note that the full width at half-maximum is FWHM $\approx 1.67 r_0$.

### 7.3.1 Monoenergetic Proton Beams

Let us first consider a monoenergetic beam with on-axis current density $J_0$. Because thermal conductivity is ignored, the spatial dependence ultimately derives from time-independent $J(r)$. Eq. 7.1 then simplifies to

$$\mathbf{E} = -\eta(r,t)J(r)\hat{\mathbf{z}} \tag{7.9}$$

$$\frac{\partial \mathbf{B}}{\partial t} = -\frac{\partial}{\partial r}[\eta(r,t)J(r)]\hat{\phi} \tag{7.10}$$

$T_e(r,t)$ can be solved numerically from Eq. 7.4 and used to find $\eta(r,t)$ and subsequently the resistive fields as above. Note that since there is yet no longitudinal ($z$) dependence, this model

applies to a thin sliver $\delta z$ of bulk material, across which stopping power does not vary significantly (valid for $\sim MeV$ protons). The free parameters in this model are therefore initial Al temperature $T_0$ at solid density 2.7 $g/cm^3$, beam parameters $J_0$, $r_0$, and proton energy $\varepsilon_p$.

To start, we investigate the impact of initial temperature $T_0$ on magnetic field generation. Fig. 7.5 displays $\eta(r,t)$ and $B_\phi(r,t)$ due to a monoenergetic 2.25 $MeV$ proton beam with $J_0 = 10^{10}$ $A/cm^2$ and $r_0 = 17$ $\mu m$, for initial temperatures (a-b) 0.03 $eV$, (c-d) 10 $eV$ (warm dense Al, middle), and (e-f) 200 $eV$ (hot dense Al). The first peculiar feature is – even though the initial temperatures 0.03 $eV$ and 10 $eV$ differ by three orders of magnitude, both conditions yield the same magnetic field evolution capping at 25 $T$. This can be explained by the characteristic rate of proton heating. The inset of Fig. 7.5(a) displays the temperature of Al along the beam axis in the first 500 $fs$. The protons instantly heat the Al to about 5 $eV$, reaching 10 $eV$ after only 100 $fs$. One can imagine that this temperature evolution scales locally with the smoothly varying Gaussian current density. Since 10 $eV$ is reached so quickly on the time scale of the field generation and since the resistivity explicitly depends on temperature, both scenarios follow an almost identical evolution.

However, the maximum magnetic field reached with initial temperature 200 $eV$ is less than half that of the above, as shown in Fig. 7.5(f). This is because the initial resistivity is much lower at 200 $eV$ than at 10 $eV$. Eq. 7.10 shows that the field generation is proportional to the resistivity, so the sharp decrease in Spitzer resistivity from resistive saturation largely inhibits magnetic field generation. The significance of the initial heating period on field generation will be explained further in Sec. 7.4.

Before proceeding, it is important to benchmark these calculations with simulations. The hybrid-PIC code LSP (106) is used here to benchmark the fields calculated numerically by Eq. 7.10. As a PIC code, LSP advances electromagnetic fields via Maxwell's equations (Faraday's and Ampere's Laws). To model the collisions of background particles in the cold and warm dense regimes, the LMD and Spitzer modules within LSP were used. Prism PrOpacEOS (24) tables

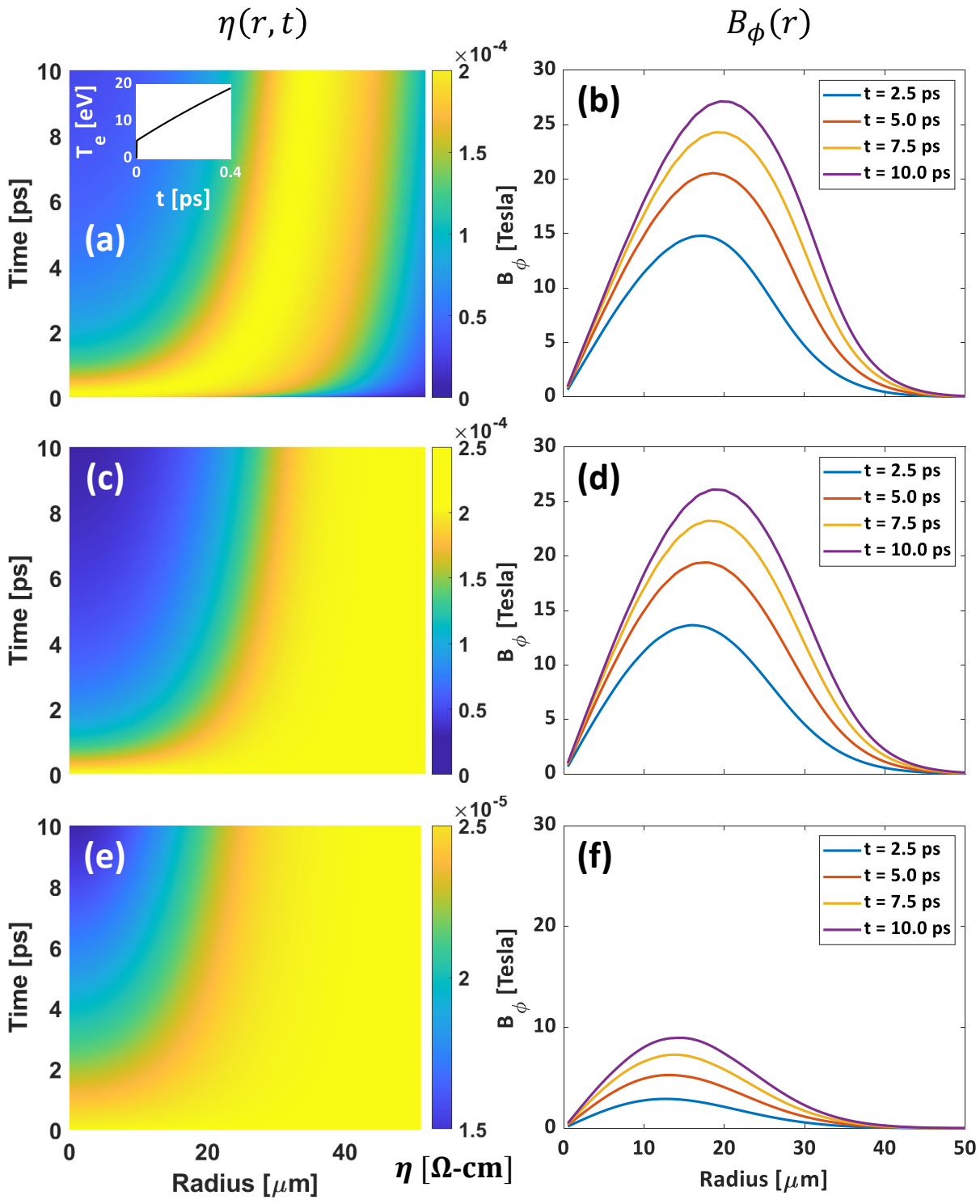


**Figure 7.5**: Comparison of resistivity $\eta(r,t)$ (left plots) and corresponding magnetic field profiles $B_\phi(r)$ (right plots) from proton beam propagation when varying the initial temperature of Al - 0.03 *eV* room temperature (top plots), 10 *eV* (middle plots), and 200 *eV* (bottom plots).

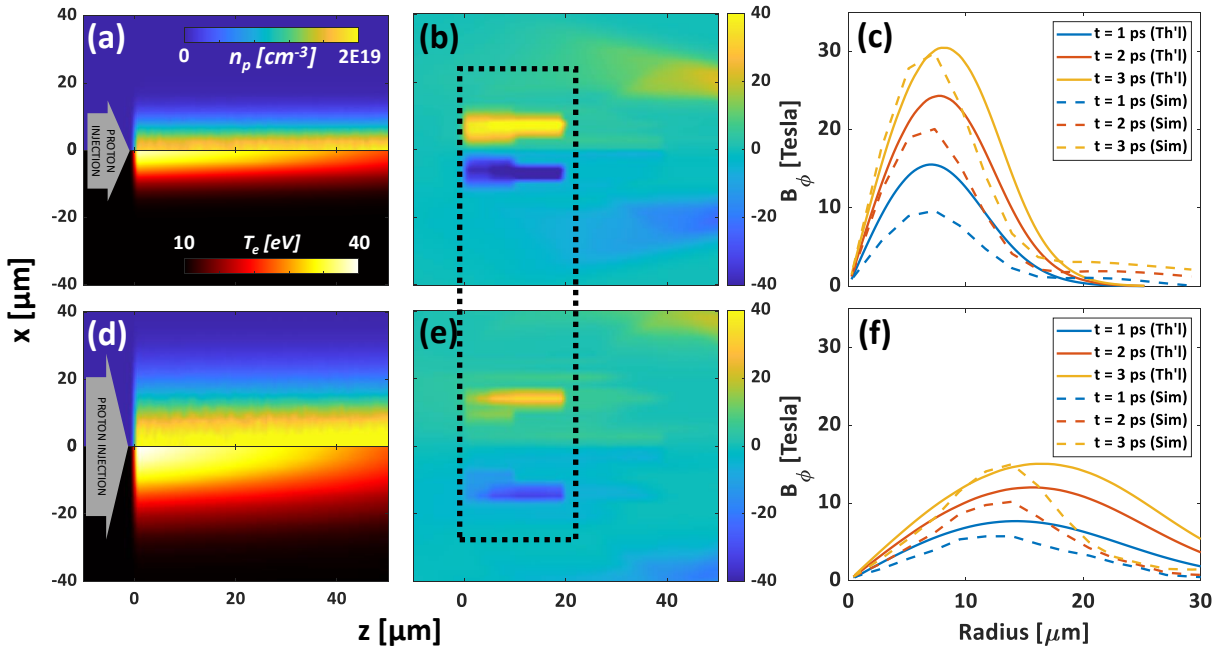


**Figure 7.6**: Comparison of 2-D hybrid-PIC simulations (a,b,d,e) and theoretical calculations (c,f) of magnetic field generation for characteristic beam radii $r_0 = 8.4\ \mu m$ (a-c) and $r_0 = 17\ \mu m$ (d-f). All images are taken at $t = 3\ ps$ after beam front enters at $z = 0$.

were also imposed to calculate the average ionization degree of aluminum as a function of density and temperature. The comparison of total electron collision frequency between the Eidmann-Chimier model and LSP LMD module was shown in Fig. 7.4(a). Proton energy deposition in LSP was calculated the same way as outlined in Sec. 7.2.3, where at each time step stopping power was calculated dynamically based on temperature and density (25).

Comparisons of simulated to theoretical calculations of magnetic field are shown in Fig. 7.6. Figs. 7.6(a-b, d-e) display the simulation results of monoenergetic (5 $MeV$) proton beam propagation ($J_0 = 10^{10}\ A/cm^2$) through Al with initial temperature 10 $eV$, where the beam was injected at $z = 0$ in the $+z$ direction. Although a smaller viewing window is displayed, the simulation box spanned $-50\ \mu m$ to $400\ \mu m$ longitudinally and $70\ \mu m$ radially to avoid boundary effects. Note that the appropriate magnetic field profile is within the dotted regions in Figs. 7.6(b,e). Figs. 7.6(c,f) show good agreement between the simulated (dotted curves) and calculated (solid curves) magnetic field profiles. In both cases, the simulated and theoretical fields

converge with time in both shape and magnitude, with only a minor discrepancy in radial spread. The radial discrepancy is possibly due to the rigid nature of the theoretical model, which assumes perfect beam neutralization and electron-ion thermal equilibrium at all radii. In simulations, beam neutralization takes time and background electrons may even be pulled in from the beam periphery. Despite this discrepancy, it is important to note that simulations respond almost identically to theoretical calculations when beam radius is doubled, i.e. field magnitude halves and radial spread doubles.

Looking closer at the simulated fields in Fig. 7.6(b,e), it is interesting to note that there are actually two significant sets of azimuthal magnetic field — one as described above and another which aligns closely with the temperature contours near the beam front. The current model does not take into account the magnetic field development longitudinally, but one may speculate that these fields affect beam focusing or defocusing. This will be further discussed in Sec. 7.4.

### 7.3.2 Proton Beams with Maxwellian Energy Distribution

Laser-driven proton beams have proven a useful means of generating warm and hot dense plasmas isochorically and uniformly (14). In a typical proton-heating configuration, a high-intensity short-pulse laser irradiates a primary (source) target and couples primarily to bulk electrons. A cloud of hot electrons forms outside the source target, which generate an electric field capable of accelerating protons to $\sim MeV$ energies from the rear surface (75). Protons and electrons co-propagate as a quasi-neutral beam across a vacuum gap before encountering a secondary (sample) target. There, co-propagating electrons generally have $\sim keV$ energies and stop within a thin ($\sim \mu m$) front layer, leaving protons to propagate deeper into the sample. Still, protons would dominate over electrons in heating the front surface. Our theoretical model for proton beam-driven magnetic field development may also be applied to the front $\delta z$ depth of the sample, simply by incorporating a time dependence in the current density and stopping power.

Laser-driven proton beams are accelerated from a source foil into vacuum and often

exhibit Maxwellian energy spectra:

$$\frac{dN}{d\varepsilon_p} = \frac{\varepsilon_{tot}}{T_p^2} e^{-\varepsilon_p/T_p} \tag{7.11}$$

with beam temperature $T_p$ and total beam energy $\varepsilon_{tot}$. This distribution of protons would then disperse across a vacuum gap before encountering a sample foil. Due to this dispersion, incident proton energy and current density are time-varying at the sample front. Assuming the proton beam originates from an instantaneous "burst" source (valid for laser pulses $\ll ps$) and exhibits characteristic radius $r_0$, the current density is expressed as:

$$J(r,t) = \left(\frac{2e}{\pi r_0^2 \tau} \frac{\varepsilon_{tot}}{T_p}\right) \frac{\tau^3}{t^3} \exp\left(-\frac{\tau^2}{t^2} - \frac{r^2}{r_0^2}\right) \tag{7.12}$$

where $\tau = \sqrt{m_p d^2/2T_p}$ is the characteristic transit time, $e$ and $m_p$ are the proton charge and mass, respectively, and $d$ is the vacuum gap distance. Similar expressions were given in Ref. (6) for the time-varying beam power.

This configuration is depicted in Fig. 7.7(a). Note that because the energy spectrum exponentially decays, beam density also decreases with distance from the source foil. Fig. 7.7(b) shows the characteristic current density and beam power felt by the sample foil from a Maxwellian beam. Current density is near zero as very few high-energy protons reach the sample first, followed by protons with energy $\sim T_p$ forming the peak around $t \sim \tau$, and ending with a $t^{-3}$ decay ($t^{-5}$ for beam power) of low-energy protons. Here, $t = 0$ represents the "burst" source time. Previously, current density incident on a sample target was held constant. To compare to these cases, it helps to define the maximum current density incident on a sample:

$$J_{max} = \frac{\varepsilon_{tot}\ (J)}{\sqrt{T_p\ (MeV)}} \left(\frac{10\ \mu m}{r_0}\right)^2 \left(\frac{100\ \mu m}{d}\right) \times \left(2.4 \times 10^{10}\ A/cm^2\right) \tag{7.13}$$

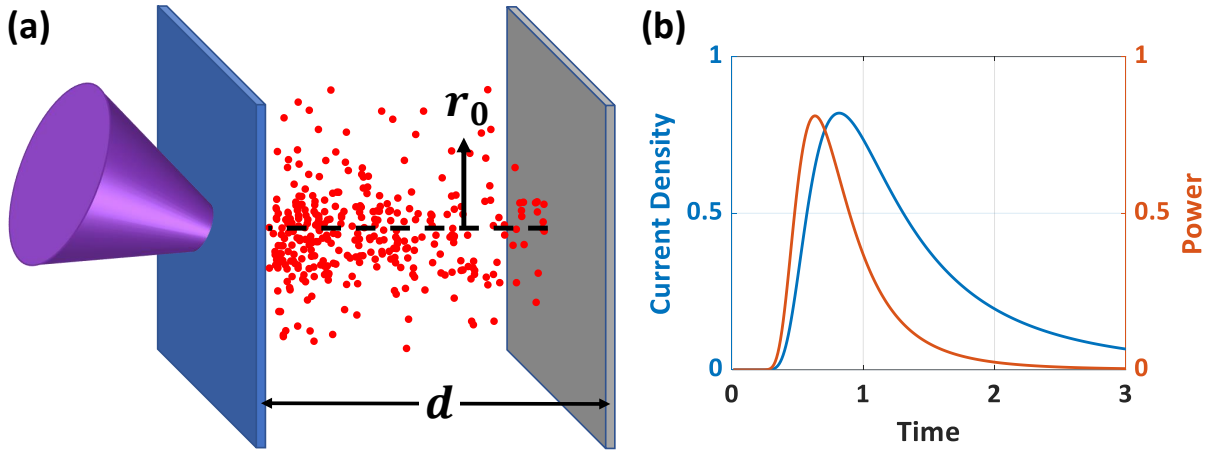


**Figure 7.7**: (a) Laser irradiation (purple) of thin-foil target (blue) drives Maxwellian proton beam (red) across a vacuum gap before hitting a sample foil (grey). (b) On-axis current density (in units of $\varepsilon_{tot} e/\pi r_0^2 \tau T_p$) and beam power (units of $2\varepsilon_{tot}/\tau$) felt by the sample as a function of time (units of $\tau$).

Importantly, $\varepsilon_p(t) = m_p d^2/2t^2$ must be used in calculating the time-varying stopping power in Eq. 7.4. Beyond this, the same strategy for calculating the resistive magnetic fields holds — solve for $T_e(r,t)$, obtain $\eta(r,t)$ and calculate $B_\phi(r,t)$.

The magnetic fields resulting from varying Maxwellian beams ($T_p = 5\ MeV$) are shown in Fig. 7.8. For all cases, the field develops steadily at early times before converging to a maximum profile. Convergence to this maximum field profile occurs when the current density decays, approximately at the inflection point past its peak, $t \sim \tau$. This is reasonable since current density decays rapidly after this time, and total magnetic flux along with it. This point will be further discussed in Sec. 7.4.

As an example, Fig. 7.8(a) displays the magnetic field evolution from a Maxwellian proton beam with $\varepsilon_{tot} = 0.33\ J$, $d = 50\ \mu m$ ($\tau \approx 1.6\ ps$), and $r_0 = 8.4\ \mu m$. The calculated fields (solid curves) rapidly increase until $\tau = 2\ ps$, within which time the current density peaks and slightly decays. For $t > 2\ ps$, the field develops at a slower pace before converging to a profile with $B_{max} \approx 30\ T$. The parameters of this beam were chosen to approximately match the overall conditions of the monoenergetic beam shown in Fig. 7.6(a), i.e. the average proton energy

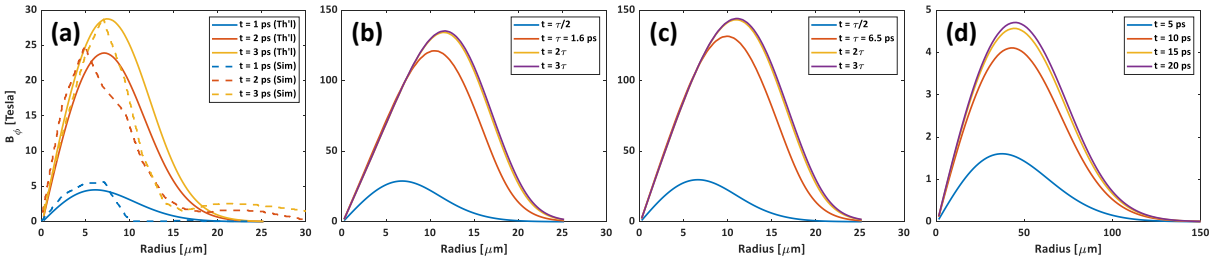


**Figure 7.8**: Evolution of magnetic field profiles driven by Maxwellian proton beams of varying parameters. The beam parameters of (a-d) are listed in Table 7.1. In all cases, sample Al is initially at 10 $eV$ and Maxwellian beam temperature is 5 $MeV$.

**Table 7.1**: Maximum magnetic field $B_{max}$ generated form intense proton beams with varying parameters outlined in body text. For Maxwellian beams, $\langle J \rangle \approx 0.15 J_{max}$ is calculated over a pulse duration $\Delta t = 3\tau$. The first four entries correspond to the results shown in Fig. 7.8.

| Distribution | $\varepsilon_{tot}$ $[J]$ | $\langle J \rangle$ $[\times 10^{10}\ A/cm^2]$ | $r_0$ $[\mu m]$ | $d$ $[\mu m]$ | $\Delta t$ $[ps]$ | $B_{max}$ $[T]$ |
|---|---|---|---|---|---|---|
| Maxwellian (a) | 0.33 | 0.56 | 8.4 | 50 | 4.8 | 30 |
| Maxwellian (b) | 10 | 17 | 8.4 | 50 | 4.8 | 135 |
| Maxwellian (c) | 10 | 4.3 | 8.4 | 200 | 19.4 | 145 |
| Maxwellian (d) | 10 | 0.12 | 50 | 200 | 19.4 | 5 |
| Monoenergetic | 10 | 19 | 8.4 | - | 4.8 | 100 |
| Maxwellian | 100 | 0.5 | 50 | 200 | 19.4 | 16 |

$T_p$ matches that of the monoenergetic beam, and the vacuum gap $d$ was chosen such that the time-averaged current density of the Maxwellian beam over 3 $ps$ is $8 \times 10^9\ A/cm$, close to that of the monoenergetic beam. Interestingly, the magnetic field profile after 3 $ps$ of the both beams approximately match, even though the field development at earlier times does not. Simulations were also conducted for the beam conditions in Fig. 7.8(a), with results shown as dashed curves. The magnetic field evolution from simulations agrees quite well in magnitude to theoretical results, but again, varies slightly with radial spread.

Fig. 7.8(b) shows the field evolution from the same proton beam configuration as in (a), except that the beam energy is increased to 10 $J$. This energy increase results in a total $B_{max}$ increase by a factor of $\sim$4.5. All else the same, amplifying the beam total energy amounts to multiplying the overall particle count and therefore current density. Conservation of energy may be employed to estimate the magnetic field amplification — since the field energy density is

proportional to $B^2$, one may roughly estimate $B_{max} \propto \sqrt{\varepsilon_{tot}}$. Amplifying $\varepsilon_{tot}$ by a factor of 30 in the above case, this would place $B_{max} \sim 160\ T$, slightly higher than the calculated 135 $T$ shown in Fig. 7.8(b). Obviously, conservation of energy here is more intricate than these relations, but this provides a rough estimate of the field amplification.

Fig. 7.8(c) shows the field profile evolution for the same beam parameters as in (b), except the vacuum distance has now been increased to $d = 200\ \mu m$. To compare the field evolutions, both (b) and (c) contain profiles at intervals with respect to $\tau$. To this end, the plots are remarkably similar in magnitude, suggesting self-similarity with the corresponding time scales. Compared to (b), the maximum current density in (c) decreases by a factor of 4 (Eq. 7.13), yet the magnetic field achieved is slightly greater. This is because the decrease in current density $J \propto 1/d$ is compensated by the increase in time scale $\tau \propto d$. The link between current density and time for magnetic field generation will be further discussed in Sec. 7.4.

Finally, the profiles shown in Fig. 7.8(d) are a result of beam parameters identical to (c), except that beam radius is increased to 50 $\mu m$. This change has by far the greatest impact on field generation, since it alters not only the current density, but also its radial gradient. Because both $J(r,t)$ and $J_{max} \propto r_0^{-2}$, widening the beam by a factor of 6 would presumably decrease the field generation by a factor of 36. This is exactly what is observed, with $B_{max} \sim 4.5\ T$ down from 150 $T$.

## 7.4 Discussion

In all of the scenarios introduced here, it is important to point out that the field generation is most significant at early times. In other words, the gain in magnetic flux during equal time intervals generally decreases with time. This can be seen in Fig. 7.5(d-f) and in Fig. 7.8, and can

be shown by integrating Eq. 7.10 with radius:

$$\frac{\partial \varphi}{\partial t} = \eta J\big|_{r=0} \tag{7.14}$$

assuming $J \to 0$ at large radii and where $\varphi$ represents a quasi-2D azimuthal magnetic flux i.e. $\varphi = \frac{\partial \Phi}{\partial z}$ with true azimuthal magnetic flux $\Phi = \iint B_\phi dr dz$. This is equivalent to invoking Stokes' Theorem on Eq. 7.1, or Faraday's Law in integral form. The magnetic fields apply up to a certain depth below which stopping power remains approximately constant, on the order of several $\mu m$ (see Fig. 7.6(b,e)). In this case, the true magnetic flux may be approximated by $\varphi \sim \Phi \Delta z$.

Eq. 7.14 shows that the rate of change of the azimuthal magnetic flux is principally dependent on the *axial* field, made of both the axial resistivity and current density. At first this may sound counterintuitive because the resistive magnetic field predominantly depends on the *gradients* of resistive electric field, i.e. resistivity and current density. But while the magnetic flux *density* ($B_\phi$) may take on large values at steep gradients, the total magnetic flux ($\varphi$) looks only at the "area under the curve" e.g. in Fig. 7.8.

Assuming a constant current density (as in Figs. 7.5-7.6), the change in magnetic flux with time is primarily determined by the resistivity, which depends on material temperature. Resistivity is maximized at the early times while temperature increases toward resistive saturation, and only decreases with temperature (Spitzer $\eta \propto T_e^{-3/2}$) beyond $\sim$100 $eV$, decreasing the gain in magnetic flux along with it.

Current density is likewise a contributor to magnetic flux gain. This is more clearly observed with Maxwellian proton beams, where the current density exhibits a rapid rise followed by a steady decay. Near the current density peak, the magnetic flux gain is maximized, as shown by the first two plots in Fig. 7.8(b-c), corresponding to $t = \tau/2$ and $t = \tau$. In this phase, the increase in magnetic flux may be approximated by

$$\Delta \varphi = [\eta J]_{r=0} \Delta t \sim \eta J_{max} \tau.$$

The combination of $J_{max} \propto 1/d$ and $\tau \propto d$ cancels the dependence on $d$ entirely, equalizing the total magnetic flux gain. For the same spatial scale ($r_0$), and self-similar spatial profile with time, $B_{max}$ is bound to match as well. This explains the stark resemblance between the field evolution in Figs. 7.8(b) and (c). The minor increase when $d = 200\ \mu m$ is likely due to the nonlinear heating and slightly prolonged phase in the warm dense regime, where magnetic flux gain is maximized. For $t > \tau$, the current density decays as $t^{-3}$, and the magnetic flux gain significantly slows down. The field profile quickly converges accordingly.

It is important to note that within this framework, electron-ion thermalization is not taken into account, which may result in inaccurate electron temperature evolution. Eq. 7.4 implies that all the energy deposited by protons goes into heating the background electrons. In reality, this energy would pass from the background electrons into background ions as they thermally equilibrate. Over several tens of picoseconds, the lattice ions are heated enough to hydrodynamically expand. Material properties including average ionization state, electron heat capacities, and stopping power calculated herein assume time-independent solid-state density, which breaks down upon material expansion.

In the extreme case where ions remain at room temperature, the resistivity curve would resemble that in Fig. 7.4(a) only in the Spitzer regime ($T_e > 10\ eV$). From room temperature up to $T_e \approx 1\ eV$, the resistivity would be constant ($T_i$-dependent), followed by a steep rise with plateau at $T_e \approx 10\ eV$. Comparing the two resistivity models, significant differences in resistive magnetic fields are only seen for current densities at or below $J \sim 10^9\ A/cm^2$. For these current densities, the material spends a significant duration within the warm dense regime, where the resistivity models differ. Higher current densities heat the material quickly to $10\ eV$, after which the field generation does not differ between models.

In theory, if electron temperature is overestimated, resistivity in the Spitzer regime would be underestimated, leading to underestimated magnetic fields. Simulations conducted for the beam conditions shown in Fig. 7.8(b), for example, show maximum B-fields reach 450 $T$, over

three times what theoretical calculations show. One possible reason that this is not seen where simulations agree with calculations is that the magnetic field maximizes within the warm dense matter regime, where resistivity varies less around saturation. The model's exclusion of electron-ion energy transfer is thus a major source of discrepancy when compared to self-consistent PIC simulations.

Maxwellian proton beams typically emerge from high-intensity ($> 10^{18}\ W/cm^2$) laser interactions with solid targets. As previously mentioned, intense lasers primarily couple with and accelerate electrons beyond the target rear. What results from this are two electron populations – hot electrons ($\sim MeV$) which reach the sample foil before the protons, and co-propagating electrons ($\sim keV$) which travel with and neutralize the protons (73). The low-energy co-propagating electrons are stopped quickly in the sample foil, but the hot electrons may have an effect on the generated fields. The analysis thus far has assumed only protons incident on the sample foil, in which case background electrons have more than enough density to form a return current, but including a forward-propagating hot electron beam may alter the physics.

By analysis of a three-species system, one may approximately find the electric field necessary to reach a steady state balance of proton, hot electron, and background electron currents, utilizing the appropriate collision frequencies. In a steady state, the equations of motion for hot and background electrons are:

$$0 = -\frac{eE}{m_e} - \nu_{he}(v_h - v_e) - \nu_{hi} v_h$$
$$0 = -\frac{eE}{m_e} - \nu_{ei} v_e - \nu_{ep}(v_e - v_p)$$

with collision frequencies $\nu$ and velocities $v$ among hot electrons, background electrons, and protons. Note that we neglect the hot electron collisions with protons in the first equation and cold electron collisions with hot electrons in the second – both collision frequencies $\nu_{hp}$ and $\nu_{eh} \ll \nu_{he}$ and $\nu_{ep}$. Assuming all currents are neutralized $J_e + J_h + J_p = 0$ and $n_h \sim n_p \ll n_e$, we

obtain for the electric field:

$$\frac{eE}{m_e} = -\frac{n_p(\nu_{ei}+\nu_{ep})(\nu_{he}+\nu_{hi})}{n_e(\nu_{he}+\nu_{hi})+n_h(\nu_{he}+\nu_{ei}+\nu_{ep})}v_p$$

This may be simplified further by assuming $\nu_{ei} \gg \nu_{he}, \nu_{ep}$:

$$E = \frac{E_0}{1+\alpha}$$

where $\frac{eE_0}{m_e} = -\frac{n_p}{n_e}\nu_{ei}v_p$ is the electric field if hot electrons were not taken into account, that is, if protons were neutralized solely by background electrons. Here, $\alpha = \frac{n_h}{n_e}\frac{\nu_{ei}}{\nu_{he}+\nu_{hi}}$ is a factor representing the hot electron contribution. Upon deeper analysis, we find that $\alpha \ll 1$, yielding electric fields that are minimally affected by the co-propagating electrons.

The fields observed in this work are relatively mild in terms of proton beam focusing ability. Simulations have shown that azimuthal magnetic fields of $\sim$30 $T$ do not significantly focus the protons, but those $\gtrsim 80$ $T$ are sufficient to affect the beam radius (47). As previously mentioned, the fields responsible for focusing may be those that contour around the beam front, as seen in Fig. 7.6(b) and (e). Similarly stronger fields may be seen in Fig. 3 of Ref. (25) and in Fig. 5 of Ref. (47). One explanation for this is the following. Expanding Eq. 7.10 yields two terms:

$$\frac{\partial B_\phi}{\partial t} = -\eta\frac{dJ}{dr} - \frac{\partial \eta}{\partial r}J \tag{7.15}$$

If the beam front always "sees" a cold solid ahead and around, the rapid proton-heating induces an instantly steep resistivity gradient

$$\frac{\partial \eta}{\partial r} = \frac{d\eta}{dT_e}\frac{\partial T_e}{\partial r} < 0$$

since $d\eta/dT_e \geq 0$ up to the warm dense regime and $\partial T_e/\partial r < 0$ because $dJ/dr < 0$. Therefore, both terms add constructively to generate the magnetic field most efficiently.

As mentioned previously, the fields investigated in this work apply to the first several microns within a material on which the proton beam is incident. Field generation deeper within a dense plasma requires further development of the model, in which proton stopping power (especially near the Bragg peak) will play a more significant role. In addition to collisional stopping power, the model would have to account for beam collective effects in order to accurately reproduce beam transport (170; 48). A more advanced model would include the $\mathbf{J} \times \mathbf{B}$ force at depth to self-consistently predict the beam evolution. When the beam starts to focus, longitudinal gradients come into play in magnetic field development. The model currently assumes $J_r = 0$, but for nonzero $J_r$,

$$\frac{\partial B_\phi}{\partial t} = \frac{\partial}{\partial z}(\eta J_r) - \frac{\partial}{\partial r}(\eta J_z).$$

As the beam front begins to focus, a positive feedback loop emerges since $\partial\eta/\partial z < 0$, $J_r < 0$, and $\partial J_r/\partial z > 0$, further strengthening the magnetic field.

## 7.5 Acknowledgements

Chapter 7 contains a partial reprint as it appears in "Investigation of Resistive Magnetic Field Generation by Intense Proton Beams in Dense Plasmas" by **K. Bhutwala**, J. Kim, C. McGuffey, M. Sherlock, M. Bailly-Grandvaux, and F. N. Beg in *Physics of Plasmas* 29(11), 113103 (2022). The dissertation author was the primary investigator and author of this publication. This work was partially supported under the auspices of the U.S. DOE NNSA High Energy Density Laboratory Plasmas program by the University of California under Contract No. DE-NA0003876.

# Chapter 8

# Conclusions and Future Work

## 8.1 Proton Heating of Warm Dense Matter

We have developed a platform upon which sample targets may be proton-heated to WDM conditions at the MEC end-station at SLAC National Accelerator Laboratory. The high-intensity short-pulse laser at MEC is capable of accelerating protons via the TNSA mechanism and focusing them via hemispherical shells, provided that the different components in the alignment system are well coordinated with the target. Additionally, the novel on-demand LCLS x-ray backlighting technique (expanding beam through Beryllium lenses) will certainly be useful in future experiments for target alignment. Background bremsstrahlung emission from irradiating the Cu source foil with the high intensity laser proved to be an issue when collecting XRTS data, as the noise from this emission confounded the scattered x-rays from the target foil. Additional shielding over the diagnostic and use of source foils with lower atomic number have since been attempted to mitigate the bremmstrahlung emission, with little success. Using mass limited targets has helped, and utilizing gated x-ray detectors (180) to remedy the issue is currently being investigated.

## 8.2 Proton Transport through Low-Density Plasma

In summary, we conducted an experiment which directed the proton beam from a typical TNSA hemi-cone configuration into CRF foam to study transport of the intense beam in a low-density plasma which may exist in, for example, proton FI schemes. The addition of a massive cone to the target hemi foil reduced the total beam energy by 50% and reduced the Maxwellian temperature by over 50%. Images of x-ray emission show a bright spot on the rear Cu film indicative of a forward-directed beam without major breakup. Simulations of the transport were conducted using a multi-injection proton source with the experimentally obtained energy spectrum but with energy-dependent angular spread. The modelling included contributions from hot electrons which broadly filled the foam. Synthetic Cu-$K_\alpha$ maps were generated through an additional simulation step and post-processing. While hot electrons produce an emission profile gently declining with radius, protons produce a centralized emission profile which drives up the emission on-axis, in qualitative agreement with experiment. This suggests that protons retain their beam-like qualities well into the low-density plasma. Simulations also showed that the intense, cone-focused proton beam was able to heat the low-density foam to temperatures above 1 $keV$, which could be important for future studies if verified experimentally.

The proton current densities generated in this experiment were not intense enough to induce significant magnetic fields within the foam, but future work includes assessing the proton transport dynamics of more intense beams through metal blocks. Proton beams can be made more intense by increasing the cone half-angle and/or reducing the tip radius, among other methods. Current calculations predict that several 10s of $kJ$ in proton beam energy must be compacted into several 10s of $\mu m$ diameter to successfully ignite a typical DT capsule. At these scales, developing analytic models to predict collective effects on proton beam transport will be crucial.

## 8.3 Theoretical Model for Intense Proton Beam Heating and Transport

We have investigated the development of resistive magnetic fields driven by intense proton beam propagation through matter. Unlike electron beams, proton beams significantly heat the target through direct collisional heating, as opposed to Ohmic heating brought about by the background electron return current. This necessitates a dynamic treatment of resistivity and heat capacity for the duration of the beam pulse since both depend strongly on temperature. Using the Eidmann-Chimier resistivity model for aluminum and the spatial and temporal evolution of temperature and resistivity, the resulting magnetic fields are solved for varying proton beam conditions. It was found that proton beams with Gaussian radial profiles induced azimuthal, annular magnetic fields.

For monoenergetic, constant current density proton beams, initial material temperature plays a significant role in total field generation. For Maxwellian proton beams, the development of resistive magnetic field is found to be self-similar with the characteristic transit time $\tau$, as evidenced by Figs. 7.8(b)-(c) and explained by Eq. 7.14. It was found that beam radius has the most significant impact on the maximum field produced, assuming constant total beam energy. For a Maxwellian beam with characteristics of a typical laser experiment with two foils, the model calculated fields as strong as 145 $T$. The agreement of the calculated field profiles with hybrid-PIC simulations (notably limited by electron-ion thermalization) shows that the model can provide a good estimate of the magnetic field. The advantage of this analytic model is to provide the essential physics involved in resistive field generation from proton beams. Since the model results are benchmarked with hybrid-PIC, resistive fields can be well estimated without the need for large processing power and time.

Aluminum was used as a sample metal in this work because the resistivity in several temperature regimes is well known, but the model can similarly be applied to other materials with

known resistivity and heat capacity. This would be particularly important for proton fast ignition studies, since understanding the self-generation of fields and resulting proton beam transport between the cone tip and the dense core is critical. Since aluminum's electric resistivity is lower than most, other transport media may produce stronger fields that are capable of self-focusing the beam.

# Bibliography


[1] H. Ritchie, M. Roser, and P. Rosado, "Energy," *Our World in Data*, 2022. https://ourworldindata.org/energy.

[2] G. Audi, A. Wapstra, and C. Thibault, "The ame2003 atomic mass evaluation: (ii). tables, graphs and references," *Nuclear Physics A*, vol. 729, no. 1, pp. 337–676, 2003. The 2003 NUBASE and Atomic Mass Evaluations.

[3] S. Atzeni and J. Meyer-ter Vehn, *The physics of inertial fusion : beam plasma interaction, hydrodynamics, hot dense matter*. International series of monographs on physics ; 125, Oxford: Clarendon, 2004.

[4] M. H. Key, "Status of and prospects for the fast ignition inertial fusion concept," *Physics of Plasmas*, vol. 14, no. 5, p. 055502, 2007.

[5] S. Atzeni, M. Temporal, and J. Honrubia, "A first analysis of fast ignition of precompressed icf fuel by laser-accelerated protons," *Nuclear Fusion*, vol. 42, no. 3, p. L1, 2002.

[6] M. Temporal, J. J. Honrubia, and S. Atzeni, "Numerical study of fast ignition of ablatively imploded deuterium–tritium fusion capsules by ultra-intense proton beams," *Physics of Plasmas*, vol. 9, no. 7, pp. 3098–3107, 2002.

[7] O. b. L. A. N. S. Los Alamos National Laboratory, "The physical regimes."

[8] M. E. Foord, T. Bartal, C. Bellei, M. Key, K. Flippo, R. B. Stephens, P. K. Patel, H. S. McLean, L. C. Jarrott, M. S. Wei, and F. N. Beg, "Proton trajectories and electric fields in a laser-accelerated focused proton beam," *Physics of Plasmas (1994-present)*, vol. 19, no. 5, pp. –, 2012.

[9] M. Roth and M. Schollmeier, "Ion acceleration—target normal sheath acceleration," *Proceedings of the CAS-CERN Accelerator School: Plasma Wake Acceleration*, vol. 1, p. 231, 2016.

[10] J. Denavit, "Collisionless plasma expansion into a vacuum," *The Physics of Fluids*, vol. 22, no. 7, pp. 1384–1392, 1979.

[11] P. Mora, "Plasma expansion into a vacuum," *Phys. Rev. Lett.*, vol. 90, p. 185002, May 2003.

[12] J. Fuchs, P. Antici, E. d'Humières, E. Lefebvre, M. Borghesi, E. Brambrink, C. Cecchetti, M. Kaluza, V. Malka, M. Manclossi, *et al.*, "Laser-driven proton scaling laws and new paths towards energy increase," *Nature physics*, vol. 2, no. 1, pp. 48–54, 2006.

[13] L. Robson, P. Simpson, R. J. Clarke, K. W. Ledingham, F. Lindau, O. Lundh, T. McCanny, P. Mora, D. Neely, C.-G. Wahlström, *et al.*, "Scaling of proton acceleration driven by petawatt-laser–plasma interactions," *Nature physics*, vol. 3, no. 1, pp. 58–62, 2007.

[14] P. K. Patel, A. J. Mackinnon, M. H. Key, T. E. Cowan, M. E. Foord, M. Allen, D. F. Price, H. Ruhl, P. T. Springer, and R. Stephens, "Isochoric heating of solid-density matter with an ultrafast proton beam," *Phys. Rev. Lett.*, vol. 91, p. 125004, Sep 2003.

[15] D. T. Offermann, K. A. Flippo, J. Cobble, M. J. Schmitt, S. A. Gaillard, T. Bartal, D. V. Rose, D. R. Welch, M. Geissel, and M. Schollmeier, "Characterization and focusing of light ion beams generated by ultra-intensely irradiated thin foils at the kilojoule scale," *Physics of Plasmas*, vol. 18, no. 5, p. 056713, 2011.

[16] T. Bartal, M. E. Foord, C. Bellei, M. H. Key, K. A. Flippo, S. A. Gaillard, D. T. Offermann, P. K. Patel, L. C. Jarrott, D. P. Higginson, M. Roth, A. Otten, D. Kraus, R. B. Stephens, H. S. McLean, E. M. Giraldez, M. S. Wei, D. C. Gautier, and F. N. Beg, "Focusing of short-pulse high-intensity laser-accelerated proton beams," *Nature Physics*, vol. 8, pp. 139–142, Feb. 2012.

[17] C. McGuffey, J. Kim, M. Wei, P. Nilson, S. Chen, J. Fuchs, P. Fitzsimmons, M. Foord, D. Mariscal, H. McLean, P. Patel, R. Stephens, and F. Beg, "Focussing protons from a kilojoule laser for intense beam heating using proximal target structures," *Scientific reports*, vol. 10, p. 9415, June 2020.

[18] B. Qiao, M. E. Foord, M. S. Wei, R. B. Stephens, M. H. Key, H. McLean, P. K. Patel, and F. N. Beg, "Dynamics of high-energy proton beam acceleration and focusing from hemisphere-cone targets by high-intensity lasers," *Phys. Rev. E*, vol. 87, p. 013108, Jan 2013.

[19] A. Higginson, *Optimisation and control of ion acceleration in intense laser-foil interactions*. PhD thesis, University of Strathclyde, 2018.

[20] G. Gathers, "Thermophysical properties of liquid copper and aluminum," *International Journal of Thermophysics*, vol. 4, no. 3, pp. 209–226, 1983.

[21] P. D. Desai, H. M. James, and C. Y. Ho, "Electrical resistivity of aluminum and manganese," *Journal of Physical and Chemical Reference Data*, vol. 13, no. 4, pp. 1131–1172, 1984.

[22] H. M. Milchberg, R. R. Freeman, S. C. Davey, and R. M. More, "Resistivity of a simple metal from room temperature to $10^6$ k," *Phys. Rev. Lett.*, vol. 61, pp. 2364–2367, Nov 1988.

[23] R. Brandt and G. Neuer, "Electrical resistivity and thermal conductivity of pure aluminum

and aluminum alloys up to and above the melting temperature," *International Journal of Thermophysics*, vol. 28, no. 5, pp. 1429–1446, 2007.

[24] "Prism Computational Sciences, Inc.."

[25] J. Kim, B. Qiao, C. McGuffey, M. S. Wei, P. E. Grabowski, and F. N. Beg, "Self-consistent simulation of transport and energy deposition of intense laser-accelerated proton beams in solid-density matter," *Phys. Rev. Lett.*, vol. 115, p. 054801, Jul 2015.

[26] G. Faussurier, C. Blancard, P. Cossé, and P. Renaudin, "Equation of state, transport coefficients, and stopping power of dense plasmas from the average-atom model self-consistent approach for astrophysical and laboratory plasmas," *Physics of Plasmas*, vol. 17, no. 5, p. 052707, 2010.

[27] J. Kim, *Study of intense proton beams: Generation and transport in Solid Density matter*. PhD thesis.

[28] M. Desjarlais, "Practical improvements to the lee-more conductivity near the metal-insulator transition," *Contributions to Plasma Physics*, vol. 41, no. 2-3, pp. 267–270.

[29] Z. Lin, L. V. Zhigilei, and V. Celli, "Electron-phonon coupling and electron heat capacity of metals under conditions of strong electron-phonon nonequilibrium," *Phys. Rev. B*, vol. 77, p. 075133, Feb 2008.

[30] J. Lelieveld, K. Klingmüller, A. Pozzer, R. T. Burnett, A. Haines, and V. Ramanathan, "Effects of fossil fuel and total anthropogenic emission removal on public health and climate," *Proceedings of the National Academy of Sciences*, vol. 116, no. 15, pp. 7192–7197, 2019.

[31] J. D. Lawson, "Some criteria for a power producing thermonuclear reactor," *Proceedings of the physical society. Section B*, vol. 70, no. 1, p. 6, 1957.

[32] M. D. Rosen, "The physics issues that determine inertial confinement fusion target gain and driver requirements: A tutorial," *Physics of Plasmas*, vol. 6, no. 5, pp. 1690–1699, 1999.

[33] M. Tabak, J. Hammer, M. E. Glinsky, W. L. Kruer, S. C. Wilks, J. Woodworth, E. M. Campbell, M. D. Perry, and R. J. Mason, "Ignition and high gain with ultrapowerful lasers," *Physics of Plasmas*, vol. 1, no. 5, pp. 1626–1634, 1994.

[34] Y. Sentoku, W. Kruer, M. Matsuoka, and A. Pukhov, "Laser hole boring and hot electron generation in the fast ignition scheme," *Fusion Science and Technology*, vol. 49, no. 3, pp. 278–296, 2006.

[35] R. Kodama, P. Norreys, K. Mima, A. Dangor, R. Evans, H. Fujita, Y. Kitagawa, K. Krushelnick, T. Miyakoshi, N. Miyanaga, *et al.*, "Fast heating of ultrahigh-density plasma as a step towards laser fusion ignition," *Nature*, vol. 412, no. 6849, pp. 798–802, 2001.

[36] W. Theobald, A. A. Solodov, C. Stoeckl, K. S. Anderson, R. Betti, T. R. Boehly, R. S. Craxton, J. A. Delettrez, C. Dorrer, J. A. Frenje, V. Y. Glebov, H. Habara, K. A. Tanaka, J. P. Knauer, R. Lauck, F. J. Marshall, K. L. Marshall, D. D. Meyerhofer, P. M. Nilson, P. K. Patel, H. Chen, T. C. Sangster, W. Seka, N. Sinenian, T. Ma, F. N. Beg, E. Giraldez, and R. B. Stephens, "Initial cone-in-shell fast-ignition experiments on omega," *Physics of Plasmas*, vol. 18, no. 5, p. 056305, 2011.

[37] M. H. Key, M. D. Cable, T. E. Cowan, K. G. Estabrook, B. A. Hammel, S. P. Hatchett, E. A. Henry, D. E. Hinkel, J. D. Kilkenny, J. A. Koch, W. L. Kruer, A. B. Langdon, B. F. Lasinski, R. W. Lee, B. J. MacGowan, A. MacKinnon, J. D. Moody, M. J. Moran, A. A. Offenberger, D. M. Pennington, M. D. Perry, T. J. Phillips, T. C. Sangster, M. S. Singh, M. A. Stoyer, M. Tabak, G. L. Tietbohl, M. Tsukamoto, K. Wharton, and S. C. Wilks,

"Hot electron production and heating by hot electrons in fast ignitor research," *Physics of Plasmas*, vol. 5, pp. 1966–1972, 05 1998.

[38] M. Roth, T. E. Cowan, M. H. Key, S. P. Hatchett, C. Brown, W. Fountain, J. Johnson, D. M. Pennington, R. A. Snavely, S. C. Wilks, K. Yasuike, H. Ruhl, F. Pegoraro, S. V. Bulanov, E. M. Campbell, M. D. Perry, and H. Powell, "Fast ignition by intense laser-accelerated proton beams," *Phys. Rev. Lett.*, vol. 86, pp. 436–439, Jan 2001.

[39] S. Atzeni, "Inertial fusion fast ignitor: Igniting pulse parameter window vs the penetration depth of the heating particles and the density of the precompressed fuel," *Physics of Plasmas*, vol. 6, no. 8, pp. 3316–3326, 1999.

[40] S. Atzeni and M. Ciampi, "Burn performance of fast ignited, tritium-poor icf fuels," *Nuclear Fusion*, vol. 37, p. 1665, dec 1997.

[41] J. Honrubia, "A synthetically accelerated scheme for radiative transfer calculations," *Journal of Quantitative Spectroscopy and Radiative Transfer*, vol. 49, no. 5, pp. 491–515, 1993.

[42] K. B. Wharton, S. P. Hatchett, S. C. Wilks, M. H. Key, J. D. Moody, V. Yanovsky, A. A. Offenberger, B. A. Hammel, M. D. Perry, and C. Joshi, "Experimental measurements of hot electrons generated by ultraintense ( $gt; 10^{19} w/\mathrm{cm}^2$) laser-plasma interactions on solid-density targets," *Phys. Rev. Lett.*, vol. 81, pp. 822–825, Jul 1998.

[43] S. Malko, W. Cayzac, V. Ospina-Bohorquez, K. Bhutwala, M. Bailly-Grandvaux, C. McGuffey, R. Fedosejevs, X. Vaisseau, A. Tauschwitz, J. Apiñaniz, *et al.*, "Proton stopping measurements at low velocity in warm dense carbon," *Nature Communications*, vol. 13, no. 1, p. 2893, 2022.

[44] A. J. Mackinnon, P. K. Patel, R. P. Town, M. J. Edwards, T. Phillips, S. C. Lerner, D. W. Price, D. Hicks, M. H. Key, S. Hatchett, S. C. Wilks, M. Borghesi, L. Romagnani, S. Kar,

T. Toncian, G. Pretzler, O. Willi, M. Koenig, E. Martinolli, S. Lepape, A. Benuzzi-Mounaix, P. Audebert, J. C. Gauthier, J. King, R. Snavely, R. R. Freeman, and T. Boehlly, "Proton radiography as an electromagnetic field and density perturbation diagnostic (invited)," *Review of Scientific Instruments*, vol. 75, no. 10, pp. 3531–3536, 2004.

[45] M. Roth, D. Jung, K. Falk, N. Guler, O. Deppert, M. Devlin, A. Favalli, J. Fernandez, D. Gautier, M. Geissel, R. Haight, C. E. Hamilton, B. M. Hegelich, R. P. Johnson, F. Merrill, G. Schaumann, K. Schoenberg, M. Schollmeier, T. Shimada, T. Taddeucci, J. L. Tybo, F. Wagner, S. A. Wender, C. H. Wilde, and G. A. Wurden, "Bright laser-driven neutron source based on the relativistic transparency of solids," *Phys. Rev. Lett.*, vol. 110, p. 044802, Jan 2013.

[46] D. Jung, K. Falk, N. Guler, O. Deppert, M. Devlin, A. Favalli, J. C. Fernandez, D. C. Gautier, M. Geissel, R. Haight, C. E. Hamilton, B. M. Hegelich, R. P. Johnson, F. Merrill, G. Schaumann, K. Schoenberg, M. Schollmeier, T. Shimada, T. Taddeucci, J. L. Tybo, S. A. Wender, C. H. Wilde, G. A. Wurden, and M. Roth, "Characterization of a novel, short pulse laser-driven neutron sources)," *Physics of Plasmas*, vol. 20, p. 056706, 05 2013.

[47] J. Kim, C. McGuffey, B. Qiao, M. S. Wei, P. E. Grabowski, and F. N. Beg, "Varying stopping and self-focusing of intense proton beams as they heat solid density matter," *Physics of Plasmas*, vol. 23, no. 4, p. 043104, 2016.

[48] J. Ren, Z. Deng, W. Qi, B. Chen, B. Ma, X. Wang, S. Yin, J. Feng, W. Liu, Z. Xu, *et al.*, "Observation of a high degree of stopping for laser-accelerated intense proton beams in dense ionized matter," *Nature Communications*, vol. 11, no. 1, pp. 1–7, 2020.

[49] H. M. MOTT-SMITH, "History of "plasmas"," *Nature*, vol. 233, pp. 219–219, Sep 1971.

[50] M. E. Glinsky, "Regimes of suprathermal electron transport," *Physics of Plasmas*, vol. 2, no. 7, pp. 2796–2806, 1995.

[51] D. Yakovlev and V. Urpin, "Thermal and electrical conductivity in white dwarfs and neutron stars," *Soviet Astronomy*, vol. 24, p. 303, 1980.

[52] K. Eidmann, J. Meyer-ter Vehn, T. Schlegel, and S. Hüller, "Hydrodynamic simulation of subpicosecond laser interaction with solid-density matter," *Phys. Rev. E*, vol. 62, pp. 1202–1214, Jul 2000.

[53] N. W. Ashcroft and N. D. Mermin, *Solid State Physics*. Holt-Saunders, 1976.

[54] B. Chimier, V. T. Tikhonchuk, and L. Hallo, "Heating model for metals irradiated by a subpicosecond laser pulse," *Phys. Rev. B*, vol. 75, p. 195124, May 2007.

[55] L. Spitzer Jr, *Physics of Fully Ionized Gases*. Interscience Publishers Inc., 1956.

[56] A. S. Sandhu, A. K. Dharmadhikari, and G. R. Kumar, "Time resolved evolution of structural, electrical, and thermal properties of copper irradiated by an intense ultrashort laser pulse," *Journal of Applied Physics*, vol. 97, no. 2, p. 023526, 2005.

[57] G. Faussurier and C. Blancard, "Resistivity saturation in warm dense matter," *Phys. Rev. E*, vol. 91, p. 013105, Jan 2015.

[58] N. Wetta and J.-C. Pain, "Consistent approach for electrical resistivity within ziman's theory from solid state to hot dense plasma: Application to aluminum," *Phys. Rev. E*, vol. 102, p. 053209, Nov 2020.

[59] M. Passoni, V. T. Tikhonchuk, M. Lontano, and V. Y. Bychenkov, "Charge separation effects in solid targets and ion acceleration with a two-temperature electron distribution," *Phys. Rev. E*, vol. 69, p. 026411, Feb 2004.

[60] E. Nardi, Z. Zinamon, E. Stambulchik, U. Zastrau, E. Kroupp, I. Uschmann, G. G. Paulus, and Y. Maron, "Target heating in femtosecond laser–plasma interactions: Quantitative analysis of experimental data," *Physics of Plasmas*, vol. 28, no. 2, p. 023101, 2021.

[61] W. L. Kruer, *The Physics of Laser Plasma Interactions*. CRC Press and Taylor & Francis Group, first ed., 2003.

[62] P. Gibbon, *Short pulse laser interactions with matter: an introduction*. World Scientific, 2005.

[63] A. B. Langdon, "Nonlinear inverse bremsstrahlung and heated-electron distributions," *Phys. Rev. Lett.*, vol. 44, pp. 575–579, Mar 1980.

[64] S. Wilks and W. Kruer, "Absorption of ultrashort, ultra-intense laser light by solids and overdense plasmas," *IEEE Journal of Quantum Electronics*, vol. 33, pp. 1954 –1968, nov 1997.

[65] D. Forslund, J. Kindel, and K. Lee, "Theory of hot-electron spectra at high laser intensity," *Physical Review Letters*, vol. 39, no. 5, p. 284, 1977.

[66] K. Estabrook and W. L. Kruer, "Properties of resonantly heated electron distributions," *Physical Review Letters*, vol. 40, no. 1, p. 42, 1978.

[67] F. Brunel, "Not-so-resonant, resonant absorption," *Phys. Rev. Lett.*, vol. 59, pp. 52–55, Jul 1987.

[68] S. Kato, B. Bhattacharyya, A. Nishiguchi, and K. Mima, "Wave breaking and absorption efficiency for short pulse p-polarized laser light in a very steep density gradient," *Physics of Fluids B: Plasma Physics*, vol. 5, no. 2, pp. 564–570, 1993.

[69] W. L. Kruer and K. Estabrook, "J x b heating by very intense laser light," *Physics of Fluids*, vol. 28, no. 1, pp. 430–432, 1985.

[70] S. C. Wilks, W. L. Kruer, M. Tabak, and A. B. Langdon, "Absorption of ultra-intense laser pulses," *Phys. Rev. Lett.*, vol. 69, pp. 1383–1386, Aug 1992.

[71] M. P. Kalashnikov, P. V. Nickles, T. Schlegel, M. Schnuerer, F. Billhardt, I. Will, W. Sandner, and N. N. Demchenko, "Dynamics of laser-plasma interaction at $10^{18}$ w/cm$^2$," *Phys. Rev. Lett.*, vol. 73, pp. 260–263, Jul 1994.

[72] G. Malka and J. L. Miquel, "Experimental confirmation of ponderomotive-force electrons produced by an ultrarelativistic laser pulse on a solid target," *Phys. Rev. Lett.*, vol. 77, pp. 75–78, Jul 1996.

[73] D. R. Rusby, C. D. Armstrong, G. G. Scott, M. King, P. McKenna, and D. Neely, "Effect of rear surface fields on hot, refluxing and escaping electron populations via numerical simulations," *High Power Laser Science and Engineering*, vol. 7, p. E45, 2019.

[74] M. Allen, P. K. Patel, A. Mackinnon, D. Price, S. Wilks, and E. Morse, "Direct experimental evidence of back-surface ion acceleration from laser-irradiated gold foils," *Phys. Rev. Lett.*, vol. 93, p. 265004, Dec 2004.

[75] S. C. Wilks, A. B. Langdon, T. E. Cowan, M. Roth, M. Singh, S. Hatchett, M. H. Key, D. Pennington, A. MacKinnon, and R. A. Snavely, "Energetic proton generation in ultra-intense laser–solid interactions," *Physics of Plasmas*, vol. 8, no. 2, pp. 542–549, 2001.

[76] A. J. Mackinnon, M. Borghesi, S. Hatchett, M. H. Key, P. K. Patel, H. Campbell, A. Schiavi, R. Snavely, S. C. Wilks, and O. Willi, "Effect of plasma scale length on multi-mev proton production by intense laser pulses," *Phys. Rev. Lett.*, vol. 86, pp. 1769–1772, Feb 2001.

[77] J. Fernández, B. Albright, F. Beg, M. Foord, B. Hegelich, J. Honrubia, M. Roth, R. Stephens, and L. Yin, "Fast ignition with laser-driven proton and ion beams," *Nuclear Fusion*, vol. 54, p. 054006, apr 2014.

[78] J. E. Crow, P. L. Auer, and J. E. Allen, "The expansion of a plasma into a vacuum," *Journal of Plasma Physics*, vol. 14, no. 1, p. 65–76, 1975.

[79] J. Allen and J. Andrews, "A note on ion rarefaction waves," *Journal of Plasma Physics*, vol. 4, no. 1, pp. 187–194, 1970.

[80] P. Mora, "Thin-foil expansion into a vacuum," *Phys. Rev. E*, vol. 72, p. 056401, Nov 2005.

[81] P. Mora, "Collisionless expansion of a gaussian plasma into a vacuum," *Physics of Plasmas*, vol. 12, no. 11, p. 112102, 2005.

[82] R. A. Snavely, M. H. Key, S. P. Hatchett, T. E. Cowan, M. Roth, T. W. Phillips, M. A. Stoyer, E. A. Henry, T. C. Sangster, M. S. Singh, S. C. Wilks, A. MacKinnon, A. Offenberger, D. M. Pennington, K. Yasuike, A. B. Langdon, B. F. Lasinski, J. Johnson, M. D. Perry, and E. M. Campbell, "Intense high-energy proton beams from petawatt-laser irradiation of solids," *Phys. Rev. Lett.*, vol. 85, pp. 2945–2948, Oct 2000.

[83] A. J. Mackinnon, Y. Sentoku, P. K. Patel, D. W. Price, S. Hatchett, M. H. Key, C. Andersen, R. Snavely, and R. R. Freeman, "Enhancement of proton acceleration by hot-electron recirculation in thin foils irradiated by ultraintense laser pulses," *Phys. Rev. Lett.*, vol. 88, p. 215006, May 2002.

[84] Y. Sentoku, T. Cowan, A. Kemp, and H. Ruhl, "High energy proton acceleration in interaction of short laser pulse with dense plasma target," *Physics of plasmas*, vol. 10, no. 5, pp. 2009–2015, 2003.

[85] D. S. Hey, M. E. Foord, M. H. Key, S. L. LePape, A. J. Mackinnon, P. K. Patel, Y. Ping, K. U. Akli, R. B. Stephens, T. Bartal, F. N. Beg, R. Fedosejevs, H. Friesen, H. F. Tiedje, and Y. Y. Tsui, "Laser-accelerated proton conversion efficiency thickness scaling," *Physics of Plasmas*, vol. 16, no. 12, p. 123108, 2009.

[86] H. Ruhl, S. Bulanov, T. Cowan, and Liseĭ, "Computer simulation of the three-dimensional regime of proton acceleration in the interaction of laser radiation with a thin spherical target,"

[87] N. B. D. Phil., "Ii. on the theory of the decrease of velocity of moving electrified particles on passing through matter," *The London, Edinburgh, and Dublin Philosophical Magazine and Journal of Science*, vol. 25, no. 145, pp. 10–31, 1913.

[88] H. Bethe, "Zur theorie des durchgangs schneller korpuskularstrahlen durch materie," *Annalen der Physik*, vol. 397, no. 3, pp. 325–400, 1930.

[89] F. Bloch, "Bremsvermögen von atomen mit mehreren elektronen," *Zeitschrift für Physik*, vol. 81, no. 5, pp. 363–376, 1933.

[90] J. F. Ziegler, "Stopping of energetic light ions in elemental matter," *Journal of Applied Physics*, vol. 85, no. 3, pp. 1249–1272, 1999.

[91] J. D. Jackson, *Classical Electrodynamics*. John Wiley & Sons, 1998.

[92] N. I. of Standards and N. Technology, "Stopping-power range tables for electrons, protons, and helium ions."

[93] J. F. Ziegler, "The stopping and range of ions in matter."

[94] B. A. Trubnikov, "Particle Interactions in a Fully Ionized Plasma," *Reviews of Plasma Physics*, vol. 1, p. 105, Jan. 1965.

[95] E. Nardi, E. Peleg, and Z. Zinamon, "Energy deposition by fast protons in pellet fusion targets," *The Physics of Fluids*, vol. 21, no. 4, pp. 574–579, 1978.

[96] T. A. Mehlhorn, "A finite material temperature model for ion energy deposition in ion-driven inertial confinement fusion targets," *Journal of Applied Physics*, vol. 52, no. 11, pp. 6522–6532, 1981.

[97] K. A. Brueckner, L. Senbetu, and N. Metzler, "Stopping power for energetic ions in solids and plasmas," *Phys. Rev. B*, vol. 25, pp. 4377–4382, Apr 1982.

[98] D. S. Hey, *Laser-accelerated proton beams: Isochoric heating and conversion efficiency*. PhD dissertation, University of California, Davis, 2007.

[99] J. Lindhard, "On the properties of a gas of charged particles," *Mat. Fys. Medd. - Dan. Vid. Selsk.*, vol. 28, no. 8, 1954.

[100] J. Lindhard, M. Scharff, and H. Schiott, "Range concepts and heavy ion range," *Mat. Fys. Medd. - Dan. Vid. Selsk.*, vol. 33, no. 33, p. 14, 1963.

[101] J. Lindhard, A. Winther, *et al.*, "Stopping power of electron gas and equipartition rule," vol. 33, no. 4, 1964.

[102] J. Lindhard and M. Scharff, "Energy loss in matter by fast particles of low charge," vol. 27, no. 15, 1953.

[103] P. Wang, T. M. Mehlhorn, and J. J. MacFarlane, "A unified self-consistent model for calculating ion stopping power in icf plasma," *Physics of Plasmas*, vol. 5, no. 8, pp. 2977–2987, 1998.

[104] G. Maynard and C. Deutsch, "Energy loss and straggling of ions with any velocity in dense plasmas at any temperature," *Phys. Rev. A*, vol. 26, pp. 665–668, Jul 1982.

[105] R. Courant, K. Friedrichs, and H. Lewy, "Über die partiellen differenzengleichungen der mathematischen physik," *Mathematische annalen*, vol. 100, no. 1, pp. 32–74, 1928.

[106] D. R. Welch, D. V. Rose, M. E. Cuneo, R. B. Campbell, and T. A. Mehlhorn, "Integrated simulation of the generation and transport of proton beams from laser-target interaction," *Physics of Plasmas*, vol. 13, no. 6, p. 063105, 2006.

[107] D. W. Hewett and A. Bruce Langdon, "Electromagnetic direct implicit plasma simulation," *Journal of Computational Physics*, vol. 72, no. 1, pp. 121–155, 1987.

[108] B. I. Cohen, A. Langdon, D. W. Hewett, and R. J. Procassini, "Performance and optimization of direct implicit particle simulation," *Journal of Computational Physics*, vol. 81, no. 1, pp. 151–168, 1989.

[109] B. I. Cohen, A. Langdon, and A. Friedman, "Implicit time integration for plasma simulation," *Journal of Computational Physics*, vol. 46, no. 1, pp. 15–38, 1982.

[110] D. Welch, D. Rose, B. Oliver, and R. Clark, "Simulation techniques for heavy ion fusion chamber transport," *Nuclear Instruments and Methods in Physics Research Section A: Accelerators, Spectrometers, Detectors and Associated Equipment*, vol. 464, no. 1, pp. 134–139, 2001. Pfoc. of the 13th Int. Symp. on Heavy Ion Intertial Fusion.

[111] S. Atzeni, A. Schiavi, and J. R. Davies, "Stopping and scattering of relativistic electron beams in dense plasmas and requirements for fast ignition," *Plasma Physics and Controlled Fusion*, vol. 51, p. 015016, Dec 2008.

[112] M. E. Jones, D. S. Lemons, R. J. Mason, V. A. Thomas, and D. Winske, "A grid-based coulomb collision model for pic codes," *Journal of Computational Physics*, vol. 123, no. 1, pp. 169–181, 1996.

[113] J. R. Davies, "How wrong is collisional monte carlo modeling of fast electron transport in high-intensity laser-solid interactions?," *Phys. Rev. E*, vol. 65, p. 026407, Jan 2002.

[114] Y. T. Lee and R. M. More, "An electron conductivity model for dense plasmas," *The Physics of Fluids*, vol. 27, no. 5, pp. 1273–1286, 1984.

[115] R. Jeanloz, P. M. Celliers, G. W. Collins, J. H. Eggert, K. K. M. Lee, R. S. McWilliams, S. Brygoo, and P. Loubeyre, "Achieving high-density states through shock-wave loading of precompressed samples," *Proceedings of the National Academy of Sciences*, vol. 104, no. 22, pp. 9172–9177, 2007.

[116] J. Dai, Y. Hou, D. Kang, H. Sun, J. Wu, and J. Yuan, "Structure, equation of state, diffusion and viscosity of warm dense fe under the conditions of a giant planet core," *New Journal of Physics*, vol. 15, p. 045003, apr 2013.

[117] N. Booth, A. Robinson, P. Hakel, R. Clarke, R. Dance, D. Doria, L. Gizzi, G. Gregori, P. Koester, L. Labate, *et al.*, "Laboratory measurements of resistivity in warm dense plasmas relevant to the microphysics of brown dwarfs," *Nature communications*, vol. 6, p. 8742, 2015.

[118] C.-K. Li and R. D. Petrasso, "Charged-particle stopping powers in inertial confinement fusion plasmas," *Phys. Rev. Lett.*, vol. 70, pp. 3059–3062, May 1993.

[119] A. Macchi, M. Borghesi, and M. Passoni, "Ion acceleration by superintense laser-plasma interaction," *Rev. Mod. Phys.*, vol. 85, pp. 751–793, May 2013.

[120] A. Mancic, J. Robiche, P. Antici, P. Audebert, C. Blancard, P. Combis, F. Dorchies, G. Faussurier, S. Fourmaux, M. Harmand, R. Kodama, L. Lancia, S. Mazevet, M. Nakatsutsumi, O. Peyrusse, V. Recoules, P. Renaudin, R. Shepherd, and J. Fuchs, "Isochoric heating of solids by laser-accelerated protons: Experimental characterization and self-consistent hydrodynamic modeling," *High Energy Density Physics*, vol. 6, no. 1, pp. 21 – 28, 2010.

[121] W. Bang, B. J. Albright, P. A. Bradley, E. L. Vold, J. C. Boettger, and J. C. Fernández, "Uniform heating of materials into the warm dense matter regime with laser-driven quasi-monoenergetic ion beams," *Phys. Rev. E*, vol. 92, p. 063101, Dec 2015.

[122] G. Dyer, B. Cho, A. Bernstein, T. Ditmire, R. Shepherd, H. Chen, Y. Ping, P. K. Patel, and L. Elberson, "Single-shot time resolved expansion and emission measurements of proton-heated warm dense matter," in *2007 Quantum Electronics and Laser Science Conference*, pp. 1–2, IEEE, 2007.

[123] D. Hoarty, T. Guymer, S. James, E. Gumbrell, C. Brown, M. Hill, J. Morton, and H. Doyle, "Equation of state studies of warm dense matter samples heated by laser produced proton beams," *High Energy Density Physics*, vol. 8, no. 1, pp. 50 – 54, 2012.

[124] G. M. Dyer, A. C. Bernstein, B. I. Cho, J. Osterholz, W. Grigsby, A. Dalton, R. Shepherd, Y. Ping, H. Chen, K. Widmann, and T. Ditmire, "Equation-of-state measurement of dense plasmas heated with fast protons," *Phys. Rev. Lett.*, vol. 101, p. 015002, Jul 2008.

[125] A. McKelvey, G. Kemp, P. Sterne, A. Fernandez-Panella, R. Shepherd, M. Marinak, A. Link, G. Collins, H. Sio, J. King, *et al.*, "Thermal conductivity measurements of proton-heated warm dense aluminum," *Scientific reports*, vol. 7, no. 1, pp. 1–10, 2017.

[126] A. Zylstra, J. Frenje, P. Grabowski, C. Li, G. Collins, P. Fitzsimmons, S. Glenzer, F. Graziani, S. Hansen, S. Hu, *et al.*, "Measurement of charged-particle stopping in warm dense plasma," *Physical review letters*, vol. 114, no. 21, p. 215002, 2015.

[127] D. Wu, X. He, W. Yu, and S. Fritzsche, "Monte carlo approach to calculate proton stopping in warm dense matter within particle-in-cell simulations," *Physical Review E*, vol. 95, no. 2, p. 023207, 2017.

[128] M. Gauthier, S. Chen, A. Levy, P. Audebert, C. Blancard, T. Ceccotti, M. Cerchez, D. Doria, V. Floquet, E. Lamour, *et al.*, "Charge equilibrium of a laser-generated carbon-ion beam in warm dense matter," *Physical review letters*, vol. 110, no. 13, p. 135003, 2013.

[129] L. Fletcher, H. Lee, T. Döppner, E. Galtier, B. Nagler, P. Heimann, C. Fortmann, S. LePape, T. Ma, M. Millot, *et al.*, "Ultrabright x-ray laser scattering for dynamic warm dense matter physics," *Nature photonics*, vol. 9, no. 4, p. 274, 2015.

[130] P. Sperling, E. Gamboa, H. Lee, H. Chung, E. Galtier, Y. Omarbakiyeva, H. Reinholz, G. Röpke, U. Zastrau, J. Hastings, *et al.*, "Free-electron x-ray laser measurements of

collisional-damped plasmons in isochorically heated warm dense matter," *Physical review letters*, vol. 115, no. 11, p. 115001, 2015.

[131] M. Gauthier, "Report on proton and ion beam measurements at the matter in extreme condition (mcc) end station at slac national accelerator laboratory," *SLAC Technical Report*, 2 2016.

[132] P. Celliers and A. Ng, "Optical probing of hot expanded states produced by shock release," *Phys. Rev. E*, vol. 47, pp. 3547–3565, May 1993.

[133] S. H. Glenzer and R. Redmer, "X-ray thomson scattering in high energy density plasmas," *Reviews of Modern Physics*, vol. 81, no. 4, p. 1625, 2009.

[134] M. Borghesi, J. Fuchs, S. Bulanov, A. Mackinnon, P. Patel, and M. Roth, "Fast ion generation by high-intensity laser irradiation of solid targets and applications," *Fusion Science and Technology*, vol. 49, no. 3, pp. 412–439, 2006.

[135] J. J. Macfarlane, I. E. Golovkin, and P. R. Woodruff, "HELIOS-CR A 1-D radiation-magnetohydrodynamics code with inline atomic kinetics modeling," *jqsrt*, vol. 99, pp. 381–397, May 2006.

[136] E. d'Humières, E. Lefebvre, L. Gremillet, and V. Malka, "Proton acceleration mechanisms in high-intensity laser interaction with thin foils," *Physics of plasmas*, vol. 12, no. 6, p. 062704, 2005.

[137] J. S. Green, A. P. L. Robinson, N. Booth, D. C. Carroll, R. J. Dance, R. J. Gray, D. A. MacLellan, P. McKenna, C. D. Murphy, D. Rusby, and L. Wilson, "High efficiency proton beam generation through target thickness control in femtosecond laser-plasma interactions," *Applied Physics Letters*, vol. 104, no. 21, pp. –, 2014.

[138] M. Roth, I. Alber, V. Bagnoud, C. Brown, R. Clarke, H. Daido, J. Fernandez, K. Flippo, S. Gaillard, C. Gauthier, *et al.*, "Proton acceleration experiments and warm dense matter research using high power lasers," *Plasma Physics and Controlled Fusion*, vol. 51, no. 12, p. 124039, 2009.

[139] K. Bhutwala, M. Bailly-Grandvaux, J. Kim, M. Dozieres, E. Galtier, C. B. Curry, M. Gauthier, E. Cunningham, H. J. Lee, P. Forestier-Colleoni, A. Higginson, N. Aybar, R. Hua, B. C. Edghill, J. Strehlow, G. M. Dyer, S. H. Glenzer, J. B. Kim, N. Alexander, E. D. Rio, M. Wei, Y. Ping, A. McKelvey, G. W. Collins, F. N. Beg, and C. McGuffey, "Development of a Platform at the Matter in Extreme Conditions End Station for Characterization of Matter Heated by Intense Laser-Accelerated Protons," *IEEE Transactions on Plasma Science*, vol. 48, pp. 2751–2758, Aug. 2020.

[140] A. J. Mackinnon, P. K. Patel, M. Borghesi, R. C. Clarke, R. R. Freeman, H. Habara, S. P. Hatchett, D. Hey, D. G. Hicks, S. Kar, M. H. Key, J. A. King, K. Lancaster, D. Neely, A. Nikkro, P. A. Norreys, M. M. Notley, T. W. Phillips, L. Romagnani, R. A. Snavely, R. B. Stephens, and R. P. J. Town, "Proton radiography of a laser-driven implosion," *Phys. Rev. Lett.*, vol. 97, p. 045001, Jul 2006.

[141] J. Cobble, R. Johnson, T. Cowan, N. Renard-Le Galloudec, and M. Allen, "High resolution laser-driven proton radiography," *Journal of applied physics*, vol. 92, no. 4, pp. 1775–1779, 2002.

[142] L. Gao, H. Ji, G. Fiksel, W. Fox, M. Evans, and N. Alfonso, "Ultrafast proton radiography of the magnetic fields generated by a laser-driven coil current," *Physics of Plasmas*, vol. 23, no. 4, p. 043106, 2016.

[143] R. Roycroft, P. Bradley, E. McCary, B. Bowers, H. Smith, G. Dyer, B. Albright, S. Blouin, P. Hakel, H. Quevedo, *et al.*, "Experiments and simulations of isochorically heated warm

dense carbon foam at the texas petawatt laser," *Matter and Radiation at Extremes*, vol. 6, no. 1, p. 014403, 2021.

[144] A. Kemp, S. Wilks, E. Hartouni, and G. Grim, "Generating kev ion distributions for nuclear reactions at near solid-density using intense short-pulse lasers," *Nature communications*, vol. 10, no. 1, pp. 1–8, 2019.

[145] J. Green, V. Ovchinnikov, R. Evans, K. Akli, H. Azechi, F. Beg, C. Bellei, R. Freeman, H. Habara, R. Heathcote, *et al.*, "Effect of laser intensity on fast-electron-beam divergence in solid-density plasmas," *Physical review letters*, vol. 100, no. 1, p. 015003, 2008.

[146] J. J. Honrubia and J. Meyer-ter Vehn, "Fast ignition of fusion targets by laser-driven electrons," *Plasma Physics and Controlled Fusion*, vol. 51, no. 1, p. 014008, 2008.

[147] S. Chen, S. Atzeni, T. Gangolf, M. Gauthier, D. Higginson, R. Hua, J. Kim, F. Mangia, C. McGuffey, J.-R. Marquès, *et al.*, "Experimental evidence for the enhanced and reduced stopping regimes for protons propagating through hot plasmas," *Scientific reports*, vol. 8, no. 1, pp. 1–12, 2018.

[148] X. Vaisseau, A. Morace, M. Touati, M. Nakatsutsumi, S. Baton, S. Hulin, P. Nicolai, R. Nuter, D. Batani, F. Beg, *et al.*, "Collimated propagation of fast electron beams accelerated by high-contrast laser pulses in highly resistive shocked carbon," *Physical review letters*, vol. 118, no. 20, p. 205001, 2017.

[149] K. Mima, J. Fuchs, T. Taguchi, J. Alvarez, J. Marquès, S. Chen, T. Tajima, and J. Perlado, "Self-modulation and anomalous collective scattering of laser produced intense ion beam in plasmas," *Matter and Radiation at Extremes*, vol. 3, no. 3, pp. 127–134, 2018.

[150] S. N. Chen, M. Gauthier, M. Bazalova-Carter, S. Bolanos, S. Glenzer, R. Riquier, G. Revet, P. Antici, A. Morabito, A. Propp, M. Starodubtsev, and J. Fuchs, "Absolute dosimetric

characterization of gafchromic ebt3 and hdv2 films using commercial flat-bed scanners and evaluation of the scanner response function variability," *Review of Scientific Instruments*, vol. 87, no. 7, p. 073301, 2016.

[151] T. J. Bartal, *Investigation of Proton Focusing and Conversion Efficiency for Proton Fast Ignition*. PhD thesis, University of California, San Diego, Jan. 2012.

[152] C. B. Curry, C. A. S. Dunning, M. Gauthier, H.-G. J. Chou, F. Fiuza, G. D. Glenn, Y. Y. Tsui, M. Bazalova-Carter, and S. H. Glenzer, "Optimization of radiochromic film stacks to diagnose high-flux laser-accelerated proton beams," *Review of Scientific Instruments*, vol. 91, no. 9, p. 093303, 2020.

[153] C. Stoeckl, G. Fiksel, D. Guy, C. Mileham, P. Nilson, T. Sangster, M. Shoup III, and W. Theobald, "A spherical crystal imager for omega ep," *Review of Scientific Instruments*, vol. 83, no. 3, p. 033107, 2012.

[154] L. Jarrott, M. Wei, C. McGuffey, F. Beg, P. Nilson, C. Sorce, C. Stoeckl, W. Theoboald, H. Sawada, R. Stephens, *et al.*, "Calibration and characterization of a highly efficient spectrometer in von hamos geometry for 7-10 kev x-rays," *Review of Scientific Instruments*, vol. 88, no. 4, p. 043110, 2017.

[155] K. U. Akli, M. H. Key, H. K. Chung, S. B. Hansen, R. R. Freeman, M. H. Chen, G. Gregori, S. Hatchett, D. Hey, N. Izumi, J. King, J. Kuba, P. Norreys, A. J. Mackinnon, C. D. Murphy, R. Snavely, R. B. Stephens, C. Stoeckel, W. Theobald, and B. Zhang, "Temperature sensitivity of Cu $K_\alpha$ imaging efficiency using a spherical Bragg reflecting crystal," *Physics of Plasmas*, vol. 14, p. 023102, Feb. 2007.

[156] J. Honrubia, A. Morace, and M. Murakami, "On intense proton beam generation and transport in hollow cones," *Matter and Radiation at Extremes*, vol. 2, no. 1, pp. 28–36, 2017.

[157] M. Roth and M. Schollmeier, "Ion acceleration—target normal sheath acceleration," *Proceedings of the CAS-CERN Accelerator School: Plasma Wake Acceleration*, vol. 1, p. 231, 2016.

[158] C. Brabetz, S. Busold, T. Cowan, O. Deppert, D. Jahn, O. Kester, M. Roth, D. Schumacher, and V. Bagnoud, "Laser-driven ion acceleration with hollow laser beams," *Physics of Plasmas*, vol. 22, no. 1, p. 013105, 2015.

[159]

[160] M. G. Pia, G. Weidenspointner, M. Augelli, L. Quintieri, P. Saracco, M. Sudhakar, and A. Zoglauer, "Pixe simulation with geant4," *IEEE transactions on nuclear science*, vol. 56, no. 6, pp. 3614–3649, 2009.

[161] C. Hombourger, "An empirical expression for k-shell ionization cross section by electron impact," *Journal of Physics B: Atomic, Molecular and Optical Physics*, vol. 31, no. 16, p. 3693, 1998.

[162] J. Honrubia and M. Murakami, "Ion beam requirements for fast ignition of inertial fusion targets," *Physics of Plasmas*, vol. 22, no. 1, p. 012703, 2015.

[163] R. Govil, W. P. Leemans, E. Y. Backhaus, and J. S. Wurtele, "Observation of return current effects in a passive plasma lens," *Phys. Rev. Lett.*, vol. 83, pp. 3202–3205, Oct 1999.

[164] C. Joshi, "The development of laser- and beam-driven plasma accelerators as an experimental field," *Physics of Plasmas*, vol. 14, no. 5, p. 055501, 2007.

[165] A. Alejo, A. G. Krygier, H. Ahmed, J. T. Morrison, R. J. Clarke, J. Fuchs, A. Green, J. S. Green, D. Jung, A. Kleinschmidt, Z. Najmudin, H. Nakamura, P. Norreys, M. Notley, M. Oliver, M. Roth, L. Vassura, M. Zepf, M. Borghesi, R. R. Freeman, and S. Kar, "High

flux, beamed neutron sources employing deuteron-rich ion beams from dsub2/subo-ice layered targets," *Plasma Physics and Controlled Fusion*, vol. 59, p. 064004, apr 2017.

[166] M. A. Dorf, I. D. Kaganovich, E. A. Startsev, and R. C. Davidson, "Collective focusing of intense ion beam pulses for high-energy density physics applications," *Physics of Plasmas*, vol. 18, no. 3, p. 033106, 2011.

[167] I. D. Kaganovich, R. C. Davidson, M. A. Dorf, E. A. Startsev, A. B. Sefkow, E. P. Lee, and A. Friedman, "Physics of neutralization of intense high-energy ion beam pulses by electrons," *Physics of Plasmas*, vol. 17, no. 5, p. 056703, 2010.

[168] K. Bhutwala, C. McGuffey, W. Theobald, O. Deppert, J. Kim, P. M. Nilson, M. S. Wei, Y. Ping, M. E. Foord, H. S. McLean, P. K. Patel, A. Higginson, M. Roth, and F. N. Beg, "Transport of an intense proton beam from a cone-structured target through plastic foam with unique proton source modeling," *Phys. Rev. E*, vol. 105, p. 055206, May 2022.

[169] A. Lévy, F. Dorchies, M. Harmand, C. Fourment, S. Hulin, O. Peyrusse, J. J. Santos, P. Antici, P. Audebert, J. Fuchs, L. Lancia, A. Mancic, M. Nakatsutsumi, S. Mazevet, V. Recoules, P. Renaudin, and S. Fourmaux, "X-ray absorption for the study of warm dense matter," *Plasma Physics and Controlled Fusion*, vol. 51, p. 124021, nov 2009.

[170] D. Wu, W. Yu, Y. T. Zhao, D. H. H. Hoffmann, S. Fritzsche, and X. T. He, "Particle-in-cell simulation of transport and energy deposition of intense proton beams in solid-state materials," *Phys. Rev. E*, vol. 100, p. 013208, Jul 2019.

[171] A. R. Bell, J. R. Davies, S. Guerin, and H. Ruhl, "Fast-electron transport in high-intensity short-pulse laser - solid experiments," *Plasma Physics and Controlled Fusion*, vol. 39, pp. 653–659, may 1997.

[172] A. Robinson, D. Strozzi, J. Davies, L. Gremillet, J. Honrubia, T. Johzaki, R. Kingham,

M. Sherlock, and A. Solodov, "Theory of fast electron transport for fast ignition," *Nuclear Fusion*, vol. 54, p. 054003, apr 2014.

[173] P. Norreys, D. Batani, S. Baton, F. N. Beg, R. Kodama, P. Nilson, P. Patel, F. Pérez, J. Santos, R. Scott, V. Tikhonchuk, M. Wei, and J. Zhang, "Fast electron energy transport in solid density and compressed plasma," *Nuclear Fusion*, vol. 54, p. 054004, apr 2014.

[174] A. P. L. Robinson and M. Sherlock, "Magnetic collimation of fast electrons produced by ultraintense laser irradiation by structuring the target composition," *Physics of Plasmas*, vol. 14, no. 8, p. 083105, 2007.

[175] P. Leblanc and Y. Sentoku, "Scaling of resistive guiding of laser-driven fast-electron currents in solid targets," *Phys. Rev. E*, vol. 89, p. 023109, Feb 2014.

[176] S. Chawla, M. S. Wei, R. Mishra, K. U. Akli, C. D. Chen, H. S. McLean, A. Morace, P. K. Patel, H. Sawada, Y. Sentoku, R. B. Stephens, and F. N. Beg, "Effect of target material on fast-electron transport and resistive collimation," *Phys. Rev. Lett.*, vol. 110, p. 025001, Jan 2013.

[177] M. Bailly-Grandvaux, J. Kim, C. M. Krauland, S. Zhang, M. Dozières, M. S. Wei, W. Theobald, P. E. Grabowski, J. J. Santos, P. Nicolaï, P. McKenna, M. P. Desjarlais, and F. N. Beg, "Transport of kJ-laser-driven relativistic electron beams in cold and shock-heated vitreous carbon and diamond," *New Journal of Physics*, vol. 22, p. 033031, mar 2020.

[178] J. R. Davies, "Electric and magnetic field generation and target heating by laser-generated fast electrons," *Phys. Rev. E*, vol. 68, p. 056404, Nov 2003.

[179] H. Bethe, "Bremsformel für elektronen relativistischer geschwindigkeit," *Zeitschrift für Physik*, vol. 76, no. 5, pp. 293–299, 1932.

[180] J. A. Oertel, R. Aragonez, T. Archuleta, C. Barnes, L. Casper, V. Fatherley, T. Heinrichs, R. King, D. Landers, F. Lopez, P. Sanchez, G. Sandoval, L. Schrank, P. Walsh, P. Bell, M. Brown, R. Costa, J. Holder, S. Montelongo, and N. Pederson, "Gated x-ray detector for the national ignition facility," *Review of Scientific Instruments*, vol. 77, no. 10, p. 10E308, 2006.